Cranfield University

Author: Andre Arelius Marcus Munoz

Imaging Near-Field Compton Backscattered X-Rays using Pinhole and Coded Masks

Cranfield Defence & Security

Degree: Ph.D

Academic Year: 2018 - 2019

Supervisor: Prof. David W. Lane

May 2019

This thesis is submitted in partial fulfilment of the requirements for the Degree of Doctor of Philosophy.

Intentionally blank page

A special dedication to my brothers:

Lincoln Munoz (1963-1998)
Richard Munoz (1971-2002)

Abstract

Research was conducted to understand the behaviour of an X-ray backscatter imaging system using coded masks to view complex scenes. These spatially multiplexing images were compared to those collected using a single pinhole and a commercial flying spot (time multiplexing) imaging system. An X-ray backscatter system was constructed to perform experiments with pinholes and coded masks. A novel fabrication technique adopting 3D printing was developed to rapidly create low-cost alternatives to the traditional drilled tungsten coded masks. Subsequently, this allowed for the retention of ideal square open elements within the mask, along with the benefit of having a self-supporting structure. Conventional methods of manufacturing coded masks compromise the encoding process by using round holes in place of the square elements to achieve a self-supporting structure.

Previous work has suggested that coded masks with a low open fraction (i.e. < 0.5) will yield a higher signal-to-noise ratio than those with a 0.5 open fraction. As part of this study, the following low open fraction coded mask was calculated; dilute uniformly redundant array (DURA), Singer and the biquadratic residue (BR). In total 111 new array patterns were calculated. X-ray backscatter images are presented from examples of these coded masks with images reconstructed via cross-correlation and blind deconvolution. Overall, for coded mask imaging, the best results were from the 19 MURA for its signal-to-noise with a typical 2-12 second (s) exposure time. Consequently, there was little evidence to support the benefit of lower open fractions. Pinhole and coded mask images were somewhat comparable with the pinhole requiring a longer exposure time of 60-300 s. While not ideal due to barrel distortion, the images from the flying spot system exhibited higher signal-to-noise ratios and resolutions but required an exposure time of 70 seconds, longer than those for the MURA.

Acknowledgements

Contents

List of Figures

List of Tables

List of Equations

List of Symbols & Abbreviations

$\dddot{\boldsymbol{G}}$ Balanced Decoding Array (Theoretical)

$\ddot{\boldsymbol{G}}$ Mismatched Decoding Array (Theoretical)

$\ddot{\boldsymbol{D}}$ Cropped, Scaled and Padded Non-Cyclic Part of $\boldsymbol{D}$

$\dot{\boldsymbol{G}}$ Matched Decoding Array of 1 and 0 Elements (Theoretical)

$\dot{\boldsymbol{D}}$ Non-Cyclic Part of $\boldsymbol{D}$

$\boldsymbol{D}$ Encoded Exposures of an Object or Scene Detected with a Camera

$\boldsymbol{M}$ Imaging Mask (in the physical form)

$\boldsymbol{O}$ Object or Imaging Scene

$\boldsymbol{R}$ Reconstructed Array/Image using Cross-Correlation

$\boldsymbol{R}^{\tau}$ Reconstructed Array/Image using Blind Deconvolution at τ Iterations

$\boldsymbol{S_n}$ Summed Reconstructed Correlated Array/Image with n Number of Terms

$\boldsymbol{S_n^{\tau}}$ Summed Reconstructed BD Array/Image with n Number of Terms

s   Second

$\lfloor n \rfloor$ Round Down n to the Nearest Integer

$\otimes$ Cross-Correlation

$\star$	Convolution
$\bar{F}$	Focal Point
$\bar{f}$	Focal Length
$\boldsymbol{A}$	Encoded Array (Theoretical)
$\boldsymbol{G}$	Decoding Array (Theoretical)
χ	Open Fraction
χ_ϕ	Open Fraction of Coded Masks with Round Drilled Apertures
$\chi_\square$	Open Fraction of Encoded Arrays or Coded Masks with Square Elements
Δ	Maximum Tolerance or Deviation from the Correct Scaling Parameter Value
δ	Dirac Delta
ℓ	Displacement or Lag
γ	Photon
$\Im$	Fourier Transform
$\Im^{-1}$	Inverse Fourier Transform
λ	Wavelength
$\mathbb{N}$	Natural Number
μ	Mean
ω	Frequency
ϕ	Diameter or Aperture
ϕ_{AP}	Aperture Size
ρ	Density
ρ_C	Calculated Density
σ	Standard Deviation or Cross Section

$\square$	Square Elements
τ	Iteration
$\underline{\mu}/\underline{\rho}$	Mass Attenuation Coefficient
$\underline{b}'$	Minimum Mask to Detector Distance to avoid Collimation Effects
$\underline{t}$	Mask Thickness or Thickness
$\underline{x}$	Mass Thickness
$\underline{a}$	Object to Mask
$\underline{b}$	Mask to Detector Focal Plane
$\underline{r}^2$	Quadratic Residue
$\underline{r}^4$	Biquadratic Residue
A_i	1D Binary Sequence
B	Background
c	Speed of Light
CNR	Contrast-to-Noise Ratio
dB	Decibel
e^-	Electron
E_b	Electron Binding Energy
E_γ	Photon Energy
h	Planck's Constant
KE_{pe}	Photoelectron Kinetic Energy
L	Length of a 1D Sequence
m_e	Electron Mass
n	Number
N_{NF}	Near-Field Magnification

$p \times q$	Dimensions of an Array
P	Pad or Array Padding (The addition or subtraction of elements in an array)
P_v	Pad Value of P
S	Signal
SNR	Signal-to-Noise Ratio
T	Transmission
t	Time
A_i'	Inverse 1D Binary Sequence
r_e	Electron Radius
ABS	Acrylonitrile Butadiene Styrene
ACF	Auto Correlation Function
Al	Aluminium
Appx	Appendix
AP	Aperture
BD	Blind Deconvolution
BPS	Base Pattern Size
BR	Biquadratic Residue
CAD	Computer-Aided Design
CCD	Charge-Coupled Device
CMI	Coded Mask Imaging
CMOS	Complementary Metal Oxide Semiconductor
CM	Coded Mask (in the physical form)
Cu	Copper
DET	Detector

DURA   Dilute Uniformly Redundant Array

EMR   Electromagnetic Radiation

Eq   Equation

FCFOV   Fully Coded Field of View

Fig   Figure

FOV   Field of View

FWHM   Full Width Half Maximum

I   Number of Open Elements in the Mask

LOF   Low Open Fraction

lp   Line Pair

MSK   Mask

MTA   Machined Tungsten Alloy (Wolfmet$^{\circledR}$ HA190)

MTF   Modulation Transfer Function

MURA   Modified Uniformly Redundant Array

NRA   Non Redundant Array

NTHT   No Two Holes Touching

OBJ   Object

Pb   Lead

PCFOV   Partially Coded Field of View

PLA   Polylactic Acid

PSF   Point Spread Function

ps   Photo-Site Size

px   Pixel

QE   Quantum Efficiency

RANDA	Random Array
RPS	Relative Perspective of a Scene
SF	Spatial Frequency
SMI	Spatial Multiplexing Imaging
TEC	Tungsten Epoxy Composite (Technon® Poly)
TMI	Time Multiplexing Imaging
TP	Twin Prime
URA	Uniformly Redundant Array
WWB	Wax Washer Bolt
W	Tungsten
XBI	X-Ray Backscatter Imaging
Z	Atomic Number

Chapter 1

Introduction

1.1 Introduction

Research into advanced X-ray imaging with the coded mask (CM) or coded aperture (CA) was conducted for defence and security applications. The work is a continuation of theoretical ground work undertaken by the Materials Science and Radiation group at the Cranfield Forensic Institute, which was lead by Prof David Lane. There were two components to the research, that consisted of theoretical and experimental work carried out by students, Anna Vella and Andre Munoz. Theoretical simulations undertaken by Anna Vella involved constructing a ray-tracing model of an X-ray backscatter imaging system similar to the experimental version established at Cranfield University. All experimental work was conducted by the author, Andre Munoz, which formed the fundamental work of this thesis.

Experimental research began with designing and constructing an X-ray backscatter imaging (XBI) system that would accommodate two main types of X-ray optics; the pinhole and coded mask. Masks were manufactured using a novel 3D printing and casting process with polymer print filaments, bismuth alloy, tungsten powder and two-part epoxy resign. Traditional tungsten[1] masks were also manufactured via machine by drilling round holes in place of ideal square elements to achieve a compromised version of the original coded mask pattern. Exposures of multiple scenes (imaging objects) were taken using both the pinhole and coded masks, which were analysed and compared to simulated work. The experiments included comparing and contrasting images captured from masks of different open fractions, where open fraction refers to the fraction of open regions within the CM. Comparisons were also made between an X-ray backscatter imaging system at Cranfield University and a prototype flying spot system at our sponsor's Laboratory; Defence Science and Technology Laboratory (dstl) in Fort Halstead.

The overall aim of the project was to determine the performance of an X-ray backscatter imaging system using coded masks and the effectiveness for use on a remotely controlled robotic vehicle. The type of objects that would mainly be imaged are improvised explosive devices (IDEs) that would pose a threat to national security. Such objects are typically comprised of organic material and range in size with typical sizes around a few centimetres. Also, another research question was to deduce how such an imaging system would compare to a single pinhole mask or flying spot system. A conclusion was made from quantifying final exposures using signal-to-noise ratio values along with the contrast-to-noise ratio and spatial resolution. To elaborate, the objects of varying composition and atomic number were investigated to determine the strength of their backscatter signal and effectiveness for imaging. Such materials include lead, aluminium, copper, nylon 66, PVC and paraffin wax.

---

[1]Tungsten heavy alloy.

The mixture of low and high atomic numbers assisted greater contrast in the final image, ultimately aiding the process of distinguishing wanted signals from its background. There was no direct concern or bias with one quantification method other the other, such as signal-to-noise ratio, contrast-to-noise ration and resolution. That is to say, no single quantification method had greater priority amongst their peers because there was no specific requests by the sponsors to focus on one aspect of the quantification process. Therefore, the experiments presented in this thesis were conducted and parameters were set to equally focus on all of these aspects mentioned above.

1.2   Importance of this Research

Traditional X-ray radiography similar to that found in hospitals involves transmitting radiation through an object to create an image. The object is placed between the source and detector with a shadow projected onto the detector as in Fig. 1.1. Material with a high atomic number (Z) and density such as bone absorb X-rays, while passing through those of low density which includes biological tissue. Both the atomic number and density of an object play a key role in image quality, and provide contrast and sharpness. Generally, objects with high Z produce the best shadows on the detector, due to their high density and therefore, yield greater signals and contrast within the final image. Conversely, low Z objects perform in the opposite way. More recent dual energy transmission radiography systems are more efficient at detecting low Z material, however, detection can sometimes be limited; particularly when the imaging scene contain many objects. Transmission radiography in general requires access to two sides of an object and can present a problem if only one side is accessible. Ultimately, this can be a limiting factor when imaging objects that pose a threat to national security.

Although X-rays are transmitted through or absorbed by an object, radiation scatter may occur from a material of low atomic number. Advances in science have utilised 'Compton scattering' (further explained later) of X-rays to yield single-sided imaging systems. The detector is placed on the same side as the X-ray source, capturing backscattered photons from the object to create an image. Consequently, accessibility issues experienced with transmission imaging are solved by imaging backscattered X-rays. As mentioned above, low atomic materials are efficient at scattering X-rays which render organic material ideal for X-ray backscatter imaging (Bell, 2009, p. 93). Images appear much brighter from relatively high scatter in comparison to objects composed of high Z. XBI has been investigated by a variety of countries and organisations mainly for defence and security. Organisations include the North Atlantic Treaty Organization (NATO), which has applied XBI simulations to detect pressure plates from buried improvised explosive devices (van den Heuvel and

Fiore, 2012).

There are two main methods used for XBI, time and spatial multiplexing imaging (Dinca et al., 2008). Time multiplexing imaging (TMI) is based on controlled backscattered X-rays from a mechanical rotating wheel, that builds up an image over a period of time. This is done by scanning the target with a sweeping X-ray pencil beam, or with the target moving across the field of view of the system. TMI requires no 'resolving medium' such as a lens because scatter in all directions is not an issue. Spatial multiplexing imaging (SMI) forms an image from simultaneous X-ray backscatter from the entire scene. As a result, backscattered radiation travelling in all direction is detected at once, thus, requires the use of a resolving medium due to the high flux. A typical optical camera lens is ineffective for X-rays because the refractive index is approximately 1 for X-ray wavelengths. However, the principle of a pinhole camera has been used to resolve XBI scenes, but at the expense of long exposures times due to low radiation throughput. Applying multiple apertures in the mask gives rise to the coded mask, which has been adopted from 'far-field' X-ray astronomy (Dicke, 1968). An example of this is seen in the imager on board the integral satellite (IBIS) (Bird et al., 2016).

Coded mask imaging (CMI) is important within the field of high energy imaging due to its potential to significantly reduce the exposure time of a scene. In theory, benefits of CMI also include the retention of spatial resolution of a single pinhole mask. Consequently, CMI could find applications in 'near-field' X-ray imaging in the medical sector, industry, (Simpson and Barrett, 1980; Accorsi et al., 2001) and in defence and security (Bell, 2009; Faust, 2002; Datema et al., 2003). Furthermore, applications of CMI can be extended to particle source imaging such as fast neutron imaging (Hausladen et al., 2013; Talebita-her et al., 2012). To summarise the main overall research question for this project, it would be as follows; How does near-field X-ray backscatter imaging perform when using coded masks. How does this compare to imaging with pinhole masks and the flying spot system? Considerations are made for the overall applications of the research, which is to determine the optimum X-ray backscatter imaging system to be mounted onto a remotely operated mobile vehicle.
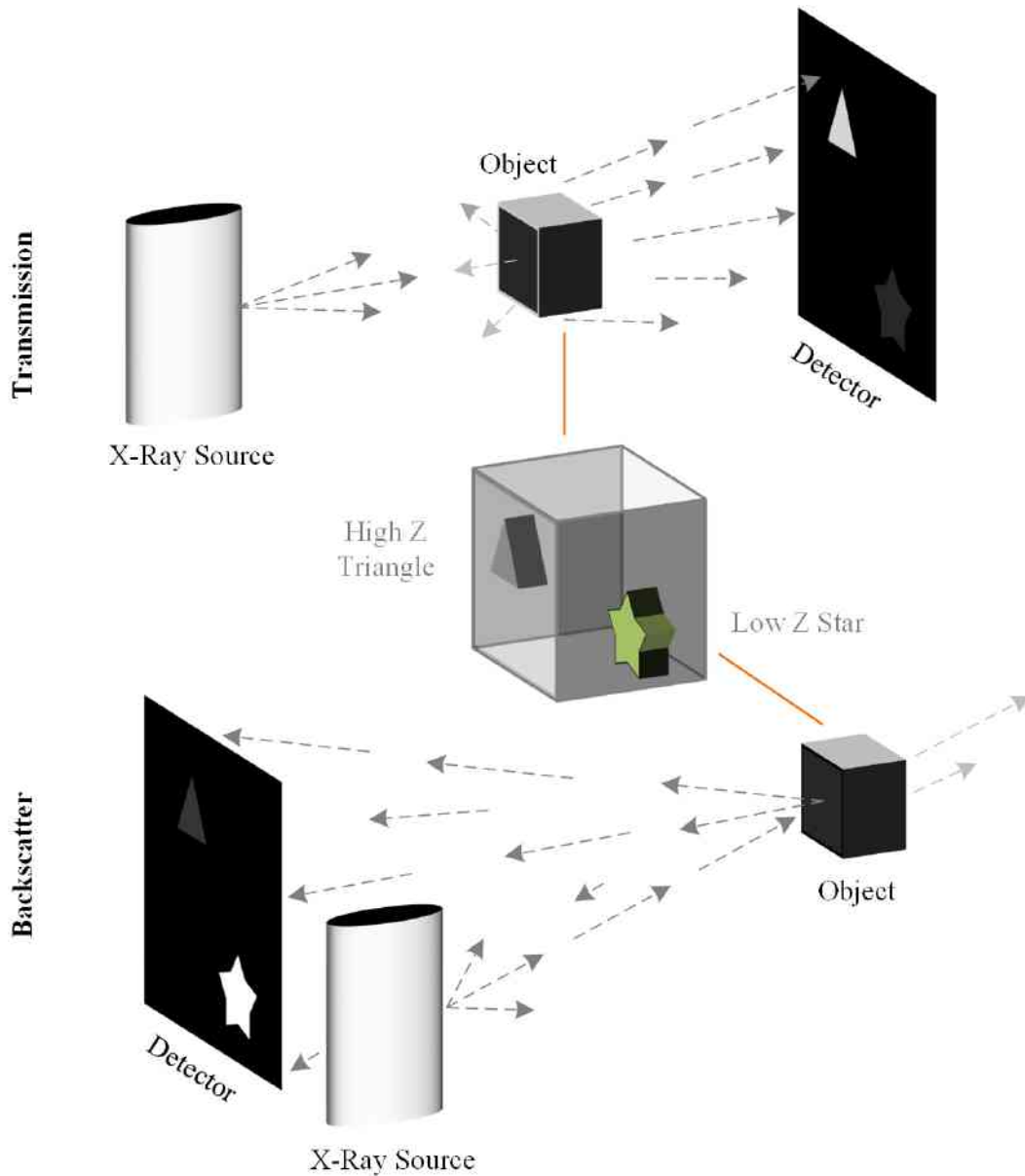
Figure 1.1: Transmission and Backscatter X-Ray Imaging Systems: The Diagram shows a high contrast for objects with greater density and high Z when imaged using traditional transmission methods. Contrast is highest with objects of low Z for the backscatter imaging system.

1.3 Aims of the Project

1. Design and construct an experimental benchtop Compton X-ray backscatter imaging system to capture exposures within a controlled environment.

2. Fabricate coded masks using novel methods of 3D printing and hot and cold casting, to address the common self-supporting structural issue with relatively high production cost.

3. Design and manufacture test imaging objects of various materials and geometries for the X-ray backscatter imaging system.

4. Obtain multiple exposures of different scenes with the X-ray backscatter imaging system to analyse, quantify and to compare with simulation from another Ph.D student at Cranfield University.

5. Perform a comparison of X-ray backscatter images from the flying spot system pinhole masks and coded masks to determine the optimum imaging system for near-field imaging.

6. Determine the performance of the X-ray backscatter imaging systems using coded masks to see the potentials for near-field imaging and uses for defence and security applications.

1.4 Novel Contributions

1. Derived a formula ('Andre's Pinhole Formula', named after the author) to determine the minimum mask to detector distance, to avoid excessive aperture collimation due to the thickness of the mask (Chapter. 3.2.1).

2. Introduced the concept of 'Relative Perspective of a Scene', from shifting the position of a single aperture in the mask and demonstrated an alternative view of the encoding process in coded mask imaging (see Chapter. 3.2.2).

3. Greatly expanded the number of low open fraction array patterns available for research by calculating a number of unpublished arrays, which include Singer arrays (both square and rectangular), dilute uniformly redundant arrays, and biquadratic residues (see Chapter. 6 and Appx. A).

4. Demonstrated vector shifting of an array to achieve ideal imaging properties (see Chapter. 6.2).

5. Determined the tolerance range of scaling parameters for coded mask image reconstruction (see Chapter. 5.2).

6. Introduced a low cost alternative method of fabricating coded masks with self-supporting properties using 3D printing and casting (see Chapter. 4, 8.3 and 10.2).

7. Presented numerous actual X-ray backscatter CM images for a number of novel arrays, such as the dilute uniformly redundant array and Singer array. Previous literature have been limited to mainly simulation and images of a radioactive source (see Chapter. 8).

8. Advanced the field of coded mask imaging by comparing 50 % open fraction arrays to those of lower < 50 % for use with near-field backscatter imaging (see Chapter. 8.2 and 10.1).

9. Comparison of the 'flying spot', pinhole and coded mask by taking X-ray backscatter exposures and quantify the final images (see Chapter. 9).

Chapter 2

Literature Review

2.1 X-Ray Physics

In 1895 an experiment was conducted by a German scientist Wilhelm Conrad Röntgen at the University of Wurzburg (Morrison, 2010). The experiment involved the flow of electrons through an evacuated tube, which was covered with a box to stop radiation from escaping. Once the experiment was in progress Röntgen noticed fluorescence from a Barium Cyanide sample across the laboratory. The cause was from radiation leaking through the experimental setup, with short enough wavelengths to penetrate the box. Radiation was produced by an inverse photoelectric effect (explained later) with electrons striking the tungsten cathode surface. Röntgen subsequently named the unknown radiation after the algebraic symbol 'X', which is now known today as X-rays. X-rays are a form of highly energetic, ionising, electromagnetic radiation (EMR) with wavelengths (λ) around 0.01 - 10 nm. X-rays are generated in an evacuated X-ray or cathode ray tube from the flow of electrons (e^-) between two electrodes (anode and cathode) with a potential difference (see Fig. 2.1). The radiation generated at this stage is sometimes referred to as 'primary X-rays'.
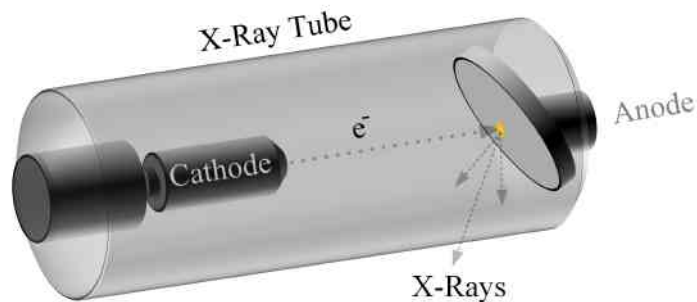
Figure 2.1: X-Ray Tube: Electrons flowing from the cathode to the anode within an evacuated tube producing X-rays.

A high vacuum is maintained in the X-ray tube to avoid particle collision and interaction with air molecules. Thermionic emission takes place from the cathode, emitting electrons at high velocity towards the anode. Kinetic energy from electrons colliding with the anode is conserved and converted into heat. During the process, radiation is emitted over a wide range of the electromagnetic spectrum including X-rays. The intensity of X-rays is determined by an increase in current as the cathode is further heated. When electrons collide with the anode heat is generated on its surface. Wherefore, the anode is usually made from Tungsten and serves as a heat sink to direct heat away from its surface. Also, rotating the anode reduces collisions in one spot which subsequently spreads over the surface of the anode. The surface of the rotating anode is at an angle so that X-rays can escape through a side window. Generated X-rays can interact with matter which has a range of outcomes and

is discussed in the sections to follow.

2.1.1 Photoelectric Effect

The photoelectric effect was introduced by physicist Heinrich Rudolf Hertz in the 1880s, describing an interaction process of radiation with atoms comprising a metallic surface. An electron (also known as a photoelectron) within the atom is released from the kinetic energy (KE_{pe}) when incident radiation with the corresponding energy (E_γ), minus the binding energy (E_b) is absorbed (Bushberg et al., 2012; Cherry et al., 2012; Prince and M, 2015) (see Eq. 2.1).

$$KE_{pe} = E_\gamma - E_b \tag{2.1}$$

A discovery was made by observing the photoelectric effect that contradicted the wave model of EMR. The wave model states that higher intensities of radiation should increase the emitted electron energy. However, this was not the case. A theory proposed by Physicist Albert Einstein (1879-1955), explaining a model of the photoelectric effect. Einstein revealed radiation waves to be quantised discrete particles called photons (γ). Subsequently, radiation can be considered as waves or particles as described by Eq. 2.2 (Hendee and R, 2002; Serway and Jewett Jr, 2011).

$$E_\gamma = \frac{hc}{\lambda} \tag{2.2}$$

2.1.2 X-Ray Scattering

Experiments conducted by physicist Arthur Compton in 1919 demonstrated the particle nature of radiation (Morrison, 2010). A beam of X-rays from a molybdenum electrode was directed onto a graphite target. The X-rays emerging from the target was at right angles to the beam of emission. Compton found that the reflected X-ray wavelength was longer than the initial emission. At the time of the experiment, it was predicted there should be an agreement between the electron vibration and electromagnetic field of X-rays. Thus, radiation of the same frequency and wavelength should be re-emitted from the sample. However, Compton found this to be in disagreement with his experiment. Consequently, this gave rise to the term Compton Scattering. The change in wavelength ($\Delta\lambda$) (Eq. 2.3) is determined by the scatter angle (θ) multiplied by Planck's constant (h) over electron mass (m_e) and speed of light (c).

$$\Delta\lambda = \frac{h}{m_e c}\left(1 - \cos\theta\right) \tag{2.3}$$

There are multiple terminologies that describe the scattering process; which include elastic, inelastic, coherent and incoherent. When energy is conserved during the process, this is referred to as elastic scattering also known as 'classical scattering'. Otherwise, it is inelastic. If the interaction occurs with the whole group of electrons within the atom, the process is coherent (Hendee and R, 2002). Conversely, incoherent scattering describes interaction with a single electron. Radiation from Compton scattering is inelastic and incoherent as energy is lost. Additionally, scattering takes place with a single loosely bound electron in the outer electron shell and at energies corresponding to X and gamma rays (Bushberg et al., 2012; Cherry et al., 2012; Prince and M, 2015). The Klein-Nishina (KN) formula (Klein and Nishina, 1929; Thompson et al., 2009) presented in Eq. 2.4 describes the cross-section σ[1] for scattered photons from a single electron where $k = E/mc^2$, r_e is the electron radius and Ω represents the solid angle. A diagram recreated from Thompson et al. (2009) shows the cross section for both coherent (σ_{coh}) and incoherent (σ_{incoh}) scattering of photons as a function of photon energy.

$$\frac{d\sigma_{KN}}{d\Omega} \cong \frac{r_e^2\left(1 + \cos^2\theta\right)}{2[1 + k\left(1 - \cos^2\theta\right)]^2} \tag{2.4}$$

2.1.3 Characteristic X-Rays

The emission of 'characteristic X-rays' can occur from primary X-rays interacting with electrons within the inner orbital shell of an atom. Essentially, the process is the inverse photoelectric effect and the atom is unstable due to vacant orbital electron shells. Electrons from outer shells fill vacant inner shells, and during the process, a photon is released with the corresponding energy. This process is known as X-Ray Fluorescence (XRF). For example, take a piece of titanium (Ti) sample placed in between a ^{238}Pu radioactive source and a spectrometer. The source produces photons through half-life radiative decay, which then interacts with atoms within the sample. The sample absorbs radiation in the process described above which is re-emitted and detected by a spectrometer. There are characteristic K, L, M and N lines observed which correspond to electron orbital shells from where the radiation is emitted. In addition, the electron orbital shell lines (K, L, M, N) are described as Kα, Kβ and so on. The Greek letters represent transitions of electrons from orbital

---

[1]The σ symbol represents cross-section in this section only. Otherwise the symbol makes reference to the standard deviation.
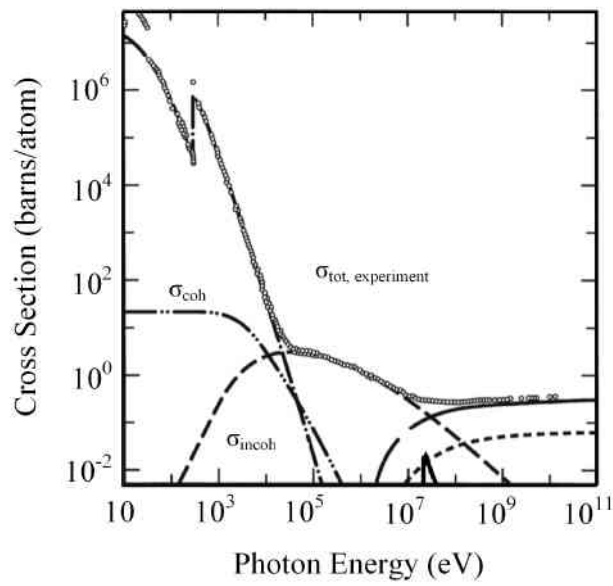
Figure 2.2: Scattering Cross Section Diagram (Thompson et al., 2009): Coherent and incoherent cross sections are presented as σ_{coh} and σ_{incoh}.

shells. E.g. Kα are emission lines from an electron transition of orbital shells L to K (see Fig. 2.3).
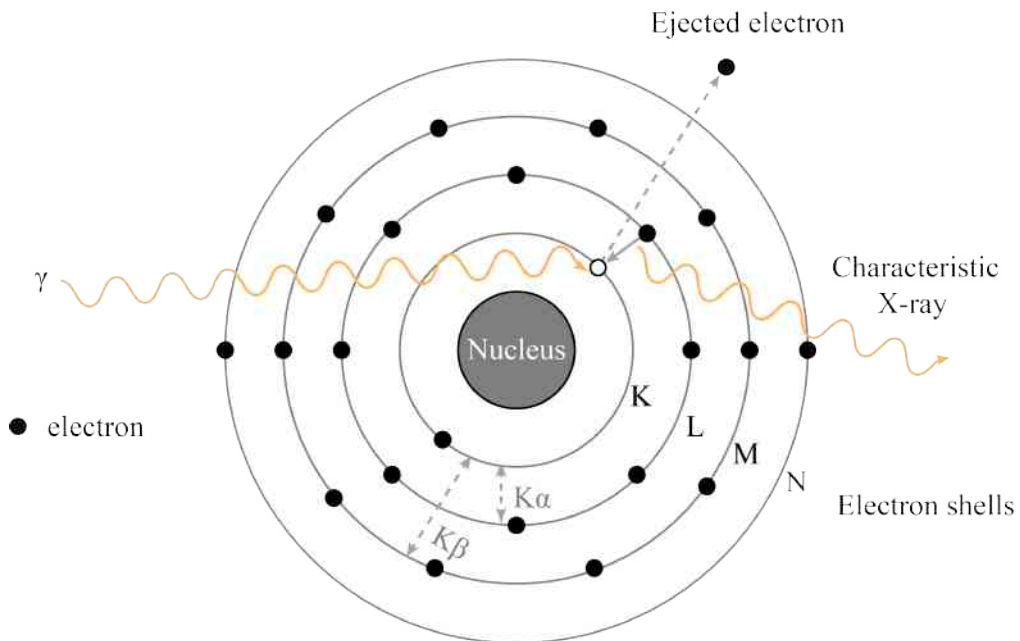
Figure 2.3: The Production of Characteristic X-rays within the Atom: The process within the diagram is known as X-ray florescence.

2.2   Optics & Imaging

An imaging system at the very least, consist of a scene, radiation and a radiation sensitive detector. Within the study of optics, it is commonly known that placing a radiation emitting or reflecting object directly in front of a detector yields no images. The detector is overwhelmed with photons from all directions, and the scene will not be resolved. Resolution is achieved using a traditional camera lens for imaging in the visible range. The lens consist of a convex glass, used to converge 'light' rays to a 'focal point' $(\bar{F})$ on the image plane. Between the point of conversion and $\bar{F}$ is the 'focal length' $(\bar{f})$, the distance it takes from the convergence to the focal point. Consequently, the recorded image is inverted and subsequently corrected. A visual conception can be seen in Fig. 2.4, demonstrating the process for each 'point source' of radiation.
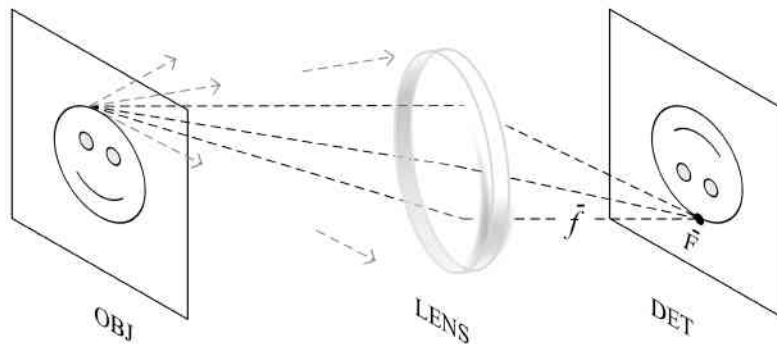
Figure 2.4: Camera Lens: An image is formed onto the detector by the convergence of light within the optical glass lens.

Traditional methods of focusing light onto a detector by means of a convex lens do not apply to high energy EMR. X and gamma rays are high-frequency waves with short wavelengths that typically pass through a standard lens without much interaction. A solution can occur by applying the principle of pinhole optics to form images with high energy EMR.

A conveyance of information about the behaviour of some phenomenon is known as a 'signal' (S). Examples include the propagation of electromagnetic radiation through space as a function of time. Additionally, this can be extended to images, which are two-dimensional (2D) arrays of discrete values as in Fig. 2.5. Each element within the array represent intensity or colour of objects that comprise a scene. The range of intensity is known as 'bit-depth' and is described by 2^n, where n is the number of bits. A 1-bit monochrome image has a range of $2^1 = 2$ with black $= 0$ and white $= 1$. Note, lower values indicate darker pixels. Similarly, grey scale images can have 8-bits ranging in intensity of $0 - 255$ with $2^8 = 256$ values or 16-bits of $2^{16} = 65536$ and so on.

```
0  0  0  0  0  0  0  0
0  0  1  0  0  1  0  0
0  0  1  0  0  1  0  0
0  0  1  1  1  1  0  0    →
0  0  1  0  0  1  0  0
0  0  1  0  0  1  0  0
0  0  0  0  0  0  0  0
```
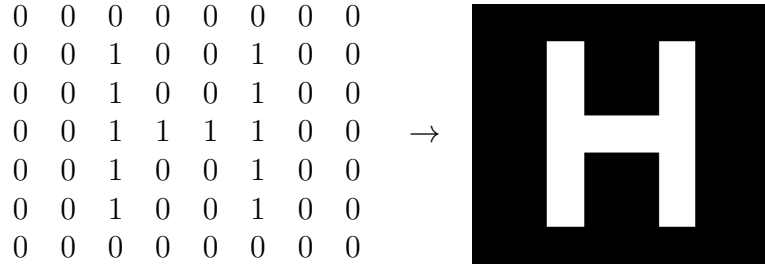
Figure 2.5: 1-bit Digital Image Array Example: (Left) A binary representation of the image presented on the (right).

2.2.1 Pinhole Optics

The *Camera obscura* or 'pinhole' camera dates back hundreds of years and is one of the first lens-less imaging cameras (Young, 1971). A single aperture in a piece of material opaque to the desired wavelength of radiation serves as the resolving medium. The radio-opaque material is described as a 'mask' for the remainder of this thesis and consequently referred to as a 'pinhole mask' if it contains a single aperture. When photons from an object (OBJ) pass through a single aperture (AP) in the mask an inverted image is resolved on a detector (DET) (see Fig. 2.6). Smaller apertures have higher resolving capabilities, but fewer photons are allowed through the opening (Mertz and Young, 1961; Ivanov et al., 1999). As a result, an increase in exposure time is required to build an adequate image. Coded masks provide a solution by increasing the number of apertures to reduce exposure time, while theoretically retaining image resolution (Busboom et al., 1997; Woolf et al., 2015).
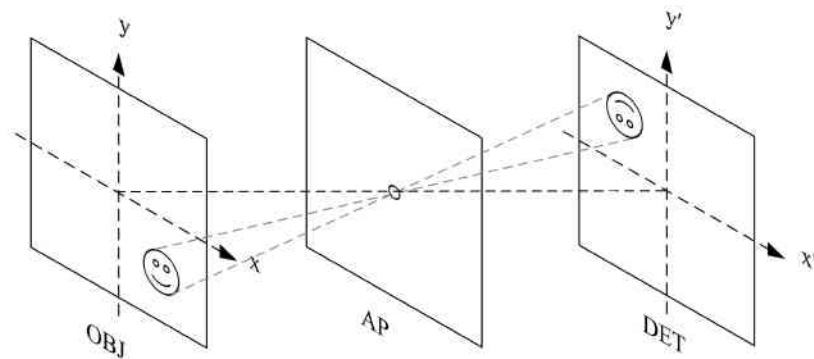
Figure 2.6: Pinhole Camera: Light from the object is resolved through the aperture and detected as an inverted image.

2.2.2   Coded Mask Imaging

Early coded masks were initially used in high energy astronomy (Dicke, 1968) and date back to the 1960s with the Fresnel Zone Plate (Mertz and Young, 1961). Fresnel zone plate are masks containing opaque and transparent concentric rings that allow radiation to pass through to a detector. Optical radiation from the opaque boundaries causes diffraction and zones of constructive interference. Consequently, a focal point is formed for optical light with low resolution. Conversely, diffraction is somewhat irrelevant for X-rays due the their wavelengths being smaller than the opaque boundaries of the mask, so reconstruction takes place from the projected shadow of the rings. The concept of the Fresnel zone plate was further advanced by replacing the concentric rings with a random distribution of apertures in the mask (Dicke, 1968). Previously literature has reported that each opening projects a sum of overlapping images of the object or scene onto a detector, which is unresolvable and encoded (see Fig. 2.7) (Fenimore and Cannon, 1978; Cannon and Fenimore, 1980) (Accorsi, 2001, p. 22).
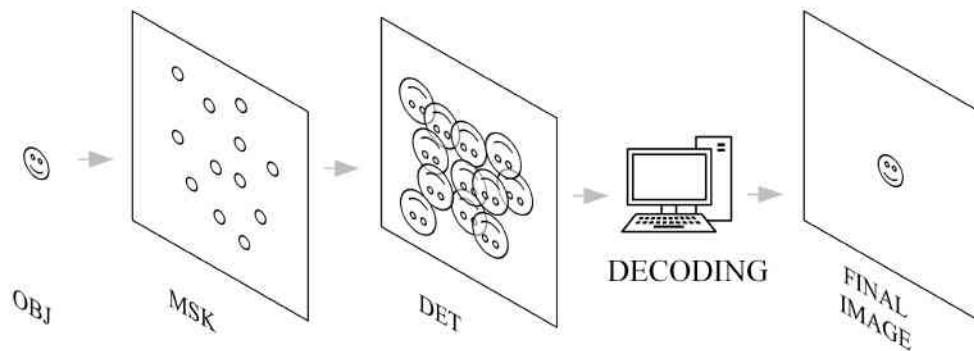
Figure 2.7: Encoding Process: The diagram demonstrates the encoding process of CMI, which is only applicable for imaging far-field scenes. The concept is correct for far-field scenes such as a source at infinity where its relative position would remain the same for each aperture. Conversely, near-field scenes are much closer to the mask, which would see slight changes in the scene from each aperture's relative position in the mask and this is not depicted in the figure.

A decoding procedure must follow to reconstruct a resolvable image of the scene. The encoding and decoding process is performed using mathematical operations common to signal processing including cross-correlation, convolution and deconvolution. However, the process in Fig. 2.7 is not entirely correct, as each opening has a relative perspective of the imaging scene (explained later on). That is to say, different parts of each smiley face in Fig. 2.7 would be projected onto the detector relative to the apertures position on the mask. This is addressed in greater detail in Chapter. 3.2.2.

2.2.2.1 Cross-Correlation

Cross-Correlation ($\otimes$) or cross-covariance is a mathematical operation used to find similarities between signals which in this case are two images. One of the two signals (represented as functions f and h of $g(x,y) = [f \otimes h](x,y)$) is a template or 'kernel' that slides or scans across the other along the x and y axis. As a result, output values are maximised when a match occurs. A mathematical expression of cross-correlation is presented in Equation 2.5 and 2.6 for continuous and discrete signals, where the 'lag', displacement or amount by which the template slides over the main function is represented by ℓ. Also, R is $-\infty \leq x \leq \infty$ and $-\infty \leq y \leq \infty$ (Jordan and Smith, 2008)(Brigham, 1988, p. 65). u and v in Equation 2.5 and 2.6 represent the lag in 2D.

$$[f \otimes h](x,y) = \iint_R f(u,v)h(x+u,y+v)dudv \tag{2.5}$$

$$= \sum_{v=-\ell}^{\ell}\sum_{u=-\ell}^{\ell} f(u,v)h(x+u,y+v) \tag{2.6}$$

When a function is cross-correlated with itself the process is known as an autocorrelation. Commonly, this is sometimes referred to as the autocorrelation function (ACF) and is mathematically described in Eq. 2.7.

$$\text{ACF} = [f \otimes f](x,y) \tag{2.7}$$

2.2.2.2 Convolution

Convolution ($\star$) is another method used to detect similarities between multiple signals, however, the operation differs slightly from cross-correlation with the plus sign in h changed to minus (see Equation 2.8) (Brigham, 1988, p. 50).

$$[f \star h](x,y) = \sum_{v=-\ell}^{\ell}\sum_{u=-\ell}^{\ell} f(u,v)h(x-u,y-v) \tag{2.8}$$

A visual representation of the correlation and convolution process is demonstrated in Fig. 2.8. If f is an image then h may be a template or kernel that scans over f to yield the output array g. The values in each element of g are accumulated individually by conceptually aligning the central element h_0 of

the template over elements in f. This is often referred to as template matching. A multiplication is performed with elements under the template which is subsequently summed as in Eq. 2.9. Similarly, neighbouring elements of g are found by sliding h over f by ℓ (which is usually 1) and then repeating the previous step. When sliding h past the boundary of f an overhang will occur. Consequently, there are no elements for parts of h to multiply with, therefore a pad (P) is required to complete the multiplication stage which is usually 0 (see Fig. 2.9 for example). Alternatively, the pad may be a mirror of adjoining elements in the array.

$$f \begin{vmatrix} P & P & P & P & P \\ P & f_0 & f_1 & f_2 & P \\ P & f_3 & f_4 & f_5 & P \\ P & f_6 & f_7 & f_8 & P \\ P & P & P & P & P \end{vmatrix} \otimes h \begin{vmatrix} h_{-4} & h_{-3} & h_{-2} \\ h_{-1} & h_0 & h_1 \\ h_2 & h_3 & h_4 \end{vmatrix} = g \begin{vmatrix} . & . & . \\ . & g_4 & . \\ . & . & . \end{vmatrix}$$

Figure 2.8: The Cross-Correlation Process: Cross-correlation takes place with the superimposition of array h on top of f so that their central elements are aligned.

$$\begin{aligned} g_4 =& f_0 h_{-4} + f_1 h_{-3} + f_2 h_{-2} + f_3 h_{-1} + f_4 h_0 + \\ & f_5 h_1 + f_6 h_2 + f_7 h_3 + f_8 h_4 \end{aligned} \tag{2.9}$$
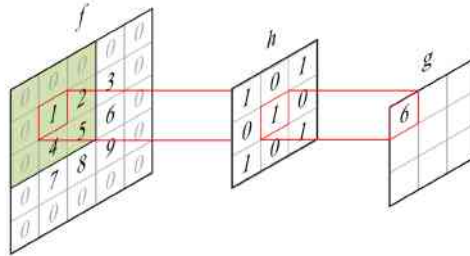
Figure 2.9: Visual Cross-Correlation Process Example: The superimposition of image h on top of f demonstrates how values in g are formed during cross-correlation.

Coordinates of an array generally begin in the upper left corner beginning with $(x = 0, y = 0)$. However, the coordinates of h originate at the centre, thus, this is the reason why template matching starts with the central element. For cross-correlation, the coordinates are negative and positive in the upper and lower corners of the array respectively. This arrives from the application of lower and upper limits $-\ell$ and ℓ in Equation 2.6 with $+u$ and $+v$ resulting in a $-$ and $+$ for the lower and upper limits of coordinates. The coordinates

are reversed for convolution due to the change in signs from $+$ to $-$ as in Eq. 2.8 which then rotates h by 180° (see Fig. 2.10 for example). Consequently, $f \otimes h = f \star h$ If h is symmetrical, otherwise, $f \otimes h(-) = f \star h$ (Bracewell, 2000). The reverse process of convolution is Deconvolution.

$$
h(x,y) \quad
\begin{array}{|ccc|} \hline
\multicolumn{3}{c}{\text{Correlation}} \\
-1,-1 & \cdot & \cdot \\
\cdot & 0,0 & \cdot \\
\cdot & \cdot & 1,1 \\ \hline
\end{array}
\begin{array}{|ccc|} \hline
\multicolumn{3}{c}{\text{Convolution}} \\
1,1 & \cdot & \cdot \\
\cdot & 0,0 & \cdot \\
\cdot & \cdot & -1,-1 \\ \hline
\end{array}
$$

Figure 2.10: Cross-Correlation & Convolution Template: A demonstration of how rotating h by 180 degrees reveals a relationship between cross-correlation and convolution for arrays with symmetry.

2.2.2.3 Fourier Transform

One-dimensional signals can be manifested as waves travelling through space as a function of time (t). The same information can also be conveyed as frequency (ω) or Fourier space. A transformation process used to convert signals from one domain to another is termed the 'Fourier transform' $(\Im)$, named after physicist and mathematician Joseph Fourier (1768-1830) (see Fig. 2.11). Converting signals from the time $f(t)$ to frequency $F(\omega)$ domain is mathematically presented in Eq. 2.10 (Brigham, 1988, p. 9), where $i = \sqrt{-1}$. To convert back to time from the frequency domain the inverse Fourier transform $(\Im^{-1})$ is applied as in Eq. 2.11 (Brigham, 1988, p. 11).

$$F(\omega) = \Im[f(t)] = \int_{-\infty}^{\infty} f(t)e^{-i2\pi\omega t}dt \tag{2.10}$$

$$f(t) = \Im^{-1}[F(\omega)] = \int_{-\infty}^{\infty} F(\omega)e^{-i2\pi\omega t}d\omega \tag{2.11}$$

Fourier transform is very useful in signal processing which is demonstrated by the convolution and correlation theorem. Both theorems reveal a less complex process of achieving results of convolution and correlation by simply multiplying the arrays f and g in Fourier space as in Eq. 2.12 and 2.13, where $*$ is the conjugate (Brigham, 1988).

$$[f \otimes g](t) = F(\omega)H^*(\omega) \tag{2.12}$$

$$[f \star g](t) = F(\omega)H(\omega) \tag{2.13}$$
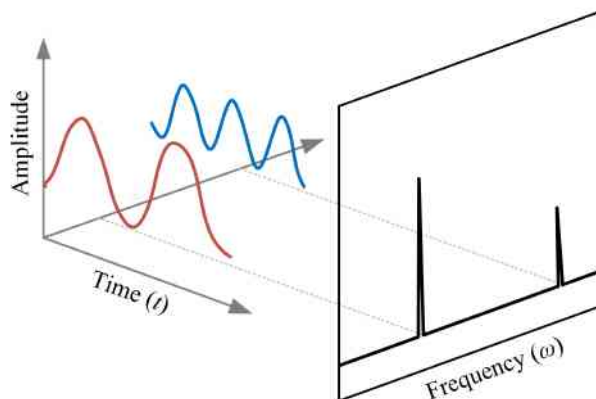
Figure 2.11: Graphical Illustration of the Fourier Transform: The diagram shows the perspective of a signals in the time and frequency domain.

2.2.3 Encoding & Decoding Arrays

Fundamentally, coded masks are based on 2D arrays of 1 and 0 elements that represent open and closed regions of the imaging mask, where the open regions refer to the apertures. It is important to distinguish the different terminologies used in the remainder of this document to avoid ambiguity. Theoretical 'encoding arrays' or coded mask patterns (images) are denoted by $\boldsymbol{A} = A_{i,j}$. When a physical version of the $\boldsymbol{A}$ is constructed onto a mask then the term 'coded mask' is used (CM or $\boldsymbol{M}$). There are a wide variety of encoding array patterns with a range of 'open fractions' (χ) sometimes referred to as the 'aperture density' or 'aperture transmission' (Busboom et al., 1998). Open fraction is the fraction of open elements within the array which can be described in Eq. 2.14 for square elements (χ_{I}), where p and q are vectors that comprise the dimension of the entire array pattern, and n is the number of square open elements $(I_{\square})$. Please note, the $\times$ symbol refers to multiplication and not the mathematically symbol for cross product.

$$\chi_{\square} = \frac{nI_{\square}}{p \times q} \tag{2.14}$$

Decoding arrays $\boldsymbol{G} = G_{i,j}$ are always non-physical and as the names suggest, performs the function of decoding information encoded by the encoding array. The pattern in $\boldsymbol{G}$ is similar to that of $\boldsymbol{A}$ and when $\boldsymbol{A}$ is cross-correlated with $\boldsymbol{G}$ information of the imaging system response can be extracted in the form of a 'point spread function' (PSF) or 'impulse response system' (Bushberg et al., 2012, p. 61). The imaging system in this case is the encoding array and the PSF communicates how it responds to a single point source by presenting a 2D array or image. An ideal PSF displays similar characteristics of the Dirac delta

20

function $\delta(x, y)$, named after theoretical physicist Paul Dirac (1902-1984). The Dirac delta function is a thin 1D line or column in 2D, representing the signal or point source that is equal to 1 and its independent values x and y are equal to 0 (see Fig. 2.12 for example). The mathematical expression for $\delta(x, y)$ is presented in Eq. 2.15, where R is $-\infty \leq x \leq \infty$ and $-\infty \leq y \leq \infty$ (Schmeelk, 1994)(Hecht, 2017, p. 547).

$$\iint_R \delta(x, y) dx dy = 1 \quad \Rightarrow \quad \delta(x, y) = \begin{cases} 1, & \text{if } x, y = 0 \\ 0, & \text{otherwise} \end{cases} \tag{2.15}$$

The PSF of an array pattern used for imaging would be an approximation of that presented in Fig. 2.12 (Gunson and Polychronopulos, 1976). A signal is represented by the central column, and black squares at the base or 'plateau' indicate noise when its intensity is other than 0. All four white lines at the base of the signal that extend out to the boundary illustrate where 'side-lobes' would be located that introduces artefacts when its value is $\neq 0$. Ideally, for imaging, the central column would taper off to a thin point, as the height increases with a plateau and side-lobes equal to zero (see Fig. 2.12).
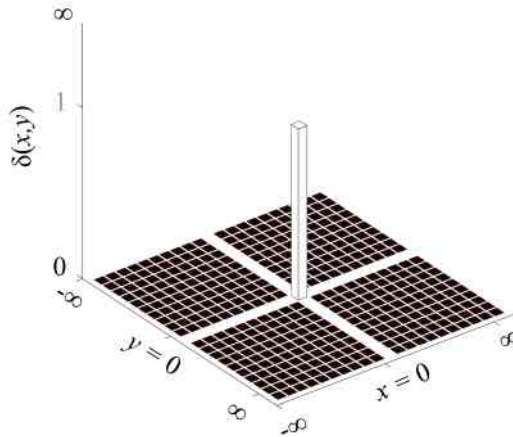
Figure 2.12: δ-Function: The tall central column represents a signal while the base indicates where noise is potentially present. The four white lines at the base are regions where side-lobes can occur. Note, the side-lobes and background are equal to zero, rendering the δ-function to be a good example of PSFs with ideal imaging properties.

When calculating PSFs of encoded arrays in this document the expression in Eq. 2.16 was used which was normalised in order to significantly speed up processing times. $\ddot{G}$ refers to 'balanced' decoding (discussed later on) and it determines the optimum values for closed elements in the array (Accorsi, 2001, p. 68).

$$\delta = \boldsymbol{A} \otimes \ddot{\boldsymbol{G}} \tag{2.16}$$

Earlier methods of decoding $\chi = 0.5$ arrays with randomly generated elements (discussed later on) utilised the 'matched' array ($\dot{\boldsymbol{G}}$), also known as autocorrelation which followed the conditions in Eq. 2.17.

$$G_{i,j} = \begin{cases} 1, & \text{if } A_{i,j} = 1, \\ 0, & \text{if } A_{i,j} = 0, \text{ for } \dot{\boldsymbol{G}} \\ \text{-}1, & \text{if } A_{i,j} = 0, \text{ for } \ddot{\boldsymbol{G}} \\ \eta, & \text{if } A_{i,j} = 0, \text{ for } \dddot{\boldsymbol{G}} \end{cases} \quad \text{where, } \eta = -\frac{\chi}{1-\chi} \tag{2.17}$$

A PSF using $\dot{\boldsymbol{G}}$ resulted in the increase of elemental values within the array as x and y approach zero. Consider the correlation process in Fig. 2.9 where there is no pad for array f. When both arrays f and h are perfectly superimposed, the central elemental value in g is at its highest due to the number of elements that are present when summing. As h scans f the superimposition is now imperfect and there are less elements to sum. Hence, elemental values in g should naturally decrease as h approaches the boundary of f. Subsequently, the PSF of g would have a pyramid shape. To balance the values in the background 'mismatched' ($\ddot{\boldsymbol{G}}$), the conditions in Eq. 2.17 are applied for a $\chi = 0.5$ randomly generated array. Furthermore, this could be applied to other encoded array patterns with $\chi = 0.5$. With the evolution of arrays with lower χ, $\dddot{\boldsymbol{G}}$ is found to be the optimal solution and an extension of $\ddot{\boldsymbol{G}}$, which has the same values when $A_{i,j} = 0$ and $\chi = 0.5$ (Cannon and Fenimore, 1980; Brown, 1974; Fenimore and Cannon, 1978; Accorsi, 2001). An example PSF is shown in Fig. 2.13.

2.2.3.1 Uniformly Redundant Array

The uniformly redundant array (URA) (Fenimore and Cannon, 1978) is a 2D encoded array constructed from a 1D sequence ($\dot{A}_i$) of cyclic different sets. A cyclic different set is a set of positive integers in an initial sequence modulo L, that is less than L (Park, 1972)(Sambo, 2011, p. 133). The length (L) of A_i is a prime number and according to Fenimore and Gottesman (1989) $L = 4n + 1$ yields a vector with symmetrical properties where, $n \in \mathbb{N}$. 1D binary sequences can also be generated without symmetrical properties and to further expand on this, an expression is presented in Eq. 2.18 for L that is both symmetrical and non-symmetrical.
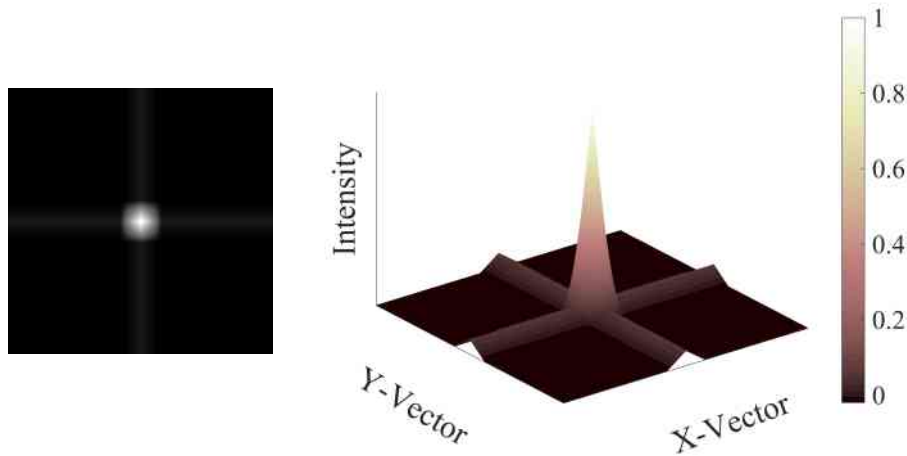
Figure 2.13: Example 2D & 3D PSF: (Left) A 2D PSF and (right) its 3D plot with its normalised pixel intensity.

$$L = \begin{cases} 4n + 1, & \text{for symmetric} \\ 4n + 3, & \text{for non-symmetric} \end{cases}, \; n \in \mathbb{N} \tag{2.18}$$

When L is found values for individual elements of the sequence begin with $[A_i]_{i=0}^{L-1}$. For example, if $L = 5$ then $A_i = 0,1,2,3,4$. Modular arithmetic is used to further calculate the binary elements of the 1D sequence (A_i) to determine any quadratic residues $(\underline{r}^2)$ (see Eq. 2.19), where i is the individual elements of A_i.

$$\underline{r}^2 \equiv i \bmod{L} \tag{2.19}$$

To expand, the values of each element of A_i becomes 1 if it is a quadratic residue of L and 0 otherwise (see Eq. 2.20). Hence, the reason why $\chi = 0.5$ URAs are named quadratic residues.

$$A_i = \begin{cases} 0 & \text{if } i = 0 \\ 1 & \text{if } i \text{ is a quadratic residue modulo } L \\ 0 & \text{otherwise} \end{cases} \tag{2.20}$$

The 1D binary sequence for $L = 5$ develops into $A_i = 0\,1\,0\,0\,1$. Consequently, following $A_{1,1} = 1$ then yields the sequence in Eq. 2.21, with it's inverse (A_i') in Eq. 2.22 that is fundamental for the 'mapping' (Fenimore and Gottesman, 1989) process when generating a 2D array from A_i. Mapping refers to a method

23

of generating 2D arrays by entering the 1D binary sequence in the first row and column. Based on the value of the first column, each row is filled with the 1D binary sequence or it's inverse.

$$A_i = 1\,1\,0\,0\,1 \tag{2.21}$$
$$A'_i = 0\,0\,1\,1\,0 \tag{2.22}$$

The final process of constructing 2D encoded arrays begin with a blank template with vector sizes $p \times q$. 2D URA vectors are twin prime (TP) and follow the form $q = p + 2$, where $p = L$. Namely, if $L = 5$ for a TP URA, then it's vectors $p \times q = 5 \times 7$. Note, to avoid ambiguity the twin prime URA will be referred to as 'TP URA' for the remainder of this document. An example mapping process for a 5×7 TP URA is demonstrated in Fig. 2.14, starting with (a) mapping A_i in the first row of the 2D array template. A_i for this example is taken from Eq. 2.21. However, as the vectors of a TP URA $p \neq q$, a different A_i is generated for q where $L = 7$ and then mapped in the first column of the 2D array. The array template is then complemented with A'_i when $A_{i,1} = 0$ as in Fig. 2.14b to form (c). Subsequently, the final 5×7 TP URA (d) is complete following $A_{i,1} = 1$ then $A_{1,j} = 0$.

	(a)					(b)					(c)					(d)			
1	1	0	0	1	1	1	0	0	1	1	1	0	0	1	0	0	0	0	0
1	.			.	1	.			.	1	1	0	0	1	1	1	0	0	1
1				.	1				.	1	1	0	0	1	1	1	0	0	1
0		.	.		0	0	1	1	0	0	0	1	1	0	1	0	1	1	0
1				.	1				.	1	1	0	0	1	1	1	0	0	1
0			.	.	0			.	.	0	0	1	1	0	1	0	1	1	0
0	.	.	.	.	0	.	.	.	.	0	0	1	1	0	1	0	1	1	0
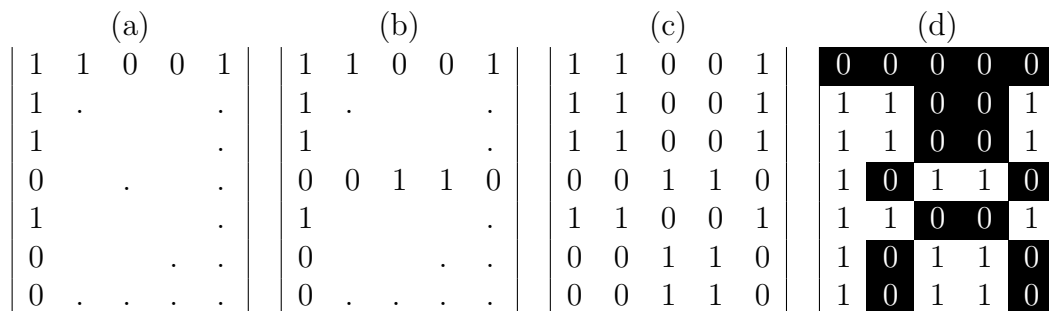
Figure 2.14: Example Mapping Process of a 5×7 TP URA: (a) the initial sequence mapped in the first row and column of the array, (b-c) complementary sequence added, which (d) completes the encoded array.

The uniformly redundant array's name is derived from the fact that all separation distances of open regions are constant (Accorsi, 2001, p. 44). Consequently, neighbouring open regions connect at the corners resulting in a non-self-supporting structure when a physical CM is manufactured. TP URAs are $\chi = 0.5$ with perfect PSFs as in Fig. 2.15.

2.2.3.2 Modified Uniformly Redundant Array

The modified uniformly redundant array (MURA) is part of the URA family sharing similar properties, such as $\chi = 0.5$ (Fenimore and Gottesman, 1989).
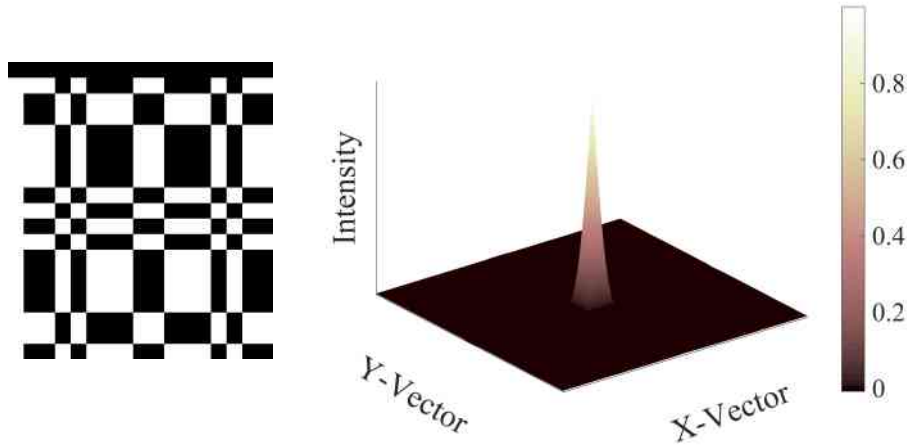
Figure 2.15: 17×19 TP URA and its PSF.

The MURA's vectors are based on prime numbers, following the form $p \times q = 0$. That is to say, both vectors are the same resulting in a perfectly square array. This has an advantage over the TP URA with array sizes limited to a pair of numbers that are twin prime. Conversely, MURAs can be generated from any prime number. Note, for the remainder of this document the vectors of square arrays will be referred to with only one vector (for example; a 5×5 MURA is the same as 5 MURA). MURAs are generated from quadratic residue 1D binary sequences using Eq. 2.18 - 2.20. An example using the $L = 5$ binary sequence in Eq. 2.21 begins with mapping A_i in both the first row and column of the array template as in Fig. 2.16(a). The template array's vector size adheres to $p = q = L$ and complemented with A_i' when $A_{i,1} = 0$, as in Fig. 2.16b. The conditions $A_{i,1} = 1$ then $A_{1,j} = 0$ are applied (see Fig. 2.16c) and a MURA is generated. A centred version may be generated by performing a 'circular shift' (CS) of elements for each vector by $\lfloor L/2 \rfloor$. A circular shift moves the last element of an array so that it becomes the first. See Fig. 2.16d for example. MURAs are either symmetric or invariant depending on Eq. 2.18. If A_i has L that is symmetric, then the generated centred MURA inherits symmetrical properties when rotated every 90° on its central axis. On the other hand, when L is non-symmetric then the MURA posses 'invariant' properties, meaning it's pattern contains 180° rotational symmetry. An example of a symmetric and invariant centred MURA are presented in Fig. 2.17. Note, all MURAs in the remainder of this document are centred by default, thus the term 'centred' will be omitted when describing MURAs. Invariant MURAs that are centred have ideal 'anti-mask' properties (discussed later on) due to their ability to be inverted when rotated 90° (Byard, 2014).

The MURA is commonly chosen for CMI as a result of its ideal imaging properties that are inherent to the design. The PSF of the MURA has a resemblance to that of the TP URA (see Fig. 2.18). The decoding array for the MURA

$$
\begin{array}{ccc}
\text{(a)} & \text{(b)} & \text{(c)} \qquad\qquad \text{(d)}
\end{array}
$$
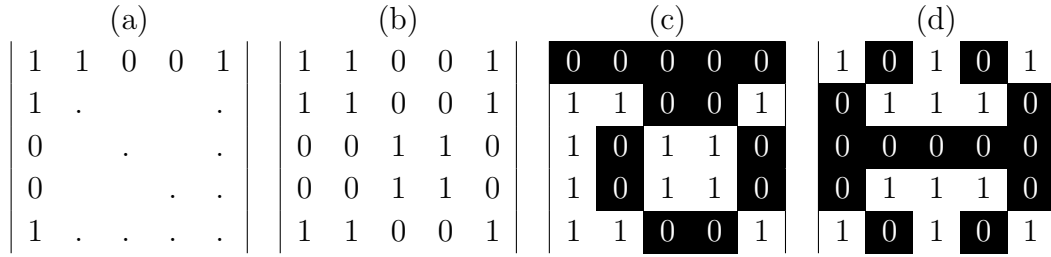
Figure 2.16: Example Mapping Process of a 5 MURA: (a) the initial sequence mapped in the first row and column of the array, (b) complementary sequence added, (c) then the MURA conditions $A_{i,1} = 1$ $A_{1,j} = 0$ are applied which completes the encoded array. (d) a centred version of the encoding array.

(a) Symmetric.   (b) Invariant.
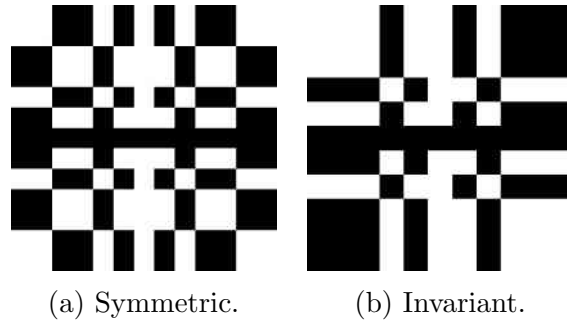
Figure 2.17: Symmetric 13 MURA vs Invariant 11 MURA.

is minutely different from the TP URA, which is modified to follow the form $G_{1,1} = 1$ when $A_{1,1} = 0$ for a non-centred MURA (Fenimore and Gottesman, 1989). Although the MURA's imaging properties are ideal, fabricating a physical CM out of a single piece of material is difficult due to the poor self-supporting structure.
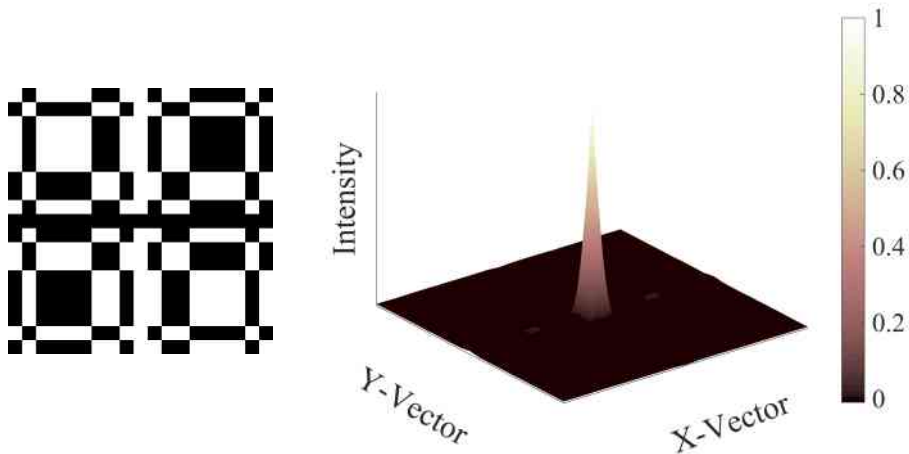
Figure 2.18: 19 MURA and its PSF.

2.2.3.3   Non-Redundant Array

The non-redundant array (NRA) are arrays with separation distances between pairs of apertures that are not repeated. That is to say the separation distances for apertures only occur once (Golay, 1971; Kopilovich, 1988; Fenimore and Cannon, 1978). The result is a PSF consisting of a central spike and side-lobes that are approximately constant, which can oscillate between 1 and 0 but eventually drops to zero (Accorsi, 2001, p. 41). In addition, the side lobes are not uniformly flat (see Fig. 2.19 for an example of a 19 NRA with $\chi = 0.05$) where the 'valley' like feature within the PSF result from the mask pattern configuration. The nature of the element spacing and the fact that the mask pattern has symmetry along one axis may explain such artefacts and the overall reconstructed image will therefore contain artefacts (Fenimore and Cannon, 1978). The peak of the PSF is governed by the open area. The number of holes in known NRAs are small with the largest at 27. Consequently, NRAs have a very low open fraction (Caroli et al., 1987) and in the past have been used in nuclear medicine (Skinner, 1984). Due to the NRAs extremely low open fraction they have good self-supporting properties.
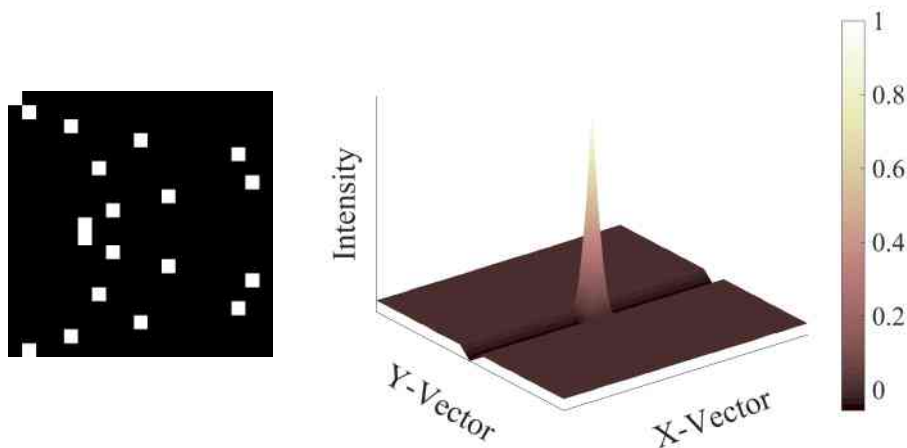
Figure 2.19: 19 NRA and its PSF.

2.2.3.4   Pseudo-Noise Product Array

A Pseudo-noise product array (PNP) is as the name suggests, a product of two pseudo-noise (PN) sequences. 2D PNP arrays have ideal imaging properties from their calculated PSF (see Fig. 2.20). The decoding array differs from those typically found in others, such as the URA and take on the form of that presented in Fig. 2.20. This is because the decoding array is formed from a 'point by point' multiplication of 1D decoding coefficients. It has been postulated that the PN sequences used to make PNPs are formed from 1D quadratic

residues (Accorsi, 2001, p. 51). Consequently, the initial 1D sequences are 0.5 in open fraction and the final array tends to be around $\chi = 0.25$ once constructed. With such low open fraction of the array, this inherently introduces self-supporting properties when fabricating a physical coded mask. However, only a small number of PNP arrays are known due to the complexity of their construction method (Gottesman and Schneid, 1986).

Encoding Array $\boldsymbol{A}$ Decoding Array $\ddot{\boldsymbol{G}}$
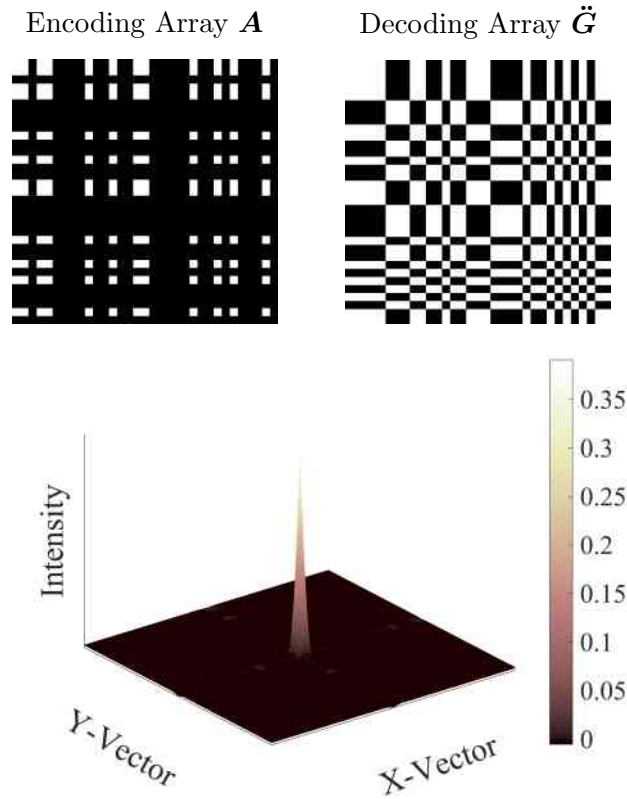
Figure 2.20: 33 PNP Encoding Array, Decoding Array and its PSF.

2.2.3.5   Dilute Uniformly Redundant Array

The dilute uniformly redundant array (DURA) was introduced in the 1980s and are low in open fraction ($\chi < 0.5$) (Barker, 1953; Wild, 1983). Sequences that comprise a DURA are limited in number and are computer generated Barker codes (Accorsi, 2001, p. 47). DURAs inherently contain traits similar to that of a URA's PSF with the plateau levelling at zero, and side-lobes resembling those of a non-redundant array (Golay, 1971; Kopilovich, 1988) (Accorsi, 2001, p. 42). The terminology 'non-redundant' makes reference to the spacing of open elements that are non-repeating. 1D DURA sequence lengths L are limited to 13, 21, 31, 57 and 73. L can be described in Eq. 2.23, where the number of elements within the sequence that are open is assigned the letter I.

28

$$L = I(I - 1) + 1 \tag{2.23}$$

There is little prior publication with regards to constructing 2D DURAs, with the exception of Munoz et al. (2017a). However, to further expand on previous literature, it was found that the same mapping process used for the MURA can be applied when forming 2D DURAs. The 1D binary sequences presented in Wild (1983) are inverted as in Eq. 2.22 to form A_i' which starts the mapping process in Fig. 2.16a. To complete the array, mapping follows by complementing the array with the original sequence (oppose to the MURA which follows with A_i') as in Fig. 2.16b. An example 13 DURA, $\chi = 0.43$ along with it's PSF is presented in Fig. 2.21. There are 15 DURAs in total which is presented in Appx. A, along with their open fractions.
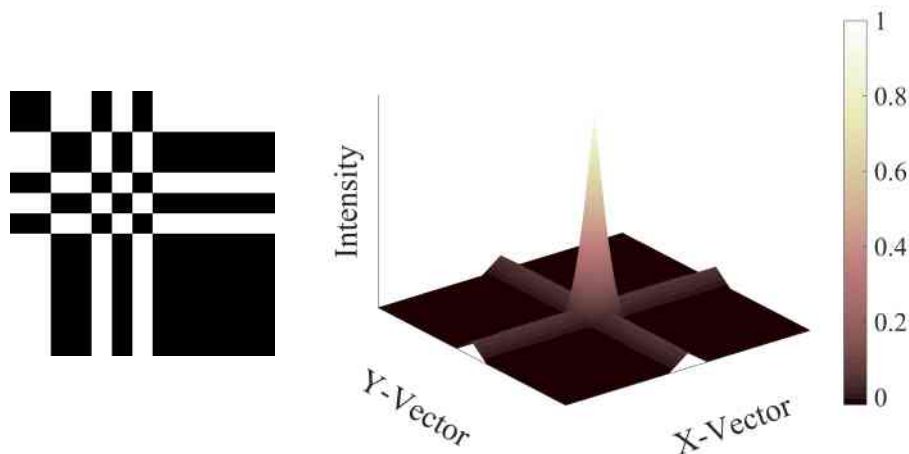
Figure 2.21: 13 DURA and its PSF.

DURAs are sectioned into five groups consisting of 13, 21, 31, 57 and 73, for their vector sizes. An example would see group 21 containing arrays 21×21, 21×31, 21×57 etc. The signal-to-noise ratio (signal-to-noise ratio is discussed later on) of each array shows a trend for groups consisting of square and rectangular arrays. Square arrays perform better than their counterparts because there is an increase in side-lobes in the PSF with non-square arrays. Additionally, the 13 DURA presents the best imaging properties amongst all DURAs. This arises due to a decrease in side-lobe intensity with decreasing vector sizes (see Chapter. 6.1.1 for signal-to-noise ratio values). Like the TP URA, DURAs do not have good self-supporting structures.

2.2.3.6 Biquadratic Residues

A biquadratic residue (BR) is a low open fraction array based on cyclic (different) sets with $\chi = 0.25$. BRs are sometimes referred to as biquadratic residue

'URAs', which may be due to some similarities in its PSF with the TP URA (Nagell, 1951; In 't Zand et al., 1994) (Accorsi, 2001, p. 47). It may be argued that there are no significant similarities for two reasons. One; comparing the PSF of a 26 BR in Fig. 2.22 shows it is dissimilar to that of the 17×19 TP URA in Fig. 2.15 with its plateau and side-lobes equalling to zero. Two; BR array patterns are not 'uniformly redundant'. Nonetheless, BRs or BR 'URAs' do have good imaging properties that are only second to the TP URA and both are based on cyclic difference sets . At the time of writing this document, there appear to be no prior publications on 2D BR array examples with information only on the 1D sequence.
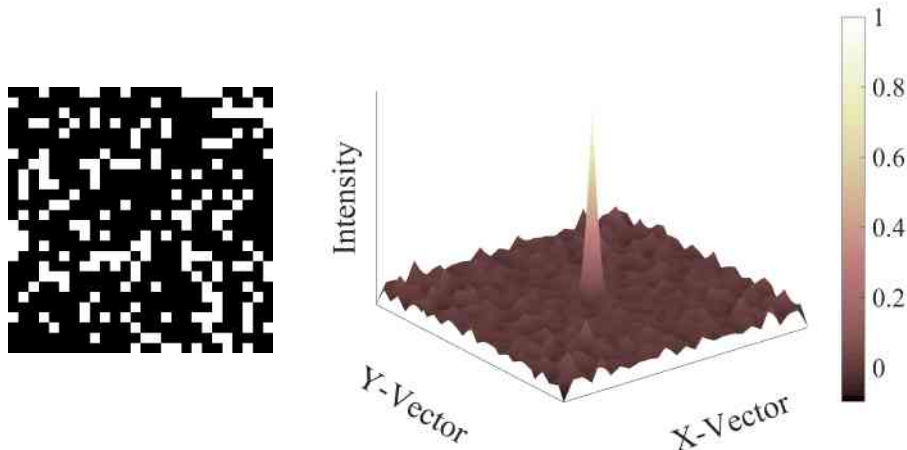
Figure 2.22: 26 BR and its PSF.

Calculating the 1D sequence begins with $L = 4n^2 + 1$ which is prime, where $n \in \mathbb{N}$ that is odd. Note, not all n produces a sequence of $\chi = 0.25$. Once L is determined the initial sequence follows $[A_i]_{i=1}^{L-1}$. A search for biquadratic residues ($\underline{r}^4$) continues the process using $\underline{r}^4 \equiv i$ modulo L, which then follows conditions in Eq. 2.24 to complete the 1D sequence (In 't Zand et al., 1994).

$$A_i = \begin{cases} 0 & \text{if } i = 0 \\ 1 & \text{if } i \text{ is a biquadratic residue modulo } L \end{cases} \tag{2.24}$$

Further expanding on gaps in previous literature, 2D arrays are folded into square arrays. First, the sequence must be padded with an element because L only has a divisor of one, and its 2D vectors p and q must also be divisors. A pad (P) of ± 1 would result in 1 extra element of pad value (P_v) with 0 added or subtracted from A_i to yield $L|p$ and $L|q$. The sequence folding process is presented as an example in Fig. 2.23 using hypothetical values for A_i. In this scenario, $L = 10$, $p = 2$ and $q = 5$ to complete the 2D array $A_{i,j}$. Consequently, that is how arrays such as that in Fig. 2.22 are generated.

$$A_i = 1,\ 2,\ 3,\ 4,\ 5,\ 6,\ 7,\ 8,\ 9,\ 10. \quad \rightarrow \quad A_{i,j} = \begin{vmatrix} 1 & 6 \\ 2 & 7 \\ 3 & 8 \\ 4 & 9 \\ 5 & 10 \end{vmatrix}$$

Figure 2.23: An Example of Sequence Folding.

There are many arrays > 100 that can be generated using the above technique. However, only a few rectangular arrays suitable for imaging can be constructed, and have been calculated and presented in Appx. A. Although BR arrays are 'partially redundant' , not all open elements of BRs touch at the corners, however they still lacks self-supporting properties.

2.2.3.7 Singer Array

The Singer array (Singer) previously referred to as Singer 'URAs' in other literature (Busboom et al., 1998) is based on cyclic difference sets (Baumert, 1971; Shutler et al., 2013, 2014). Similar to the BR, its array pattern does not have features that are uniformly redundant, neither does its PSF bear similarities to that of the TP URA. This can be seen in Fig. 2.24 with the plateau not equalling to zero as presented in Fig. 2.15. Though not perfect, Singers poses good imaging qualities due to a low-level plateau.
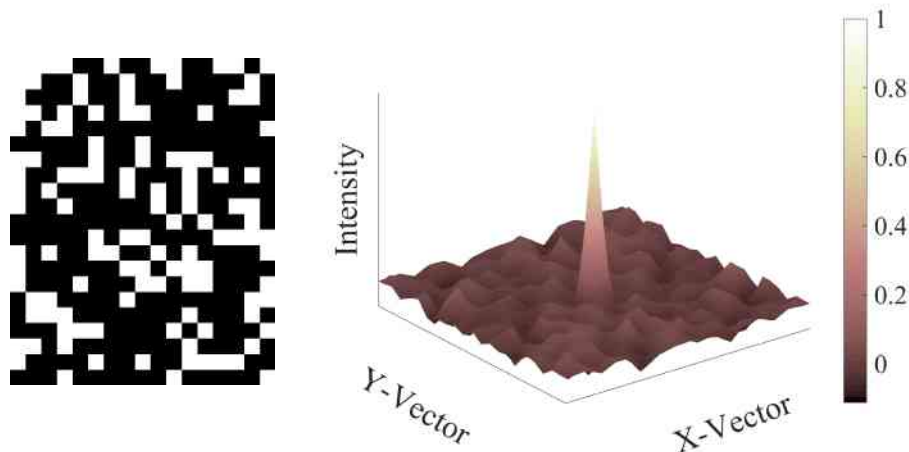
Figure 2.24: 17×21 Singer and its PSF.

Singer open fractions vary with vector sizes following the rule of being co-prime. The 1D sequence (A_i) is generated from a feedback shift register defined by the number of shifts (ν) and $\Theta = 1/\chi$ (see Eq. 2.25).

$$A_i = \frac{\Theta^\nu - 1}{\Theta - 1} \qquad (2.25)$$

An executable program 'cdsgen.exe' has been previously published by Shutler et al. (2013) which calculates the 1D sequence based upon χ. Applying conditions in Eq. 2.26 to the generated sequence creates a Singer binary 1D sequence.

$$M_0 = \begin{cases} 0 & \text{if } i > 0 \\ 1 & \text{if } i = 0 \end{cases} \qquad (2.26)$$

Previous literature by Shutler et al. (2013) states that the vectors of a 2D array must be co-prime. The length of some 1D sequences may not be divided perfectly into potential co-prime vectors $p \times q$, thus a pad may be required, which follows Eq. 2.27. Subsequently, the 1D sequence is folded into a 2D array using the technique in Fig. 2.23.

$$p \times q = \begin{cases} A_i & \text{if } p | A_i \\ A_i + P & \text{if } p \nmid A_i \end{cases} \qquad (2.27)$$

A limited number of Singer arrays exist due to their vectors adhering to the co-prime rule. Evidence of this is shown in Shutler et al. (2013). Such limitations contribute to the low number of arrays < 0.5 and it is possibly due to the fact that each 1D sequence must be individually calculated to determine the vectors that are available. Chapter. 6.1.2 details and addresses the problem of the sparse variation of Singer arrays.

2.2.3.8 Random Array

Randomly generated arrays are often referred to as random arrays (RANDA) and were amongst the original CMs used for imaging (Dicke, 1968). The random array's imaging properties are not perfect like the TP URA, nonetheless, it still has rather good imaging properties with a low plateau for its PSF (see Fig. 2.25). An advantage of the random array over CMs mentioned earlier is that there are no limits to its vector sizes, dimension and to a degree the open fraction. RANDAs do not have good self supporting-structures, however, this may improve with lower open fraction arrays.

2.2.3.9 No Two Holes Touching

Fabricating physical CMs of encoded arrays can be challenging due to the lack of self-supporting properties of closed elements. This is more prevalent with
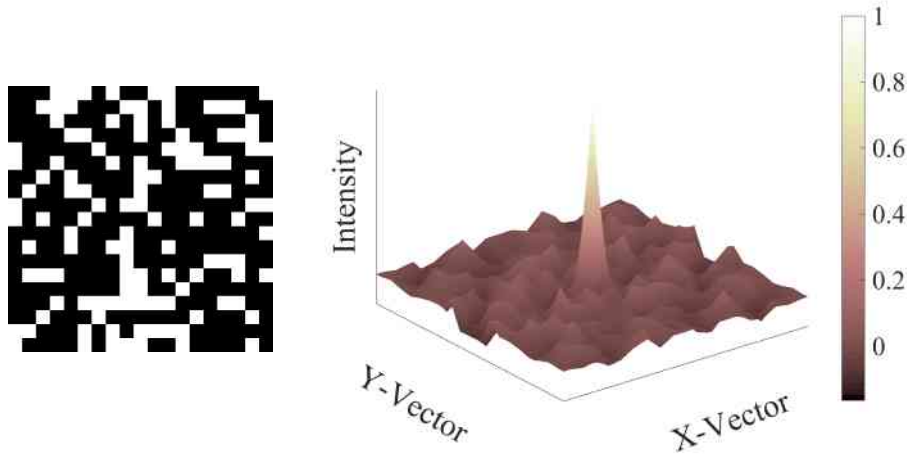
Figure 2.25: 19 Random Array and its PSF.

arrays of higher open fraction such as the $\chi = 0.5$ TP URA, where closed regions are mostly connected to one another at the corners. Introducing 0 elements between each row and column of the encoded array produce a version with 'no two holes touching' (NTHT), as in Fig. 2.26 which is a NTHT of the 19 MURA in Fig. 2.18 (Fenimore and Cannon, 1981). NTHTs degrade the imaging properties of the original array, which is likely a result of the extra row and column of zeros being indistinguishable from those of closed elements. This is evident from the PSF in Fig. 2.26 cross-correlated with $\boldsymbol{A}$ of white = 1 and black = 0 elements with $\ddot{\boldsymbol{G}}$ of white = 1 and black = -1 elements. An improved PSF may be achieved by distinguishing closed elements of $\ddot{\boldsymbol{G}}$. An example PSF is found in Fig. 2.27 showing its $\dddot{\boldsymbol{G}}$ of white = 1, grey = 0 and black = -1 elements. Note, the $\boldsymbol{A}$ in Fig. 2.26 serves as the encoding array for Fig. 2.27 and Fig. 2.28. Similarly, imaging properties of the NTHT can be improved by adopting $\underline{\ddot{\boldsymbol{G}}}$ in Fig. 2.28, which is the original array pattern of white = 1 and black = -1 elements (Note, $\underline{\dddot{\boldsymbol{G}}}$ refers to a modification in the decoding array being the original array pattern). Consequently, the sharp peak in Fig. 2.26-2.27 is now compromised in Fig. 2.28. A summary of NTHT properties including previously mentioned arrays are presented in Table. 2.1.

2.3   Imaging Detectors

A camera consists of a light sensitive detector that collects incoming photons from a source. Photons cannot form an image by themselves, so a conversion process is required to convert the photon signal into a form that is readable as a visual 2D image. Below briefly introduces some detectors used to form an image.

A & $\ddot{G}$
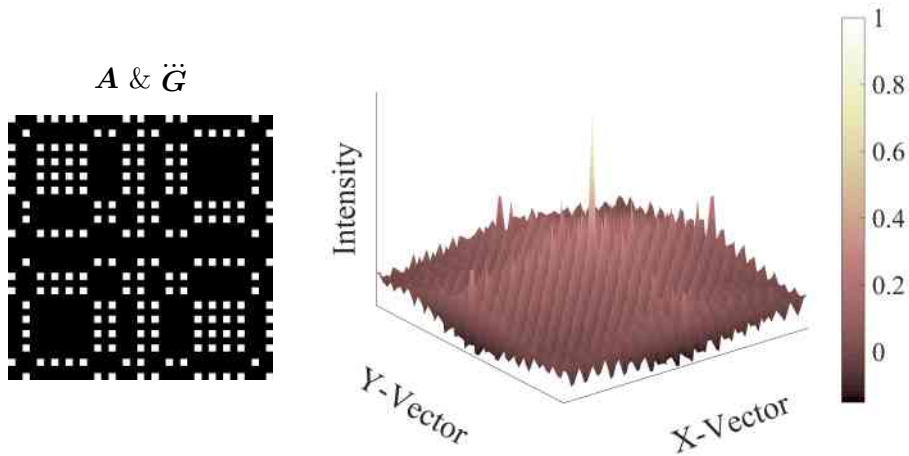
Figure 2.26: NTHT Decoding Method 1.

$\dddot{G}$
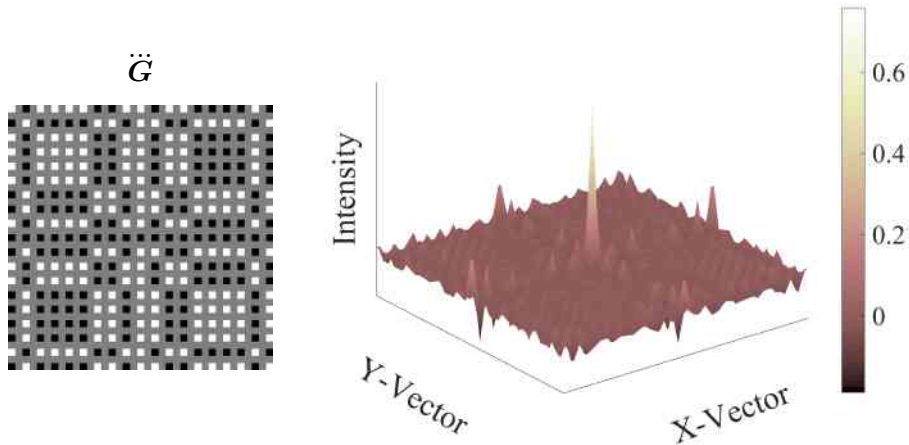
Figure 2.27: NTHT Decoding Method 2 with A in Fig. 2.26.

2.3.1 CCD & CMOS Sensors

Digital imaging detectors utilise a number of sensor types to detect photons from a source. Semiconductor detectors, such as the complementary metal oxide semiconductor (CMOS) and charge-coupled device (CCD) are example sensors used in direct detectors. Incident photons landing on an area of the semiconductor are converted into electrical signals in the form of electrons (e^-). A 2D array of tiny 'Wells' or photo-sites that is microns across, comprise a substrate, which integrates photo-induced charge over time (see Fig. 2.29). The accumulation of e^- reaches saturation when the photo-site is full and it is then discharged or read out from the array during the analogue to digital conversion process. The intensity of the pixel in the final image is proportional to the number of electrons in each photo-site.

$$\overset{\cdots}{\underline{\boldsymbol{G}}}$$
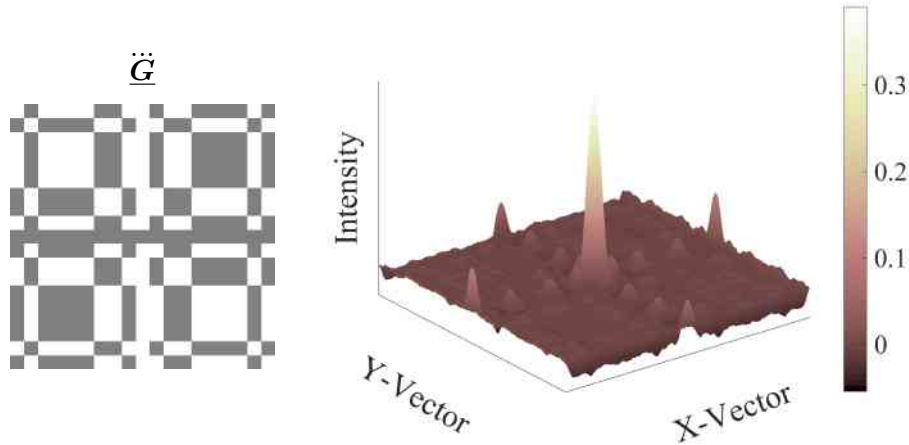
Figure 2.28: NTHT Decoding Method 3 with $\boldsymbol{A}$ in Fig. 2.26.

Table 2.1: Summary of Encoded Array Patterns.

Array Pattern	Construction Method	χ	PSF Plateau	PSF Side-Lobe	Size Range
TP URA	Mapped	$= 0.50$	$= 0$	$= 0$	Any TP
MURA	Mapped	$= 0.50$	$= 0$	$= 0$	Any prime
DURA	Mapped	< 0.50	$= 0$	$\neq 0$	Limited
BR	Folded	$= 0.25$	$\neq 0$	$\neq 0$	Limited
Singer	Folded	≤ 0.50	$\neq 0$	$\neq 0$	Fair
NRA	-	≤ 0.50	$= 0$	$\neq 0$	Limited
PNP	-	$= 0.25$	$= 0$	$= 0$	Limited
RANDA	-	≤ 0.50	$\neq 0$	$\neq 0$	Excellent
NTHT	-	< 0.50	$\neq 0$	$\neq 0$	-

Until now the process for both CMOS and CCD sensor are essentially the same. The main difference between sensors are the way in which conversion from analogue to digital signal occurs. The CCD sensor's conversion take place by reading out the charge from the photo-sites one at a time at some location, and shifting the charge row by row (Norton, 2004). On the other hand, CMOS sensor's conversion process is local and occurs at each photo-site. This has the advantage of reading out charge faster than the CCD sensor, preparing the photo-sites for another exposure. The disadvantages of this is that if the camera is moving faster than the conversion process then the final image may suffer from 'rolling shutter artefacts'. Such artefacts present a distortion in the image as a result of charge leaking to neighbouring pixels. This is addressed in CCD sensors by its method of reading out charge from the photo-sites.
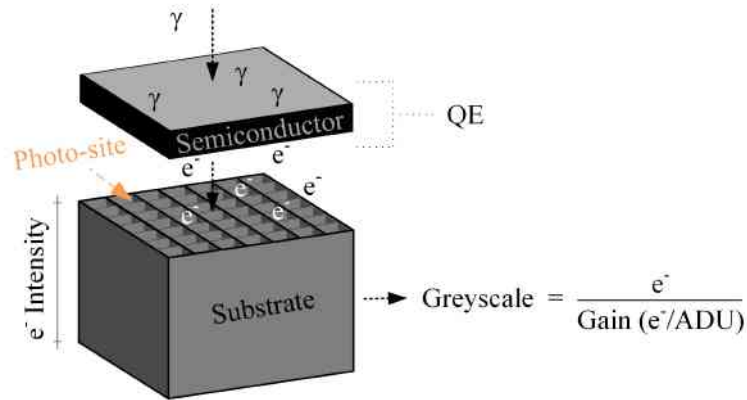
Figure 2.29: A Diagram of CCD & CMOS Sensors: Note, QE refers to quantum efficiency.

2.3.2 Scintillator Detector

A scintillator detector is commonly used in a gamma camera, also known as an 'Anger camera' and used to detect faint ionizing radiation. The detector utilises a luminescence material to convert incoming ionising radiation to visible light. Common types of crystals used in detectors are sodium (NaI) iodide and caesium iodide (CsI). The energy state of electrons within the crystal is changed when interacted with ionizing radiation. Consequently, photons are emitted in the optical range. A photocathode in a photomultiplier tube (PMT) then converts the optical photons to electrons, which is then multiplied as the electrons interact with multiple anodes and dynodes (Bousselham et al., 2010). At the end of the process sufficient amounts of signal can be analysed to form a 2D image.

Image intensifiers are a form of detection systems that detects radiation such as X-rays with a photocathode. The X-rays are converted into electrodes and accelerated within an evacuated tube towards the anode by a high voltage. The initial detection is performed using scintillator crystals, such as cadmium zinc telluride (CZT). During the process, electrons are focused onto the anode by electrodes, interacting with a phosphorus screen; which is then converted into light. Subsequently, the light is detected and an image is formed. Image intensifiers with CZT as the scintillator crystals are commonly used for imaging in astronomy and medical imaging due to its benefits of high resolution, energy selection and stable performance.

36

2.3.3 Signal-to-Noise Ratio

Signals convey information and in the experimental world there is a probability of its measured value deviating from the actual one (Norton, 2004). The deviation value or error is unwanted signal and thus, termed 'noise' (N). Errors may occur systematically and usually can be corrected easily with given information. Same errors may be random and are more challenging to address. When a signal is analysed it is imperative to understand if the change in detected and real values are 'statistically significant' and this can be determined through signal-to-noise ratio (S/N) (SNR), (Simpson and Barrett, 1980). The theoretical ideal SNR is defined in Eq. 2.28, where μ_S is the mean of a group of signals and σ_B is the standard deviation of the background. The mean and standard deviation are defined in Eq. 2.29 - 2.30, where i is each element in a total of n that comprise a signal S.

$$SNR = \frac{S}{N} = \frac{\mu}{\sigma} = \frac{\mu_S}{\sigma_B} \tag{2.28}$$

$$\mu = \frac{1}{n}\sum_{i=1}^{n} S_i \tag{2.29}$$

$$\sigma = \sqrt{\frac{1}{n}\sum_{i=1}^{n}\left(S_i - \mu\right)^2} \tag{2.30}$$

High SNR values indicate less error in the signal and greater significance. To the contrary, low SNR reveal greater errors in the signal (Hainaut, 2005). When defining the signal of an image the scene or a target object is used. As stated in Simpson and Barrett (1980) Barrett and Swindel (1981), the true scene is never completely accurate because image quality is degraded, and partly defined by the system's PSF or resolution. Consequently, errors may be introduced into the image as a result of poorly distinguishing boundaries of a signal from the noise. The presence of noise is not exclusive to one event, but a sum of many events discussed below. SNR can be increased if the nature of such noise terms is understood and addressed, resulting in a final image with better quality and lower uncertainties.

2.3.3.1 Photon Noise

'Photon', 'shot' or 'Poisson' noise ($N_{\underline{P}}$) is noise associated with the random nature of detected discrete photons. In statistics, Poisson distribution ($\underline{P}$) is

used to calculate the number of events randomly occurring in a given time where, k in this case is the mean of number events in the time specified, x is the number of successes, where 'successes' refers to the outcome in question. In an imaging scenario, x is the number of photons detected in a given area with its mean represented by k. Therefore, the probability of detecting photons $\underline{P}(x)$ is shown in Fig.2.31.

$$\underline{P}(x; k) = \frac{k^x e^{-k}}{x!} \tag{2.31}$$

An important property of Poisson distribution is $k = \mu = \sigma^2$ (Gupta and Guttman, 2013, pp. 129-131). Due to the nature of Poisson statistics $\sigma = \sqrt{\mu}$ and Eq. 2.28 becomes Eq. 2.32 to calculate the photon noise in an ideal experimental scenario (excluding other noise terms) (Simpson and Barrett, 1980; Schroeder, 2000).

$$SNR = \frac{\mu}{\sqrt{\mu}} = \sqrt{\mu} \tag{2.32}$$

For the remainder of this chapter the mean group of signals of an image follows the form $\mu = N_{\mathrm{S}}$ and photon noise with $\sqrt{\mu} = \sqrt{N_{\mathrm{S}}}$. The units for photon noise is usually expressed in photons per second ($\gamma \cdot s^{-1}$).

2.3.3.2 Background Noise

In order to take the mean of a group of desired signals the signal must be distinguished from the remaining image or scenery. This area outside the mean signal is considered the background (B). (Howell, 1989, 2006). An example can be the PSF of a system, where the signal is at the centre of the image and the background is the region outside. Background noise follows Poisson statistics with the units of photons per second per pixel ($\gamma \cdot s^{-1} \cdot \mathrm{px}^{-1}$) (Dhillon, 2010). Thus, background noise follows the expression $\sqrt{N_B}$.

2.3.3.3 Dark Current

The detector of a camera produces heat when operated generating unwanted electrons in the CCD. Dark current (DARK) refers to the number of electrons that are generated in a second when there are no other light sources being detected. Consequently, 'dark' or thermal noise ($\sqrt{N_{\mathrm{DARK}}}$) follows Poisson statistics with units in electrons per second per pixel ($\mathrm{e}^- \cdot s^{-1} \cdot \mathrm{px}^{-1}$). Dark current is reduced by cooling the CCD generally with a thermoelectric cooler. Dark frames are also taken and subtracted from the 'light' frame where 'light' refers to the exposure of the main imaging scene. The same condition used

for taking light frames is applied to a dark frame, which includes the exposure time (Norton, 2004).

2.3.3.4 Read Noise

When the sensor of a camera converts the photons into electrons in each photo-site, the electrons are read out via the analogue to digital conversion process. During this process, random noise from the sensor's electronics is added to form readout noise or read noise (R^2). Readout does not follow Poisson statistics and its units are presented as electrons or electrons per pixel ($\mathrm{e}^- \cdot \mathrm{px}^{-1}$).

2.3.3.5 CCD Equation

SNR for CCD images are calculated by applying the contributing noise terms to Eq. 2.32 to form Eq. 2.33 where, N_S is the mean signal of the source, N_B is background noise, N_DARK is dark current and R is the read noise. The formula presented in Eq. 2.33 is generally known as the 'CCD equation', which has been expressed in this thesis as SNR_{CCD} (Mortara and Fowler, 1981; Howell, 1989, 2006).

$$SNR_{CCD} = \frac{N_\mathrm{S}}{\sqrt{N_\mathrm{S} + n_\mathrm{px}(N_B + N_\mathrm{DARK} + R^2)}} \qquad (2.33)$$

Ideally, the CCD equation is applied when determining SNR of digital images, as there are lower uncertainties from addressing various noise terms. However, unknown variables may prevent the use of such formula and SNR in its simplest form can be applied by using Eq. 2.28.

2.3.3.6 SNR and Uncertainty

Results presented as numerical values are derived through calculations, simulation or experiment and are generally accompanied by an error or uncertainty value[2]. However, not all results are presented as explicit numerical values, and can be in the form of an image. So the question arises; what is the uncertainty associated with an image and how is this calculated. It so happens that SNR is an error value of the mean and the mean in the case of imaging is taken from the signal (Hughes and Hase, 2010, p. 14). Consequently, SNR measures the reliability of the signal within an image as stated in Simpson (1978, chap. 4). Although this is 'common knowledge' there is a lack of literature explaining how this is the case. Evidence of SNR being an uncertainty value of an image

---

[2]Note, error and uncertainty are interchangeable

is visible when calculating the fractional uncertainty where ΔS is the error. The signal (S) in this scenario is a value and N represents the error of S (see Equation 2.34) (Hainaut, 2005; Richmond, 2018).

$$\text{Fractional Uncertainty} = \frac{\Delta S}{S} = \frac{N}{S} = \frac{1}{S/N} \tag{2.34}$$

Furthermore, the reciprocal of the fractional uncertainty in Equation 2.34 would be equivalent to SNR, as in Equation 2.35. Higher values mean greater certainty and reliability of signals within the image.

$$\frac{1}{\text{Fractional Uncertainty}} = \frac{S}{\Delta S} = \frac{S}{N} \tag{2.35}$$

An example is given with the following values $S = 70$ and $N = 3.5$, which results in $SNR = 20$ or $1/SNR = 0.05$ (5 % uncertainty), when using Equation 2.34 and 2.35. Higher SNR values indicate a good distinguishing of a signal from any noise present within an image. Another example is presented in Newberry (1991), where $SNR > 200$ has an uncertainty of less than 0.5%. Previous literature have suggested $SNR > 5$ to be a reliable value which is based on the 'Rose Criterion' (Burgess, 1999; Howell, 2006) (Bushberg et al., 2012, p. 92). Fractional uncertainty is another approach to quantifying the error of signals within an image where, a 20 % uncertainty would be the maximum acceptable error value corresponding to a $SNR = 5$. A plot of SNR as an uncertainty is given in Fig. 2.30 for a range between 0 - 100. The plot shows a profile that is logical and consistent to applications of uncertainty. Firstly, the uncertainty in Fig. 2.30 becomes infinitesimally small when there is an increase in SNR, nonetheless, never reaches zero. This is true for all digital images as camera sensors are subject to various noise terms. Secondly, increasing SNR describe greater reliability in the signals of an image, which would result in a reduction in uncertainty. Also, there is no uncertainty correlating to a $SNR = 0$ as this would be absurd. Uncertainties cannot exist if a value is absent.

Overall, the above presents information on SNR being an uncertainty value of signals presented within a digital image. This is the main reason why SNR values are commonly expressed with uncertainties and it is not necessary to take the error of an error. See the following Accorsi and Lanza (2001); Newberry (1991) Simpson (1978, chap. 6) for examples.
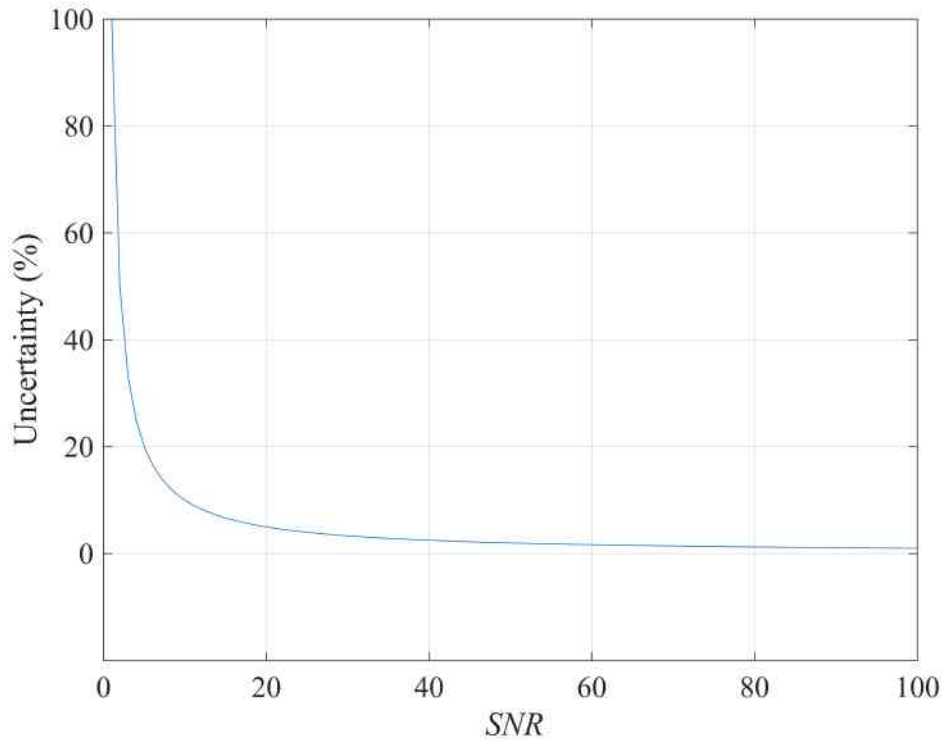
Figure 2.30: A Signal-to-Noise Ratio and Uncertainty Plot.

2.3.4 Contrast-to-Noise Ratio

Contrast is a term used to describe the difference between two or more things, such as the colour, shade or intensity of an object. Contrast-to-noise ratio (CNR) is another method of quantifying images by analysing the contrast between a signal and background noise. The formula in CNR marginally differs from SNR by subtracting the noise term from the signal, as in Eq. 2.36.

$$CNR = \frac{|\mu_S - \mu_B|}{\sigma_B} \qquad (2.36)$$

A standard of reference values for CNR does not appear to be clearly defined in literature. Nonetheless, higher values would indicate a better contrast between regions of an image, suggesting that there is a good distinction between the region of an image and ambient background noise (Bushberg et al., 2012, p. 91) (Welvaert and Rosseel, 2013).

41

2.3.5   Resolution

Imaging systems contain the ability to display varying levels of details within a processed image. Resolution or to be specific, spatial resolution is a term commonly used to describe such ability; which reveals the smallest objects that can be seen by the system. There are a number of factors to consider that affect the resolution of an image. This includes but is not limited to, size of photo-sites, pixel density, and aperture size. It must be noted that digital imaging systems cannot resolve objects smaller than the size of its sensors individual photo-site (Bushong, 2017, p. 309). There are numerous ways of measuring the resolution of an image and some are presented below (Bushberg et al., 2012, p. 60) (Smith, 1999, p. 423).

2.3.5.1   Full Width Half Maximum: Unresolved Object

The simplest form of measuring spatial resolution would take place by using a PSF or of an imaging system. Slicing the PSF through the central region to produce a 1D plot reveals a shape similar to that of the Gaussian distribution function as in Fig. 2.31, following Eq. 2.37.
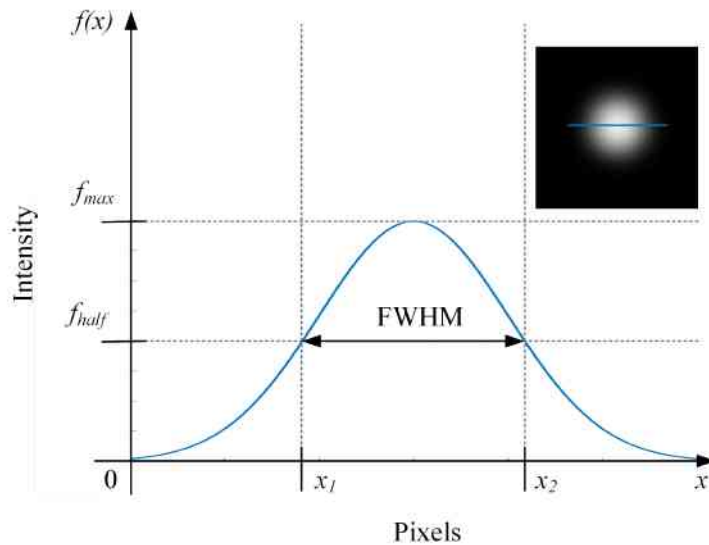
Figure 2.31: FWHM Diagram: The plot is a 1D slice of the PSF above.

$$f\left(x\right) = \frac{1}{\sigma\sqrt{2\pi}}\exp\left[-\frac{(x-x_0)^2}{2\sigma^2}\right] \tag{2.37}$$

Calculating the full width at half maximum (FWHM) of the Gaussian or point spread function is performed with $x_1 + x_2$ as in Fig. 2.31. A relationship

between FWHM and σ of the Gaussian distribution function can be found in Eq. 2.38. and states that FWHM is approximately 2.4 σ in width as in Fig. 2.32.

$$\text{FWHM} = \sigma\sqrt{2\ln 2}\,\sigma \approx 2.4\,\sigma \tag{2.38}$$
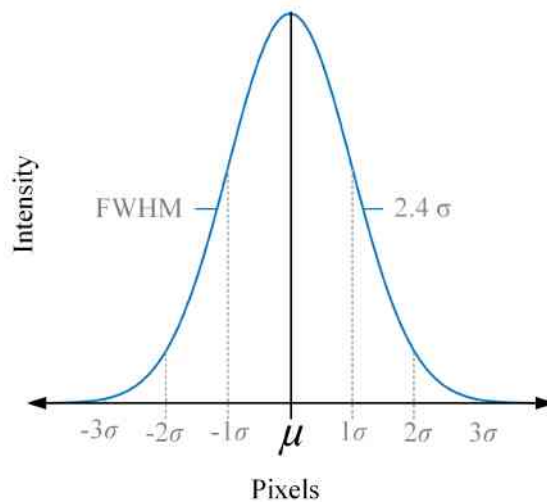
Figure 2.32: Gaussian Distribution: The above diagram shows the size of the FWHM in standard deviations which is always 2.4 σ.

Determining FWHM for resolution is ideal for unresolved images that are similar to PSFs, such as a star in the night sky or those of a small radioactive source. Smaller values for the width of a PSF indicate higher resolutions.

2.3.5.2 Edge Response: Resolved Object

Generally, images are comprised of a 'complex scene' with objects containing distinctive features, such as sharp edges. Objects within a scene may be blurred or distorted by the limited PSF of the system. Take for example a sample of a square white block in front off a black background as in Fig. 2.33. The sharp edge of the block has been degraded by the PSF of the imaging system. By measuring the width of a degraded edge between 10-90 % of the intensity difference yields an edge response or edge spread function value. As with FWHM, smaller edge response values indicate higher resolution (Smith, 1999, p. 427).

43
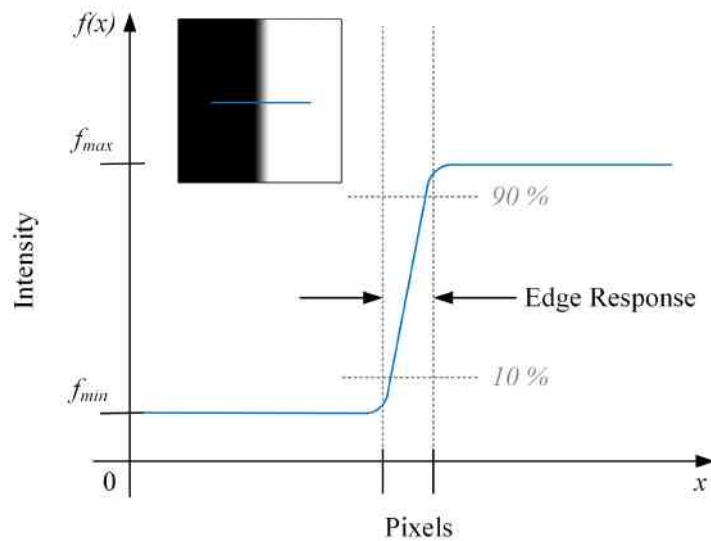
Figure 2.33: A Diagram of an Edge Response: The plot is a 1D slice from the resolved image above.

2.3.5.3 Line Pair

The most common method of calculating spatial resolution in medical imaging is done by measuring 'line pairs' (lp). A line pair may refer to a pair of bright lines with an intensity of 1 for binary images on a dark background of 0 for contrast that both share the same width. The separation distance between individual lines in the pair is equal in width to each line as in Fig. 2.34. Spatial frequency describes the resolution through a relationship between the number of line pairs within a given spatial dimension. This is usually expressed in line per mm (lp/mm). Fig. 2.34 demonstrates six line pairs with a range of sizes and their corresponding spatial frequency. Take the line pair where 1 lp has a total width of 10 mm. By taking the reciprocal of 10 mm (1/10) reveals a resolution of 0.1 lp/mm. Higher spatial frequencies equate to higher resolution of an imaging system (Bushong, 2017, p. 309).

There is a relationship between resolution and contrast of an imaging system. Take for example line pairs in Fig. 2.34 representing an imaging object that become degraded by the imaging systems PSF as shown in Fig. 2.35. The clear contrast between black and white has diminished and various levels of grey scales are introduced rendering a loss in sharp edges. If a section of the image in Fig. 2.35 is sliced and plotted as a graph, visible sinusoidal waves can be seen instead of square waves. A modulation transfer function (MTF) describes an imaging systems ability to transfer levels of detail with regards to contrast or modulation. A modulation of 100 % would indicate full preservation of contrast of the object that is imaged and can be calculated using Eq. 2.39, where I_{min} and I_{max} are the minimum and maximum intensities. Conversely, a

44
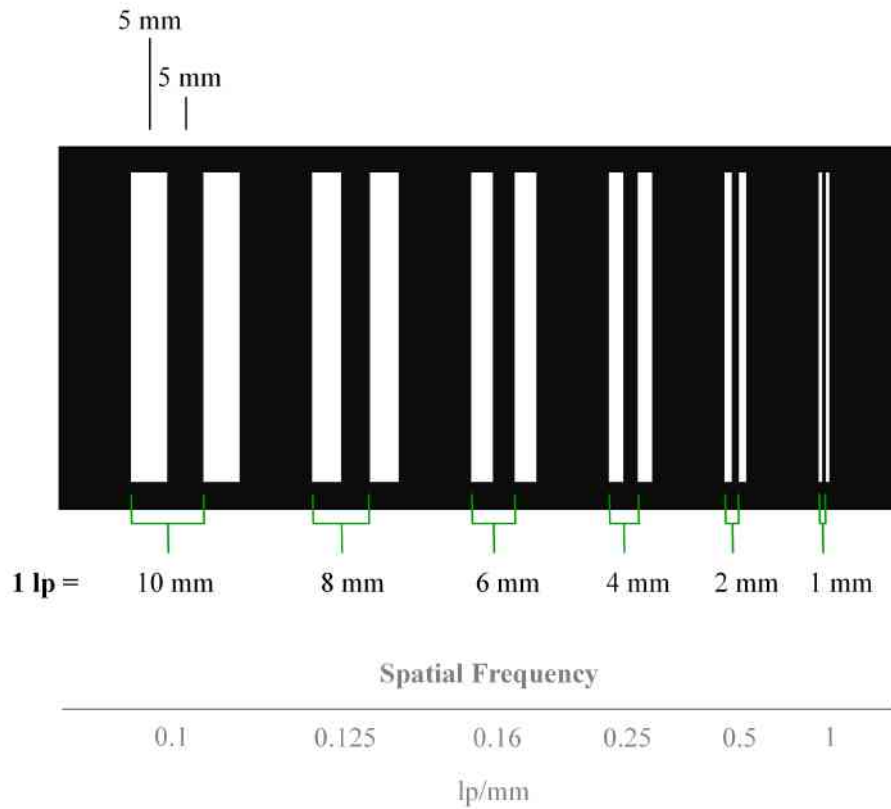
Figure 2.34: A Diagram of Line Pairs: Each line in the pair is the same size as the distance that separates them.

decrease in contrast would see grey levels introduced into the image, so white would be represented as say 0.9 in intensity instead of 1. This is prevalent in Fig. 2.35, where a correlation exists for increasing spatial frequency and decreasing modulation, showing grey values depicting those that should be white.

$$\text{Modulation } (\%) = \left(\frac{I_{\max} - I_{\min}}{I_{\max} + I_{\min}} \right) \times 100 \qquad (2.39)$$

Overall, measuring the spatial resolution of a system using spatial frequency can be achieved by visually determining the smallest line pair that is resolved, which would yield the limits of the imaging system. This maybe achieved by using the Rayleigh criterion for the line pairs, which appear as two PSF when fully resolved.A value then can be obtained by calculating the spatial frequency (Bushberg et al., 2012, p. 76).

45

2.3.6   X-Ray Backscatter Imaging

X-ray backscatter imaging has been used in the past for industrial applications, and for defence and security (Bell, 2009, p. 93). There are two types of methods used, which include time and spatial multiplexing imaging (Dinca et al., 2008). Time multiplexing imaging is the most commonly used of the two and it is based on building up an image over time, from X-rays using a rotating mechanical wheel. The scene is scanned with an X-ray pencil beam and the system requires no 'resolving medium' because mainly backscatter from the scene is detected. On the other hand, spatial multiplexing images are formed from parts of the scene being detected all at the same time. Consequently, backscattered X-rays travelling in all direction is detected at the same time, therefore, requires a resolving medium due to the high flux.

The main X-ray backscatter imaging system constructed at Cranfield University detected signal from a scene via spatial multiplexing. Typical X-ray energies used were between 70 - 160 kV. The goal was to primarily analyse the imaging system using coded masks to determine the increase in sensitivity and other benefits over the pinhole mask and flying spot system. As the X-ray backscatter imaging system was designed to detect IDEs typically a few centimetres in size, a large field of view was not necessary. To be specific a field of view of around 90° was sufficient enough to accommodate imaging objects at a distance of 1 m from the camera.
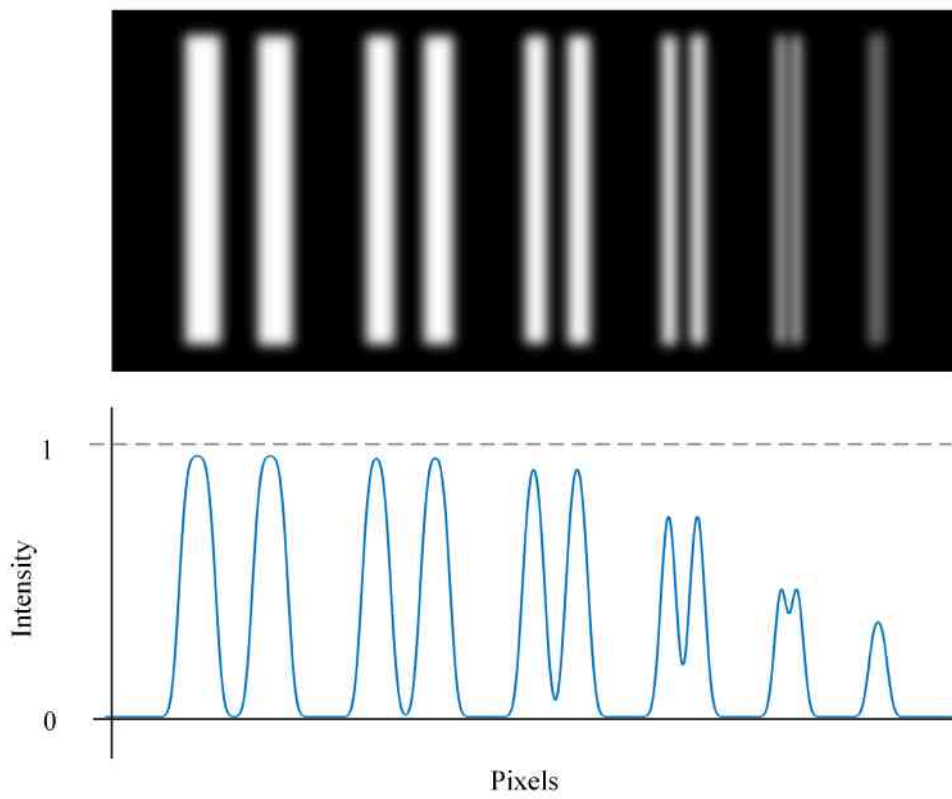
Figure 2.35: A Diagram of Degraded Line Pairs.

Chapter 3

Methods

3.1 Design & Construction of the XBI System

An XBI 'staring system' was designed and constructed for the experimental aspects of the project at Cranfield University. The fundamental components that formed the entire system included an X-ray generator, photon sensitive detector, imaging masks and test objects. Mounts were designed and made from aluminium for the camera and X-ray source, then clamped to an optical table. A similar mount was also manufactured for test objects and lined with lead to reduce X-ray scatter (see Fig. 3.1).
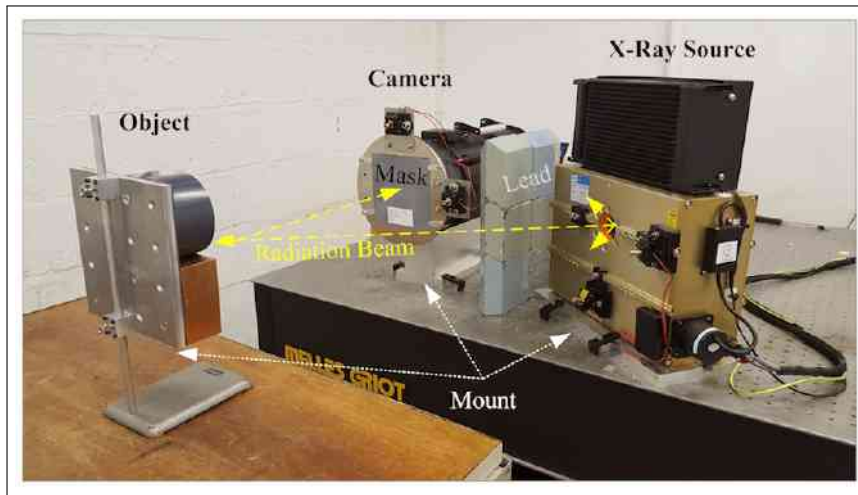
Figure 3.1: X-Ray Backscatter Imaging System at Cranfield University.

The system was constructed in a dedicated radiation cell lined with thick concrete walls to attenuate the potentially harmful ionising radiation. The cell was fitted with circuit breaking interlocked doors with operations taking place remotely and requiring a castellated key. Additional safety measures included closed-circuit television cameras and a trapped persons alarm.

3.1.1 X-Ray Source

A VJ Technology (VJT) X-ray generator (VJT, 2017) formed a fundamental part of the XBI system with an operational range between 70 - 160 kV. The generator was fan cooled and provided a total power output of 800 W. Parameters of the VJ Technology X-ray generator can be found in Table. 3.1 along with its X-ray spectra in Fig. 3.2. The spectra were recorded with an Amptek® X-123 cadmium telluride (CdTe) spectrometer (Inc, 2015) which had a 300 μm diameter tungsten collimator to attenuate unwanted radiation. The spectra were collected with 0.02 mA of current for 300 s with the detector placed around 1.5 m from the X-ray generator, to keep the 'dead time' at a minimum (< 10 %). Dead time refers to the percentage of time where photons

were not detected due to the detector being busy processing previous events. The detector resolution at low energies was good, which is visible with the counts falling to 0 at corresponding keV. For example, 70 kV would see a drop to zero counts at 70 keV. Prominent emission peaks from tungsten $K\alpha_1$ and $K\alpha_2$ were resolved at around 57 - 59 keV. Possible lines with lower peaks, such as Cd were resolved at 26 keV, Te at $\sim$ 32 keV, and traces of Pb $\geq$ 72 keV (Rubio and Mainardi, 1984; Redus et al., 2008).

Table 3.1: VJ Technology X-Ray Source Parameters.

Parameters		Values
Input Power	AC Voltage Range	240 V $\pm$ 10 %
	Current RMS Max	5.3 A
Output	Maximum Power	800 W
	Operation Voltage Range	70 - 160 kV $\pm$ 2 %
	Anode Current	0.02 - 10 mA
X-Ray Beam	Field of View (FOV)	40 °
	Focal Spot ϕ Size in Tube	1.2 mm
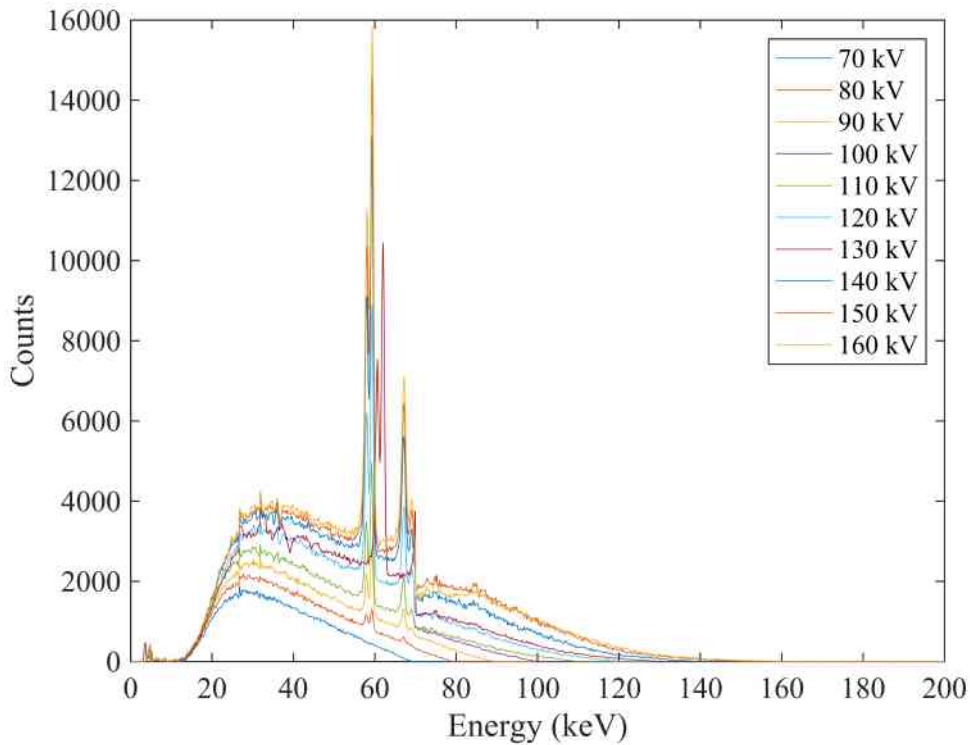
Figure 3.2: Continuous Spectra of the VJT X-ray Generator at Different kV.

3.1.2   Imaging Objects

A variety of objects were designed and manufactured with the purpose of testing the response of the XBI system. The primary object that was used for testing SNR and CNR was a 'quadrant' consisting of a solid copper (Cu) block in the top left, polyvinyl chloride (PVC) cylinder top right, nylon 66 bottom left and aluminium (Al) in the bottom right (see Fig. 3.3a). Another imaging object was fabricated with distinguishable features and was made from paraffin wax, stainless steel washers and a bolt (WWB). The upper left, right and lower left and right contained M5, M10, M6 and M8 washers, which surrounded a bolt in the centre (see Fig. 3.3b). Additionally, a line pair object was machined out of solid aluminium and filled with paraffin wax to test the resolution of the XBI system (see Fig. 3.3c). Note, the white bar in Fig. 3.3 serves as a scale indicator of 100 mm. All materials forming the test objects were selected to provide good contrast.

(a)   (b)   (c)
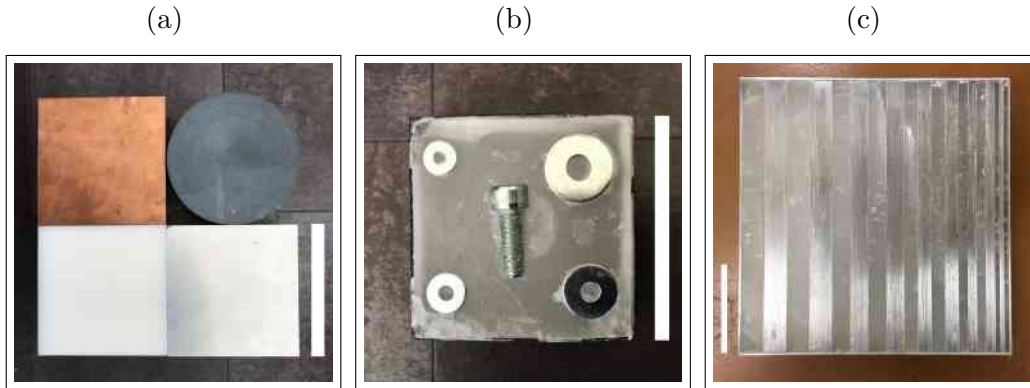
Figure 3.3: Imaging Objects: (a) Quadrant, (b) WWB object and a (c) line pair object.

Details of the line spacing for each line pair imaging object can be found in Table. 3.2, which were based on the theoretical framework of literature in Chapter. 2.3.5.3. Also, Table. 3.2 presents information on the dimensions of imaging objects and their composite material.

Table 3.2: Imaging Object Parameters

Object	Dimensions (mm)	Material	Information
Al lp	$300 \times 300 \times 50$	Al & Wax	lp/(25, 20, 15, 10, 5) mm
Quadrant	$200 \times 200 \times 50$	Cu, PV, Nylon 66 & Al	-
WWB	$100 \times 100 \times 50$	Wax & Stainless Steel	M5, M6, M8 & M10 Washers

3.1.3 Camera System

The detector that formed part of the XBI system was a 1.4 mega-pixel Photonic Science Gemstar image intensified camera (Photonic Science, 2017). The detector used for the project was supplied by the sponsors and detailed information on its specifications were limited. Attempts were made to obtain more information from the manufacturer via email (personal communication, 6 March 2019), however, this was unsuccessful. Nonetheless, know facts on the camera's specification are presented in this section. The native resolution of the camera measured 1392×1040 px with each photo-site (ps) measuring 108 μm or 0.108 mm. Only a part of the sensor in the camera was active to incoming photons, which is referred to as the active region (see Fig. 3.4). The circular active region was 115 mm in diameter and a square area of 81×81 mm was contained within the circular area. Consequently, when the camera was exposed, there was an inactive dark region that was presented in the digital image similar to that presented in Fig. 3.4. A side view of the camera's detector revealed the front glass window of the detector with a scintillator sitting 13.8 mm behind the glass. This was the point where photons were initially detected. The camera was placed in a radiation shielding tube with a front end attached to accommodate imaging masks, all of which formed the camera system (see Fig. 3.5 and 3.6). The front end of the camera system consisted of an extender tube that connected the camera to the mask. The purpose of the extender in addition to serving as a mount for the imaging mask was to allow room for the detector to be displaced closer or further away from the imaging mask.
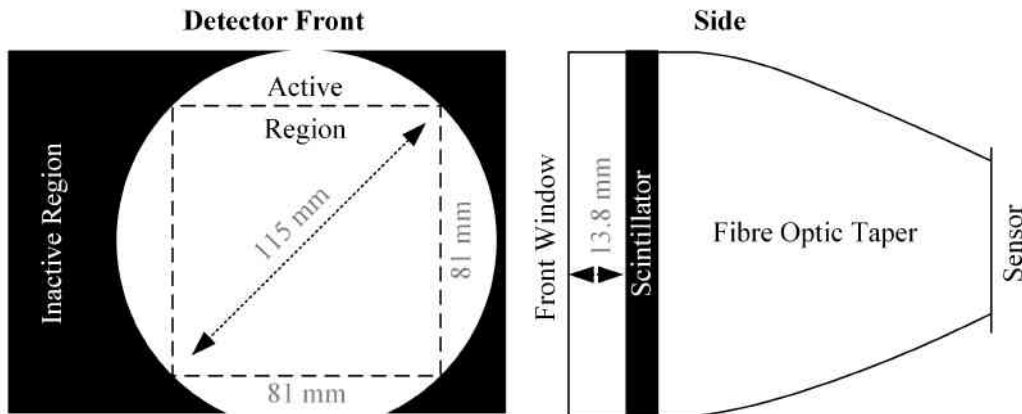
Figure 3.4: Detector Active Region and a Side View of the Detector.

The majority of CMI in defence and security have used intensified imaging systems that inherently do not have energy discrimination. Hence, the detector used for the experimental aspect of the project was not concerned with energy discrimination. This was briefly investigated on the theoretical aspect of the
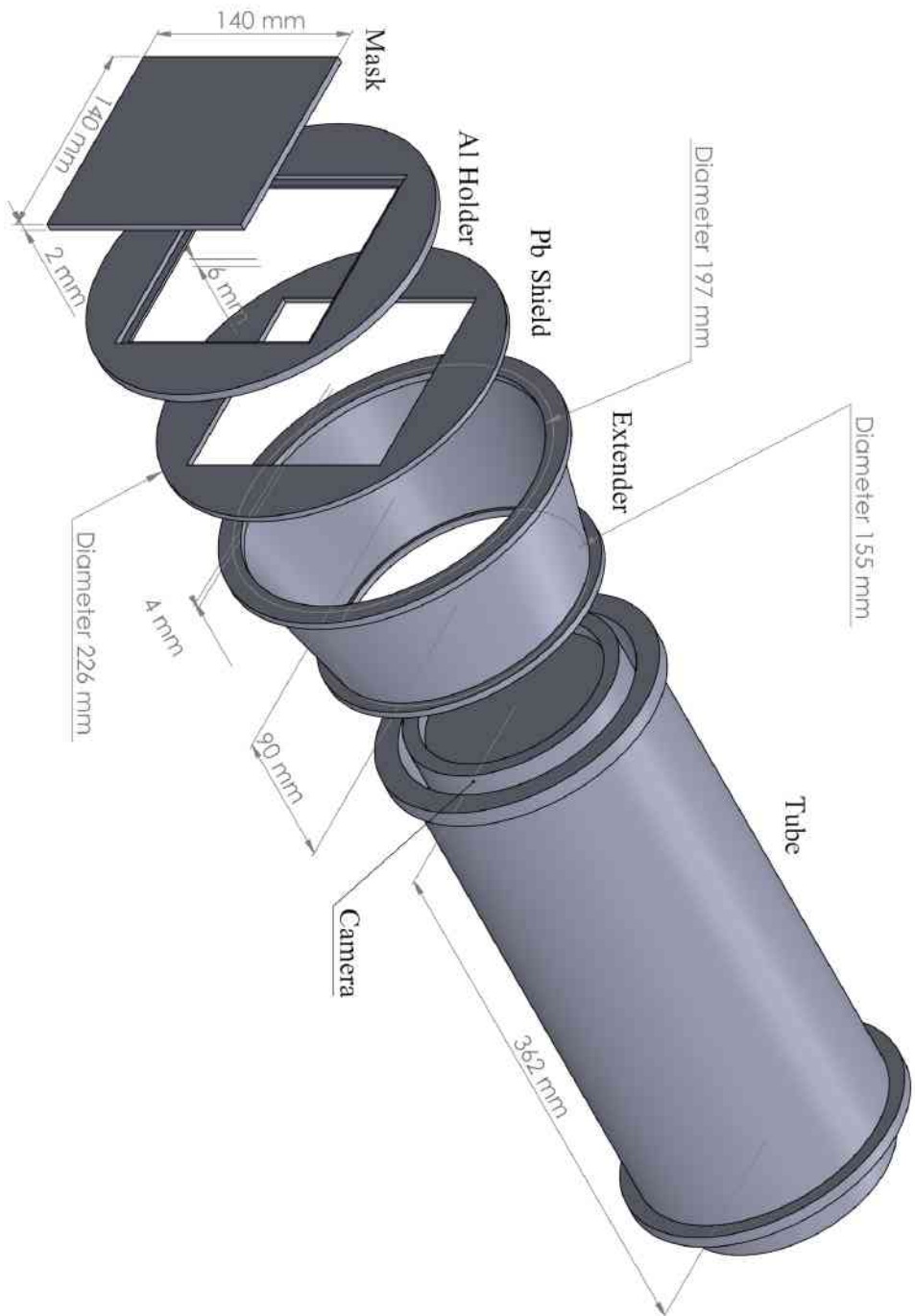
Figure 3.5: CAD Drawing of X-Ray Camera System: This a rendered drawing of components that comprise the camera system at Cranfield University.
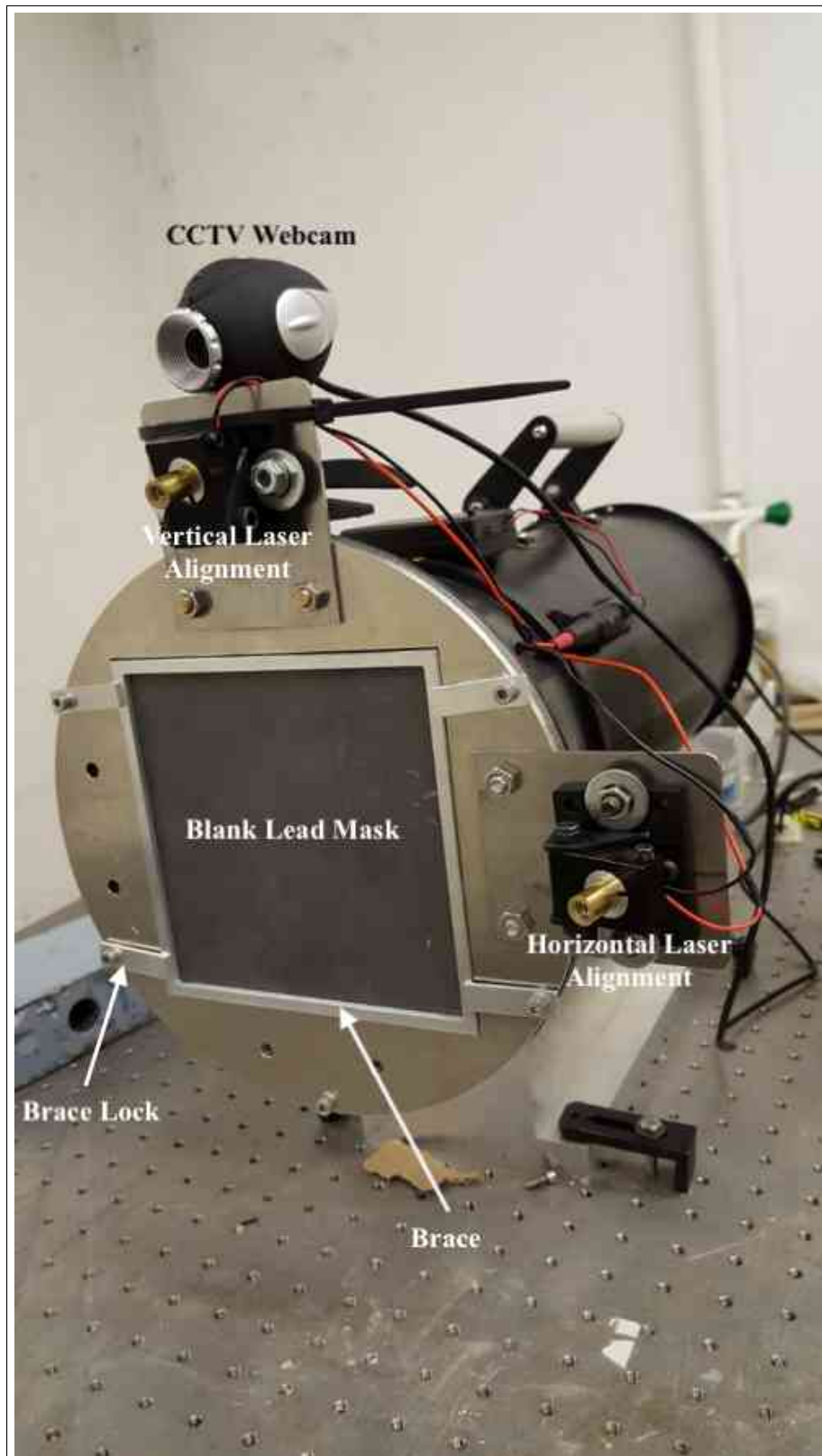
Figure 3.6: X-Ray Camera System at Cranfield University: The diagram shows the various components that make up the camera system.

project with a HEXITEC detector and again this was not the focus on the experimental side. This was largely due to the sensor size on the HEXITEC being very small with poor resolution, all of which did not justify using such a detector for the experimental side of the project.

3.2 Mask Geometry

Imaging masks play a critical role in resolving incoming radiation emitted from a scene. The pinhole mask is the simplest form requiring no post-processing for an image to be resolved. The principle of the pinhole mask can be found in Chapter. 2.2.1. For optical imaging, diffraction is a limitation for wavelengths of visible light (Rayleigh, 1891b,a; Mielenz, 1999). Such limitations are not so much of a concern for X-ray imaging due to shorter wavelengths. Careful considerations were made to determine the optimum thickness and aperture size of the mask. Masks that are too thin may result in radiation leakage into the camera, leading to overexposure and unwanted unresolved signals. Conversely, when the mask thickness ($\underline{t}$) is too large then unwanted 'collimation' effects may arise.

3.2.1 Aperture Collimation Effect

Imaging masks with a single central aperture can sometimes restrict the field of view (FOV) of the detector, resulting in a 'collimation effect' or 'collimation'; similar to vignetting in conventional photography. That is to say, the detector suffers a loss of peripheral vision like the recreated collimation effect in Fig. 3.7a of an image captured at the 'San Diego Convention Center' in Fig. 3.7b.

Collimation arises when the aperture's FOV (α) is smaller than the detector's FOV (β). Thus, the following conditions to avoid collimation $\alpha \geq \beta$ must apply. A plan view example of the collimation effect is presented in Fig. 3.8 with the black dashed lines, and grey dashed lines showing boundaries of the aperture's FOV and detector's FOV respectively. ϕ_{AP} symbolises the mask's aperture size, where $\underline{t}$ is the mask thickness, ϕ_{DET} is the detector size and $\underline{b}$ indicates the mask to detector distance. The FOV for a single aperture mask depended on the mask thickness and aperture size. The distance between the mask and detector also are governing factors that defined the detector's FOV. Mathematical expressions for FOV are found in Eq. 3.1 and Eq. 3.2.

$$\alpha = 2\tan^{-1}\left(\frac{\phi_{AP}}{\underline{t}}\right) \tag{3.1}$$
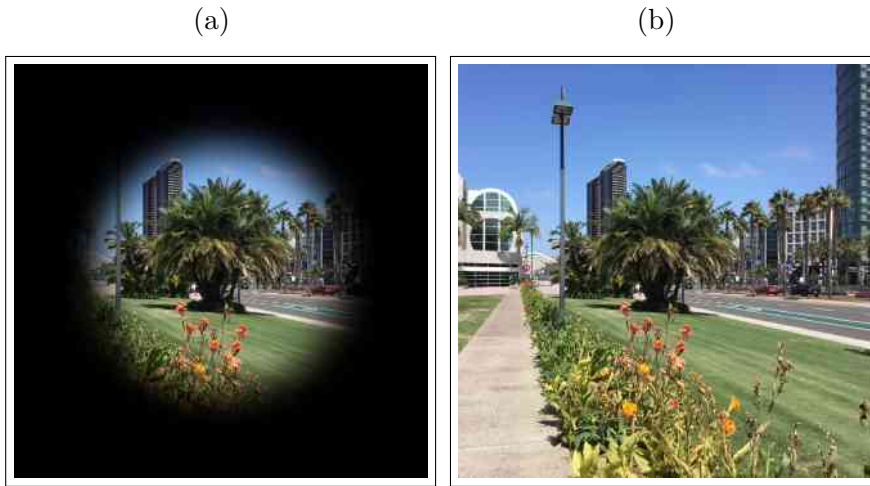
Figure 3.7: Collimation Effect Example: (a) demonstrates collimation effects of (b) the image on the right.
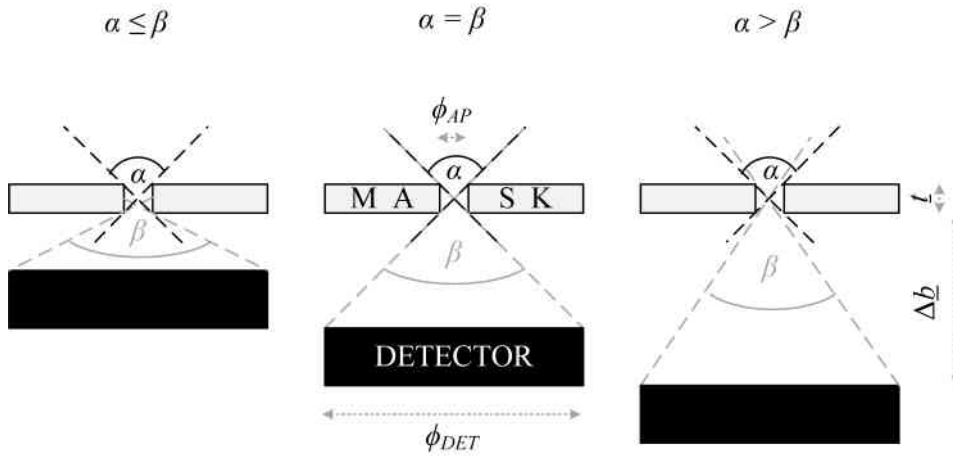
Figure 3.8: Collimation Effect Diagram: Note, the mask to detector distance affects collimation when changed.

$$\beta = 2\tan^{-1}\left(\frac{\frac{1}{2}\phi_{DET}}{\underline{b}}\right) \tag{3.2}$$

Assuming there is a relationship between α and β, where $\alpha = \beta$, an expression can be written using Eq. 3.1 and Eq. 3.2 to form Eq. 3.3. Note, $2\tan^{-1}$ operates on both sides of the equation, therefore, it can be removed.

$$\frac{\phi_{AP}}{\underline{t}} = \frac{\frac{1}{2}\phi_{DET}}{\underline{b}} \tag{3.3}$$

57

Collimation effects were avoided by placing the single aperture mask at a 'safe' distance from the detector. A formula was derived in Eq. 3.4 ('Andre's Pinhole Formula', named after the author) by solving for $\underline{b}$ in Eq. 3.3. $\kappa = (\underline{t}/\phi_{AP})$ holds information regarding the mask thickness and aperture size. The new expression in Eq. 3.4 yielded 'safe' distances between the mask and detector ($\underline{b}'$) that rendered a collimation free imaging system. The = symbol was replaced with $\geq$ as there are multiple mask to detector distances that were in the collimation free zone.

$$\underline{b}' \geq \kappa \left(\frac{\phi_{DET}}{2} \right) \tag{3.4}$$

If $\kappa = 1$ which arises from $\underline{t} = \phi_{AP}$, then $\underline{b} = \phi_{DET}/2$ which is the minimum 'safe' mask to detector distance . Fig 3.9 to 3.13 demonstrates the minimum 'safe' mask to detector distance with a vertical boundary left of the shaded region (which is blue in Fig. 3.9 to 3.13). The shaded blue region represents collimation free zones for $\underline{b}$, and the thin curved blue line shows the detectors FOV. Namely, the condition $\alpha \geq \beta$ begin at the left boundary and extended to the shaded area within the figures. Note, the physical limits of the detector was 200 mm and increasing $\underline{b}$ would decrease the systems FOV.

Two visible trends were present in Fig. 3.9 to 3.13. An increase in ϕ_{AP} with constant $\underline{t}$ resulted in the shaded blue area or 'safe' zone expanding. Consequently, the minimum mask to detector distance decreases and the observation revealed itself with $\underline{t}$ of 1, 2 and 3 mm in Fig. 3.9 to 3.13. Additionally, the same was true with constant ϕ_{AP} and decreasing $\underline{t}$. The second trend was manifested in Fig. 3.9 to 3.13, when $\underline{t}$ was equal to that of the ϕ_{AP}. Subsequently, $\kappa = 1$ when $\underline{t} = \phi_{AP}$, resulting in $\underline{b} = \phi_{DET}/2$ as mentioned earlier. In this case, $\underline{b} = \phi_{DET}/2 = 57.5$ mm which was half of the detector size of 115 mm. An ideal $\underline{t}$ for XBI would be infinitesimally small. Nonetheless, this was not realistic for attenuating X and gamma rays, so the optimum $\underline{t}$ of 2 mm was chosen when taking into consideration the material properties and operational photon energy range (discussed later). Smaller apertures retain resolution, however at the cost of FOV and an increase in collimation effect. Consequently, a 2 mm ϕ_{AP} was chosen as the optimum size for the imaging masks within this thesis which was consistent with research and simulations in Vella et al. (2018).

The theoretical framework for collimation effects could not be proven by experiment due to restrictions in the experimental equipment. The projected X-ray illumination area was much smaller than the detector's viewing area as seen in Fig. 3.14. There was a 2 m distance between the X-ray source and wall, where a 40 ° illumination cone was projected. As the chosen mask thickness and aperture size were both equal at 2 mm, an experiment would require taking exposures where $\underline{b} = 57.5$ mm to validate $\underline{b} = \phi_{DET}/2$ as shown in Fig.
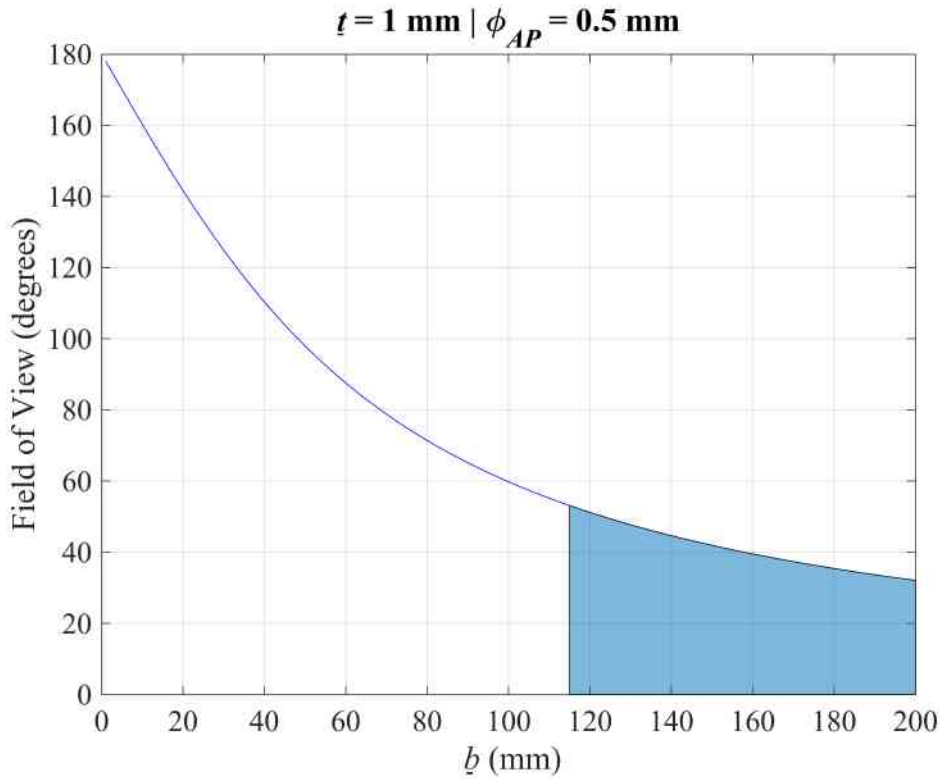
Figure 3.9: Collimation Free Region for 0.5 mm Aperture & 1 mm Thickness.

3.11. Also, at this mask to detector distance the detectors FOV was 90 °, being much larger than that from the X-ray source. Imaging with such conditions would naturally lead to dark regions at the edges of the image, masking any potential signs of collimation. This was also true for most other detector FOVs.

3.2.2 Relative Perspective of a Scene

Chapter 2.2.2 presents some inaccuracies in previous literature regarding the way a CM encoding process works. Commonly, a pictorial account of the encoding procedure is shown similar to Fig. 2.7 with examples found in (Fenimore and Cannon, 1978; Cannon and Fenimore, 1980; Brown, 1974) and (Accorsi, 2001, p. 22). The overlapping scene from each aperture in the CM is depicted as exactly the same. However, in near-field CMI, a more accurate version would see overlapping accounts of the scene on a detector that is not the same, but slightly different for each aperture. That is to say, the detector would have a different perspective of the imaging scene, as a result of each aperture's relative position on the mask. Therefore, the detector would have a 'relative perspective of a scene' (RPS) based on each apertures position in the mask. A more accurate version of Fig. 2.7 is presented in Fig. 3.15.

59
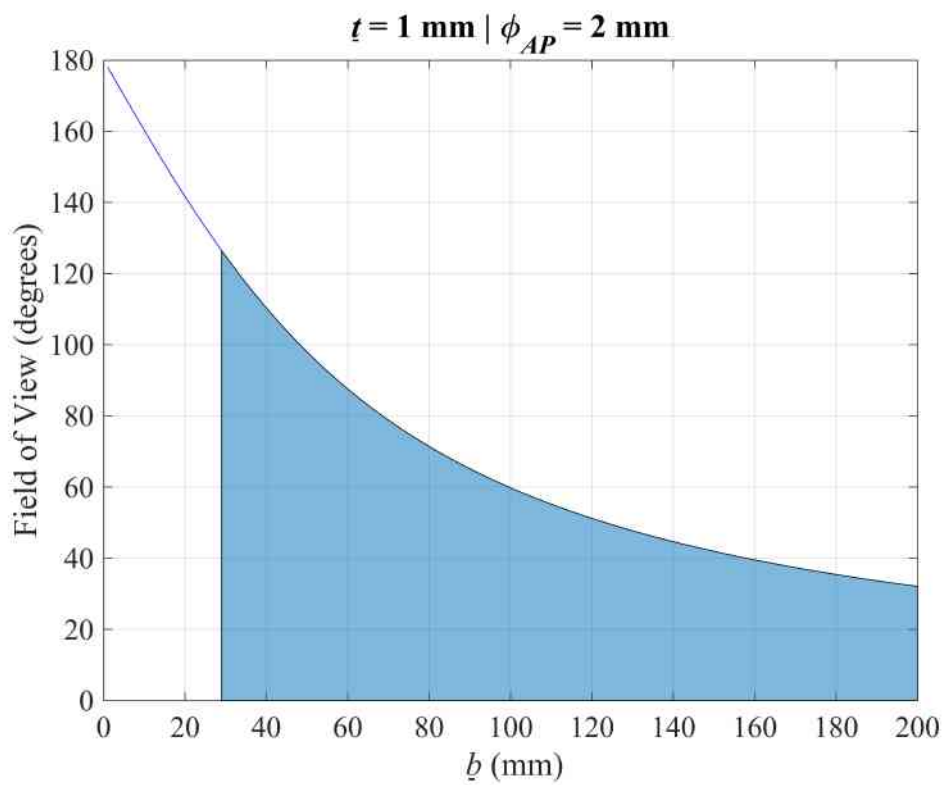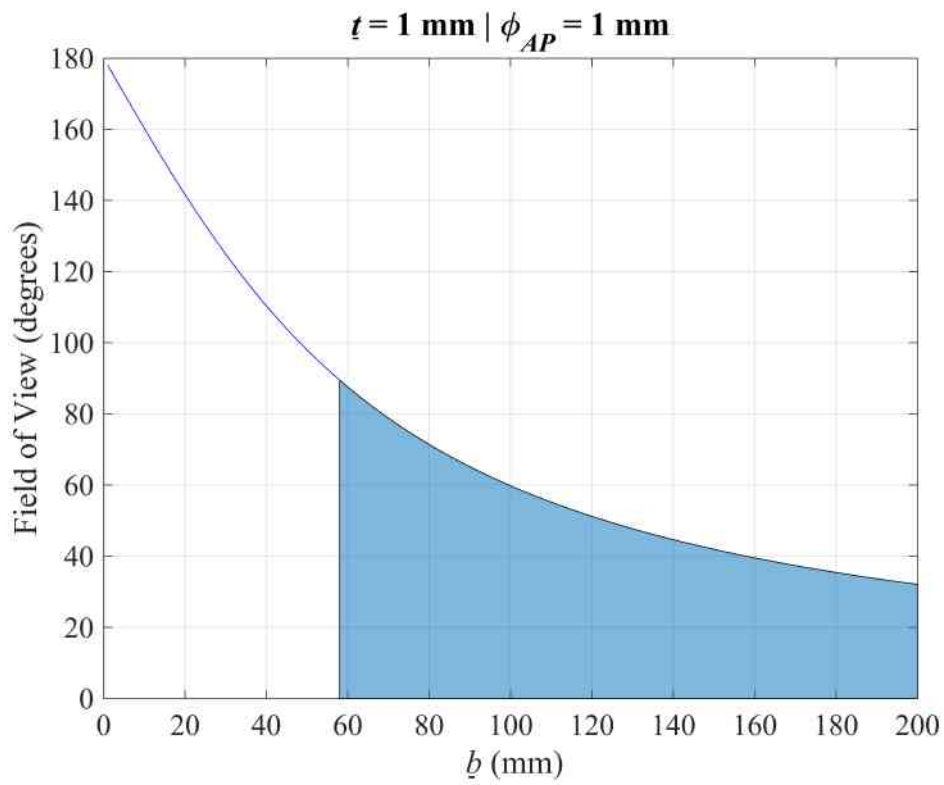
Figure 3.10: Collimation Free Region for 1-2 mm Aperture & 1 mm Thickness.
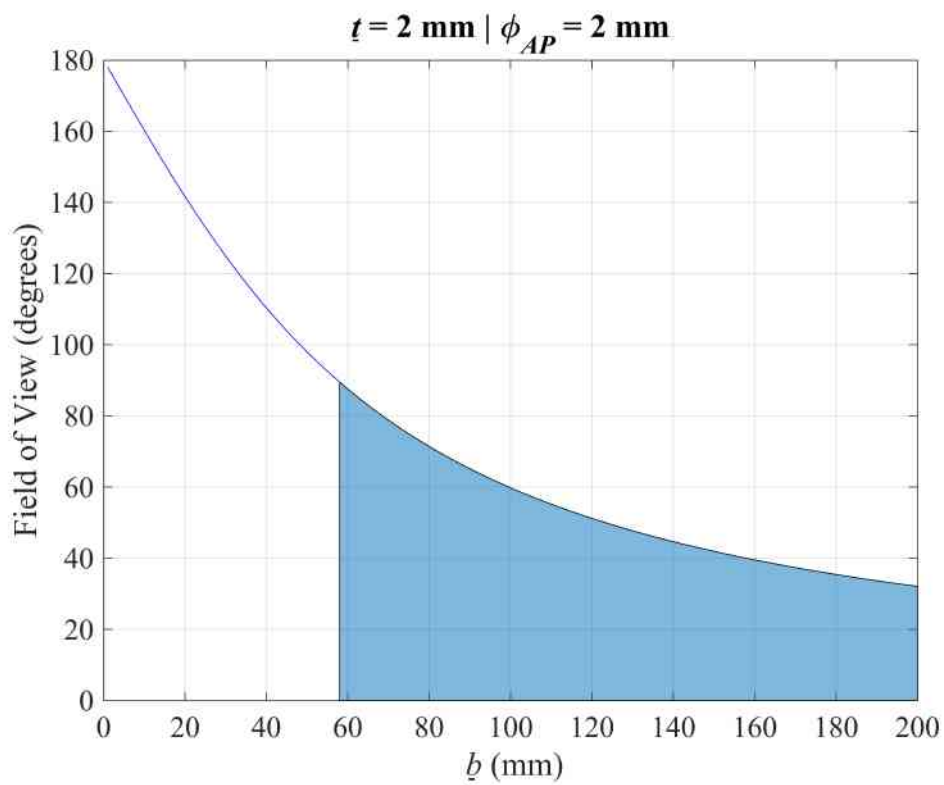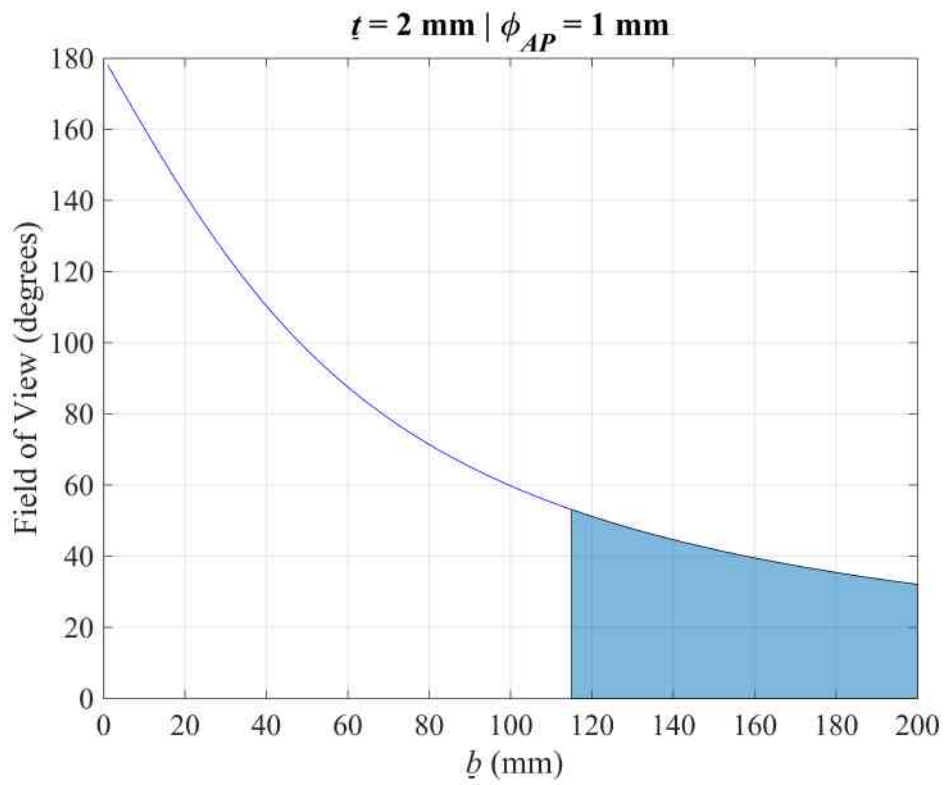
Figure 3.11: Collimation Free Region for 1-2 mm Aperture & 2 mm Thickness
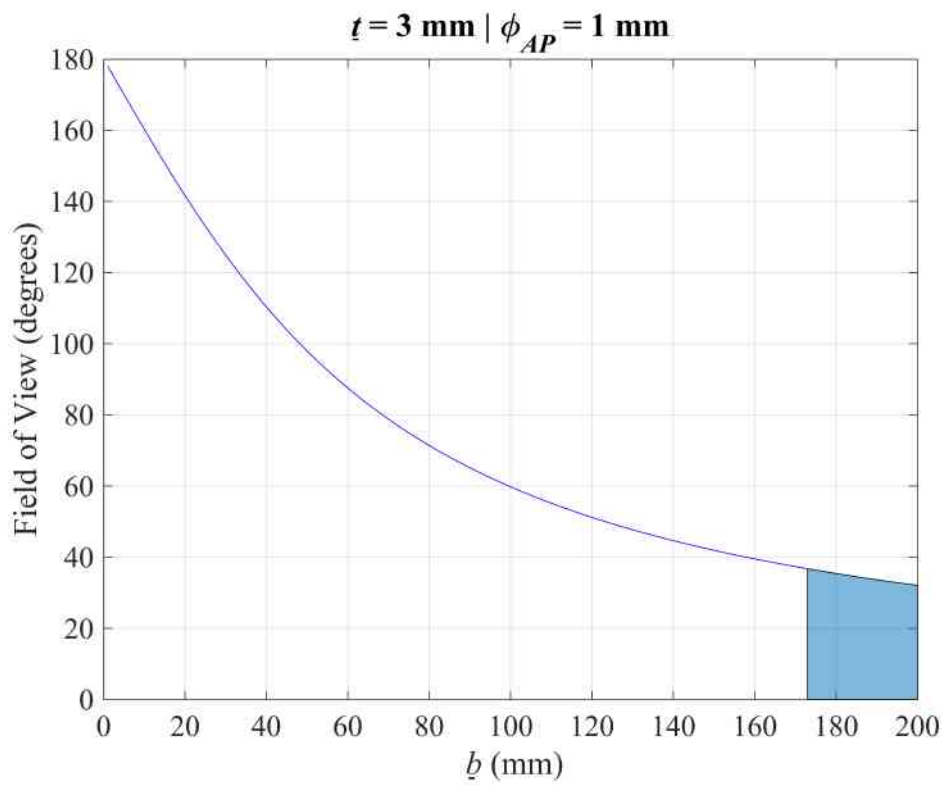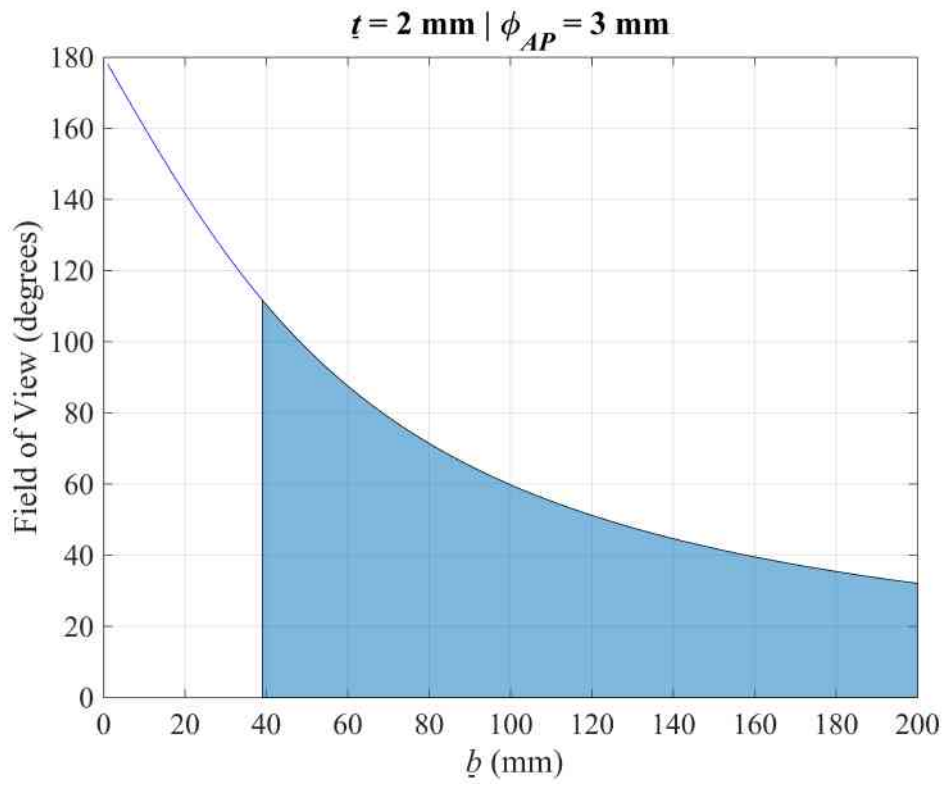
Figure 3.12: Collimation Free Region for 1 & 3 mm Aperture & 2-3 mm Thickness.
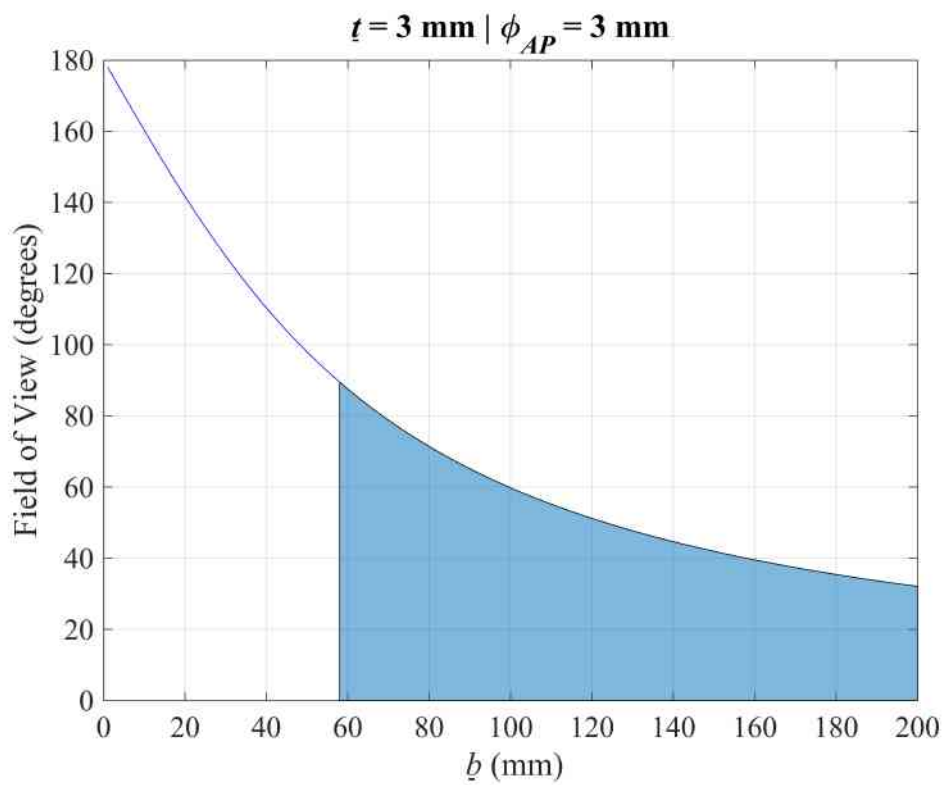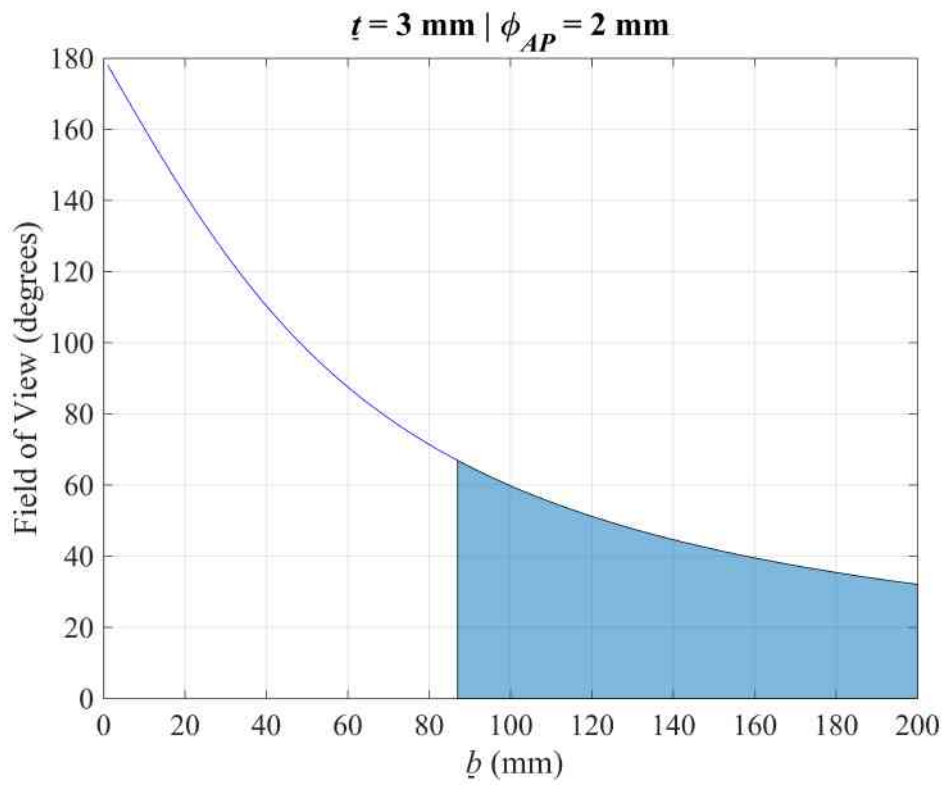
Figure 3.13: Collimation Free Region for 2-3 mm Aperture & 3 mm Thickness.
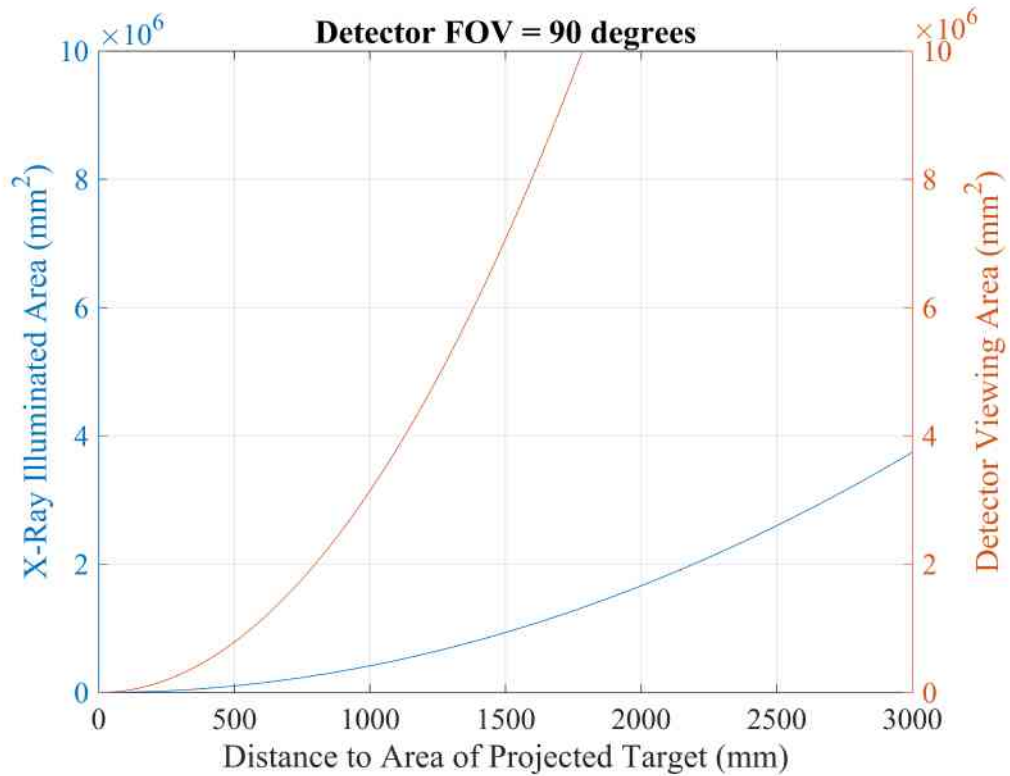
Figure 3.14: X-Ray Source Illumination and Detector Viewing Area: The red line on the left indicates X-ray illumination and the blue line on the right represents the detector viewing area.
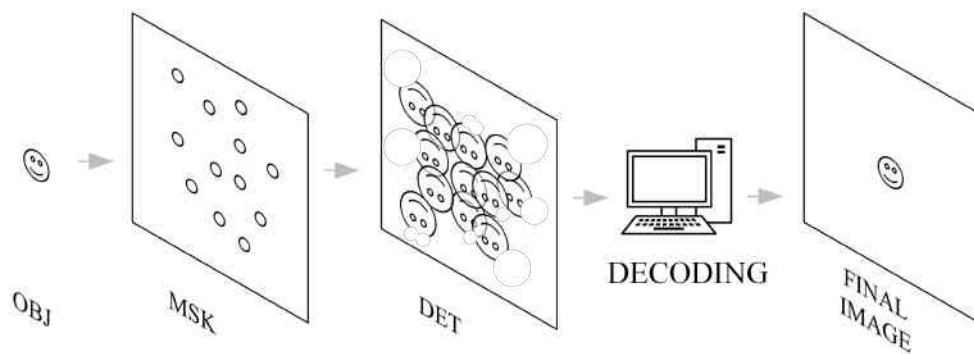
Figure 3.15: Corrected Encoding Process: This diagram is applicable for near-field CMI.

The consequence of RPS include parts of an imaging scene being introduced or lost. This is presented in Fig. 3.16, detailing how distance to the object in a scene, object size and relative aperture position on the mask play a crucial role in affecting the detector's RPS. An aperture positioned centre on the mask has a FOV that encompasses the object in its entirety. A shift in the position of the aperture, off-axis from the centre, decrease the chance of the entire object remaining in the FOV, as the detector sees a different perspective of the scene. When the object is closer to the mask in distance with an off centred aperture, then the chances of parts of a scene being lost increases due to the geometry of the FOV (see Fig. 3.16). Larger objects are also susceptible to the same phenomenon, which again is due to the geometry of the FOV when the aperture on the mask is off centre.

Exposures of the WWB object were captured to confirmed the RPS hypothesis and displayed in Fig. 3.17. Two 2 mm aperture and thickness pinhole masks were used; one with the mask's aperture centred and another off centre to the right by 32 mm. The scene was exposed with the WWB object positioned at a distance from the mask of 250 and 500 mm and fixed in its position for each exposure. When the aperture was centred on the mask the WWB object was within the detectors FOV in its entirety. The case was true for both distances, when the object was nearer and further away from the mask, agreeing with the model in Fig. 3.16. A change in aperture position (off centre) in the mask revealed a different perspective of the imaging scene. Only parts of the WWB object was visible and newer parts of the scene were introduced, as a result of RPS. Also, at a closer distance of 250 mm more of the WWB object was lost, agreeing with the model in Fig. 3.16. The fact that CMs contain multiple apertures positioned at different locations on the mask, relative to each other and the exposures from each aperture with changing views of the scene are summed during the decoding image process; may have implications on the quality of the final reconstructed image.

3.2.3   Geometry of Coded Masks

When taking into consideration the geometry of CMs one must take considerable care in its design. Provisions that were made for a pinhole mask must also apply to CMs in addition to the following. While an object within a scene is inverted through a pinhole and immediately resolved on the detector plane (see Fig. 2.6), a shadow of CM pattern is projected onto the detector plane. See Fig. 3.18 for the example of the 'box camera' (Hammersley et al., 1992). Complete projection of the full CM pattern is referred to as a 'full cycle' and can be seen in Fig. 3.18 for a photon source that is on-axis to the central imaging plane (the axis is invisible in the figures). Note, OBJ is exactly perpendicular to DET in Fig. 3.18 and near-field magnification is not applied (explained later on). This is the ideal scenarios in CMI, where there is only
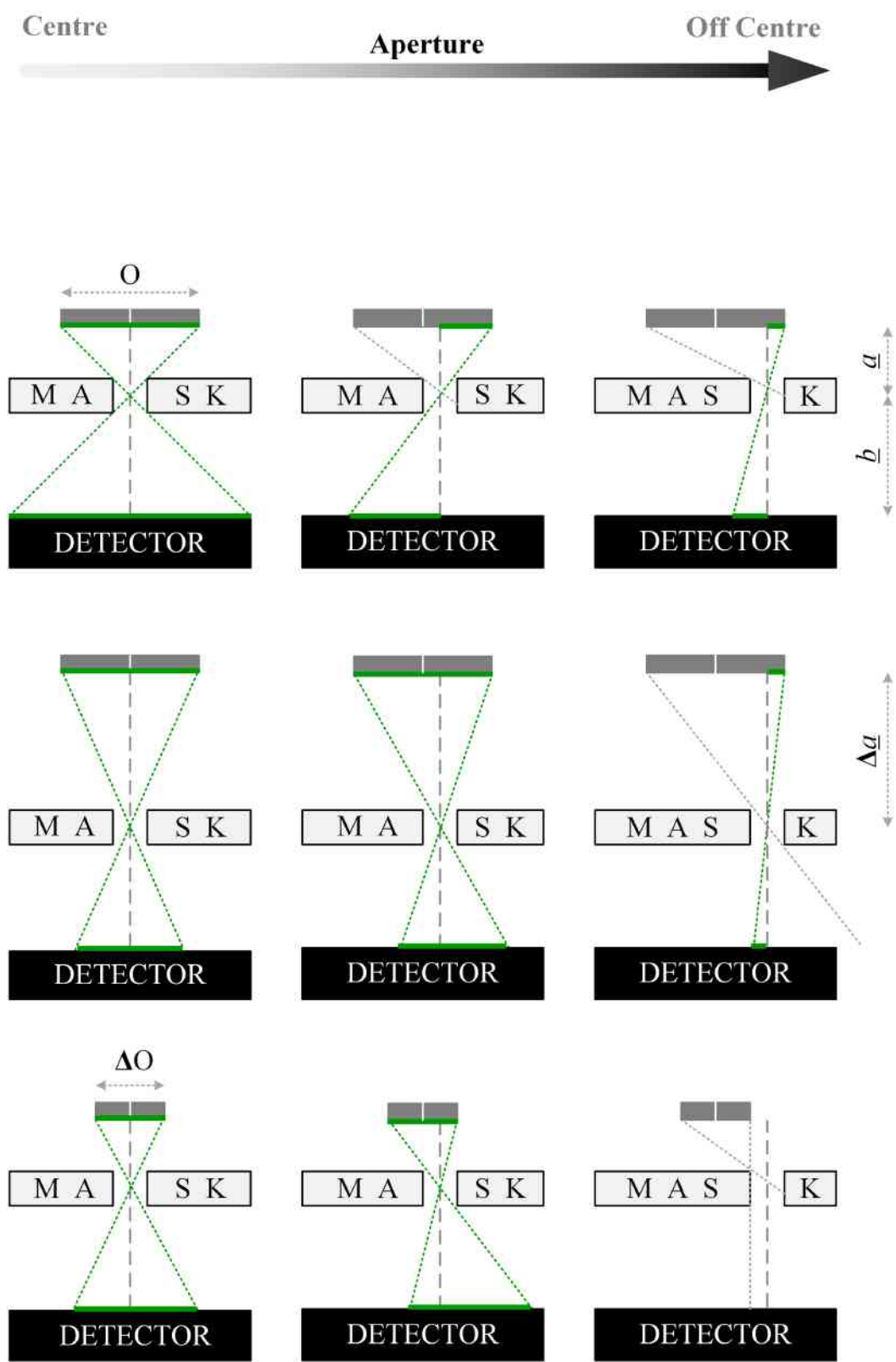
Figure 3.16: Relative Perspective of a Scene.

Centre Aperture   **Off-Axis Aperture**

$\underline{a} = 500$ mm $\underline{a} = 500$ mm

$\underline{a} = 250$ mm $\underline{a} = 250$ mm
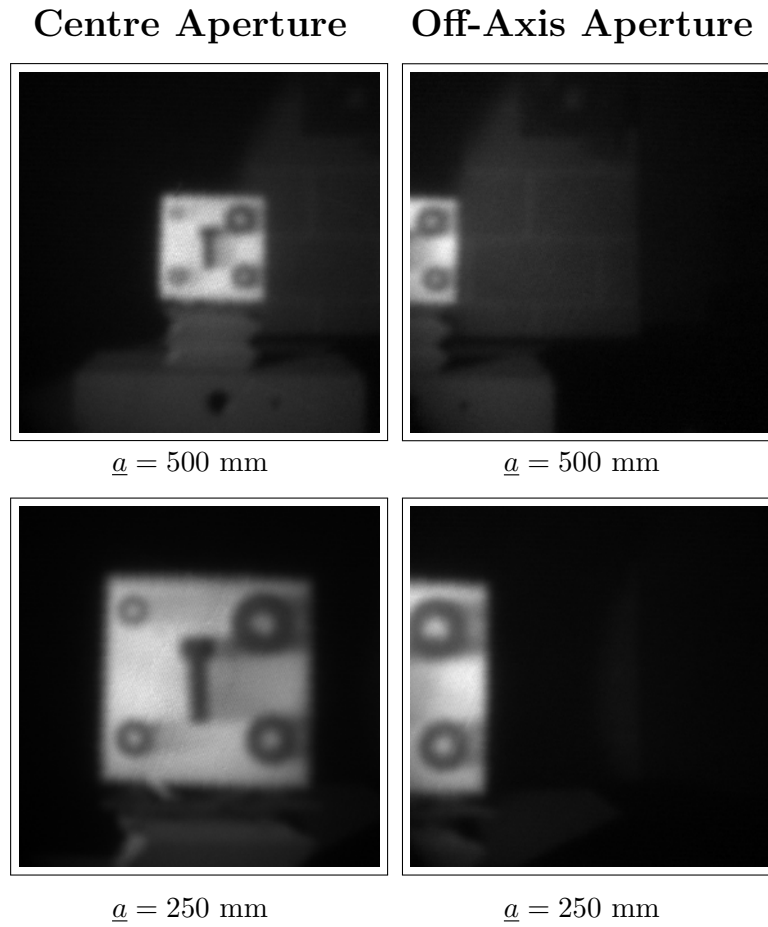
Figure 3.17: RPS Exposures from Shifting the Aperture Position.

a single on-axis source not subject to any magnification (discussed later on) (Skinner, 1984).

OBJ   MSK   DET
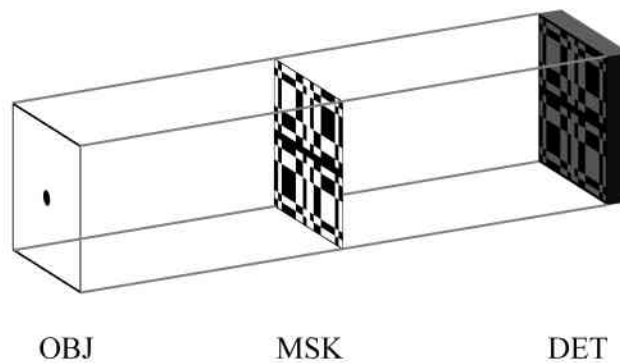
Figure 3.18: On-Axis Full Cycle Projection.

To complicate matters further, a change in position of the object/source shifts

the projected shadow and a full cycle is no longer projected as in Fig. 3.19. In this instance, there is only a 'partial cycle' that is projected so the signal is lost and errors will be introduced during the encoding process. A change in position of OBJ in Fig. 3.19 extending from the central imaging axis can be referred to as an 'extended scene'. Up until now the CM pattern in both Fig. 3.18 and 3.19 are referred to as 'non-cyclic' because the cycles do not repeat and are equal to 1 (Accorsi, 2001; Skinner, 1984, p. 62) . By repeating the cycle or extending the CM pattern so that a mosaic is created restores parts of the partially lost cycle, as in Fig. 3.20. Such CMs are then considered 'cyclic' in geometry (Fenimore and Cannon, 1978).
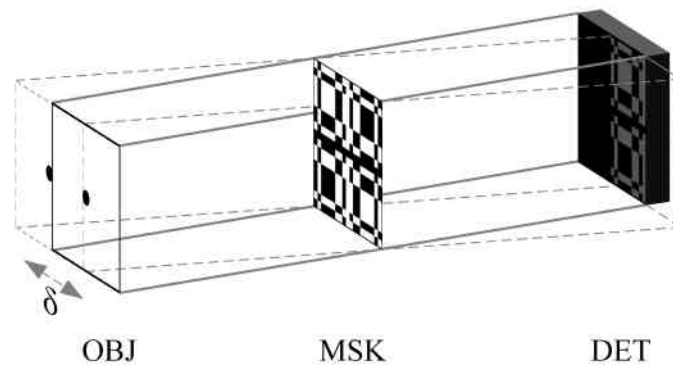
Figure 3.19: Off-Axis Partial Cycle Projection: Note, parts of the projected CM shadow has shifted off the detector plane.
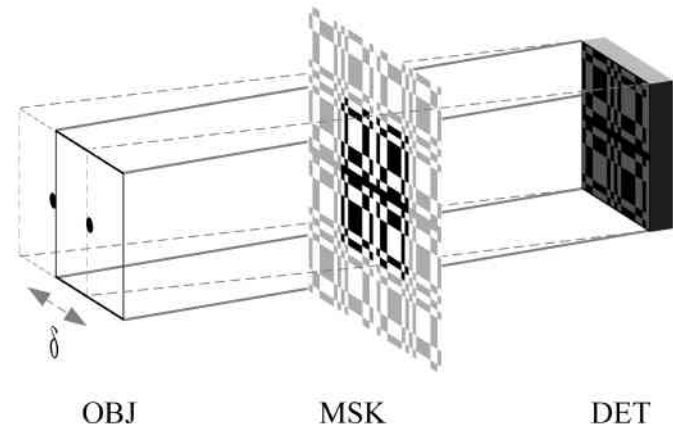
Figure 3.20: Off-Axis Full Cycle Projection: Note, a cyclic CM fills in parts of the projected CM shadow that has shifted off the detector plane.

The field of view of an XBI system had limiting factors for both the pinhole and coded mask. For CMs the FOV contained regions that were fully and partially coded for both cyclic and non-cyclic CMs. Fully coded field of view

68

(FCFOV) describes a region of a scene where photons passing through the CM projects a full cycle of its pattern onto the detector. Partially coded field of view (PCFOV) on the other hand refers to photons from parts of the scene that only projects a partial cycle (see Fig. 3.21) (Accorsi, 2001, pp. 59-60) (Sun et al., 2015). Creating a cyclic version of the CM pattern reduces the effects of PCFOV. This is seen with the example in Fig. 3.20. A cyclic CM pattern that exceeds the dimension of the detector plane also increase the FCFOV region of the imaging systems FOV as seen in Fig. 3.21.
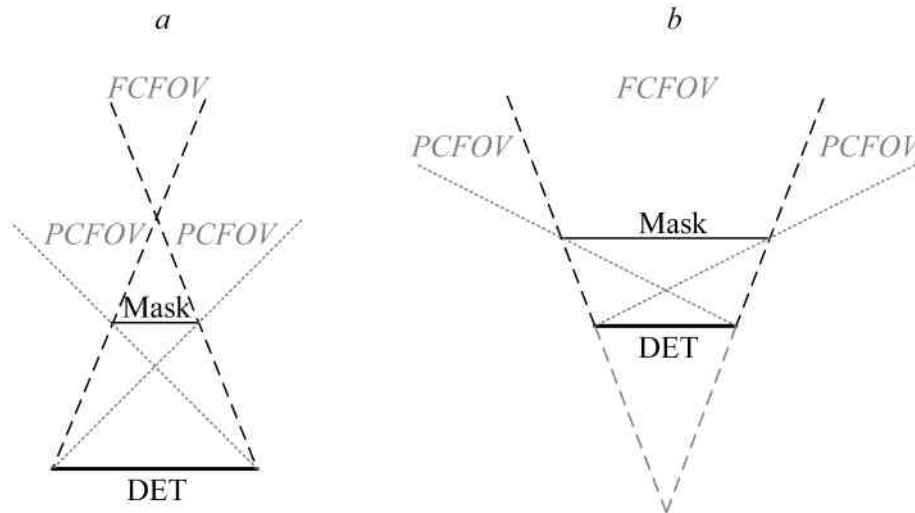
Figure 3.21: FCFOV & PCFOV: The diagram shows how FCFOV & PCFOV changes with masks and detectors of different sizes.

3.2.3.1 Mask Mosaicking or Cyclic Coded Masks

A cyclic or mosaicked version of the CM pattern was constructed starting with a blank template twice the size of the CM's dimensions. Take for example the non-cyclic 19 MURA pattern in Fig. 3.22, with vector sizes $p = 19$ and $q = 19$ elements used to generate the $2p$ and $2q$ template. Notice how four cycles of CM patterns can comfortably fit into the template. Consequently, this gives rise to a template that is 38×38 elements. Proceeding onwards, one row and column was deleted from the template with its size decreasing to 37×37 elements to avoid any ambiguity (Faust, 2002; Skinner, 1984). To further expand, the entire cyclic pattern should only amount to one full cycle of the non-cyclic pattern. The non-cyclic pattern was then placed and centred within the template and the pattern was then repeated outwards to complete a cyclic version of the non-cyclic CM pattern (Fenimore and Gottesman, 1989; Cieślak et al., 2016) (Jupp, 1996, pp. 42-43). The process of generating cyclic patterns were undertaken in MATLAB (MathWorks, 2018) using the 'padarray' function with a 'circular' pad. A cyclic version of the non-cyclic mask was

created using Fig. 3.22 and the non-cyclic pattern may be extracted from the cyclic CM by cropping out the extended pattern. This is useful, particular for imaging single on-axis radioactive gamma ray sources which is presented later on.

Near-field magnification (M_{NF}) was accounted for when designing CMs for the XBI system, which arises when the object ($\boldsymbol{O}$) is closer to the mask ($\boldsymbol{M}$) (a coded mask in this case). The projection of $\boldsymbol{M}$ onto the detector ($\boldsymbol{D}$) was larger in size as a consequence of M_{NF}. Similarly, this is also true when $\boldsymbol{D}$ was further away from the CM as in Fig. 3.23. Calculating M_{NF} was done using Eq. 3.5, where $\underline{a}$ = object to mask distance and $\underline{b}$ = mask to detector focal plane distance.

$$M_{NF} = \frac{\underline{a} + \underline{b}}{\underline{a}} \tag{3.5}$$

3.3 System Calibration

The XBI system was subject to calibration to reduce errors and achieve the best results. Horizontal and vertical fan beam optical lasers were installed onto both the X-ray source and camera to ensure the imaging object remained central in the FOV of the camera and radiation beam. The first calibration process took place with aluminium plates placed at approximately 300 mm from both camera and X-ray source. Each plate had a central target 'crosshair' marked onto their surfaces, and the fan laser beams were aligned to the target, forming a cross that would be perfectly aligned when the plates were removed (see Fig. 3.24).

A radioactive isotope ^{241}Am source was centred in the FOV of the detector against a lead background to approximate an ideal point source or imaging scene similar to a single star in the night sky. The ^{241}Am source was exposed with the MTA 19 MURA NTHT so that a 'perfect' shadow of the pattern would be projected onto the detector as in Fig. 3.25. Placing a horizontal line similar to that in Fig. 3.25 indicated if square elements were perfectly levelled. If not corrections were applied before the decoding process. Projected shadows of the CM pattern onto the detector plane revealed if there were concerns with collimation of the mask as presented in Mu and Liu (2006). When reconstructing the ^{241}Am radioactive source exposure the final image was a true representation of the scene. Subsequently, this verified the encoding and decoding process and was used for more complex scenes. Exposures of the ^{241}Am radioactive source were captured and decoded using the experimental masks. As expected the reconstructed images resembled their calculated PSF and are presented later on in Chapter. 7.

Non-Cyclic

q

p

2×2 mosaic template

$2q$

$2p$

Crop out extended cycles for non-cyclic patterns

Cyclic

$2q - 1$

$2p - 1$

Minus a row and column

$2q - 1$

$2p - 1$

Extend non-cyclic pattern with repeating cycles
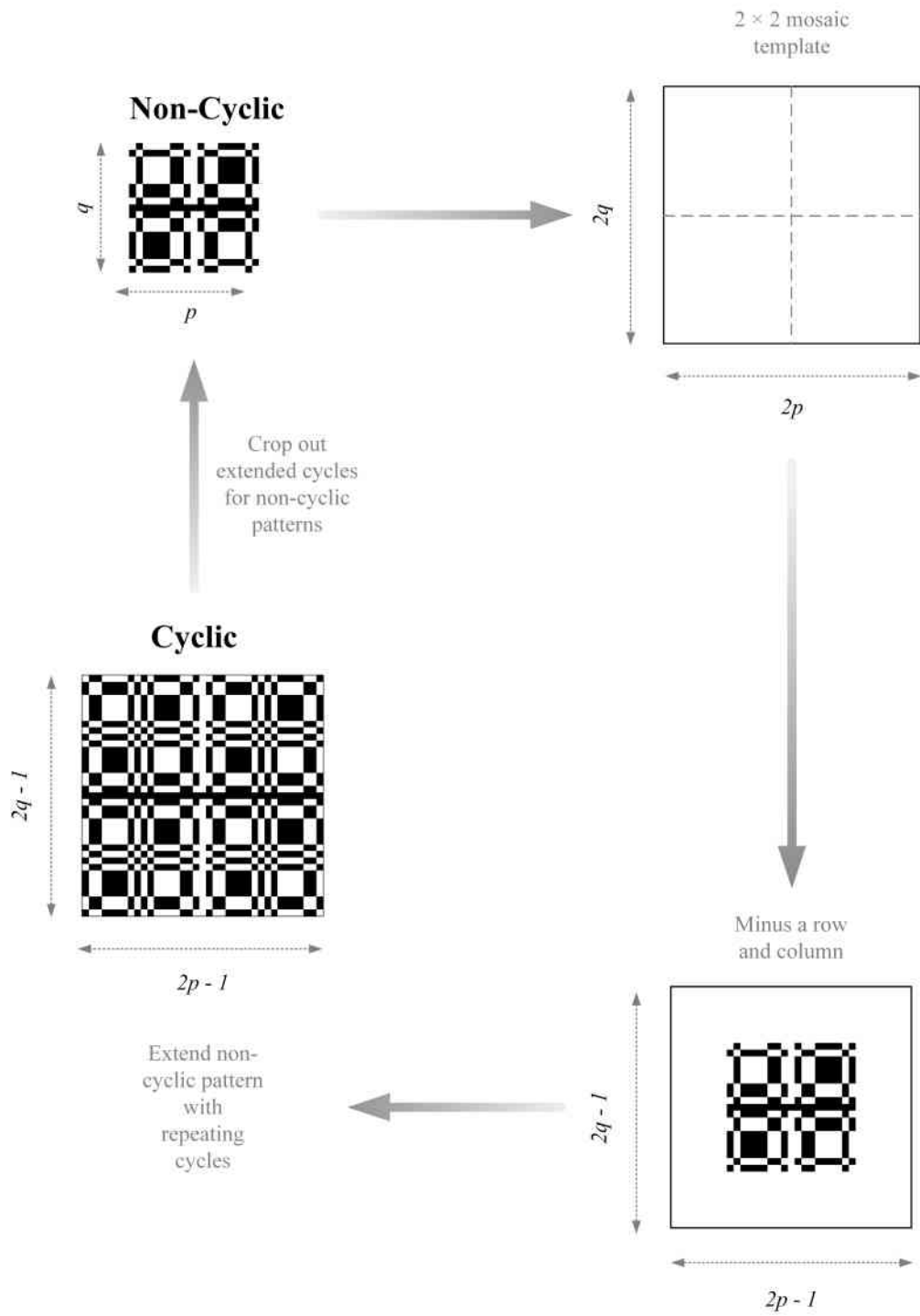
Figure 3.22: Cyclic & Non-Cyclic Coded Masks Creating Process.

71
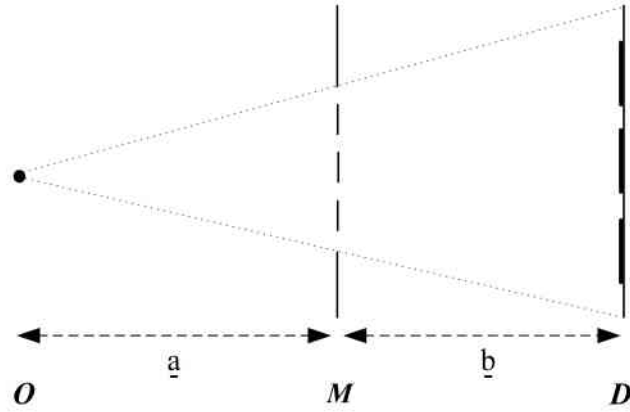
Figure 3.23: Near-Field Magnification: The diagram demonstrates the magnification of M onto D.

Figure 3.24: Laser Alignment Calibration.

3.4   Image Processing & Quantification

Previous chapters have used the symbol A to denote encoding arrays which are used to determine its PSF. For actual exposures of an object or imaging scene that are encoded and detected with a camera's sensor, the symbol (D) will be used from now on to avoid any confusion between the two. Exposing a scene with the coded mask M to yield D can be mathematically represented as in Eq. 3.6.. This is similar to Eq. 2.5, with the exception of an additional noise term N added.

$$D = (O \otimes M) + N \tag{3.6}$$
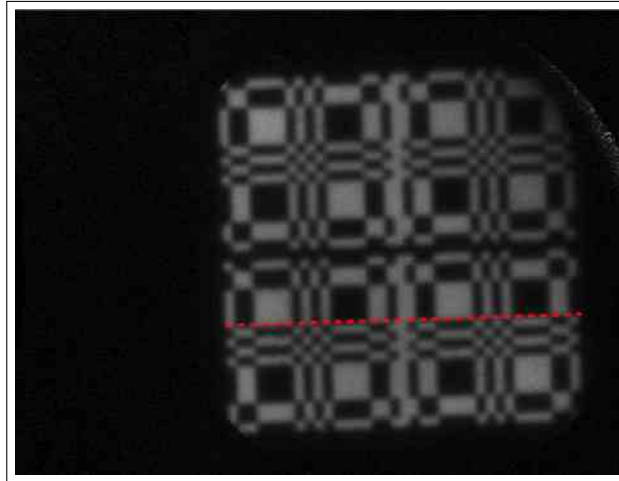
Figure 3.25: Levelling a Projected CM Exposure.

It is important to note that M for the encoding process was usually performed with cyclic masks unless stated otherwise. In the real world, photons emitted or reflected from O cast a shadow of M on D as in Fig. 3.26. Each opening in M contained information of O as in Fig. 3.15, which demonstrates the encoding process. Fig. 3.26 shows the encoding and decoding process for a single source. If the scene were complex, then the projected mask pattern on D would be unrecognisable and scrambled.
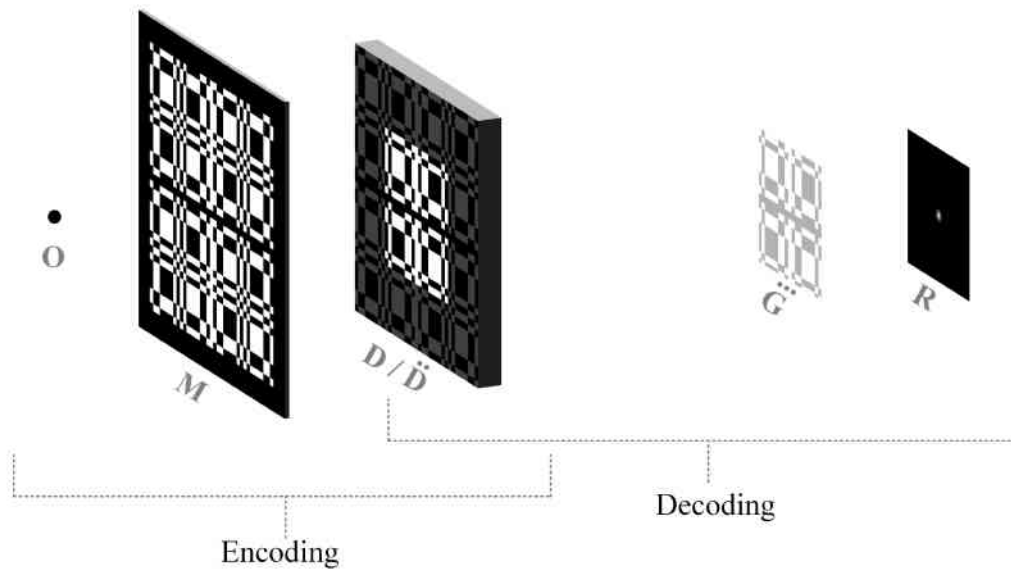
Figure 3.26: Encoding & Decoding Process of CMI: Note, the diagram demonstrates the process for a point source.

3.4.1 Decoding Encoded Exposures

Image reconstruction (R) of CM exposures in this thesis were decoded using cross-correlation (unless stated otherwise). If M is cyclic in the encoding process, then its projected non-cyclic or base pattern pixel (px) size must exactly match that of $\ddot{G}$. The non-cyclic part of D in Fig. 3.26 refers to the lighter region in the centre and was cropped out to yield $\dot{D}$. Subsequently, $\ddot{G}$ was scaled to the same size as $\dot{D}$. To ensure the array sizes and dimensions in pixels of $\ddot{G}$ were equal to $\dot{D}$, Eq. 3.7 and 3.8 were used to calculate and find the new dimensions of $\ddot{G}$. The scaling dimensions in px in Eq. 3.7 and 3.8 were p_{px} and q_{px} with ps indicating the photo-site size of 0.108 mm per px. p and q represented the physical non-cyclic base pattern size (BPS) of M, while M_{NF} is the near-field magnification from Eq. 3.5.

$$p_{\text{px}} = p\frac{M_{NF}}{\text{ps}} \tag{3.7}$$

$$q_{\text{px}} = q\frac{M_{NF}}{\text{ps}} \tag{3.8}$$

With $\dot{D}$ and $\ddot{G}$ being the same in size of $p \times q$, it must be remembered that one array must be larger than the other for cross-correlation to occur, as in Fig. 2.9. To achieve this, $\dot{D}$ was subjected to a 'circular pad' using the pad function in MATLAB; forming $\ddot{D}$ with the new dimensions of $2p_{\text{px}} - 1 \times 2q_{\text{px}} - 1$. The mathematical expression for image reconstruction of a single CM exposure via cross-correlation is found Eq. 3.9 and was used for all images in this thesis (unless stated otherwise).

$$R = \ddot{D} \otimes \dddot{G} \tag{3.9}$$

In the real world of CMI, scenes can be considered to be made from multiple point sources that are off-axis, and the projected image on the detector may be subject to greater near-field magnification. This is referred to as a 'complex scene'. Consequently, D in Fig. 3.26 would be scrambled and unrecognisable. When decoding exposures of a complex scene, it is important to know that the projection of M may exceed the detector size, due to near-field magnification. Also, off-axis sources from a complex scene will cause a shift in the CM shadow that is projected onto the detector as in Fig. 3.19. It was imperative that the shift in the non-cyclic pattern in D did not exceed the boundaries of the detector plane to avoid PCFOV.

Any noise and artefacts presented from CM exposures of a single source that was on-axis was intensified with a complex scene. This included artefacts and

noise inherent to the CM. Nonetheless, second exposures were captured with the 'anti-mask' (Jayanthi and Braga, 1991; DeWeert and Farm, 2015), which is an inverse version of the CM. The concept behind the anti-mask is to obtain a second exposure of the scene with an inverted version of the mask. This inverts inherent artefacts. By summing images from both mask and anti-mask, it cancels any inherent artefacts that is presented in the final image, while signal from the scene remains relatively constant. However, this procedure is costly and time consuming because an extra CM must be fabricated. Similar results are achieved by rotating the mask with the artefact travelling with rotations of the mask. Again the signal from the scene was somewhat constant. Note, this will not work for symmetric CMs and it is best suited with those that are invariant.

All X-ray backscatter images of complex scenes other than those of the ^{241}Am radioactive source were summed from two exposures by rotating the CM at 90°. A formula was derived in Eq. 3.10 to distinguish summed CM images decoded via correlation ($\boldsymbol{S_n}$) from those of single decoded images, such as $\boldsymbol{R}$. The i in Eq. 3.10 refers to the number of exposures or terms with rotations and n indicating the maximum. Note, $\boldsymbol{R}$ contains only one exposure so the '1' is implied and $\boldsymbol{R_1} = \boldsymbol{R}$. Overall, summed images decoded via cross-correlation would be referred to as $\boldsymbol{S_2}$ (see Fig. 3.27 for a visual representation). All image reconstructions were automated in MATLAB with processing times between 1 - 6 s for cross-correlation and blind deconvolution at 30 iterations (discussed later on).

$$\boldsymbol{S_n} = \boldsymbol{R} + \sum_{i=1}^{n} \boldsymbol{R_i} \tag{3.10}$$

$$= \boldsymbol{R} + \boldsymbol{R_2} + \boldsymbol{R_3} + \boldsymbol{R_4} + ...\boldsymbol{R_n}$$

Unless stated otherwise, all X-ray backscatter images captured with the system constructed in Chapter. 3.1 were generally exposed to X-rays of 100 kV at 8 mA to utilise maximum power; while avoiding X-ray unwanted leakage through the mask. X-ray backscatter CM exposures required that the radiation source was collimated so that only the object of interest was illuminated. This came as a result of high scatter from the small enclosed environment of the radiation cell.

3.4.2 Image Quantification Process

Exposures taking with the XBI system were quantified by calculating their SNR using Eq. 2.28. Data from the signal and background were sampled

75
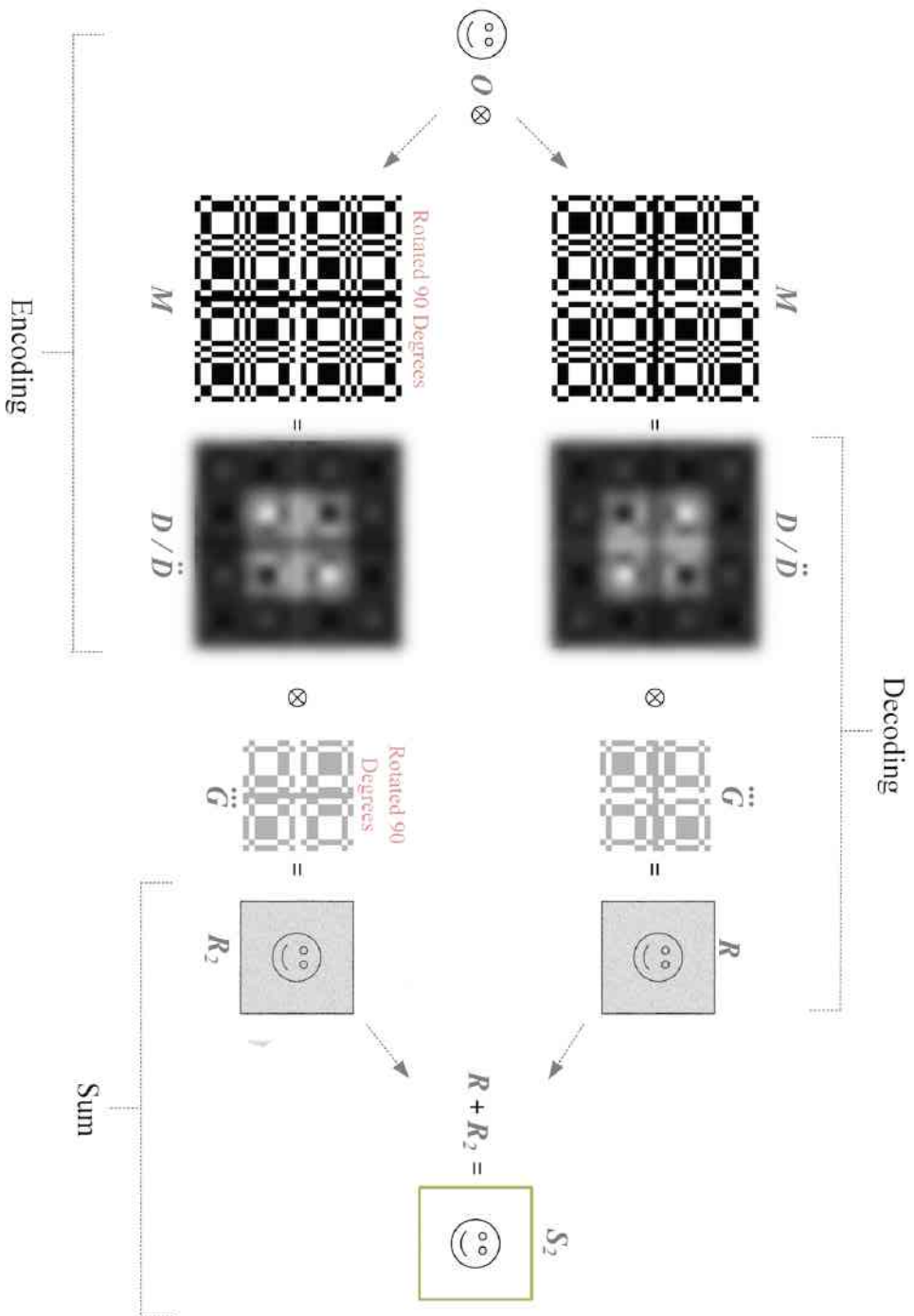
Figure 3.27: Summed Exposures with an Anti-Mask using Cross-Correlation.

76

from images, as in Fig. 3.28. Data from the sample was collected within the boundaries of the signal and the mean value was determined. If you take into consideration the signal of a PSF, only the peak value is used along with the standard deviation of the background. That is to say, the brightest area of the signal is well within its boundaries. However, hot pixels may be present (saturated pixels as a result of damage to parts of the camera's sensor) and an inaccurate value for the signal might be interpreted. This was avoided by taking the mean value of a range of samples for the signal, which would still be close to the peak value. This method was the one used in this thesis and it is supported in Simpson and Barrett (1980). Great care was taken when cropping the signal as, noise may be included from the background, due to difficulties distinguishing the boundaries between the two.

Note, the background in the quantified images presented in following chapters comprised of a lead backdrop. For occasions when SNR of multiple images were compared with a wide variation in their values, the results were given in decibels (dB) as in Eq. 3.11. Samples were extracted from the strongest signal in the image, and the data was also used to calculate CNR. Great care was taken to ensure the signal was not saturated in the encoded exposures, as the pixel intensities would multiply during the decoding process (cross-correlation), which could potentially result in a saturated final image.

$$SNR\,(dB) = 10\log_{10}\,(SNR) \qquad (3.11)$$

(a) (b)
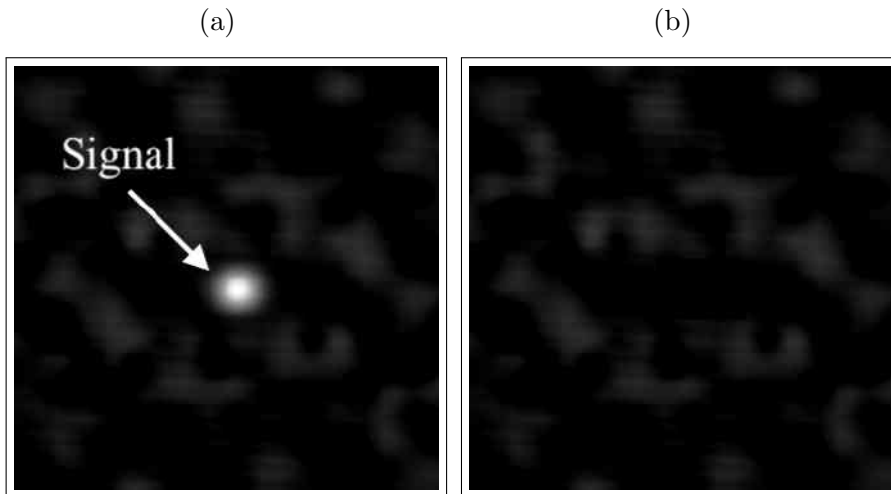
Figure 3.28: SNR and CNR Quantification Process: (a) shows the signal where the mean is calculated over most of the region. (b) the signal is cropped out with the background remaining. Taking the standard deviation of the background yields the noise (N).

Dark frames at similar exposure times of the main images in this thesis were captured and subtracted to reduce dark current noise. Also, the quadrant and WWB presented in Chapter. 3.1.2 were exposed to find the optimum exposure times for SNR. The experimental parameters such as, object to mask distance and mask to detector distance were the same for images presented later on this thesis. SNR data from the experiment were plotted as a function of exposure time for each mask used in this thesis to determine the optimum times. Fig. 3.30 to 3.33 revealed such exposure times at the region were the lines levelled off at a relatively constant SNR value (Richmond, 2018)(Ghaye, 2015, p. 66). Conversely, photon noise dominated before the SNR became constant. Therefore, optimum exposure times was chosen from the regions where SNR was constant and the photon noise was least dominant.
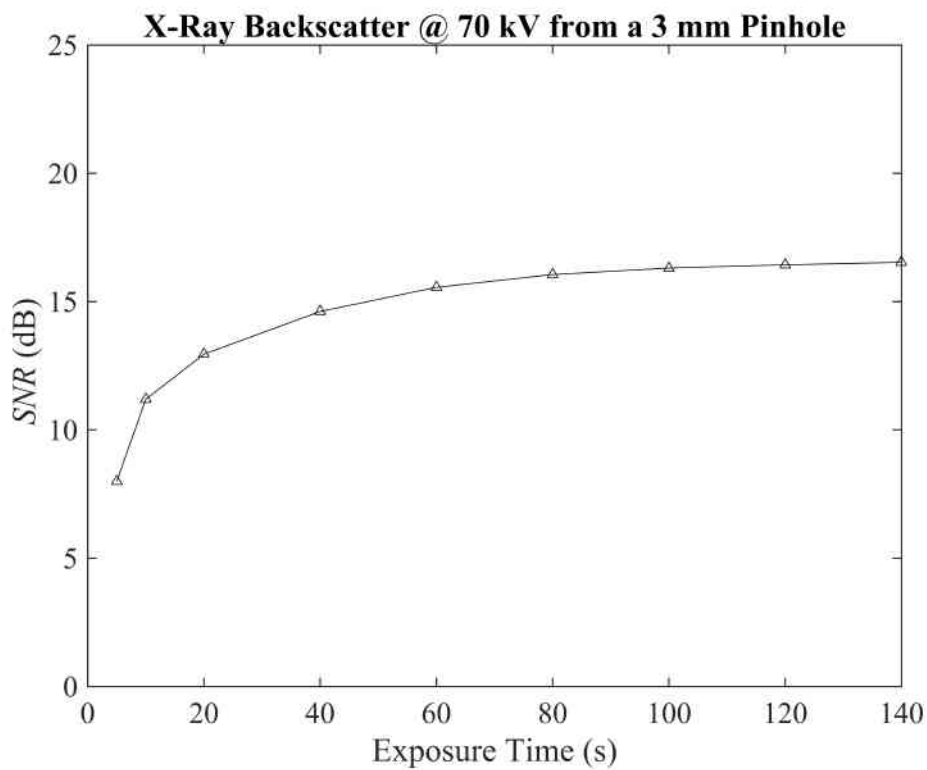
Figure 3.29: Optimum Exposure Time of 100 s for the 3 mm Pinhole XBI.
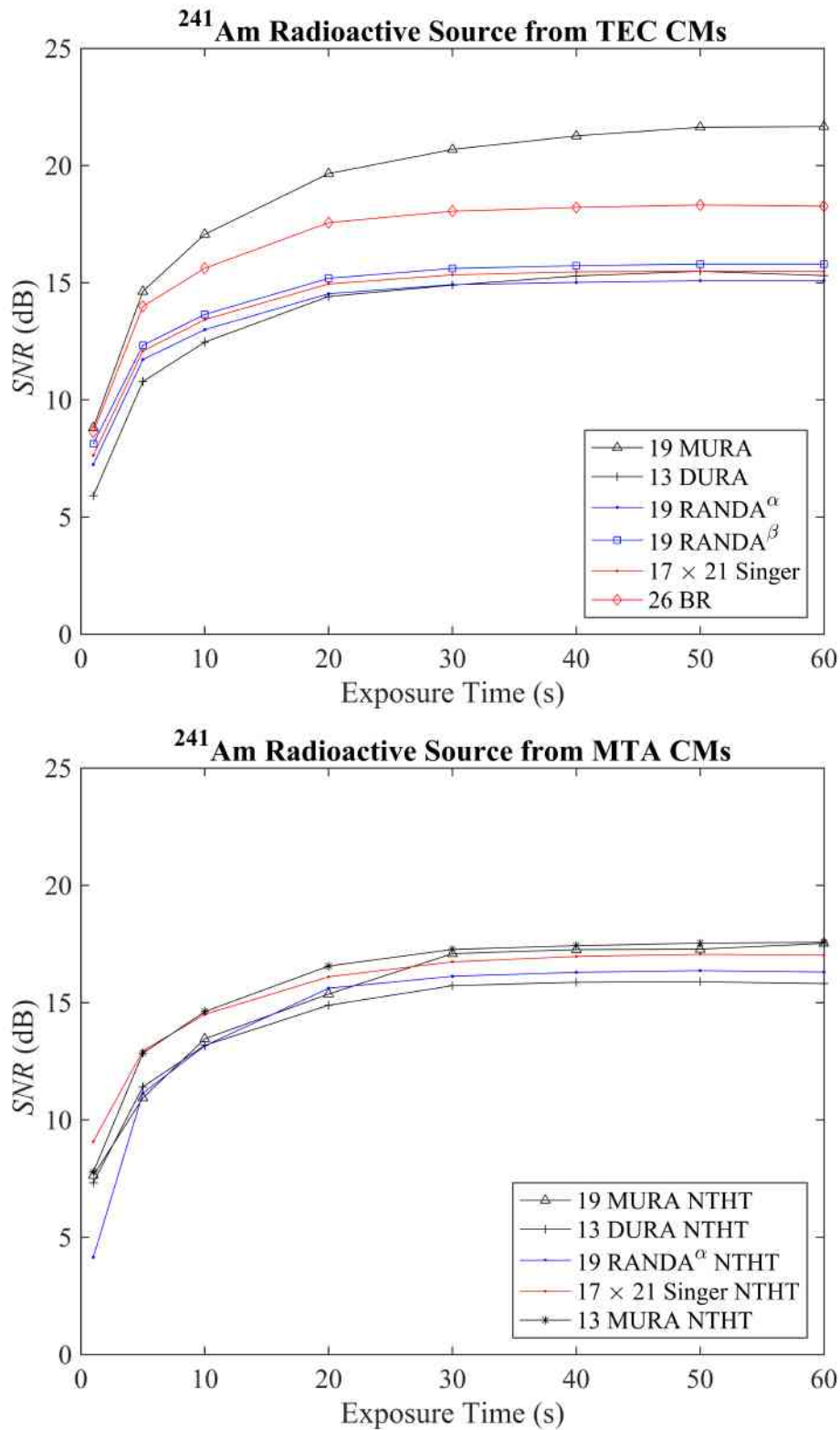
Figure 3.30: Optimum Exposure Time of 30 s for the ^{241}Am Source.
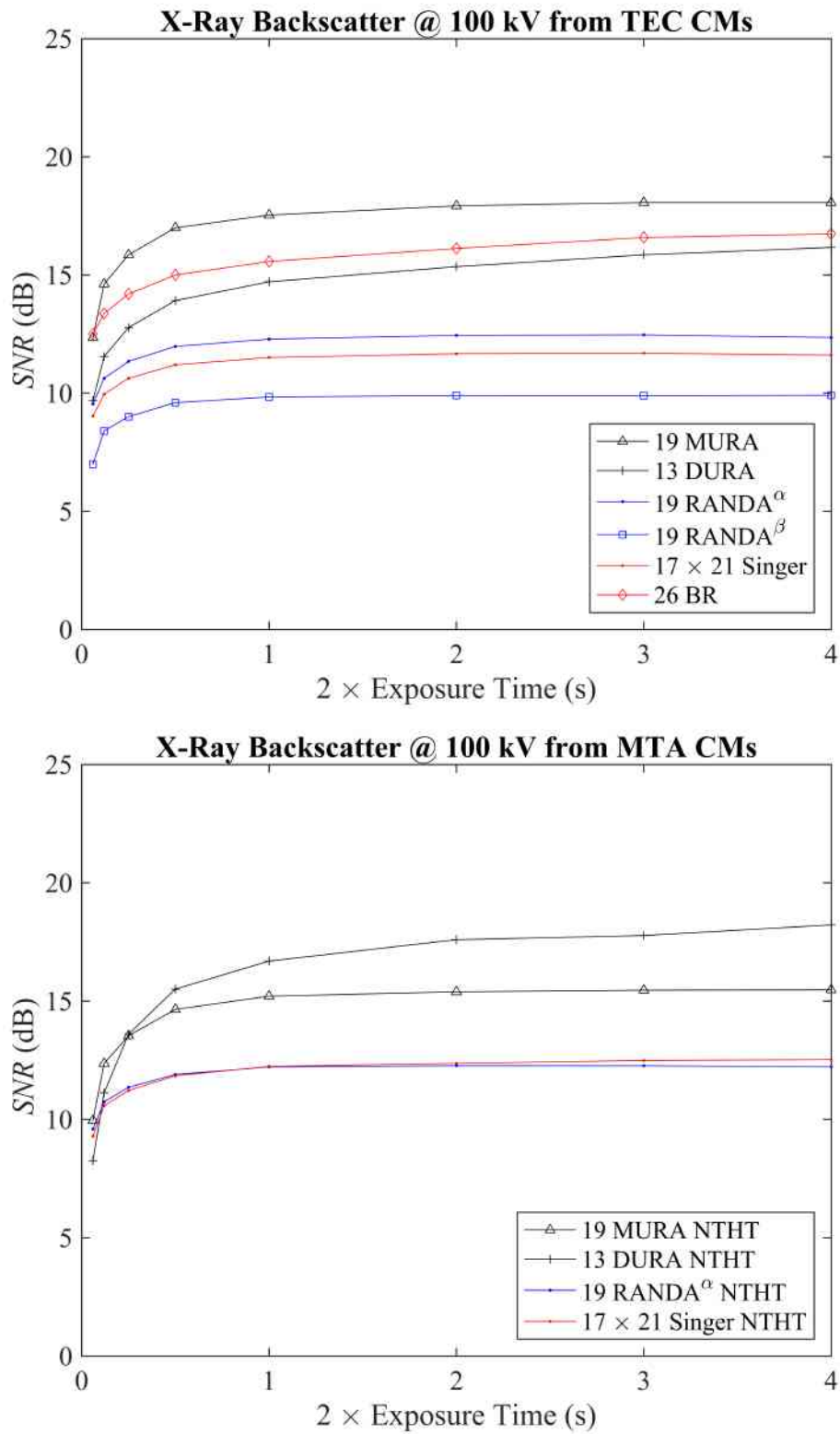
Figure 3.31: Optimum Exposure Time of 3 s for the CM XBI with 100 kV.
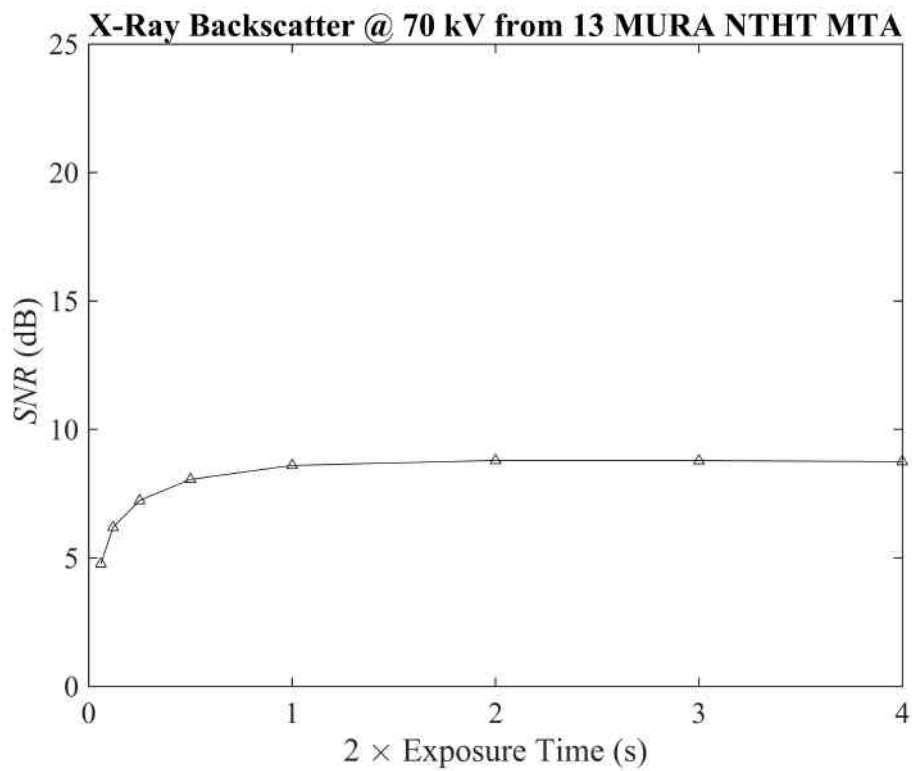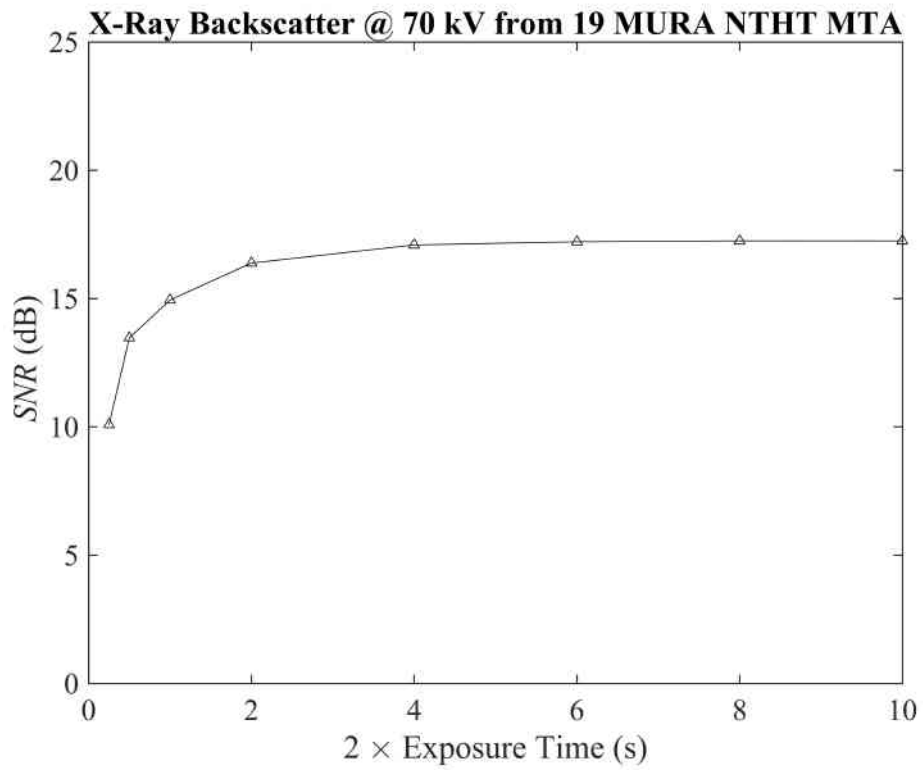
Figure 3.32: Optimum Exposure Time of 2 s for the CM XBI with 70 kV.
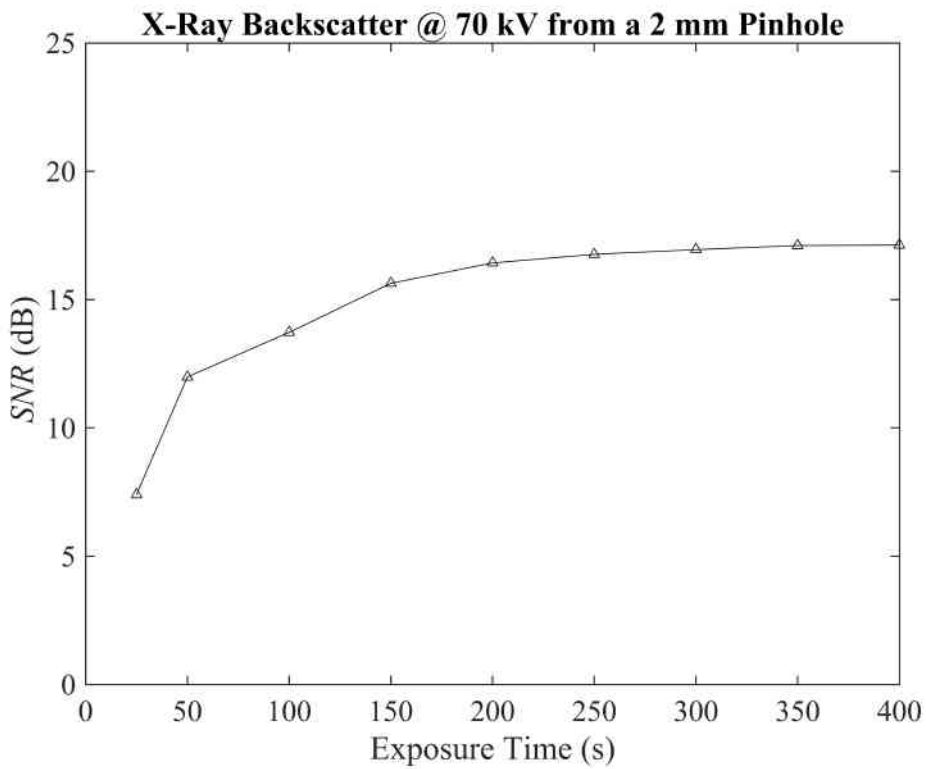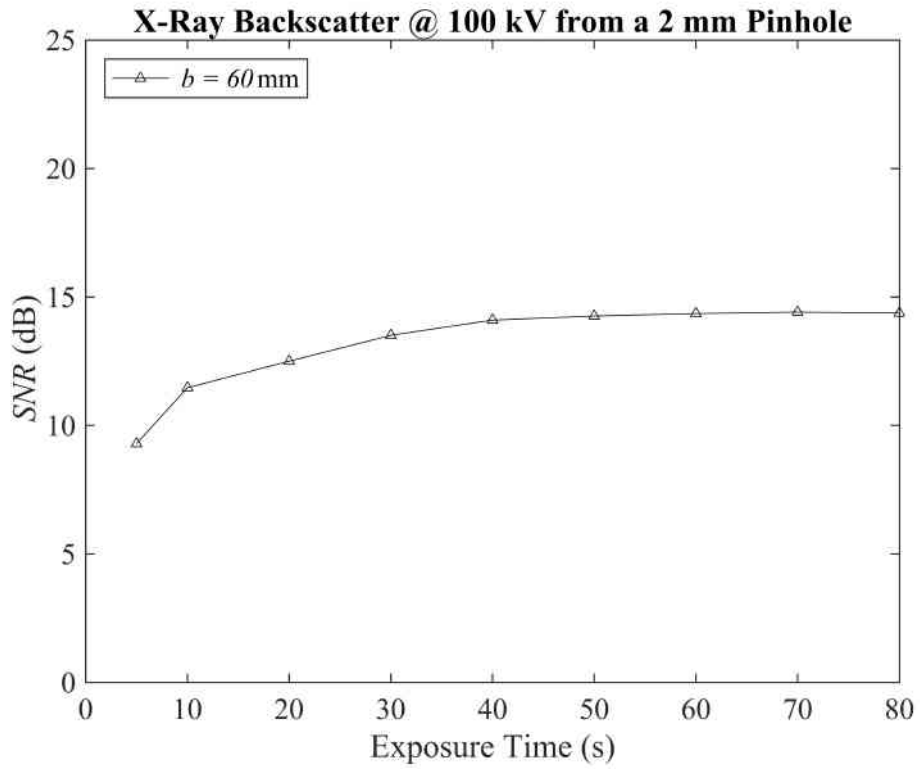
Figure 3.33: Optimum Exposure Time of (top) 60 s and (bottom) 350 s for the 2 mm Pinhole XBI.

Chapter 4

Development of Mask Manufacturing

Traditional methods of fabricating high density imaging masks from theoretical arrays are subject to a compromise in their pattern design. Most encoded arrays do not have good self-supporting structures to keep the opaque regions of the mask intact. Therefore, a compromise and modification in the array pattern is often implemented to construct the physical mask. Ideally, square openings are required to replicate elements of an array. Options to achieve square openings include laser cutting, or etching (Accorsi, 2001, p. 142) (Starfield, 2009, p. 48) (Accorsi et al., 2001). However, these methods can be costly and do not provide a solution to the problem, because square openings must be rounded at the corners to form a support structure for the elements. An alternative option would involve generated a NTHT version of the original array and machine drilling round holes in place of square elements. Not only is this relatively cheaper, but the process is somewhat simpler.

Although machined NTHT CMs provide a self-supporting structure, it is at the detriment of desirable imaging properties of the original array, as square elements become circular. A solution to the above problem is presented by 3D printing a radio-lucent mould, which was then cast with radiation attenuating material (Miller et al., 2011; Munoz et al., 2017b; Muñoz et al., 2018b). The 3D printed mould included open elements of the array pattern attached to a base, which served as a support structure. In addition, square elements are retained, preserving ideal imaging properties. Such techniques provides a low-cost method of fabricating CMs along with rapid prototyping using an off the shelve equipment such as a 3D printer. This chapter details two methods of constructing 3D printed CMs for X and gamma ray imaging. The materials used to manufacturer CMs are analysed to determine their integrity for imaging. Additionally, a brief instruction on how machined NTHTs were fabricated. Note, all masks were manufactured in house at Cranfield University.

4.1 Mask Design & 3D Printing

The 3D printed mask manufacturing process started with generating coordinates of open elements of the encoded array. They were in the form of a text file which was then imported into SOLIDWORKS® (Dassault Systemes, 2015) as a 'table-driven pattern'. A single element representing a $1 \times 1 \times 1$ mm cube was drawn, which formed the basis of open elements in the array pattern. The cube was then replicated using coordinates generated earlier to form the array pattern (see Fig. 4.1a). The pattern was subsequently merged to a cavity in the mould Fig. 4.1b to complete the final CM mould Fig. 4.1c.

An Ultimaker 2 Extended 3D printer (Ultimaker, 2015) was used to print the CM mould. The type of print filament depended on the casting temperature, which included polylactic acid (PLA) and acrylonitrile butadiene styrene
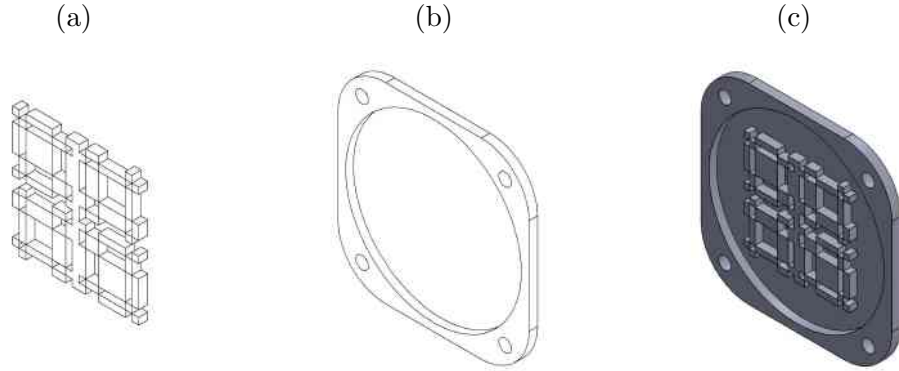
Figure 4.1: CAD Mask Design: (a) pattern (b) mould (c) final CM pattern.

(ABS). Print settings for PLA and ABS were different and are presented in Table 4.1.

Table 4.1: Ultimaker 2 Extended$^{©}$ 3D Printer Settings for Masks.

Settings		PLA	ABS
Quality (mm)	Layer Height	0.1	0.1
	Shell Thickness	0.8	0.8
	Initial Layer Thickness	0.3	0.3
Speed (mm s^{-1})	Travel Speed	150	250
	Bottom Layer Speed	30	20
	Infill Speed	100	50
	Outer Shell Speed	40	50
	Inner Shell Speed	80	50
Temperature (°C)	Nozzle Temperature	210−220	240−260
	Build Plate Temperature	60	100
Support	Infill (%)	20	20
	Brim	No	Yes
	Build Plate	Glue stick	Kapton$^{®}$

4.2 Hot Casting with Acrylonitrile Butadiene Styrene

Hot casting was performed with a ternary bismuth alloy (Bi 57 wt%, Sn 26 wt%, In 17 wt%) with a eutectic temperature of 80 °C. The temperature was crucial for the casting process to avoid mould damage through heat transfer. The fabrication stage began with melting elements containing the highest

melting point, then subsequently adding all other elements to the liquid metal. The liquid alloy mixture was cooled to 90 - 100 °C, high enough to maintain a liquid state but lower than the 'glass transition temperature' (T_g) of 105 °C for the acrylonitrile butadiene styrene mould. Consequently, this was to avoid any structural damage. A cooling period off 3 - 4 hours was in place before polishing to expose the ABS elements. The hot casting Process is presented in Fig. 4.2a-c. The final solidified alloy was measured for its density (ρ) with 8.6 g cm^{-3}. Observation revealed elements becoming detached as a result of flexibility in the ABS mould from poor adhesion (see Fig. 4.3). Note, the white bar in Fig. 4.3 is a scale indicator that measures 50 mm. Consequently, experiments with the hot cast CMs were not pursued any further. Additionally, the manufacturing processes were rather challenging and the densities were lower than that from CMs from the cold cast method.

(a)   (b)   (c)
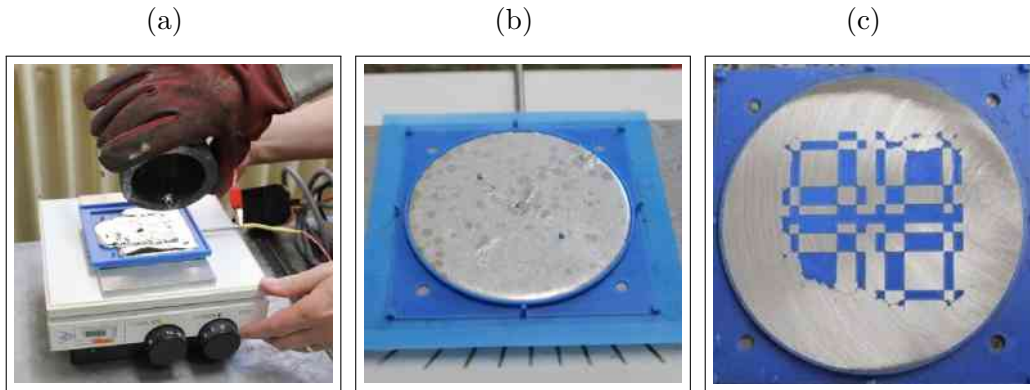
Figure 4.2: Hot Casting Process: The digram shows the hot casting process with (a) the molten liquid alloy being poured into the ABS mould. (b) a cured version of the CM is demonstrated, which is then (c) polished to reveal the open elements of the mask.

4.3   Cold Casting with Polylactic Acid

3D printed CMs were fabricated with cold castings taking place at room temperature. The mould was printed from polylactic acid with a T_g of 60 °C. A tungsten epoxy resin composite (TEC) material was used (also known as the Technon$^{\circledR}$ poly kit Inc (2001)) for casting with a maximum particle size of 149 microns (100 mesh). Epoxy resin forming the TEC comprised of two-parts (E_P) (BJB Enterprises, 2014) and when mixed with tungsten powder according to the manufacturer's guideline yielded densities in the range of 9.6 - 10.6 g cm^{-3}. Once the TEC was cast into the mould, a curing time of 24 hours was required, followed by polishing to complete the process (see Fig. 4.4a-c, where
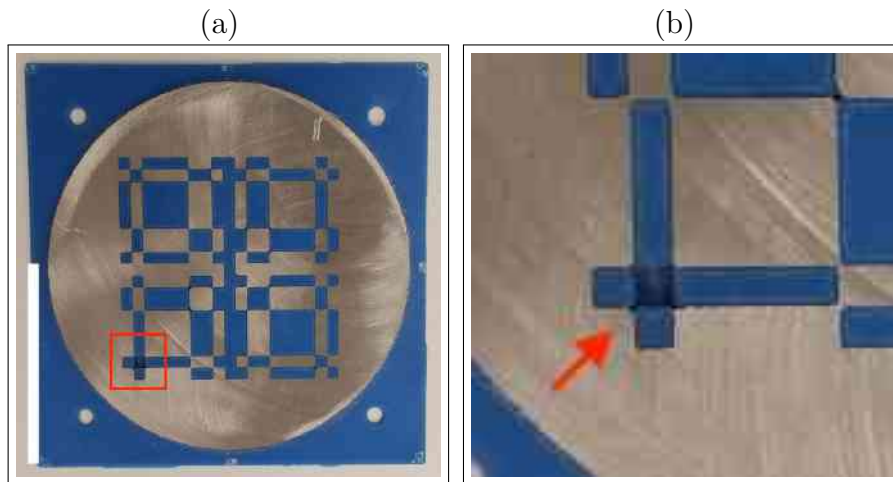
Figure 4.3: Hot Cast CM Structural Problems: The red arrow in the diagram points to elements that have become loose from the mould, due to poor adhesion.

the white bar indicates a scale of 50 mm). Complete example 3D printed CMs include the cyclic 17×19 URA 'anti-mask' (discussed later on) and 19 MURA is presented in Fig. 4.5. CMs manufactured using the cold cast method were more robust than that of the hot CMs. Contrary to hot cast CMs, elements remained intact within the mould due to strong adhesion. Because of the high densities of cold cast CMs and its structural integrity, all 3D printed CM exposures in this thesis were taken with masks produced with the cold casting method.
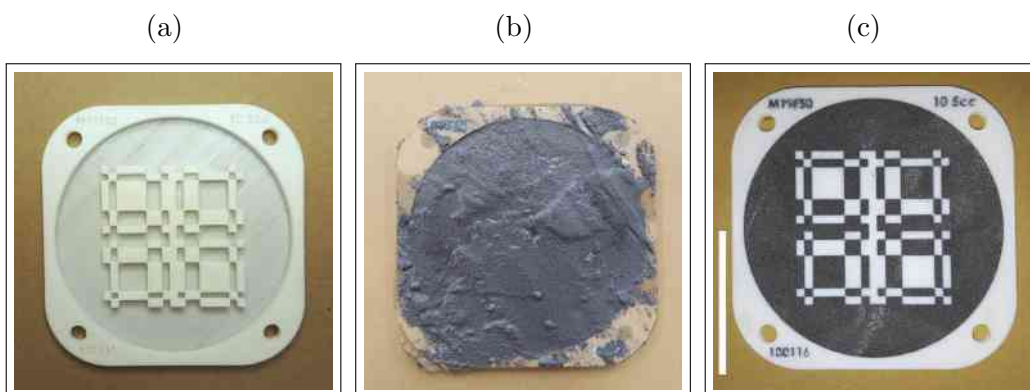
Figure 4.4: Cold Casting Process: (a) the 3D printed PLA CM mould is (b) filled with the TEC and then cured. (c) reveals the final CM after polishing has occurred.

Figure 4.5: 3D Printed TEC CM Examples: (left) a 17×19 TP URA anti-mask, (centre) 3D printed CM view from the back and (right) a cyclic 19 MURA. Note, the feature sizes are extremely different because they are demonstration CMs and the 17×19 TP URA was not used during the project.

4.4   Material Analysis

The materials used to cast 3D printed CMs were analysed to determine their integrity. Voids in the cast material may present a number of issues, which include densities different from those predicted. Trapped air was the main cause of voids in the cast material and samples were investigated to confirm their densities. The densities of samples of both the TEC and bismuth alloy were measured using an Accupyc pycnometer (Micromeritics, 1996). The measured densities and those calculated (ρ_C) were found to agree well, apart from the sample of the TEC with 94.9 wt % tungsten that was found to have a lower ρ than expected. The composition of the bismuth alloy was confirmed by X-ray fluorescence using an SII Nanotechnology Inc SEA6000VX X-ray fluorescence spectrometer (Table. 4.2).

Calculated densities of the radiation attenuating metals were determined using Eq. 4.1 and 4.2, with η representing the ratio by weight of each element/compound i in a 100 g sample (Ω). An additional variable includes the volume (V_i) of each element/compound in the sample. For example, TEC at 9.6 g cm^{-3} contained 93.5 % W and 6.5 % E$_P$ by weight. Using Eq. 4.1, the volume for each element/compound in the sample would be $V_W = 93.5 \, \text{g} / 19.3 \, \text{g cm}^{-3} = 4.84 \, \text{cm}^{-3}$ and $V_{E_P} = 6.5 \, \text{g} / 1.17 \, \text{g cm}^{-3} = 5.5 \, \text{cm}^{-3}$, where the density of E$_P$ is 1.17 g cm^{-3}. When calculating the density with the above, the volumes were plugged into Eq. 4.2.

$$V_i = \frac{\eta}{\rho} \tag{4.1}$$

$$\rho_C = \frac{1}{\sum\limits_i V_i} \Omega \qquad (4.2)$$

Table 4.2: Attenuating Material Density for 3D Printed CMs.

Attenuating Material	Concentration (wt %)	ρ_C (g cm^{-3})	ρ (g cm^{-3})
TEC	93.5 W, 6.5 E$_P$	9.6	9.57 ± 0.02
TEC	94.6 W, 5.4 E$_P$	10.5	10.63 ± 0.06
TEC	94.9 W, 5.1 E$_P$	10.8	10.09 ± 0.08
Bismuth Alloy	Bi 57, Sn 26, In 17	8.5	8.61 ± 0.02

Each CM of different densities were sampled by taking a slice through its centre, revealing information on its structure. This is displayed in Fig. 4.6a revealing a good cast free from air pockets for the hot cast CM . However, tiny air pockets were present in the cold cast CM at $\rho = 9.6$ and 10.6 g cm^{-3} (see Fig. 4.6b - c). An increase in air-pockets was prevalent at higher densities for the TEC due to an increasingly viscous mixture easily trapping air bubbles. Scanning electron microscope images were captured with a HITACHI SU5000 (HITACHI, 2001) showing air pockets present in the TEC, approximately 200 - 250 μm in size (see Fig. 4.6d). Note, the white bar in Fig. 4.6 is a scale indicator of 1 mm.

According to the manufacturers specification, print resolution capabilities of the Ultimaker 2 Extended 3D printer was as small as 0.06 mm. However, similar results were found when printing at 0.1 mm. Three test samples of MURA CMs were 3D printed in Fig. 4.7 where the smallest square elements in (a) was 2.89×2.89 mm, (b) 2.39×2.39 mm and (c) 1.03×1.03 mm. The white square indicator represents 3×3 mm. It was found that the visual integrity of features less than 2.89 mm were somewhat compromised with straight edges and corners appearing increasingly misaligned and rounded with decreasing feature sizes. Elements smaller than 2.89×2.89 mm significantly deteriorated in print quality. This was true for both PLA and ABS. In addition, smaller elements meant smaller cavities to fill when casting which cause problems when casting such viscous material.

4.5   X-Ray Attenuation & Transmission

The X-ray transmission (T) for pure tungsten at a density of 19.3 g cm^{-3}, TEC at 9.6 g cm^{-3} and bismuth alloy at 8.6 g cm^{-3} was found using Eq. 4.3 and 4.4 (Hubbell et al., 1996). For Eq. 4.3 and 4.4, μ/ρ represents the mass
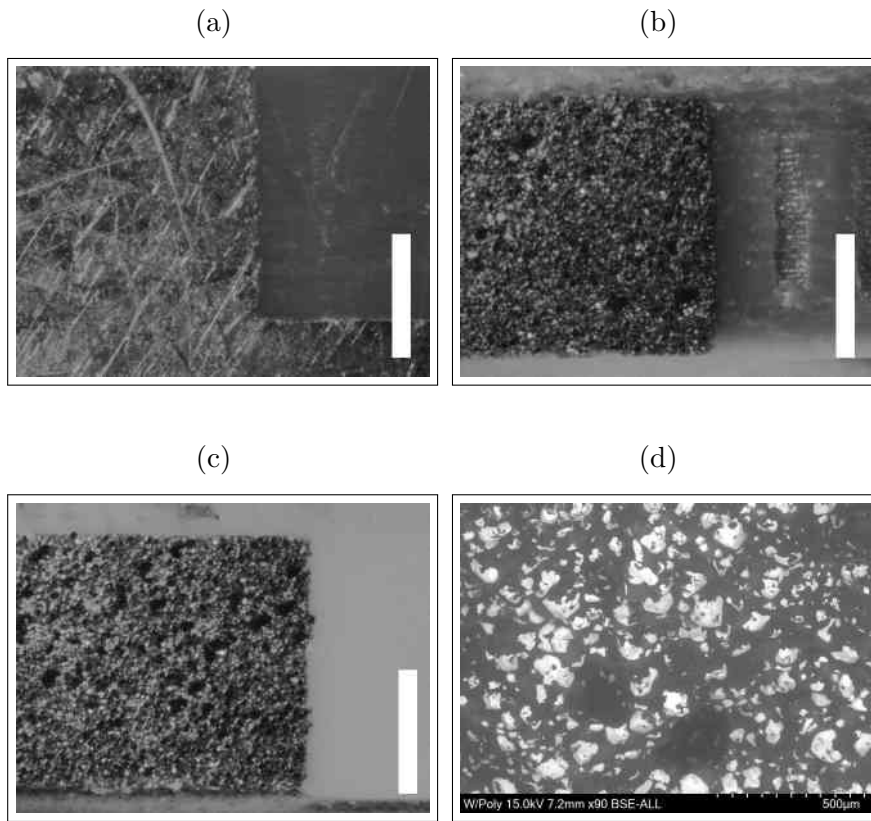
Figure 4.6: Images of Samples from the 3D Printed CMs: (a) Hot cast sample, (b) cold cast samples with 9.6 g cm^{-3} (c) and 10.6 g cm^{-3}. (d) is the SEM image of the TEC sample.
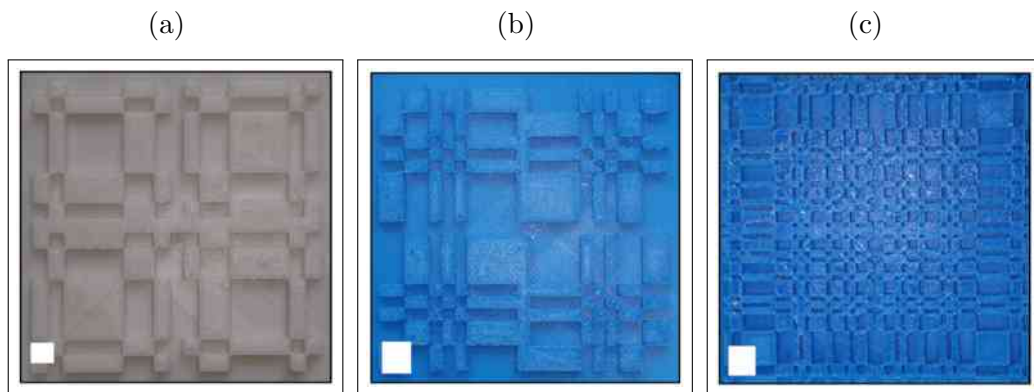
Figure 4.7: 3D Print Quality for three Samples: Note, there is a decrease in print resolution with decreasing feature size.

attenuation coefficient, w is the fraction by weight of element i, and the mass thickness $\underline{x}$. X-ray transmissions with energies ranging from 1 - 200 keV are

presented in Fig. 4.8. Both Bi alloy and the 2 mm TEC shared similar X-ray transmissions of less than 1 % up to approximately 120 keV. Nevertheless, there is leakage of X-rays with 4 % transmission for Bi at 87 keV due to the K absorption edge. X-ray transmission through 2 mm thick tungsten was the same as 4 mm thick TEC because TEC is half the density of tungsten, which have a transmission < 1 % to around 160 keV.

$$\underline{\mu}/\underline{\rho} = \sum_i w_i (\underline{\mu}/\underline{\rho})_i \tag{4.3}$$

$$T = e^{-(\underline{\mu}/\underline{\rho})\underline{x}} \tag{4.4}$$

X-Ray transmission radiographs of two 4 mm thick 3D Printed CMs with a density of 10.6 g cm^{-3} were taken with the settings 170 kV and 0.023 mA. Four circular features near the corners of (a) show full X-ray transmission. Dark regions represent the attenuating material while lighter parts show transmission through PLA (see Fig. 4.9). The transmission of the mask were on average 3-4 % which is close to the theoretical value.

4.6   3D Printed Tungsten Alloy Coded Masks

The prospects for directly printing metal have also been considered. These include Bound Metal Deposition (BMD) (Laserlines, 2017), which is very similar to the polymeric 3D printing used at Cranfield University. Metal powder is formed into feedstock rods using a binder and is printed by extrusion. Radiative heaters and high powered microwaves are then used to sinter the final component after the binder has been removed. This is said to result in densities of > 98 % of the raw metal. Selective Laser Melting (SLM) is one of the most common techniques for high resolution metal additive manufacture, where successive layers of metallic powder are melted using a directed laser beam to build up a 3D structure. SLM has recently been adopted by M&I Materials (MI, 2015) to print their Wolfmet® tungsten alloy[1] for complex radiation collimators (see Fig. 4.10a).

It should be noted that this test object was not intended to be a functioning CM, but is a combination of different elements designed to test the resolution of the SLM process. The resulting tungsten was examined in greater detail in Fig. 4.10, and show that some printing defects and small voids are present and that the surface had a granular structure making it slightly rough to the

---

[1]The same alloy used for manufacturing machined NTHTs in this thesis.
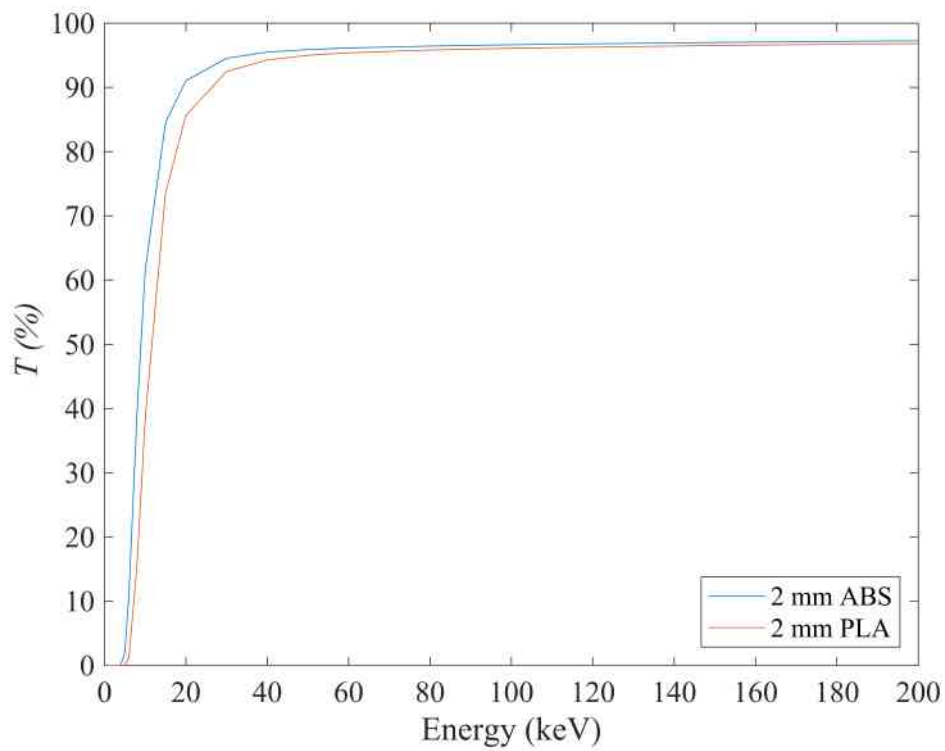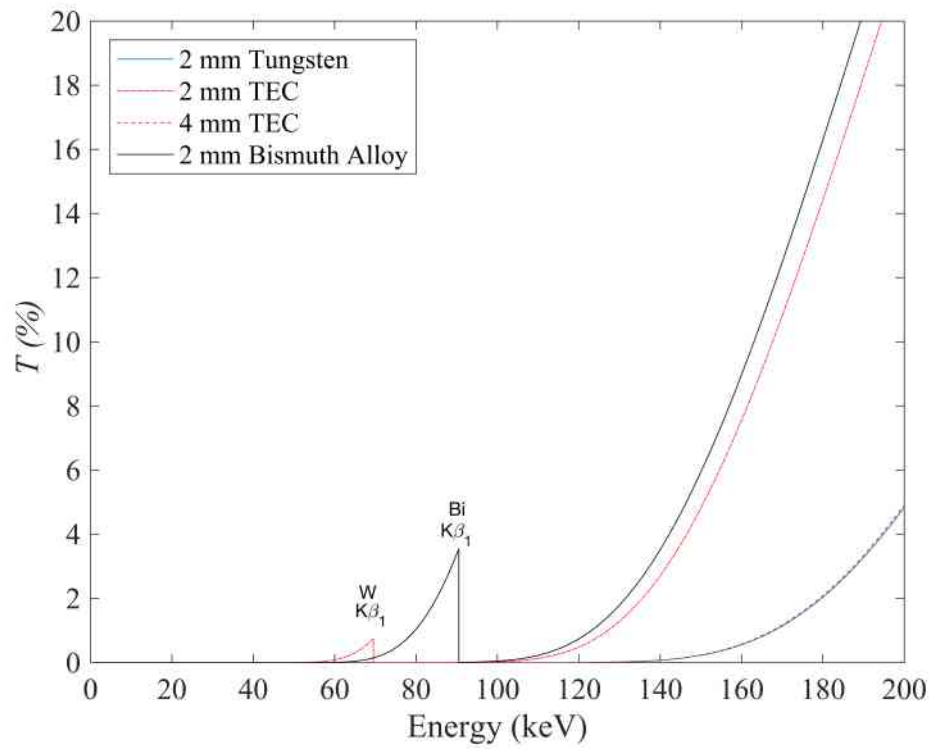
Figure 4.8: X-Ray Transmission of Samples taken from the Masks.
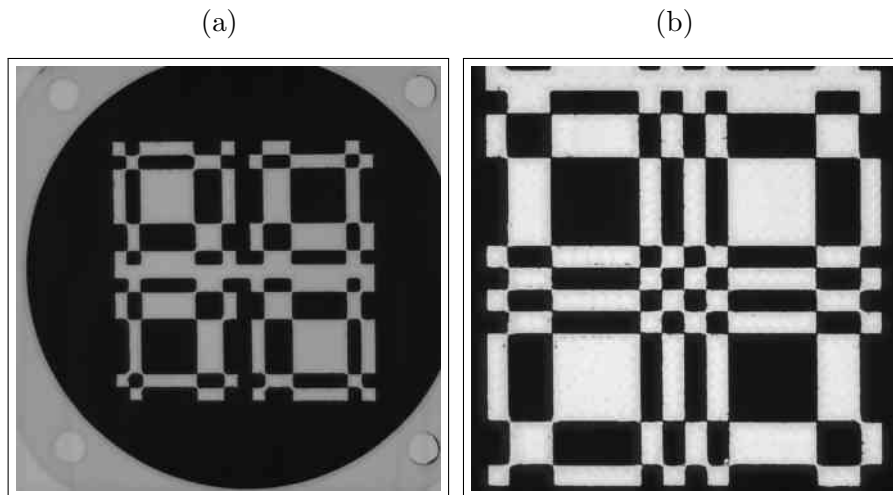
Figure 4.9: X-Ray Transmission Radiographs of 3D Printed CMs.

(a)   (b)
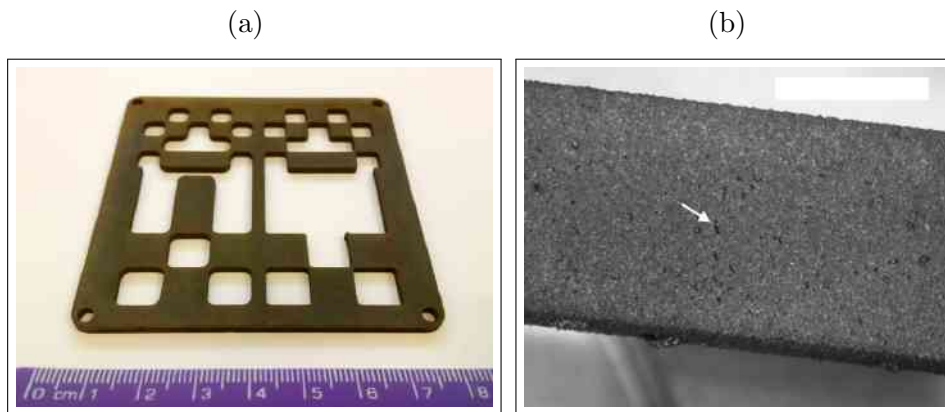
Figure 4.10: Wolfmet® Tungsten Mask: The arrow shows a small defect in the tungsten sample.

touch. Note, the white bar in Fig. 4.10 is a scale indicator measuring 4 mm. This also makes the metal brittle and prone to damage, which is evident in Fig. 4.10 where a relatively large central piece of the mask has become detached. Additionally, SEM micrographs give another perspective on the Wolfmet® Tungsten Fig. 4.11.

4.7 Machined Tungsten Alloy Masks

CMs were manufactured from a machined tungsten alloy (MTA) comprised of 90 % W and Ni/Cu binder elements (Wolfmet, 2016). The alloy is also referred to as Wolfmet® HA190. This material was chosen over pure tungsten because
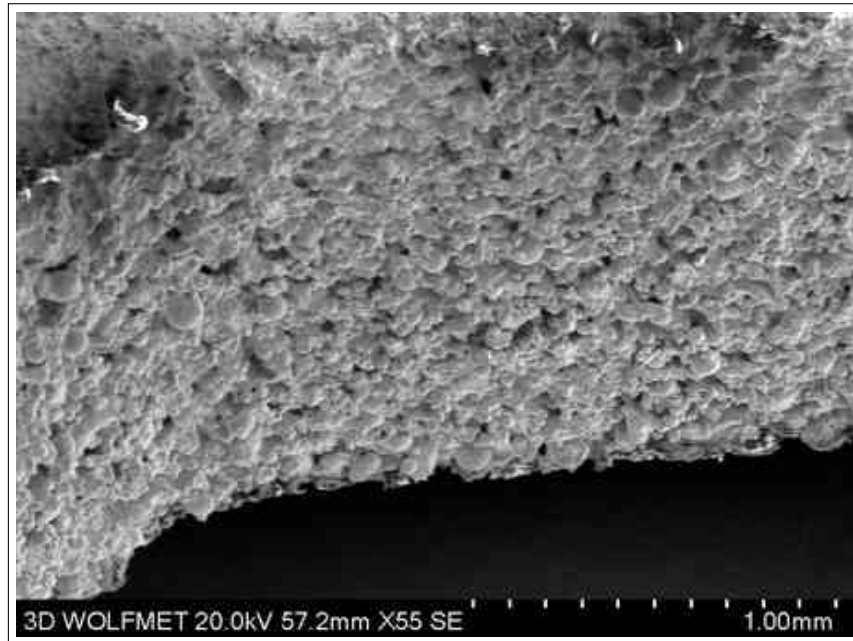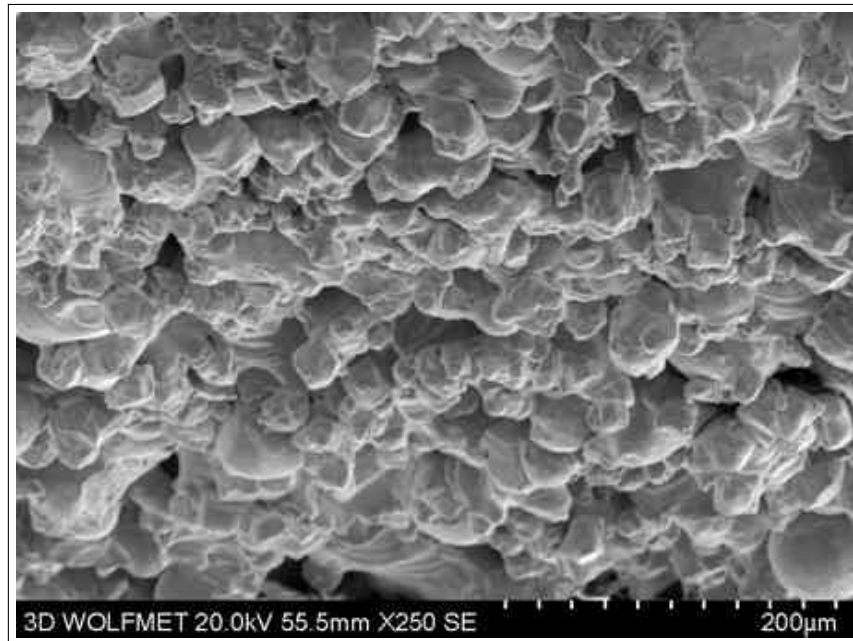
Figure 4.11: Wolfmet® Tungsten Mask SEM Micrographs: (a) Micrograph of the sample at x55 magnification and (b) at x250 magnification. .

94

of its CM manufacturing abilities. The density of Wolfmet® HA190 is 17.1 g cm^{-3}. Fabricating MTA CMs began with planing the alloy sample down to the desired thickness. Holes were then drilled with tungsten carbide drill bits on a computer numerical control (CNC) machine with a 'pecking' motion to avoid drill bits from breaking. This completed the CM manufacturing process, which is revealed in Fig. 4.12a-c. Note, the white scale bar indicates 50 mm. Examples of additional complete MTA CMs are found in Fig. 4.13 with the (a) 13 DURA NTHT, (b) 19 RANDA$^{\alpha}$ NTHT and (c) 13 MURA NTHT.

(a) (b) (c)
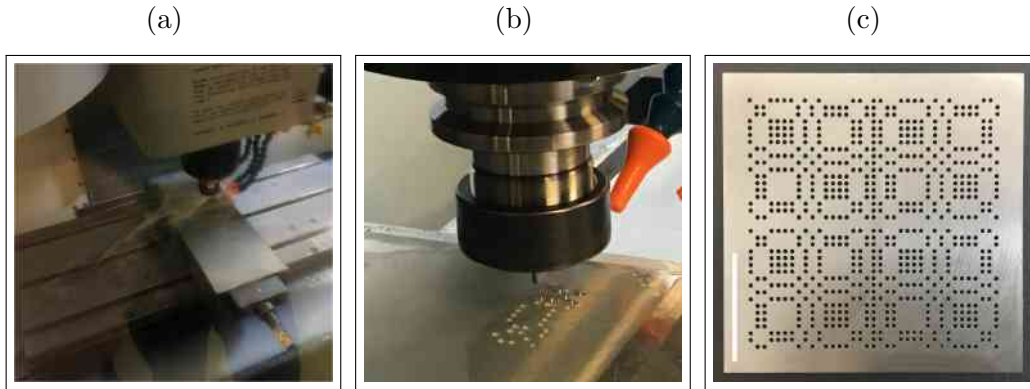
Figure 4.12: Machined Alloy Tungsten Mask: The white scale bar indicates 50 mm.
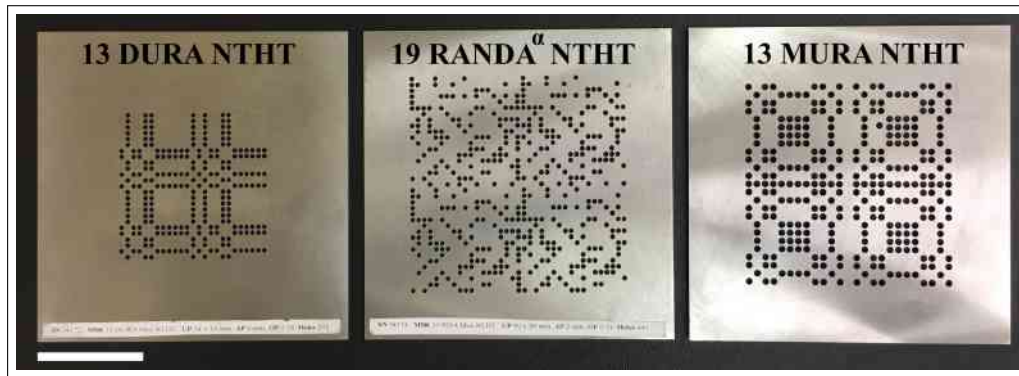
Figure 4.13: MTA CM Samples: The white scale bar indicates 50 mm.

4.8 Experimental Imaging Masks

Mask parameters are presented in Table. 4.3, where $\underline{t}$ represents mask thickness, I is the number of open elements in the mask and PLA/TEC refers to 3D printed CMs. Non-cyclic versions of CMs manufactured for the project can be seen in Fig. 4.14.

Table 4.3: The Experimental Masks used in the Project and their Parameters

Mask	Non-Cyclic Array	Cyclic Array	Base Pattern Size (mm)	Overall Pattern Size (mm)	Smallest Aperture/Feature Size (mm)	$\bar{t}^a$ (mm)	χ^b	ρ (g cm^{-3})	Material	I
19 MURA	19 × 19	37 × 37	38 × 38	74 × 74	2 × 2	2	0.50	9.6	PLA/TEC	684
13 DURA	13 × 13	25 × 25	26 × 26	50 × 50	2 × 2	2	0.40	9.6	PLA/TEC	252
17 × 21 Singer	17 × 21	33 × 41	34 × 42	66 × 82	2 × 2	2	0.34	9.6	PLA/TEC	464
26 Biquadratic Residue	26 × 26	50 × 50	52 × 52	100 × 100	2 × 2	2	0.25	9.6	PLA/TEC	622
19 RANDA$^\alpha$	19 × 19	37 × 37	38 × 38	74 × 74	2 × 2	2	0.32	9.6	PLA/TEC	440
19 RANDA$^\beta$	19 × 19	37 × 37	38 × 38	74 × 74	2 × 2	2	0.50	9.6	PLA/TEC	687
13 MURA NTHT	25 × 25	49 × 49	47 × 47	90 × 90	3	1	0.27	17.1	MTA	312
19 MURA NTHT	37 × 37	73 × 73	60 × 60	117 × 117	2	2	0.16	17.1	MTA	684
13 DURA NTHT	25 × 25	49 × 49	34 × 34	66 × 66	2	2	0.18	17.1	MTA	252
17 × 21 Singer NTHT	33 × 41	65 × 81	45 × 55	87 × 109	2	2	0.23	17.1	MTA	464
19 RANDA$^\alpha$ NTHT	37 × 37	73 × 73	50 × 50	98 × 98	2	2	0.14	17.1	MTA	440
Pinhole 1	-	-	-	-	1	3	-	17.1	MTA	-
Pinhole 2	-	-	-	-	2	2	-	17.1	MTA	-

^{a}Attenuating material only.
^{b}Calculated from cyclic arrays.

96

19 MURA   13 DURA   17×21 Singer

26 BR   19 RANDA$^\alpha$ 19 RANDA$^\beta$

13 MURA NTHT   19 MURA NTHT   13 DURA NTHT

17×21 Singer NTHT   19 RANDA$^\alpha$ NTHT
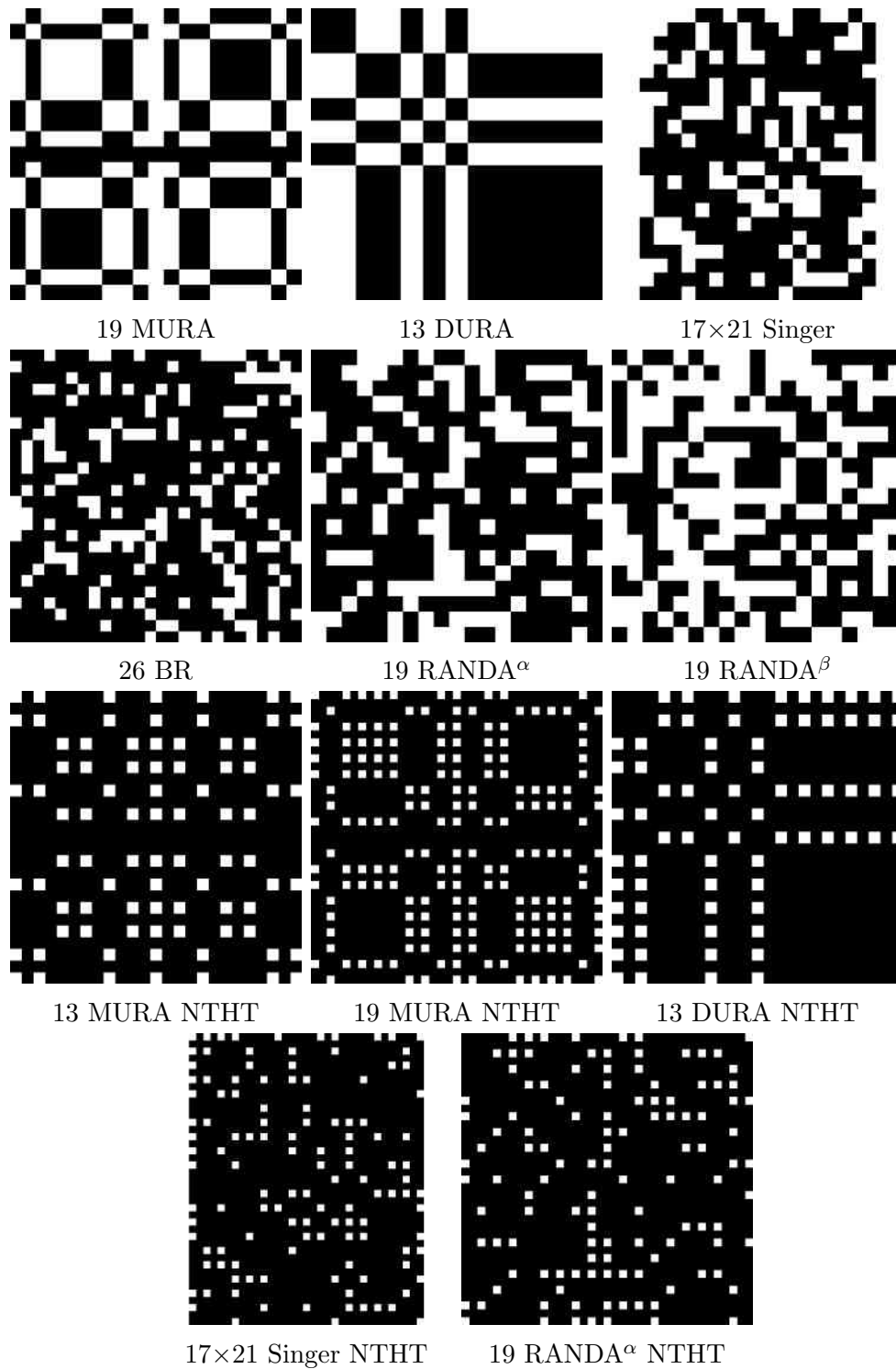
Figure 4.14: Non-Cyclic Array Patterns of CMs used in Experiments.

Note, the formula for open fraction of MTA NTHTs (χ_ϕ) slightly differs from Eq. 2.14 due to circular elements. The new formula is found in Eq. 4.5, where ϕ_n represents the number of apertures and their radius r.

$$\chi_\phi = \pi r^2 \left(\frac{\phi_n}{p \times q} \right) \tag{4.5}$$

4.9 Discussion

The speed of constructing the masks in Table. 4.3 were approximately 1-2 days for the MTA masks and 1 day for all 3D printed masks, which excludes any curing time. Calculating the exact time was very challenging because of the different construction methods used and the fact that even though MTAs were manufactured on site, the production process was carried out by trained persons in another department. Additionally, 3D printing times could significantly vary from one print to another. There were challenges manufacturing hot cast CMs because of the higher temperatures required for the printing and casting process. The pouring process of the molten alloy mixture in the mould was difficult, as a result of the rapid cooling of the alloy. Overall, finish quality of the ABS print was inferior to that of PLA. In addition, metallic elements became loose from the CM mould from the lack of adhesion (see Fig. 4.3). Consequently, cold casting was the way forward due to problems faced with hot casting. Fewer risks were involved with cold casting with higher quality yields.

When fabricating all masks within the experiment the aim was to have the same vector size for all CMs, so that their base pattern size or 'detector area' were the same. Consequently, this would lead to a fair SNR and CNR comparison when quantifying images. However, the above was difficult to achieve because CMs of different designs and open fractions varied in vector sizes for some designs. Such compromise was unavoidable as each encoded array had to be scaled accordingly so that the smallest feature size of all CMs were the same. CMs with varying feature sizes may result in some masks not resolving a scene, due to very large apertures and this would also lead to an unfair and in some case an impossible comparison. Additionally, all patterns that comprised a CM had to be scaled so that the base pattern did not exceed the detector area.

Chapter 5

The Effects of Imaging Parameters

When imaging with coded masks there are a number of parameters that can affect the outcome and quality of a decoded image. If the incorrect parameters are used, such as those used for calculating the near-field magnification then errors are introduced into the decoding process. In addition, a different bit-depth can significantly change the overall image details of a scene, contrast and noise. This chapter investigates such parameters in detail.

5.1 Grey Scale of Images

The X-ray camera at Cranfield University converted analogue signals to 12-bit digital images. However, all final images exported by the camera's software were 16-bit and thus, treated as such for this project. Most modern computer software do not operate with images of 12-bit and usually upscales the grey scale to 16-bits. When CM exposures were previously decoded in MATLAB, they were automatically converted to 8-bit images. Example images of the quadrant are found in Fig. 5.1 and in past publications (Munoz et al., 2017a,b; Muñoz et al., 2018a,b). Discoveries later on in the project along with personal communication with staff member Pooja Sethia at MathWorks® technical support (personal communication, 3 October 2018) revealed alternative methods of exporting the images as 16-bit. Consequently, all XBI images presented in this thesis are 16-bit except those from the flying spot system that were 8-bit. Fig. 5.1 shows the 16-bit images found earlier on in the thesis, that failed to present signals from expected parts of the quadrant. Those signals were now visible in the 8-bit images due to the decrease in grey scale. However, 16-bit images yielded far less noise . Note, exposing the scene longer for the 16-bit images did not reveal the expected signals and the exposures remained the same. Again, this may be due to the larger difference in contrast for 16-bit images over those with 8-bit grey scale.

5.2 Tolerance of Scaling Parameters

When exposing a scene with CMs, information on parameters such as $\underline{a}$, $\underline{b}$ and BPS must be known for the scaling and decoding process as in Chapter. 3.4.1. Incorrect values cause errors in the final reconstructed image from inaccurate near-field magnification scaling. Multiple decoded exposures of the quadrant are found in Fig. 5.2 with $\underline{a}$ varying from the true value of 1000 mm. The central image highlighted green indicates the correct parameter. Prominent visual change in the image of the scene began when there was a deviation beyond $\underline{a} = 100$ mm, thus, the tolerance of $\underline{a}$ was ±100 mm. Similarly, the tolerance of $\underline{a}$ and BPS was ±20 mm ±1 mm which can be seen in Fig. 5.3 and Fig. 5.4. The correct parameters for the experiments in Fig. 5.2, 5.3

8-bit   **16-bit**

19 RANDA$^\alpha$ 19 RANDA$^\alpha$

19 RANDA$^\beta$ 19 RANDA$^\beta$

17×21 Singer   17×21 Singer
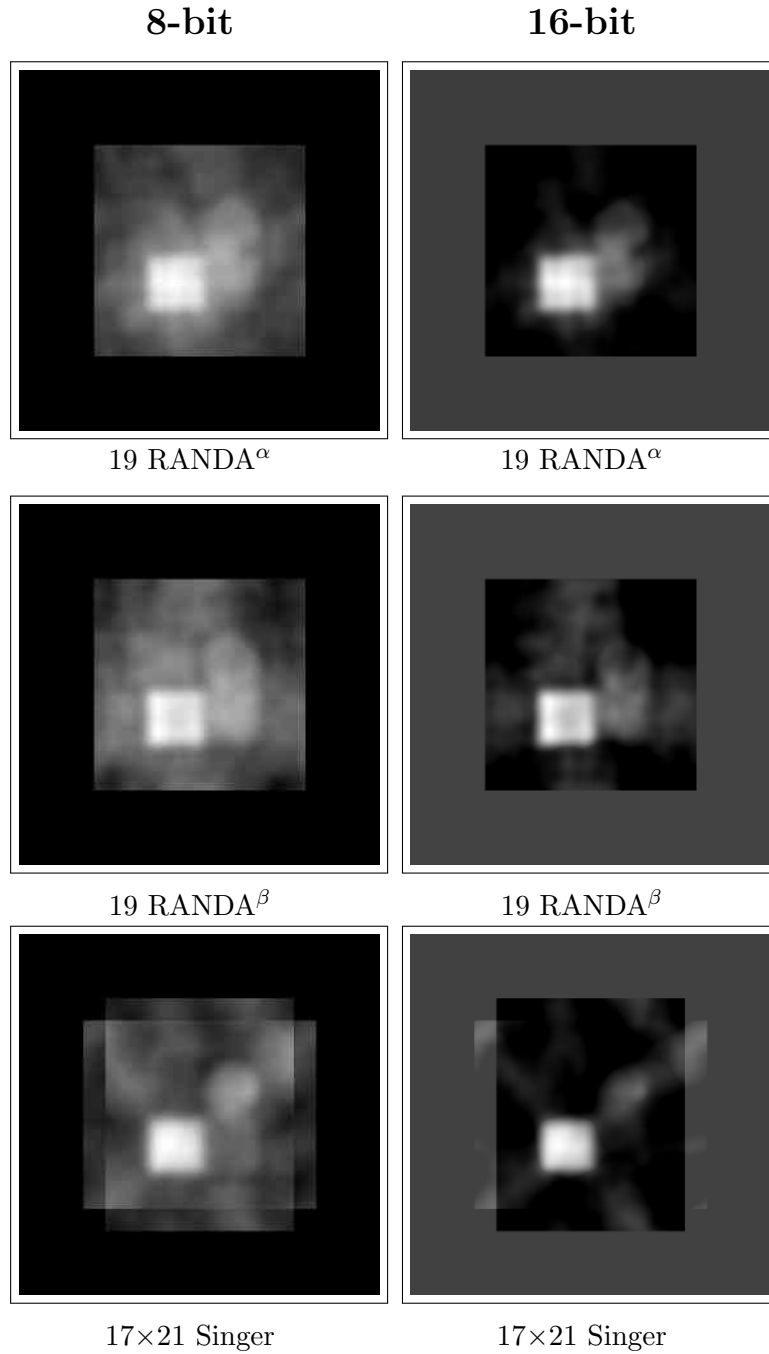
Figure 5.1: 8 vs 16-bit X-ray Backscatter Images.

and 5.4 were $\underline{a}$ = 1000 mm, $\underline{b}$ = 100 mm and BPS = 60 × 60 mm with the 19 MURA NTHT. The trends were quantified and plotted in Fig. 5.5 - 5.6. The standard deviation of signals from the brightest part of the images were calculated and plotted as a function of $\underline{a}$, $\underline{b}$ and BPS. The trends in Fig. 5.5 - 5.6 confirm the tolerances presented earlier and the 'V' shape of each plot reveals the tolerance to be somewhat symmetrical.

$\underline{a} = 600$ mm $\qquad$ $\underline{a} = 700$ mm $\qquad$ $\underline{a} = 800$ mm

$\underline{a} = 900$ mm $\qquad$ $\underline{a} = 1000$ mm $\qquad$ $\underline{a} = 1100$ mm

$\underline{a} = 1200$ mm $\qquad$ $\underline{a} = 1300$ mm $\qquad$ $\underline{a} = 1400$ mm
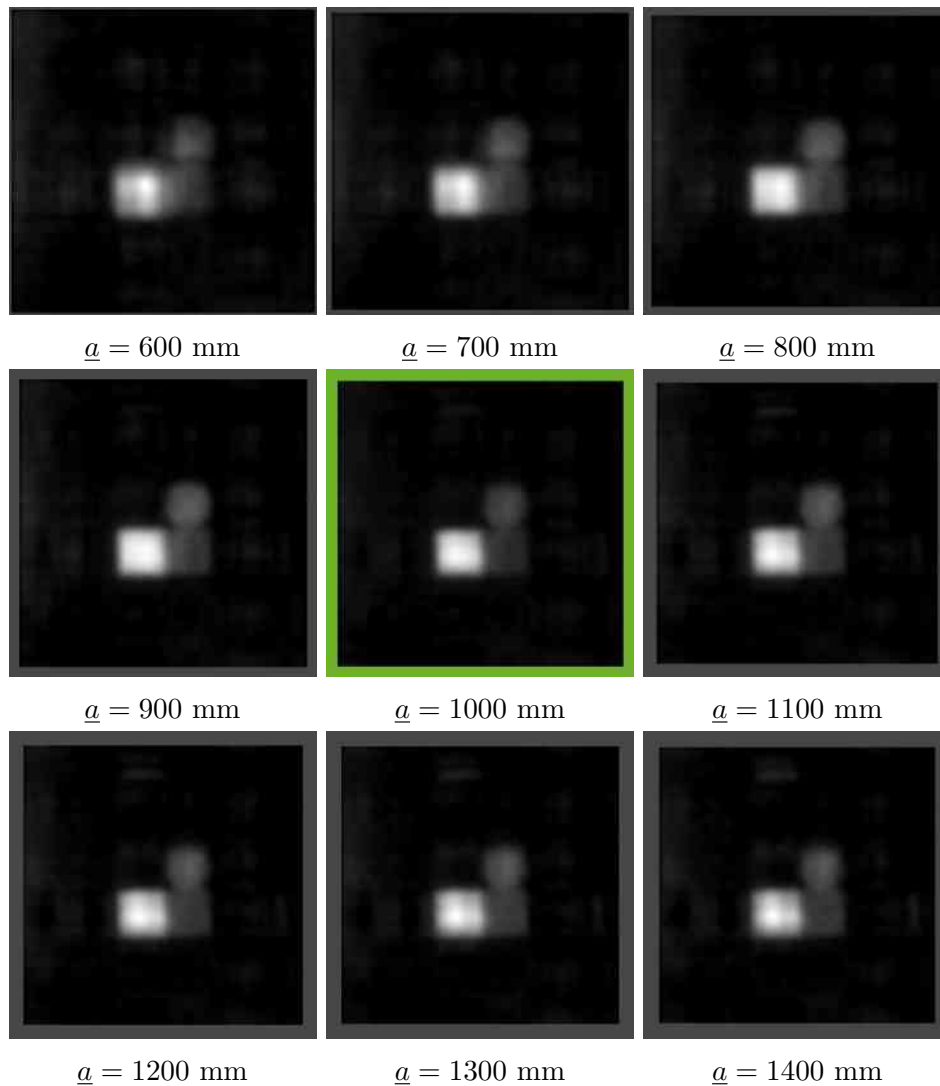
Figure 5.2: Tolerance of Object to Mask Distance: CM images of the quadrant decoded with different object to mask parameters ranging from 600 mm to 1400 mm. The correct value is $\underline{a} = 1000$ mm and the image that reflects this is highlighted in green. Note, the images begin to show signs of significant change when there is a deviation beyond $\underline{a} \pm 100$ mm.

5.3   Discussion

Images in Fig. 5.1 demonstrate the change in quality when a different bit-depth is used. Images were decoded close to the bit-depth value that was originally exported by the camera (which was 16-bit) and although this saw a reduction in noise, signal from parts of the scene were not detected.

Scaling parameters such as $\underline{a}$, $\underline{b}$ and BPS may impact the decoded image if values are incorrect. It was found that if there was a deviation from the true
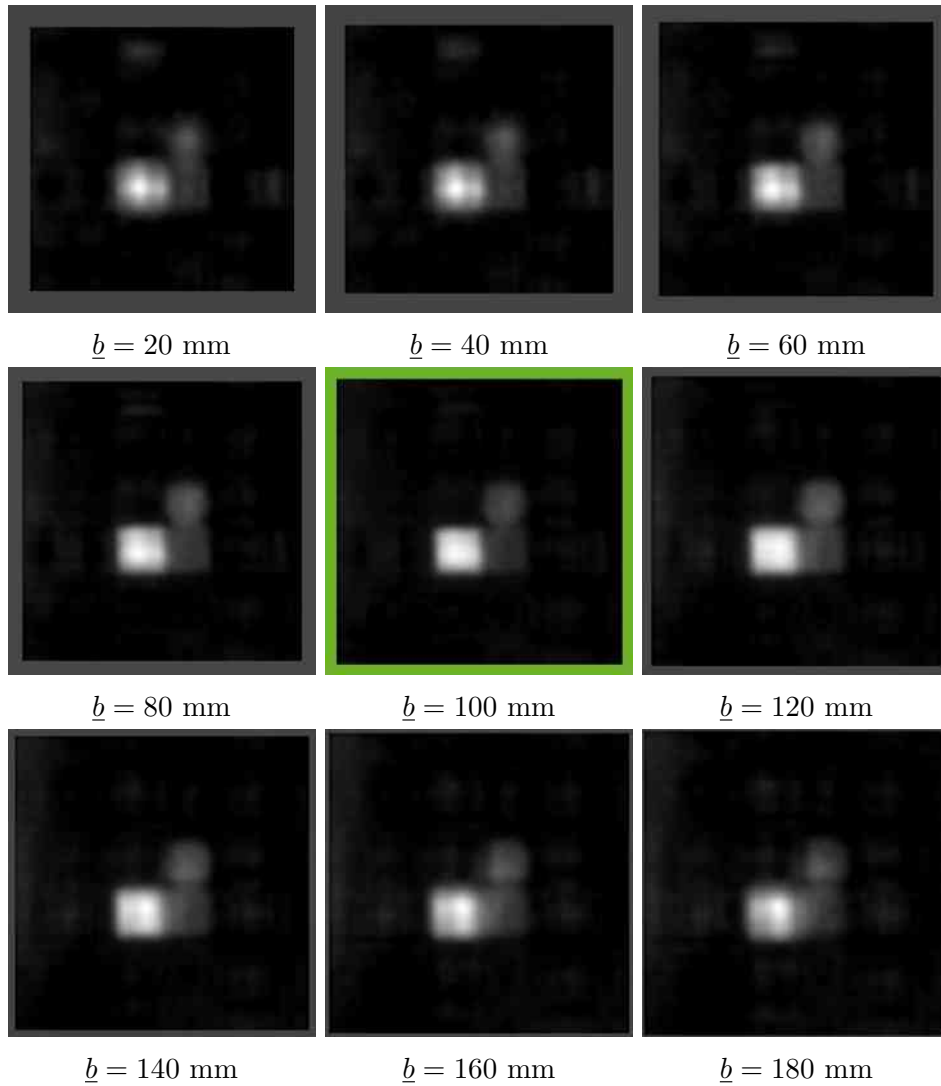
Figure 5.3: Tolerance of Mask to Detector Distance: CM images of the quadrant decoded with different mask to detector parameters ranging from 20 mm to 180 mm. The correct value is $\underline{b} = 100$ mm and the image that reflects this is highlighted in green. Note, the images begin to show signs of significant change when there is a deviation beyond $\underline{b} \pm 20$ mm.

value more than $\underline{a} \pm 100$ mm, $\underline{b} \pm 20$ mm and BPS ± 1 mm, the decoded image quality was compromised. An approximate error value as a percentage can be calculated by summing both $+$ and $-$ values, and dividing it by the range of samples. For example to find the approximate tolerance for the object to mask scaling parameter ($\Delta_{\underline{a}}$), 200 mm (from $\underline{a} \pm 100$ mm summed) would be divided by the range ($\underline{a} = 1400 - 600$ mm would become $\underline{a} = 800$ mm), which would be 0.25, therefore, $\Delta_{\underline{a}} \pm 25$ %. Similarly, tolerances for the other scaling parameters were $\Delta_{\text{BPS}} \pm 25$ % and $\Delta_{\underline{b}} \pm 12.5$ %. Note, the symbol Δ represents the maximum scaling parameter tolerance or deviation from the correct value.
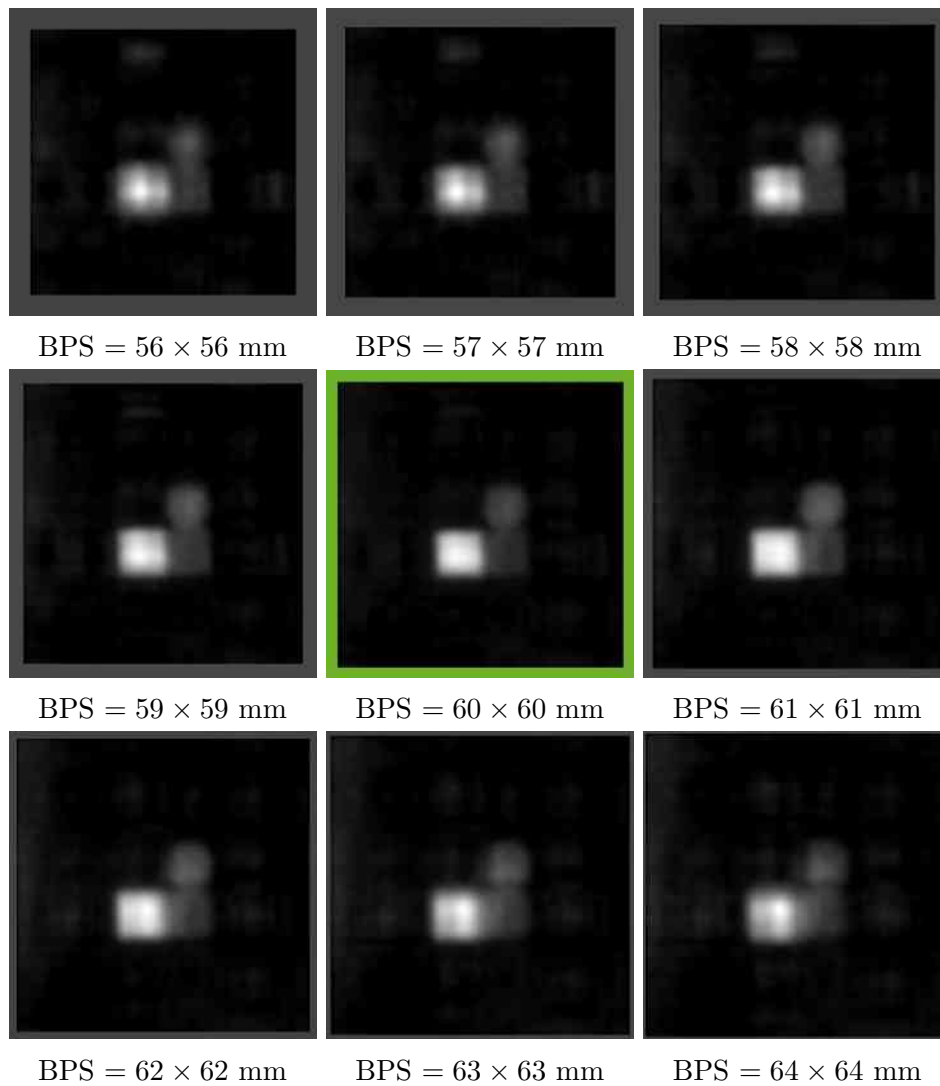
Figure 5.4: Tolerance of BPS: CM images of the quadrant decoded with different base pattern sizes ranging from 56×56 mm to 64×64 mm. The correct value is 60×60 mm and the image that reflects this is highlighted in green. Note, the images begin to show signs of significant change when there is a deviation beyond BPS ± 1 mm.
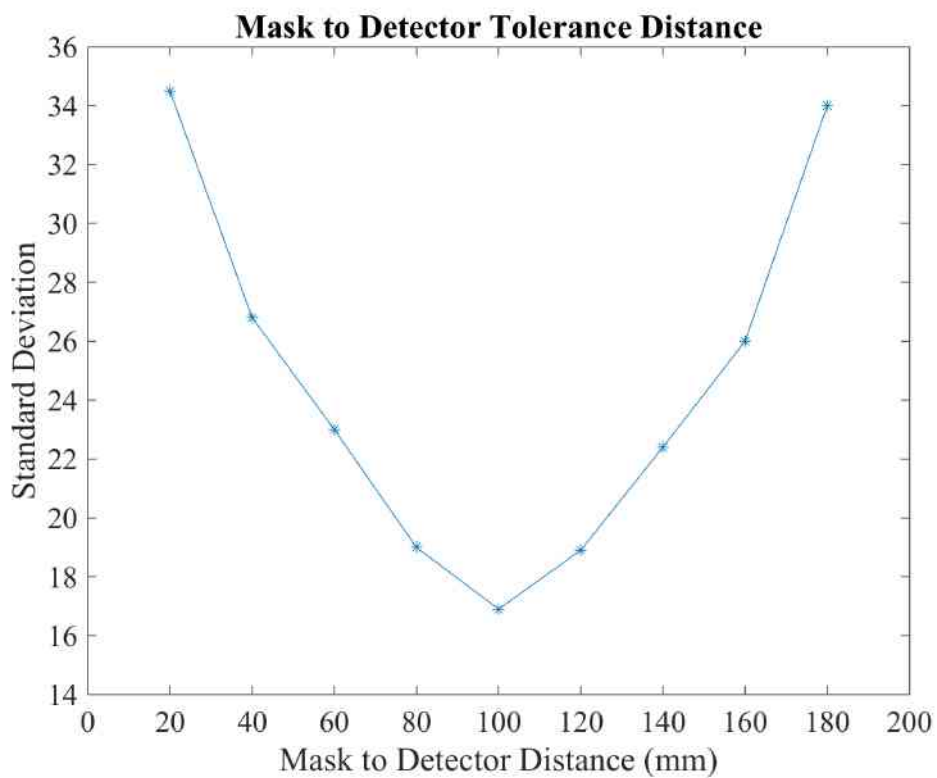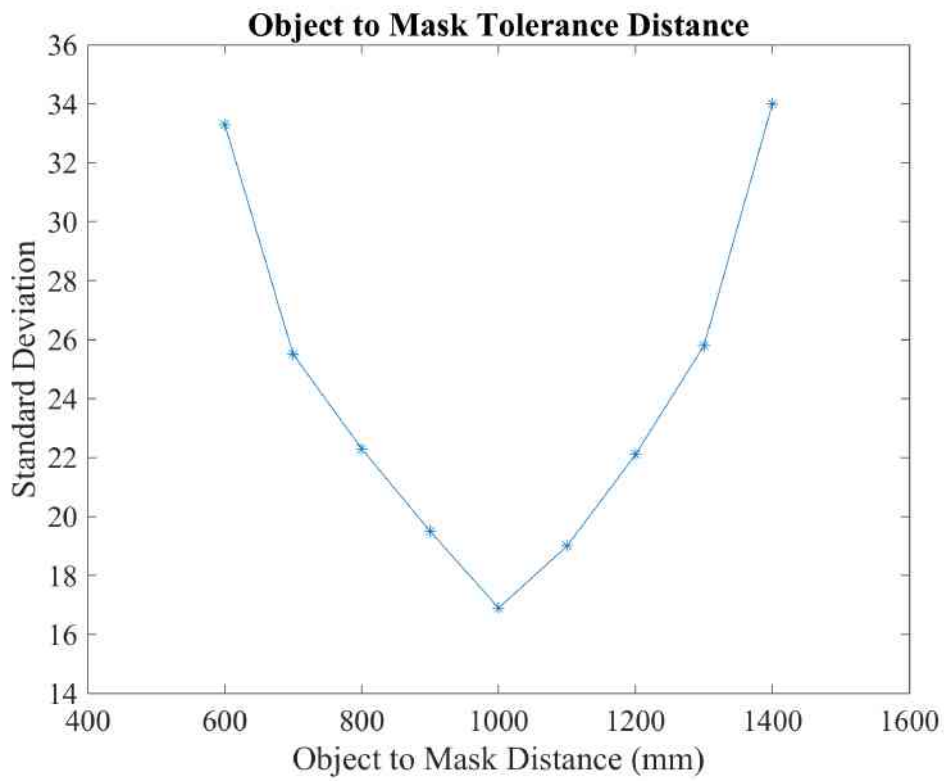
Figure 5.5: Object to Mask and Mask to Detector Distance Tolerance: The plot shows the standard deviation of distances deviating from the correct values of (top) $\underline{a} = 1000$ mm and (bottom) $\underline{b} = 100$ mm.
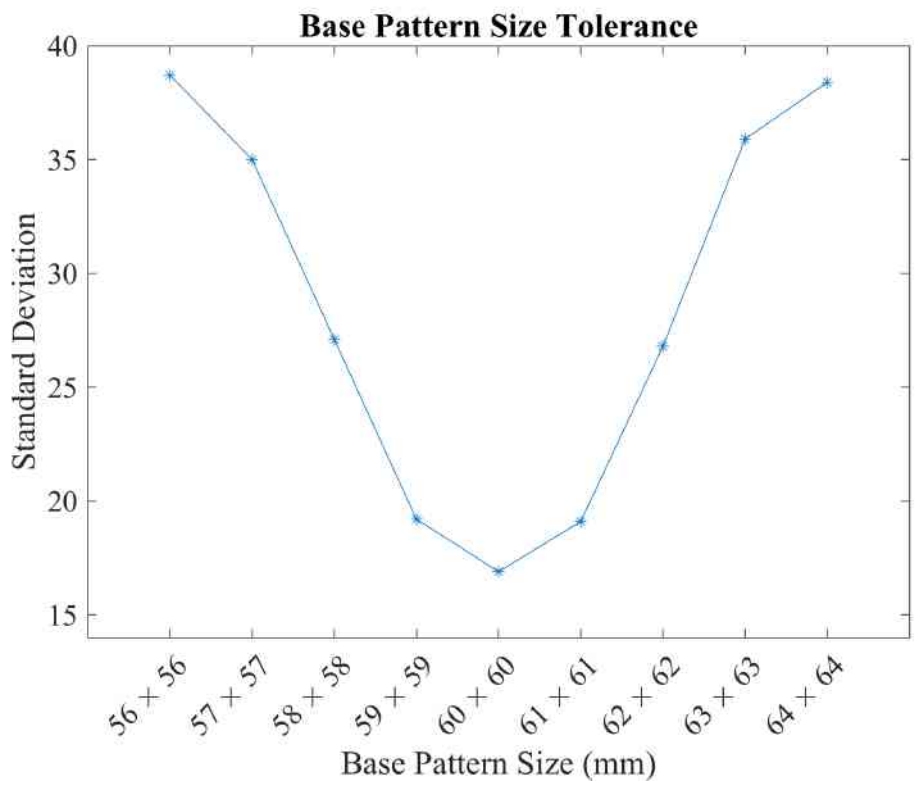
Figure 5.6: Object to Mask Distance Tolerance: The plot shows the standard deviation of BPS deviating from the correct dimension of 60×60 mm.

Chapter 6

Low Open Fraction Arrays

The definition of open fraction χ was introduced in Chapter. 2.2.3 describing the fraction of open elements within an array. Arrays with $\chi < 0.5$ often have the terminology 'low open fraction' (LOF) attached and $\chi \geq 0.5$ are considered higher open fractions arrays. The open fraction of an array and its effectiveness to image different scenes have been presented in past literature. LOF arrays may yield optimum results when imaging scenes of a point source with low backgrounds (Gunson and Polychronopulos, 1976). Fenimore and Cannon (1978) postulated higher open fraction arrays allow greater throughput of photons, thus are optimum for low-intensity sources. Simulations from the Satellite for X-ray Astronomy wide field camera (SAX-WFC) presented the optimum SNR for faint sources which was between $\chi = 0.25 - 0.33$ (In 't Zand et al., 1994). With regards to near-field complex scenes, superior results were found from a $\chi = 0.5$ MURA over LOF arrays, that included the MURA NTHT and 'New System' array (Jennings and Byard, 1997; Accorsi et al., 2001; Fenimore and Cannon, 1981). A similar case was found with the $\chi = 0.5$ MURA outperforming LOF CMs used for XBI (Munoz et al., 2017a; Muñoz et al., 2018a). The LOF arrays used in this case was the DURA, Singer and RANDA.

6.1 Limited Number of LOF Arrays

The $\chi = 0.5$ URA boasts ideal imaging properties for its PSF and it is very challenging to find in LOF masks (Busboom et al., 1998; In 't Zand et al., 1994; Accorsi et al., 2001; Busboom et al., 1997). The NRA and PNPs presented earlier are the only arrays with ideal imaging properties or close. However, they are limited in range and open fraction. There is a limitation on the number of published LOF arrays in general with a wide variety of vector sizes, with the exception of the RANDA. Evidence of such limitations are found in Busboom et al. (1998) showing the sparsity of LOF arrays. Also, this is confirmed with Shutler et al. (2013) demonstrating the limited number of Singers (see Fig. 6.1). URA vectors are based on their 1D sequence which are prime numbers. Consequently, this makes it easy to identify array sizes immediately without many calculations being performed. Conversely, other arrays like the Singer require more detailed calculations as in Chapter. 2.2.3.7 and their vector sizes are not immediately clear. Additionally, 1D sequences have been previously published without any examples of 2D arrays or their construction process (besides those published from the author in (Munoz et al., 2017a; Muñoz et al., 2018a)). Examples include but are not limited to the DURA and biquadratic residue (Nagell, 1951; In 't Zand et al., 1994; Wild, 1983) (Accorsi, 2001, p. 47). This section seeks to address the limited number of LOF 2D arrays by calculating and presenting a catalogue of patterns to refer to.
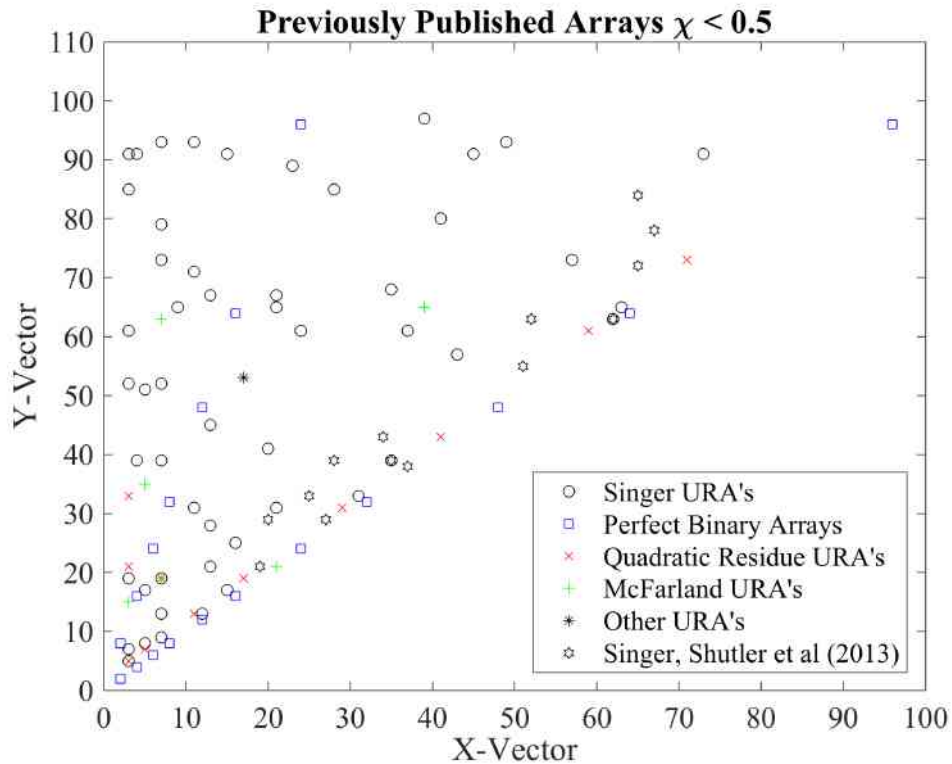
Figure 6.1: Limited Number of LOF Array (Busboom et al., 1998).

6.1.1 DURA

The DURA was introduced in Chapter. 2.2.3.5 as a LOF class of arrays with 'URA' like properties for its PSF. The remaining 14 array patterns in addition to the 13 DURA found in Fig. 2.21 were calculated and are presented in Appx. A.

DURAs were divided into five groups consisting of 13, 21, 31, 57 and 73, for their vector sizes. An example would see group 21 containing arrays 21×21, 21×31, 21×57 etc. The theoretical SNR of each array demonstrated a trend for groups consisting of square and rectangular arrays (see Fig. 6.2). Square arrays performed better than their counterparts because there was an increase in side-lobes in the PSF with non-square arrays. The 13 DURA presented the best imaging properties of all DURAs. An example of an increase in SNR for square arrays when its vector size decreases is demonstrated in Fig. 6.2. The 21, 31, 57 and 73 DURAs PSF presented greater side-lobes than those of the 13 DURA in Fig. 2.21. Also, Appx. B shows a rise in side-lobes when one of its vectors (along the Y vector in this case) increased, explaining the trend of decreasing SNR for each group as the Y vector increases in Fig. 6.2.
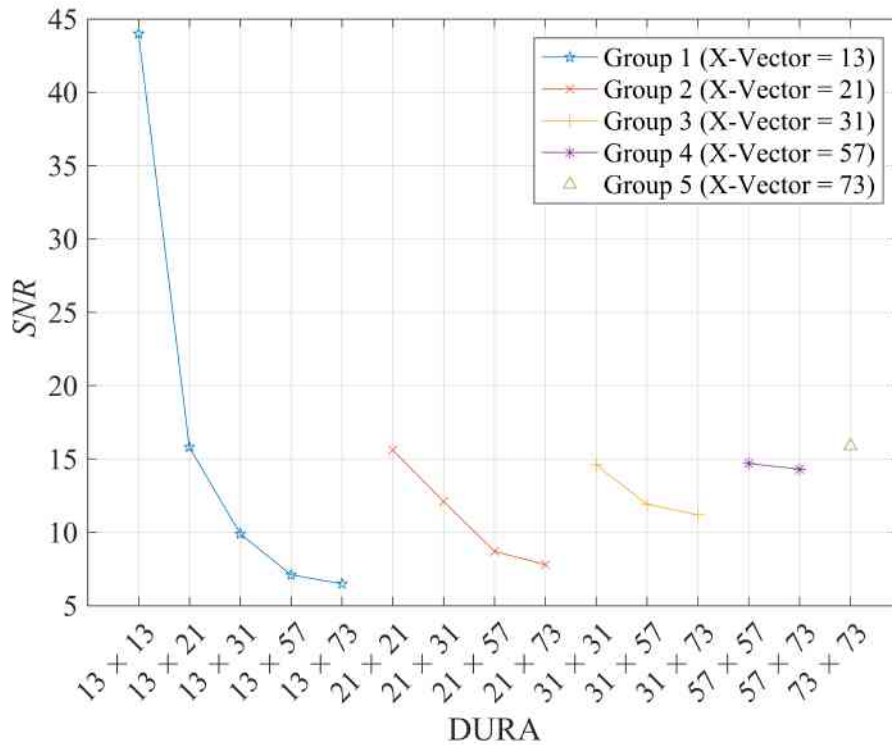
Figure 6.2: Theoretical SNR of DURA Patterns: A trend shows the square array for each group outperforming other rectangular arrays.

6.1.2 Singer

There is a limitation to the number of Singer arrays due to its vectors following the rule of being co-prime. Evidence of this is seen in Fig. 6.1 (Shutler et al., 2013). Subsequently, an additional 79 Singer arrays of LOF were calculated and published by the author in (Muñoz et al., 2018a) In addition; it has been found that Singer array vectors are not bound by the co-prime rule and can be square. A few square Singer 'product arrays' have been published in Byard and Shutler (2017). However, additional square arrays have been calculated with similar imaging properties as those with co-prime vectors. An example square 19 Singer and its PSF demonstrates this in Fig. 6.3.

The new Singer patterns are summarised in Table. 6.1 for both square and rectangular arrays. Although 79 were published in (Muñoz et al., 2018a), most are not suitable for conventional imaging due to their extreme dimensions and shapes. Therefore, only square and rectangular arrays suitable for imaging with dimensions close to that of common imaging detectors are presented here. Note, the arrays in Table. 6.1 have $P_v = 0$. See Appx. A for the array patterns.
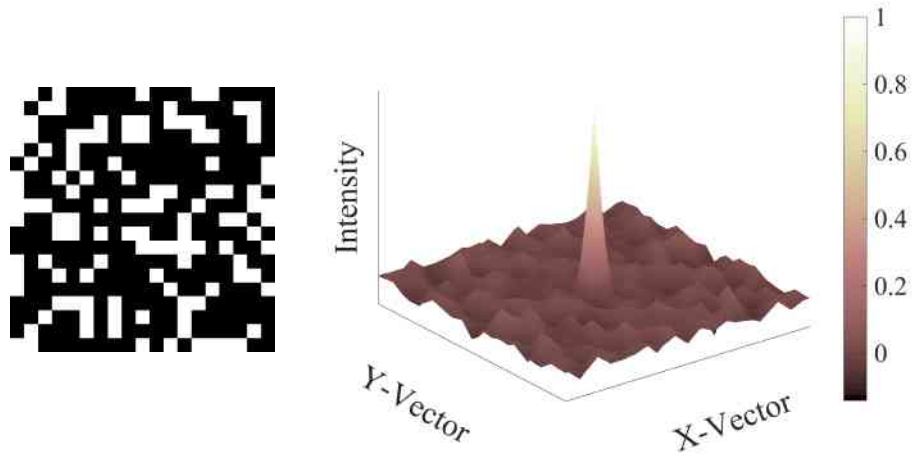
Figure 6.3: Square 19 Singer and its PSF

Table 6.1: 11 to 71×77 Singer Arrays.

1D Sequence Length	χ	P	$p \times q$
156	0.20	-2	11×14
341	0.25	$+4$	15×23
341	0.25	-5	16×21
364	0.33	$+4$	16×23
341	0.25	-1	17×20
364	0.33	-7	17×21
341	0.25	$+1$	18×19
3280	0.33	$+6$	53×62
5461	0.25	$+6$	71×77
121	0.33	0	11×11
361	0.34	-3	19×19
400	0.14	0	20×20
784	0.20	$+3$	28×28
1089	0.33	-4	33×33
1369	0.25	$+4$	37×37

6.1.3 Biquadratic Residue

Biquadratic residues were introduced in Chapter. 2.2.3.6 and are low open fraction arrays with $\chi = 0.25$. The number of arrays available for imaging is limited, and their sparsity is demonstrated in (Accorsi, 2001, p. 47). BR array sizes are not immediately known (similar to the Singer) and calculations must take place to extract such information. Until now, only the 1D lengths were previously reported in (Accorsi, 2001, p. 47), yielding no detail on their 2D vector sizes. Table. 6.2 presents the 1D lengths and dimensions of BRs available for imaging where n are odd integers used to calculate L.

Table 6.2: 10 to 75×108 BRs.

n	L	χ	P	$p \times q$
5	101	0.25	-1	10×10
7	197	0.25	-1	14×14
13	677	0.25	-1	26×26
27	2917	0.25	-1	54×54
33	4357	0.25	-1	66×66
37	5477	0.25	$+1$	66×83
		0.25	-1	74×74
45	8101	0.25	-1	75×108
		0.25	-1	81×100
		0.25	-1	90×90
47	8837	0.25	-1	94×94

6.2 Ideal PSF by Circular Shifting

—redA non-symmetrical $\chi = 0.5$, 15×17 Singer array created using the process in Chapter. 2.2.3.7 and presented in Fig. 6.4 was first observed in Skinner (1984) as symmetrical (see Fig. 6.5). However, the PSF was not given along with the array pattern. Although research was conducted to explain the difference in the two arrays in Fig. 6.4 and Fig. 6.5, there was a lack of information readily available. Careful analysis of the arrays revealed that they were in fact both the same arrays. It was found that a circular shift was performed to achieve symmetry along the y-axis (see Fig. 6.5). Consequently, the raised plateau for the corresponding PSF in Fig. 6.5 was significantly improved to that found in Fig. 6.4 (Muñoz et al., 2018a). The symmetrical 15×17 Singer array in Fig. 6.5 was attained by performing a positive circular shift in each row of the array in Fig. 6.5 to the right. Fig. 6.6 reveals the actual process

and number of shifts required. All rows were then circularly shifted down by six shifts.
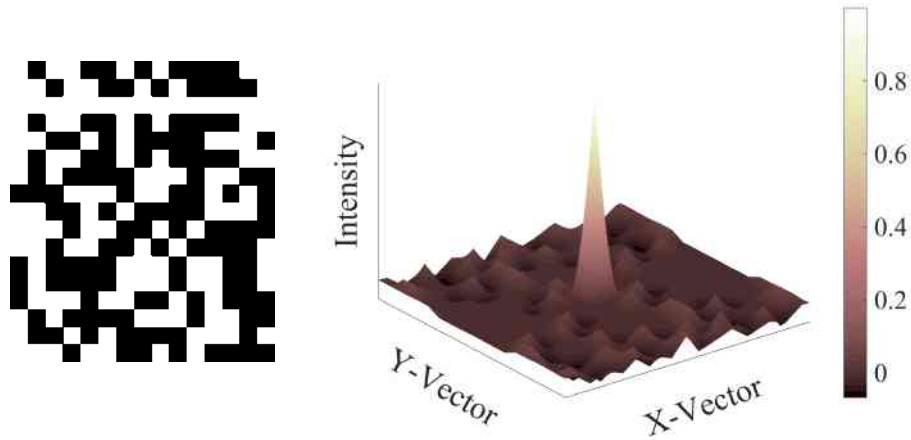
Figure 6.4: 15×17 Singer and its PSF: The array has no symmetry and its PSF is not ideal.
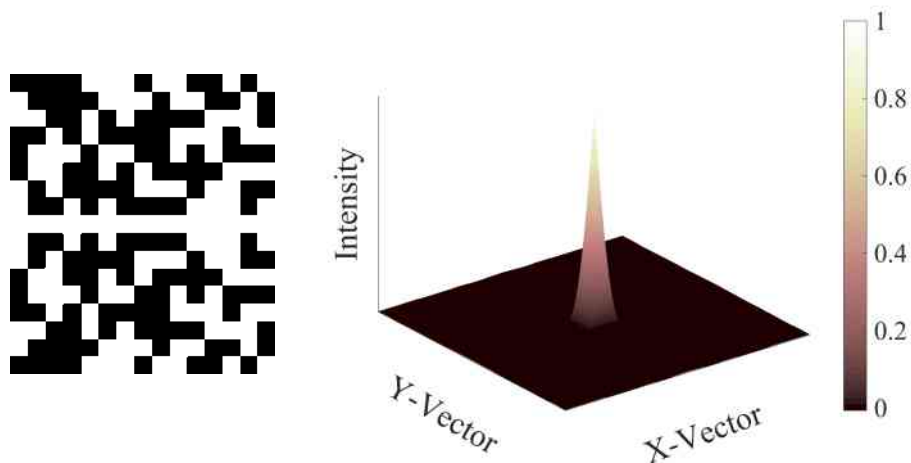
Figure 6.5: Ideal PSF from Circular Shifting: The 15×17 Singer in Fig. 6.4 has been altered via vector shifting to achieve symmetry along the y-axis. Consequently, this has resulted in an ideal PSF.

6.3 Discussion

Research was conducted to see if circular shifting could be performed on other Singer arrays of a lower open fraction. Such results would be a major advance in CMI to find more low open fraction array with a PSF matching that of the URA. As the process was performed manually, only a few Singer arrays were

Circular Shift

Shift															
9	1	0	1	1	0	0	1	0	1	0	0	0	0	1	1
11	1	1	0	1	1	0	0	1	0	1	0	0	0	0	1
0	1	1	1	1	1	1	1	1	1	1	1	1	1	1	1
12	1	0	1	1	0	0	1	0	1	0	0	0	0	1	1
11	1	1	0	0	1	0	1	0	0	0	0	1	1	1	0
14	1	0	1	1	0	0	1	0	1	0	0	0	0	1	1
9	1	0	1	0	0	0	0	1	1	1	0	1	1	0	0
6	0	0	0	1	1	1	0	1	1	0	0	1	0	1	0
0	1	1	0	0	1	0	1	0	0	0	0	1	1	1	0
5	1	1	1	0	1	1	0	0	1	0	1	0	0	0	0
5	1	1	0	1	1	0	0	1	0	1	0	0	0	0	1
13	0	1	0	0	0	0	1	1	1	0	1	1	0	0	1
14	0	1	0	0	0	0	1	1	1	0	1	1	0	0	1
10	0	1	1	1	0	1	1	0	0	1	0	1	0	0	0
2	1	0	1	0	0	0	0	1	1	1	0	1	1	0	0
6	1	0	0	1	0	1	0	0	0	0	1	1	1	0	1
12	1	1	1	0	1	1	0	0	1	0	1	0	0	0	0
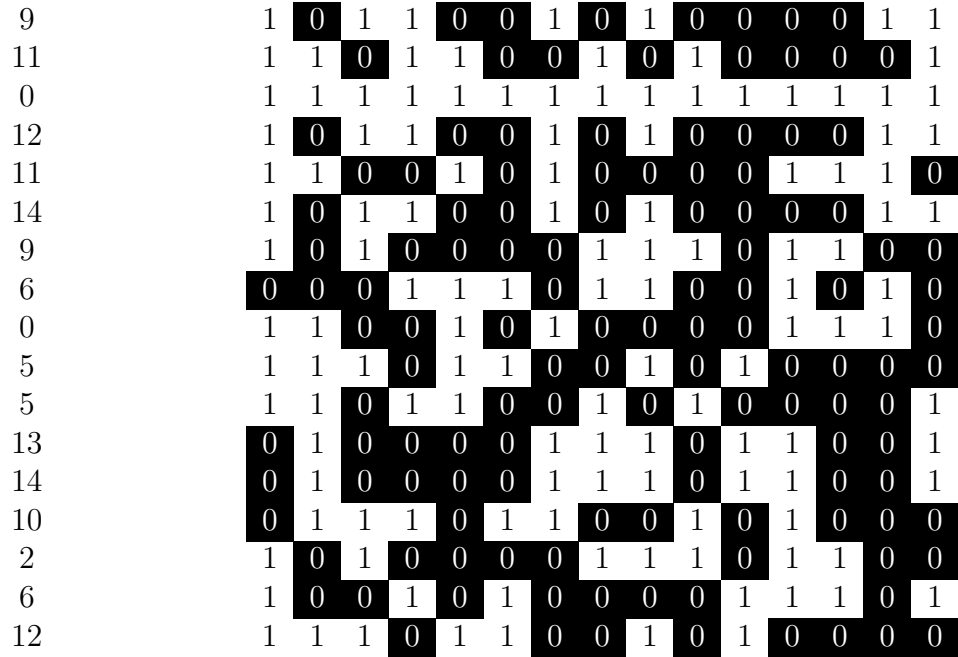
Figure 6.6: Circular Shifting a 15×17 Singer Array: The values to the left of the array are amounts by which that vector has shifted to the right. Note, all rows are then down shifted by 6.

investigated and the PSFs remained the same as the original un-shifted arrays. That is to say, similar traits were not found with other arrays. Subsequently, focus was placed on the $\chi = 0.5$ Singer array to deduce specific features that allowed for circular shifting to occur. The most prominent feature as found in Fig. 6.4 was a continuous row of 1s. Not all Singers possessed this particular trait and a trend revealed some Singers arrays with twin prime vectors containing similar features. Arrays included the 31×33, 63×65 and 127×129 Singers all with 0.5 open fraction. Nonetheless, after a subjection to circular shifting no visible changes or improvements were observed in their PSF.

Overall, a number of LOF arrays were calculated to address the limited choice of open fractions and vector sizes. Fig. 6.7 reveals a plot of 32 unreported low open fraction encoded arrays suitable for imaging, based on their array size being relatively square and similar to standard dimensions of imaging detectors. The array patterns are presented in Appx. A in addition to others that may not be suitable for imaging. More arrays were calculated and published in Muñoz et al. (2018a), but due to their extreme dimension they may be insufficient for imaging. Nonetheless, the arrays may find applications where specialised fan beam optics are utilised. Previous chapters introduced the low open fraction NRA and PNPs which, exhibit ideal imaging properties or similar for CMI. These masks have good self-supporting structures that would

render them as good candidates for fabricating physical versions of the array pattern without compromise in the design. However, such arrays are limited in vector sizes and open fraction. In addition, it was at the sponsor's request to investigate and focus on some of the masks presented earlier.
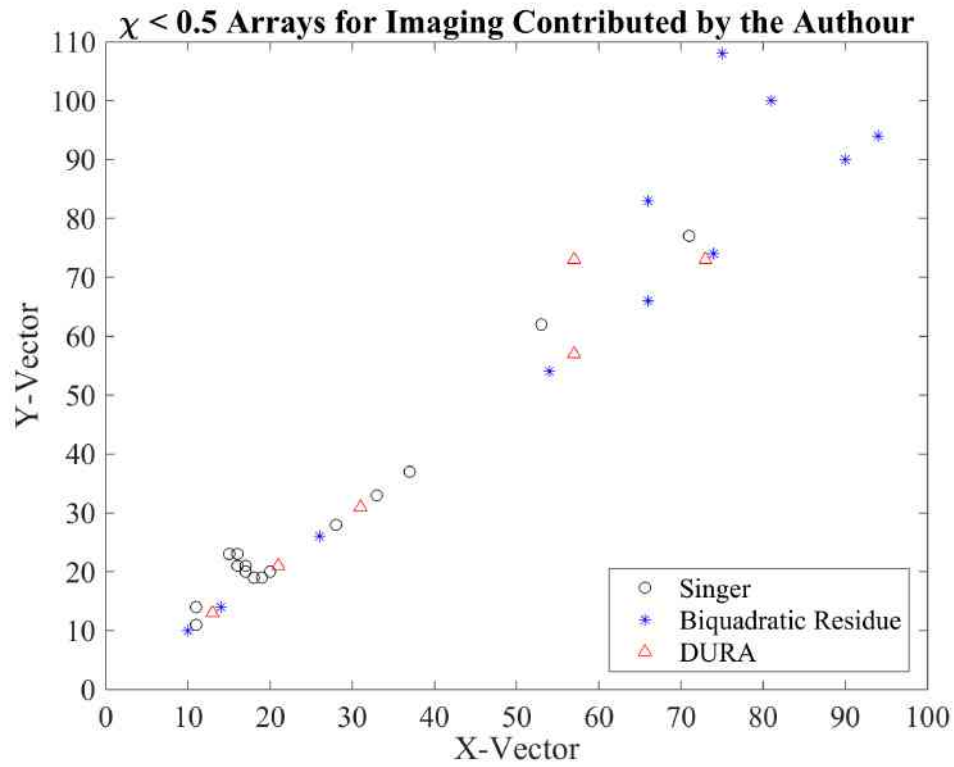
Figure 6.7: Calculated Low Open Fraction Array.

Chapter 7

Radioactive Isotope Imaging

117

CMI has been used in astronomy to image high energy sources in the night sky (Dicke, 1968). Advances in science have seen CMI applied to medical imaging to expose radioactive isotope gamma ray sources in patients (Accorsi and Lanza, 2001). This chapter investigates such use of the coded mask and takes it further by using a number of different mask patterns and new patterns such as the 13 DURA.

7.1 Radioactive Isotope Imaging

The theoretical PSF of each array in Fig. 4.14 was calculated using Eq. 3.9 and is presented in Fig. 7.1. Single 30 s exposure experiments of the ^{241}Am radioactive source, placed at 1.5 m away from the camera was conducted to replicate a far field scene; similar to that of a star in the night sky (see Fig. 7.2). Consequently, the exposures resembled those in Fig. 7.1, displaying similar artefacts and noise that is inherent to the array pattern. This served as an indication that the experimental and decoding methods conducted were correct. Also, the XBI system demonstrated the ability to expose radioactive isotopes with CMs for a simple scene, that can apply to medical imaging (Lakshmanan et al., 2017; Zhang et al., 1982). Calculated PSFs in Fig. 7.1 and the ^{241}Am radioactive source exposures found in Fig. 7.2 were quantified regarding SNR, revealing the 19 MURA to be far superior to the other array patterns, followed by the 26 BR. (see Table. 7.1 and 7.2). Note, the images in Fig. 7.2 appear to have different size due to the variation in array dimensions. This along with the inherent uncertainty in the quantifying process may be attributing factors to why the SNR of Fig. 7.1 and Fig. 7.2 were partially inconsistent. The overall results in Table. 7.1 are higher than those in Table 7.2 due to various noise terms such as photon and dark noise being introduced into the experimental exposures.

7.2 Discussion

The normalised images in Fig. 7.1 and Fig. 7.2 are calculated PSFs and radioactive source images from masks used in this thesis. Images were calculated and quantified in terms of their SNR. Although the 19 MURA outperformed all other CMs as expected, it was found that some array patterns had superior experimental results over their theoretical counterparts. The likely cause of this would be due to experimental error during the quantification process. In addition the signal in some theoretical values were much fainter than those from the experimental images.

19 MURA   13 DURA   17×21 Singer

26 BR   19 RANDA$^\alpha$ 19 RANDA$^\beta$

13 MURA NTHT   19 MURA NTHT   13 DURA NTHT

17×21 Singer NTHT   19 RANDA$^\alpha$ NTHT
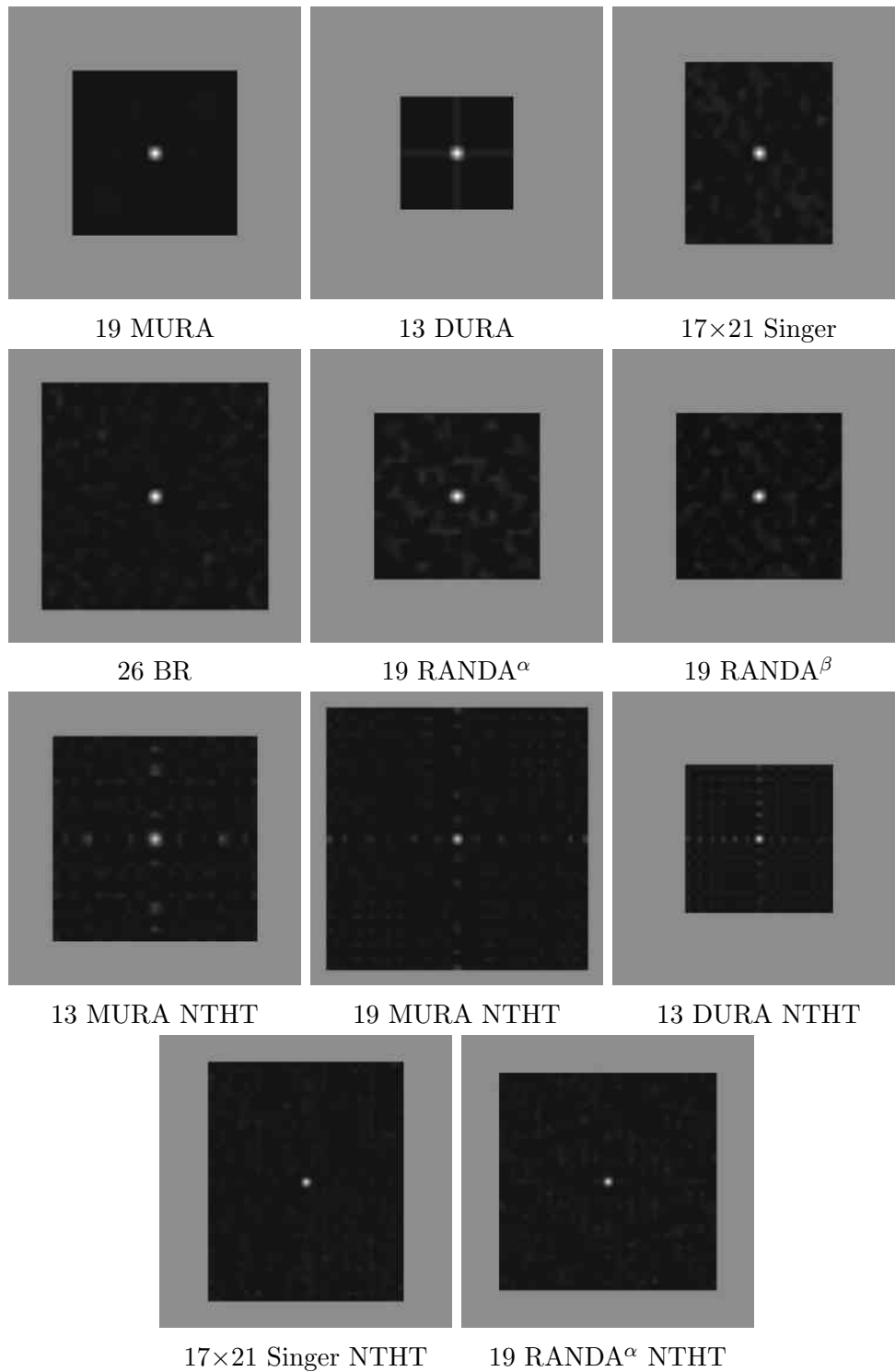
Figure 7.1: Theoretical PSF of Array Patterns in Fig. 4.14.
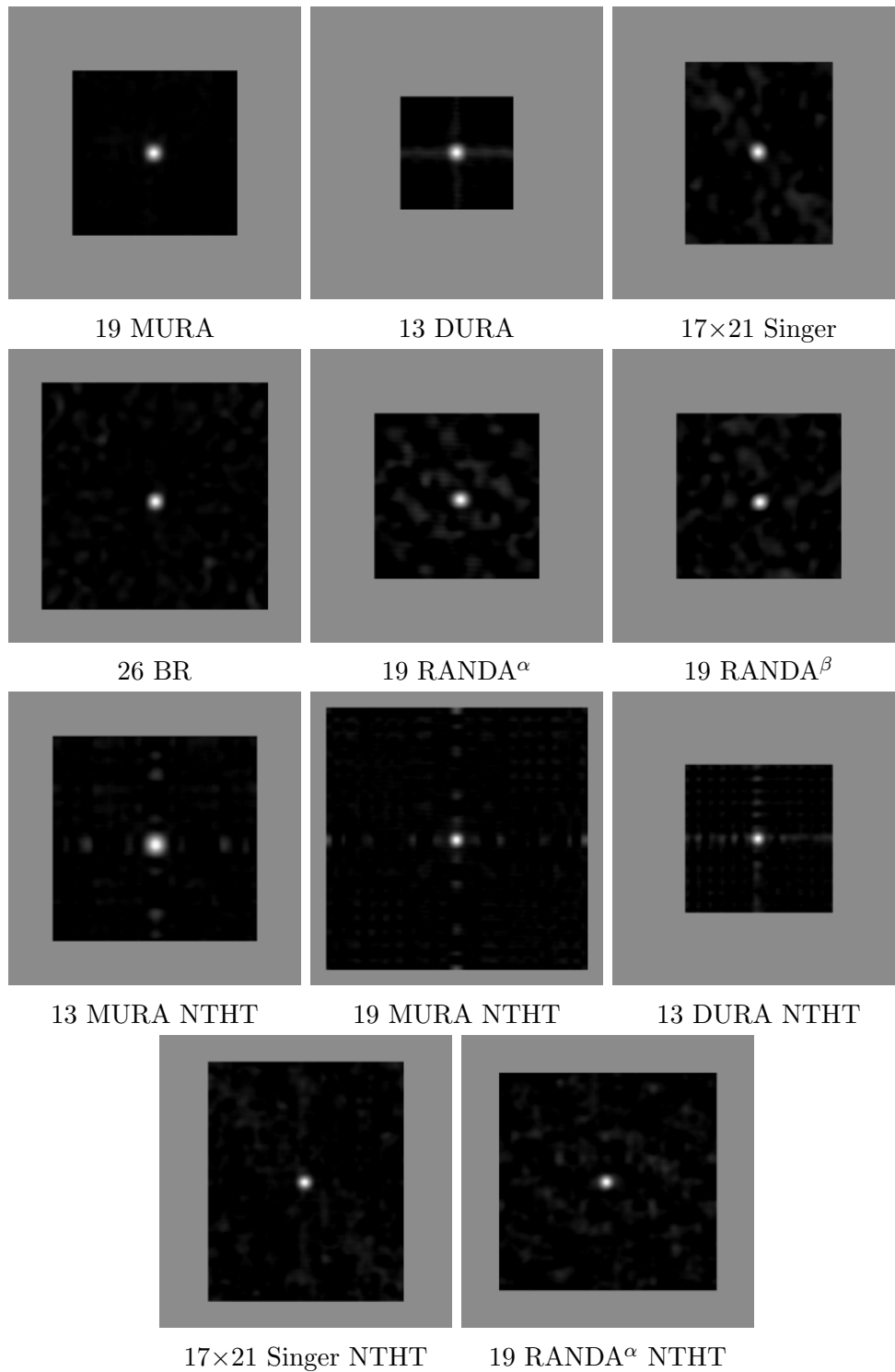
Figure 7.2: ^{241}Am Radioactive Source Exposures.

19 MURA   13 DURA   17×21 Singer

26 BR   19 RANDA$^{\alpha}$ 19 RANDA$^{\beta}$

13 MURA NTHT   19 MURA NTHT   13 DURA NTHT

17×21 Singer NTHT   19 RANDA$^{\alpha}$ NTHT

Table 7.1: Theoretical SNR from the PSF of Encoded Array Patterns.

Encoded Array Patterns	SNR
19 MURA	436.0
26 BR	63.7
17×21 Singer NTHT	61.9
19 RANDA$^{\alpha}$ NTHT	56.0
19 MURA NTHT	50.0
13 DURA	44.0
17×21 Singer	43.0
19 RANDA$^{\beta}$	37.3
19 RANDA$^{\alpha}$	33.7
13 MURA NTHT	33.6
13 DURA NTHT	31.5

Table 7.2: SNR of ^{241}Am Radioactive Source Exposures.

Coded Masks	Material	SNR
19 MURA	PLA/TEC	133.6
26 BR	PLA/TEC	66.7
13 MURA NTHT	MTA	54.6
19 MURA NTHT	MTA	53.5
17×21 Singer NTHT	MTA	50.5
19 RANDA$^{\alpha}$ NTHT	MTA	40.5
13 DURA NTHT	MTA	39.9
19 RANDA$^{\beta}$	PLA/TEC	37.0
13 DURA	PLA/TEC	36.0
17×21 Singer	PLA/TEC	35.1
19 RANDA$^{\alpha}$	PLA/TEC	31.1

Chapter 8

Spatial Multiplexed Backscatter Imaging

Spatial multiplexing imaging (SMI) systems are those that expose and detect all regions of the entire scene simultaneously. That is to say, signals from all parts of the scene are conveyed to the detector at the same time (Dinca et al., 2008; Cao et al., 2009). This section aims to compare and contrast the different masks used in Fig. 4.14 to determine the optimum resolving medium. The first experiment consisted of taking X-ray backscatter exposures of the quadrant in Fig. 3.3 with each CM. The quadrant was specifically chosen due to its diversity in materials, which would reflect a typical imaging scene of varying shapes and composition. Initial experiments were subject to greater emphasis placed on the SNR and to determining which CMs were able to resolve signals as a 16-bit image from all aspects of the scene.

8.1   Optimum Mask to Detector Distance

Imaging objects such as the quadrant were centred within the FOV of the camera and placed at a standard distance of 1 m (unless otherwise stated). An experiment was conducted to determine the optimum mask to detector distance in order to avoid collimation for masks of $\underline{t} = 2$ mm and ϕ_{AP}, as calculated in Chapter. 3.2.1. Fig. 8.1 presents $\boldsymbol{S_2}$ images showing a change in FOV as a function of mask to detector distance. Note, the MTA 19 MURA NTHT was used for the experiment presented in Fig. 8.1. Fig 8.2 reveals a trend of increasing SNR with decreasing mask to detector distance. It is important to note that when calculating the SNR, the signal was selected from the brightest part of the quadrant and the sample area was different for each image in Fig. 8.1. This is due to a change in the quadrant's size as a result of the changing FOV.

The quadrant imaging object appeared small within the scene (see Fig. 8.1); therefore, a large FOV was not required. Besides, the object in view appeared larger with increasing $\underline{b}$, displaying greater detail with smaller FOV. Consequently, mask to detector distances with higher SNR were desired, so to achieve this along with a small FOV, $\underline{b} = 100$ mm was found to be the optimum mask to detector distance for experiments in this thesis (unless stated otherwise).

8.2   Coded Masks of Different Open Fractions

X-ray backscatter $\boldsymbol{S_2}$ images from low open fraction 'URA' like CMs were compared to a $\chi = 0.5$ 19 MURA, with a summed exposure time of 6 s for each mask. The experimental masks were all 3D printed PLA/TEC and are presented in Fig. 8.3 along with their open fractions. Upon analysing Fig. 8.3,

$\underline{b} = 80$ mm $\qquad$ $\underline{b} = 100$ mm

$\underline{b} = 120$ mm $\qquad$ $\underline{b} = 140$ mm

$\underline{b} = 160$ mm $\qquad$ $\underline{b} = 180$ mm
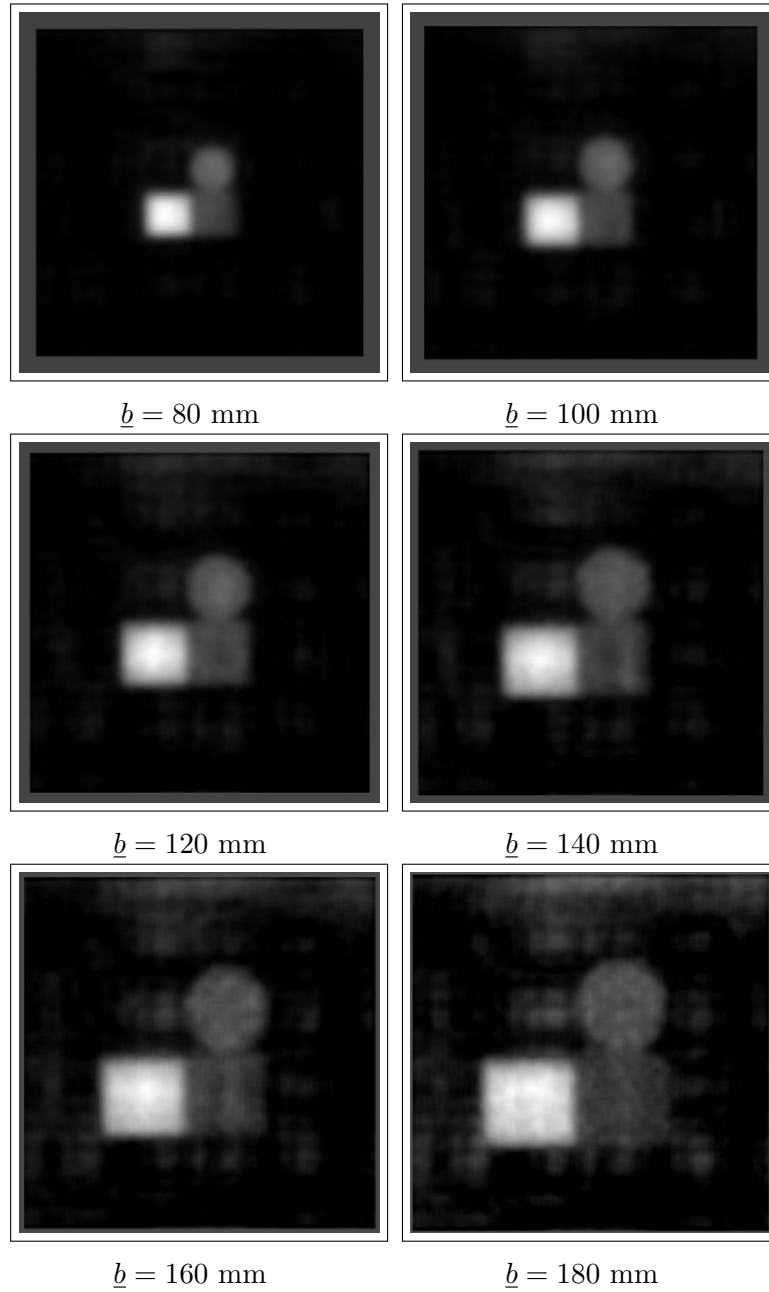
Figure 8.1: Changing FOV with Mask to Detector Distance.
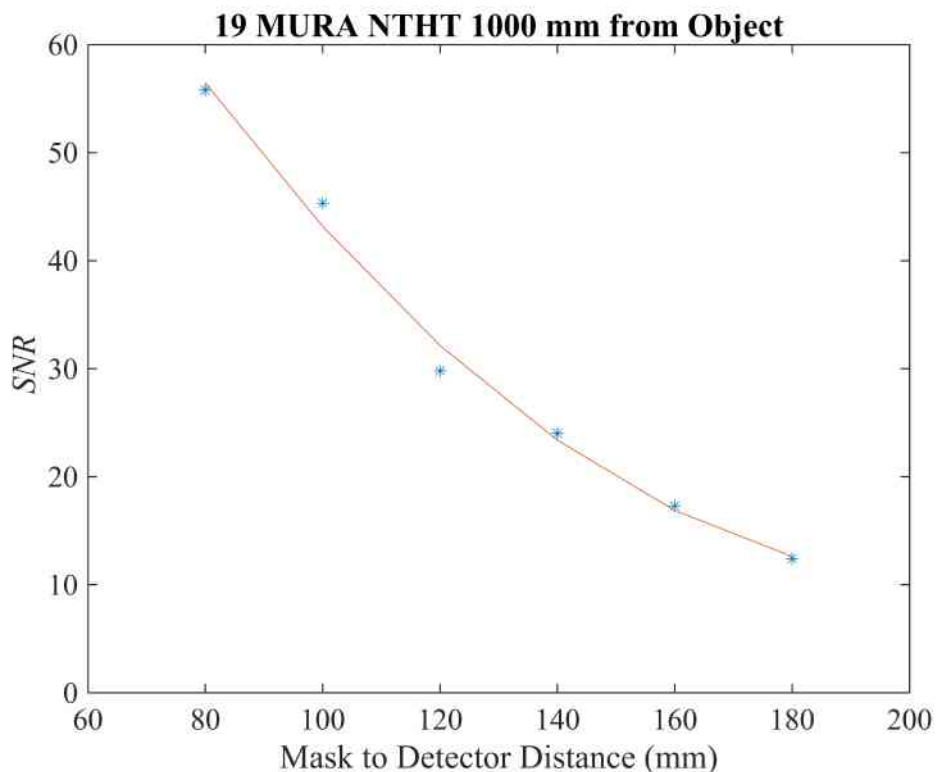
Figure 8.2: Optimal Mask to Dector Distance Determined to be at 100 mm from Quantifying Fig. 8.1.

it was visually apparent that all expected parts of the quadrant (besides the copper block in the upper right quadrant being high Z) were resolved for the 19 MURA, 13 DURA and 26 BR. This was untrue for the 17×21 Singer, where the PVC cylinder in the top right of the quadrant was barely visible and the aluminium block in lower right was not visible at all. SNR and CNR values in Table. 8.1 confirmed performances of CMs, with the $\chi = 0.5$ 19 MURA outperforming all lower open fraction mask within the experiment. This was consistent with (Munoz et al., 2017a; Muñoz et al., 2018a; Accorsi et al., 2001) which is probably due to its PSF. Because of the inability of the 17×21 Singer to display signals from most of the scene, it rendered the mask impractical for CM imaging for the system at Cranfield University. Note, this only applies to image decoding via cross-correlation. The alternative blind deconvolution decoding method is presented later on.

The 19 MURA performance may be attributed to its perfect PSF and not necessarily the open fraction of the mask. Additionally, images in Fig. 8.3 are of varying size, thus, for example; there is less background in some exposures such as the 13 DURA than the 26 BR. Consequently, some images contain less information for its background, meaning that less noise would be contributed when calculating SNR. Alternatively, a fair comparison can be

126

19 MURA, $\chi = 0.50$ 13 DURA, $\chi = 0.40$

17×21 Singer, $\chi = 0.34$ 26 BR, $\chi = 0.25$
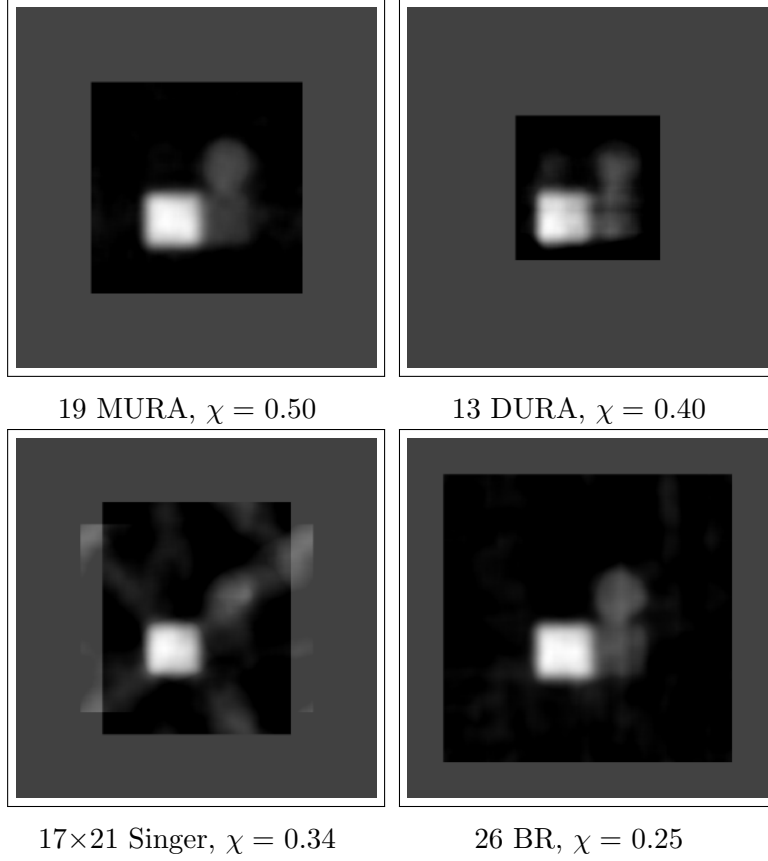
Figure 8.3: Low Open Fraction 'URA' CM Images.

Table 8.1: Low Open Fraction 'URA' CM Images.

Coded Mask	χ	SNR	CNR
19 MURA	0.50	64.2	63.6
26 BR	0.25	44.5	44.0
13 DURA	0.40	39.7	39.4
17×21 Singer	0.34	14.4	13.5

made by using CMs that are the same in size with comparable PSFs. Two 3D printed PLA/TEC random arrays with similar sizes and PSFs were fabricated and used to expose the quadrant with backscattered X-rays. Both arrays were 19×19 elements in dimension with $\chi = 0.32$ and $\chi = 0.50$. Fig. 8.4 reveals $\boldsymbol{S_2}$ images of the quadrant with a summed exposure time of 6 s. The signal from the nylon 66 block of the quadrant was visible in both images. The PVC cylinder in the 19 RANDA$^\alpha$ image was barely visible, being partially obscured by noise. Other parts of the quadrant besides the nylon 66 captured with the 19 RANDA$^\beta$ were also obscured. Overall, the image from the 19 RANDA$^\alpha$ at a lower open fraction was superior to the $\chi = 0.50$ for the 19 RANDA$^\beta$. Table.

8.2 confirmed such performance and the CNR revealed the same trend. Nevertheless, both RANDAs failed to present all expected signals of the imaging scene and were rendered impractical for use with the XBI system at Cranfield University. Again this only applies to decoding via cross-correlation and the high contrast range from a 16-bit exposure may explain the absence of parts of the imaging scene (discussed later on).

19 RANDA$^\alpha$, $\chi = 0.32$ 19 RANDA$^\beta$, $\chi = 0.50$
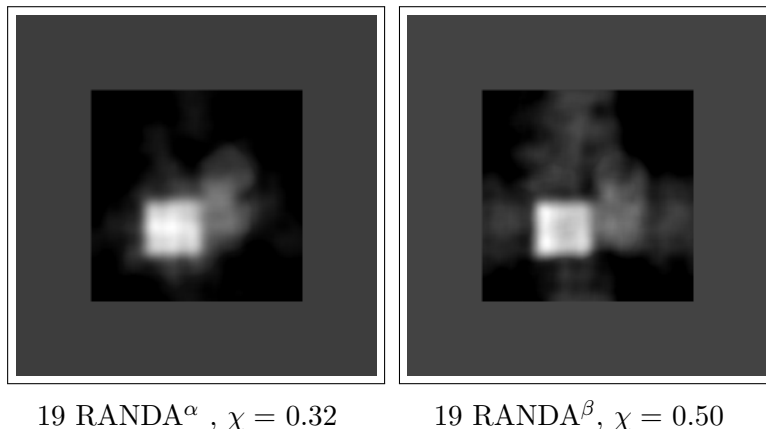
Figure 8.4: Low Open Fraction RANDA CM Images.

Table 8.2: Low Open Fraction RANDA CM Images.

Coded Mask	χ	SNR	CNR
19 RANDA$^\alpha$	0.32	17.1	16.7
19 RANDA$^\beta$	0.50	9.6	8.8

8.3 Comparison of PLA/TEC and MTA CMs

CMs were manufactured both from drilling MTA and 3D printing PLA/TEC. X-ray backscatter S_2 6 s exposures of the quadrant were collected with the PLA/TEC 19 MURA, 13 DURA, 19 RANDA$^\alpha$ and their MTA NTHT versions (see Fig. 8.5 for results). This experiment aimed to determine the performance of 3D printed CMs when compared to that of the drilled MTA CMs. Upon analysis, the PLA/TEC 19 MURA outperformed all CMs in the experiment with regards to both SNR and CNR (see Table. 8.3). The result were consistent with those from (Munoz et al., 2017a; Muñoz et al., 2018a; Accorsi et al., 2001). Subsequently, other CMs ranked below the 19 MURA with the 13 DURA NTHT, 13 DURA, 19 MURA NTHT, 17×21 Singer NTHT, 19 RANDA$^\alpha$, 19 RANDA$^\alpha$ NTHT and 17×21 Singer. An overall in-depth study of results in Table. 8.3 saw no visible trend that could be extracted. CM patterns formed with MTA sometimes

PLA/TEC **MTA**

19 MURA 19 MURA NTHT

13 DURA 13 DURA NTHT

19 RANDA$^{\alpha}$ 19 RANDA$^{\alpha}$ NTHT

17×21 Singer 17×21 Singer NTHT
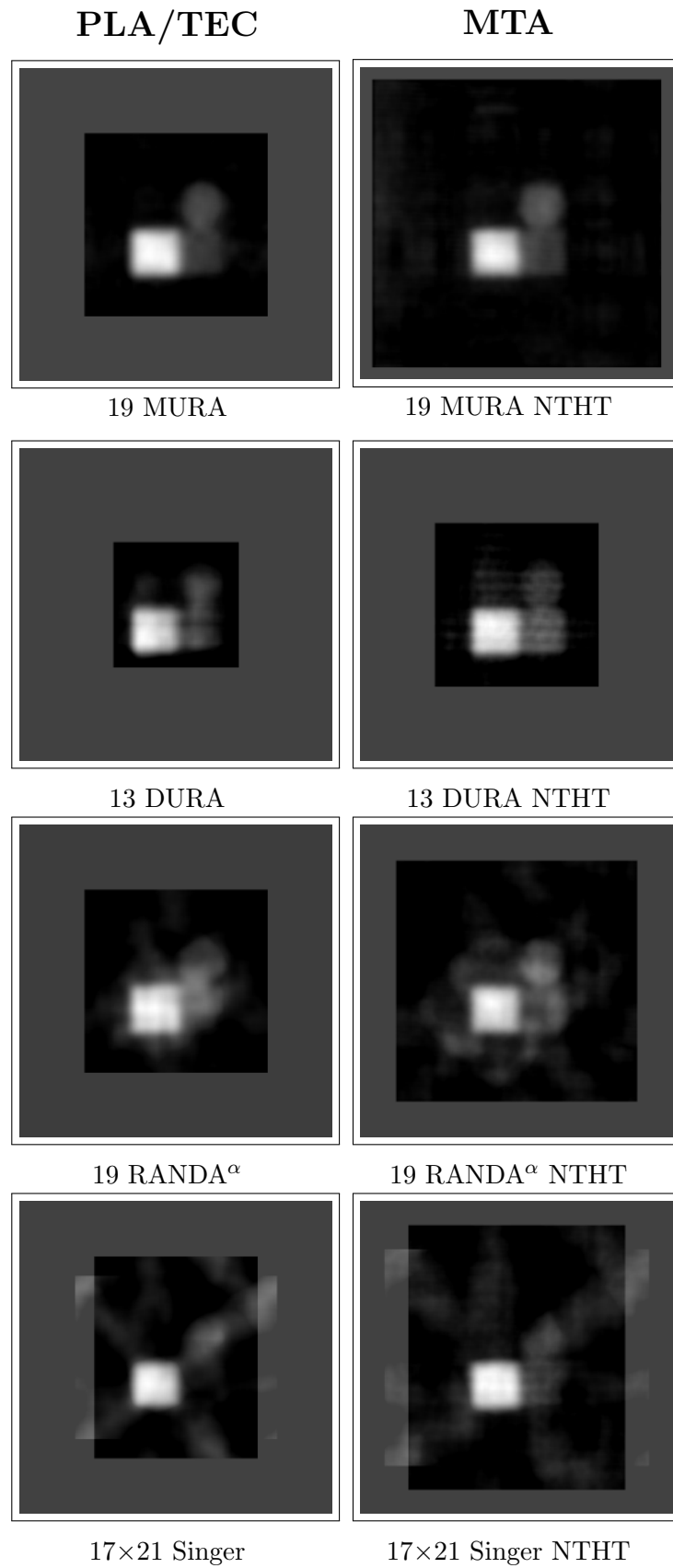
Figure 8.5: Image of the Quadrant using 3D Printed and Machined Tungsten CMs.

129

Table 8.3: Comparing 3D Printed and Machined Tungsten CMs.

Coded Mask	Material	SNR	CNR
19 MURA	PLA/TEC	64.2	63.6
13 DURA NTHT	MTA	54.0	53.6
13 DURA	PLA/TEC	39.7	39.4
19 MURA NTHT	MTA	34.6	33.7
17×21 Singer NTHT	MTA	18.0	16.9
19 RANDA$^\alpha$	PLA/TEC	17.1	16.7
19 RANDA$^\alpha$ NTHT	MTA	16.9	16.4
17×21 Singer	PLA/TEC	14.4	13.5

dominated in performance in terms of SNR and this was also the case for PLA/TEC CMs.

A comparison of images taken from the various MTA and PLA/TEC CMs are presented in Fig. 8.5 which reflects SNR values presented in Table. 8.3. The top four 19 MURA, 13 DURA NTHT, 13 DURA and 19 MURA NTHT all resolved signal from the quadrant that was expected, such as the nylon 66, PVC and aluminium. Conversely, the 17×21 Singer NTHT, 19 RANDA$^\alpha$, 19 RANDA$^\alpha$ NTHT and 17×21 Singer failed to display expected signal and were not suitable as the optimum resolving medium for this project.

8.4 Optimum Masks

The top-performing CMs presented earlier in this chapter yielding the best SNR and CNR were analysed to establish their resolving capabilities. This was achieved using the Al lp object (see Fig. 8.6 for results). Also, CMs were chosen due to the ability to resolve signals of various atomic composition when compared to others within the experiments. CM $\boldsymbol{S_2}$ images had an exposure time of 6 s and 60 s for the pinhole.

Although the 13 DURA ranked in the top group of CMs, the Al lp object used in this experiment was too large for its FOV and therefore it was not used. The $\phi_{AP} = 2$ mm pinhole imaging mask was also included in the experiment due to demonstrating the ability to resolve a variety of signals from the quadrant. The 2 mm pinhole and 19 MURA NTHT displayed highest resolutions of 0.06 lp/mm followed by the 19 MURA, 13 DURA NTHT and 26 BR (see Table. 8.4). Note, how the SNR and CNR differ from previous results due to the size of the object and decrease in background. Thus, this was an unfair comparison and therefore was omitted from the decision making process. Overall, the optimum all-around masks for imaging at 100 kV, 8 mA, $\underline{a} = 1000$ mm, $\underline{b} = 100$ would be the 2 mm pinhole mask and 19 MURA NTHT. Both had a

2 mm Pinhole

19 MURA NTHT   19 MURA

13 DURA NTHT   26 BR
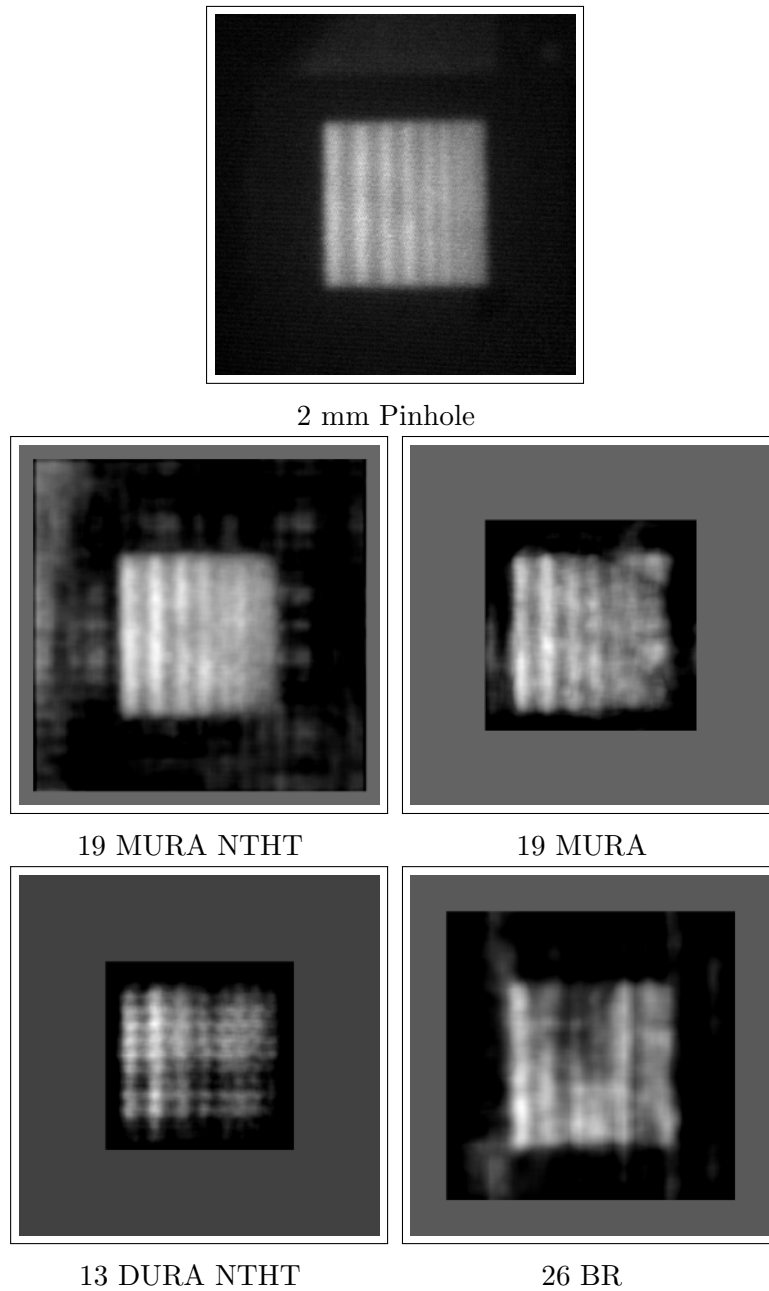
Figure 8.6: Optimum Mask Images: Images of the Al line pair object.

comparable resolution; however, the 2 mm pinhole presented superior SNR and CNR over the 19 MURA NTHT. The results are also justified visually. Nevertheless, the 19 MURA NTHT requires significantly less exposure time of 6 s than the 2 mm pinhole at 60 s.

Table 8.4: Optimum Mask Images Results.

Coded Mask	Line Pair (lp/mm)	SNR	CNR	S_2 (s)
2 mm Pinhole	0.06	16.7	15.1	60
19 MURA NTHT	0.06	6.2	5.3	6
19 MURA	0.05	9.4	8.7	6
13 DURA NTHT	0.05	15.7	15.7	6
26 BR	0.04	8.7	8.3	6

8.5 Imaging Real World Objects

X-ray backscatter exposures of the quadrant, WWB and Al lp objects were presented in the previous chapter with the purpose of quantifying the performance of each mask. This chapter demonstrates capabilities of the XBI system with 'real world' objects. The objects include a plastic box containing a digital calliper and small screwdriver, a toolkit with various items and a car door with a bottle of water and a box of icing sugar hidden within its panel. All objects were chosen because they were the most accessible at the time of experiment. The masks used in the experiment was the 2 mm pinhole and 19 MURA NTHT. For comparison, X-ray transmission radiographs were conducted with the same objects using a dual energy Heimanns airport baggage scanner operating at 170 kV(see Fig. 8.7).

Fig. 8.8 presents the X-ray transmission and backscatter images of the boxed calliper with the experimental parameters as follows; $\underline{a} = 500$ mm and the X-ray source operating at 100 kV and 8 mA. Exposure times were 60 s and 4 s for the 2 mm pinhole and S_2 19 MURA NTHT respectively. Similar settings were also applied to X-ray backscatter images in Fig. 8.9. The transmission radiograph demonstrated good contrast for the steel calliper and metallic part of the screwdriver. However, this is poor when radiographing the low Z box and screwdriver handle. Conversely, X-ray backscatter demonstrated the ability to resolve low Z material with high contrast for the box and screwdriver handle. Note, the additional noise in Fig. 8.8e appeared as a likely result of X-ray scatter within the radiation cell. It was found to be more prominent with CM exposures. Similar results are seen in Fig. 8.9 with the toolkit. Finally, the X-ray backscatter images in Fig. 8.10 were exposed for 300 s and 40s for the 2 mm pinhole and S_2 19 MURA NTHT respectively.

Parameters for the X-ray source were 160 kV at 5 mA to yield the maximum output of 800 W whilst covering a greater energy range. In addition, the tungsten alloy mask used for this experiment allowed for imaging at greater energies with very small radiation leakage. The hidden water bottle (A) and icing sugar (B) in Fig. 8.10 was detector using both masks. Note, positions

Figure 8.7: Dual Energy X-ray Baggage Scanner: The scanner was used to take all X-ray transmission images.

of the icing sugar and water were different in each scene due to the tendency of the icing sugar falling out of position. Also, the source was collimated for the 19 MURA NTHT exposures; hence only a portion of the car door was illuminated which is visible as the bright circular region in Fig. 8.10c. Overall, the X-ray backscatter system succeeded in detecting hidden objects of low Z from various scenes using both the 2 mm pinhole and 19 MURA NTHT.

8.6 Discussion

Imaging with low open fraction CMs decoded via cross-correlation did not prove to have any benefits over the MURA for XBI. The fact that the 19 MURA out performed all other CMs is likely due to its ideal PSF. Comparison and quantification in terms of SNR and CNR was not entirely fair due to the difference in detector area from the CMs base pattern size. Although this could not be avoided (as mentioned in previous chapters) attempts were made to compare two RANDAs with similar vector sizes, base pattern sizes and PSFs; but with different open fractions. It was found that the lower open fraction array performed the best in terms of both SNR and CNR. However,

(a) Caliper and Screwdriver Set

(b) Optical Image
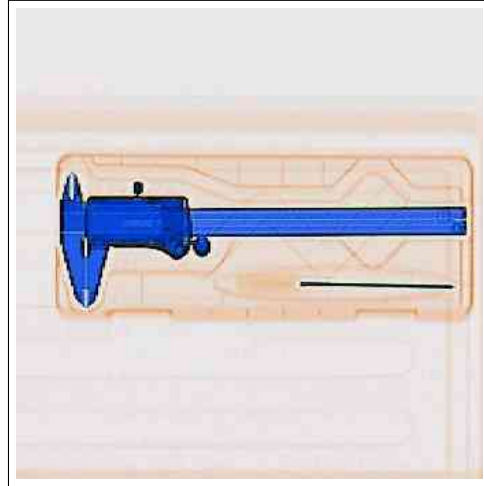
(c) Transmission Image
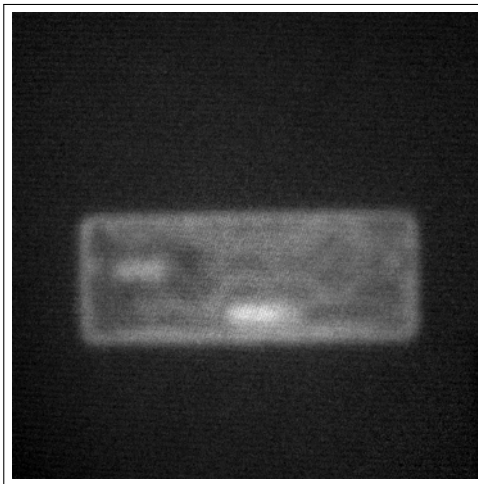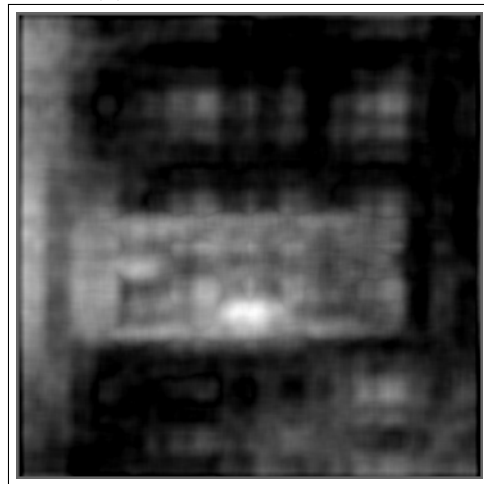
(d) XBI 2 mm Pinhole

(e) XBI 19 MURA NTHT

Figure 8.8: Caliper X-Ray Image: The low Z polymer screwdriver handle and caliper LCD display are clearly visible and resolved in the X-ray backscatter images.

(a) Tool Kit

(b) Optical Image
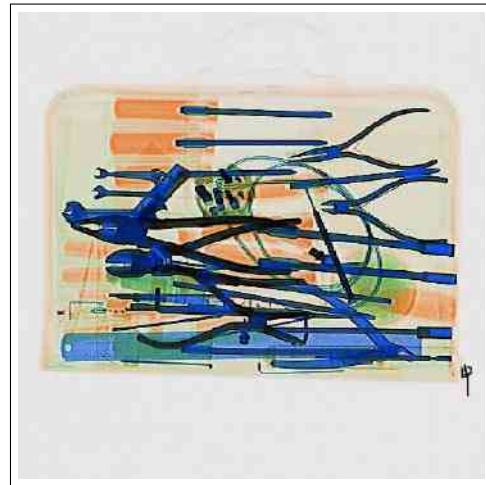
(c) Transmission Image
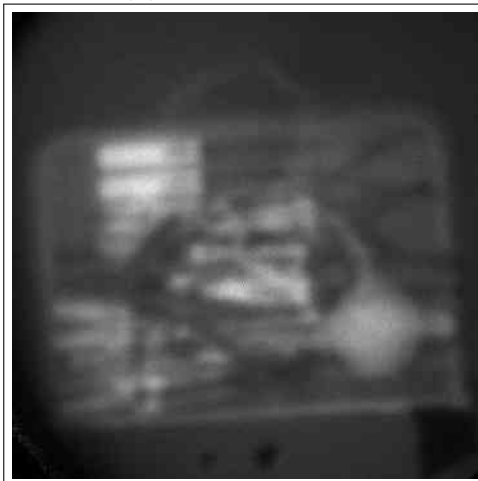
(d) XBI 2 mm Pinhole
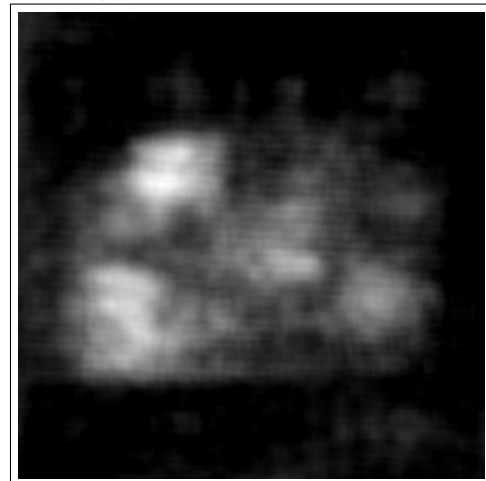
(e) XBI 19 MURA NTHT

Figure 8.9: Tool Kit X-Ray Image: The low Z polymer screwdriver handles are clearly visible and resolved in the X-ray backscatter images. They are also the prominent features of the image.

(a) Car Door with Hidden Objects
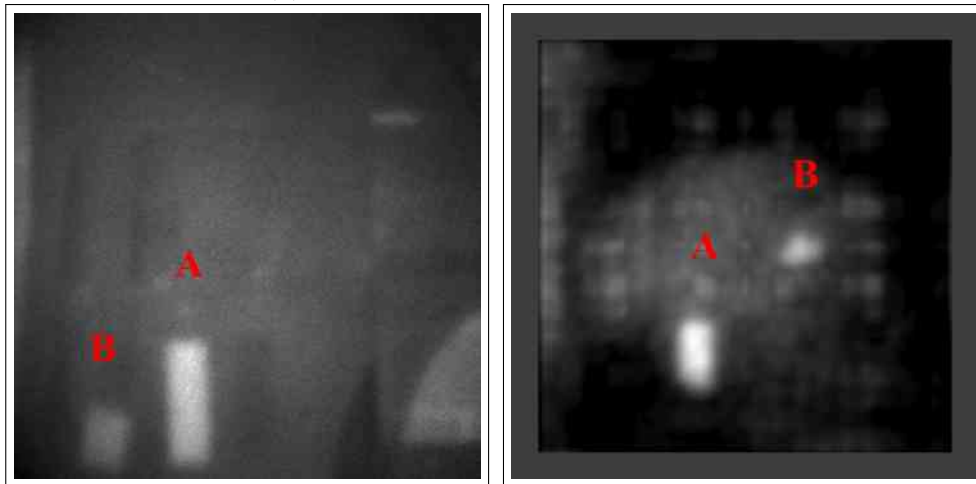
(b) XBI 2 mm Pinhole

(c) XBI 19 MURA NTHT

Figure 8.10: Car Door X-Ray Image: The low Z (A) water bottle and (B) icing sugar hidden within the car door have been detected and are clearly resolved. Note, the position of the objects have changed in the two images, due to having to be moved. This was due to the objects falling over numerous times during the exposure, as a result of an unstable platform. Additionally, the limited size of the X-ray illuminated area is visible in (c) because it was necessary that the X-ray source was collimated to reduce scatter.

further research is encouraged to confirm such results. Overall, the 19 MURA PLA/TEC CM outperformed all other CMs for SNR and CNR, and the 2 mm pinhole and 19 MURA NTHT images displayed the best spatial resolution.

When applying XBI using both the 2 mm pinhole and 19 MURA NTHT to every day 'real world' objects, results show that such type of imaging technique can indeed be applied to defence and security. Images taken of hidden objects of low Z within various shielding materials, such as a steel car door and polymer calliper box can be detected and resolved. Images taken from the XBI system demonstrates greater efficiency in detecting low Z material over the dual energy transmission system. This is clearly visible in Fig. 8.8. In this scenario, both the polymer screwdriver handle and LCD are not detected because the caliper box is comprised of similar material. Additionally, X-rays passing through the LCD region is attenuated by the metallic structure beneath, giving the false appearance of a completely metallic caplier. Nevertheless, both the polymer screwdriver handle and LCD were detected and distinguished from the caliper box with the XBI system. Although, there is room for improvement in terms of spatial resolution and noise reduction, the fact that there has been a lack of previous experimental research in CM XBI shows that there is good potential for further development with short exposure times.

Chapter 9

Time vs Spatial Multiplexed Imaging

The concept of SMI was introduced earlier describing images that are detected from all parts of the scene simultaneously. To the contra, when images are formed from a scene over a period this is sometimes referred to as 'time multiplexing imaging' (TMI). This type of imaging system is usually known as a 'flying spot' because a pencil beam of X-rays are emitted from the source, passing through multiple apertures on a rotating wheel (see Fig. 9.1) (Herr et al., 1994; Towe and Jacobs, 1981; Dinca et al., 2008). A sweeping arm scans the object on the flying spot system, which backscatters X-rays onto the detector. Subsequently, an image of the scene is built up over a given period. Experiments were conducted at dstl in Fort Halstead, with the quadrant placed at a standard distance of 1 m (see Fig. 9.2).
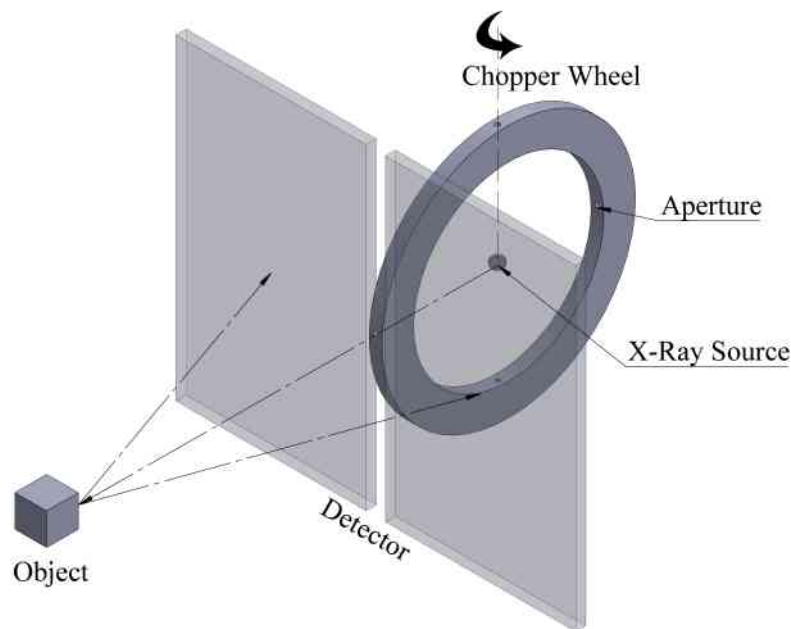
Figure 9.1: XBI Flying Spot System Diagram.

9.1 Experimental Settings 1: Standard Object Distance

Flying spot images were taken and compared to those taken with the XBI created in Chapter. 3.1 and are found in Fig. 9.3 to 9.6 and with their quantified results in Table. 9.2 to 9.5. Note, experimental parameters of the CMI system were accommodated to match those from the flying spot system.

Figure 9.2: XBI Flying Spot System at dstl: The TMI flying spot system experiments were conducted in a different laboratory from the SMI system at Cranfield University.

Consequently, this gave rise to difficulties by using settings that were not ideal for CMI, such as PCFOV; particularly at close object to mask range for experiment 2 presented later on.

Table 9.1: Experimental Settings 1: Standard Object Distance

		FSS	Pinhole	CM
Object	Object to Mask (m)	N/A	1	1
	Object to Detector (m)	1	N/A	N/A
X-Ray	Power (W)	300	300	300
	Voltage (kV)	70	70	70
	Current (mA)	4.28	4.28	4.28
	Focal Spot to Collimator (mm)	152	60	60
	Collimator ϕ Size (mm)	0.7	N/A	N/A
	Projected Spot Size ϕ (mm)	21.7	N/A	N/A
Detector	Active Area ϕ (mm)	N/A	115	115
Mask	MTA Mask	N/A	-	19 MURA NTHT
	Thickness (mm)	N/A	2	2
	Smallest Aperture Size (mm)	N/A	2	2
Exposure	Total Exposure Time (s)	70	350	12

(a) Flying Spot System
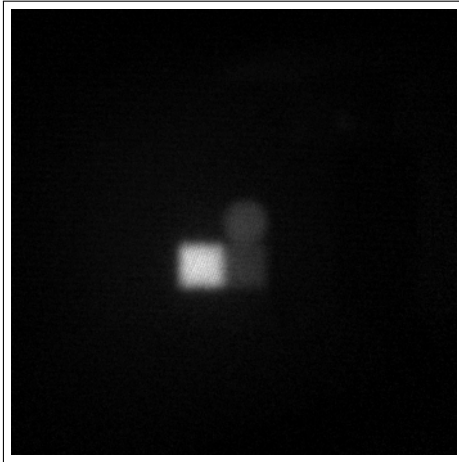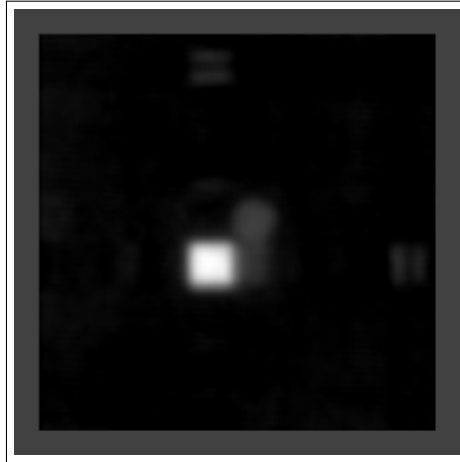
(b) 2 mm Pinhole

(c) 19 MURA NTHT

Figure 9.3: TMI & SMI of Quadrant without Barrier.

Table 9.2: TMI & SMI of Quadrant without Barrier Results.

Imaging System / Mask	SNR	CNR	Edge Response
Flying Spot System	62.3	44.6	0.10 ± 0.01
19 MURA NTHT	51.8	51.2	0.30 ± 0.01
2 mm Pinhole	45.4	44.2	0.22 ± 0.01

(a) Flying Spot System
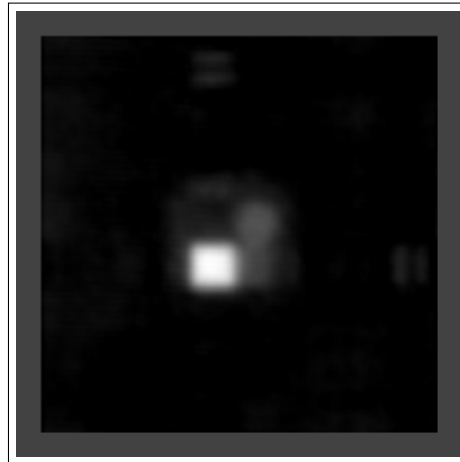
(b) 2 mm Pinhole

(c) 19 MURA NTHT

Figure 9.4: TMI & SMI of Quadrant with 3 mm Polypropylene Barrier.

Table 9.3: TMI & SMI of Quadrant with 3 mm Polypropylene Barrier Results.

Imaging System / Mask	SNR	CNR	Edge Response
19 MURA NTHT	42.1	41.5	0.31 ± 0.01
2 mm Pinhole	36.4	35.4	0.22 ± 0.01
Flying Spot System	31.9	22.7	0.13 ± 0.01

(a) Flying Spot System

(b) 2 mm Pinhole

(c) 19 MURA NTHT

Figure 9.5: TMI & SMI of Quadrant with 2 mm Aluminium Barrier.

Table 9.4: TMI & SMI of Quadrant with 2 mm Aluminium Barrier Results.

Imaging System / Mask	SNR	CNR	Edge Response
19 MURA NTHT	29.5	28.5	0.32 ± 0.01
2 mm Pinhole	22.9	22.0	0.27 ± 0.01
Flying Spot System	22.8	13.0	0.13 ± 0.01

(a) Flying Spot System

(b) Pinhole

(c) Coded Mask

Figure 9.6: TMI & SMI of Quadrant with 4 mm Aluminium Barrier.

Table 9.5: TMI & SMI of Quadrant with 4 mm Aluminium Barrier Results.

Imaging System / Mask	SNR	CNR	Edge Response
19 MURA NTHT	16.7	16.2	0.39 ± 0.01
2 mm Pinhole	14.7	14.0	0.37 ± 0.01
Flying Spot	12.6	5.9	0.20 ± 0.01

9.2 Experimental Settings 2: Constant Resolution

An additional experiment was conducted with emphasis placed on matching the projected X-ray spot size from the flying spot system to the aperture size of the CMI system at Cranfield University. Where the aperture size of a pinhole or coded mask determined the resolution of an image, the projected X-ray spot size governs resolution for the flying spot. The projected spot size was related to the distance of the object from the flying spot and was calculated by James Kirk and provided by David Lockley at dstl (personal communication, 27 March 2017). In addition, the X-ray beam collimator size played a role in the projected spot size. The smallest reasonable spot size that could be achieved for this experiment was 3 mm at a projection distance of 210 mm. Consequently, 3 mm aperture masks were fabricated for the XBI system at Cranfield University with considerations made for the effects of collimation in Chapter. 3.2.1 (see Table. 9.6 for experimental parameters).

Table 9.6: Experimental Settings 2: Constant Resolution

		FSS	Pinhole	CM
Object	Object to Mask (m)	N/A	0.21	0.21
	Object to Detector (m)	0.21	N/A	N/A
X-Ray	Power (W)	300	300	300
	Voltage (kV)	70	70	70
	Current (mA)	4.28	4.28	4.28
	Focal Spot to Collimator (mm)	152	60	60
	Collimator ϕ Size (mm)	0.7	N/A	N/A
	Projected Spot Size ϕ (mm)	3	N/A	N/A
Detector	Active Area ϕ (mm)	N/A	115	115
Mask	MTA Mask	N/A	-	13 MURA NTHT
	Thickness (mm)	N/A	1	1
	Smallest Aperture Size (mm)	N/A	3	3
Exposure	Total Exposure Time (s)	70	100	2

Imaging at such close range increased near-field magnification and decreased FOV of the scene. Therefore, the quadrant was inadequate for this experiment due to being too large to image at such close range. As a result, the smaller WWB object was used in replacement of the quadrant. To conduct the experiment at Cranfield University, the X-ray source had to be placed at an extreme angle next to the camera to illuminate the scene (as seen in Figure. 9.7). Consequently, parts of the camera obstructed a portion of the X-ray cone, casting a shadow of the camera component onto the scene (Indicated by

the red arrow in Figure. 9.7). The shadow was detected and visible in some of the pinhole exposures. All images for the experiment are presented in Fig. 9.8 to 9.11 which were quantified in Table. 9.7 to 9.10.

Figure 9.7: Issues with XBI Sytem Setup.
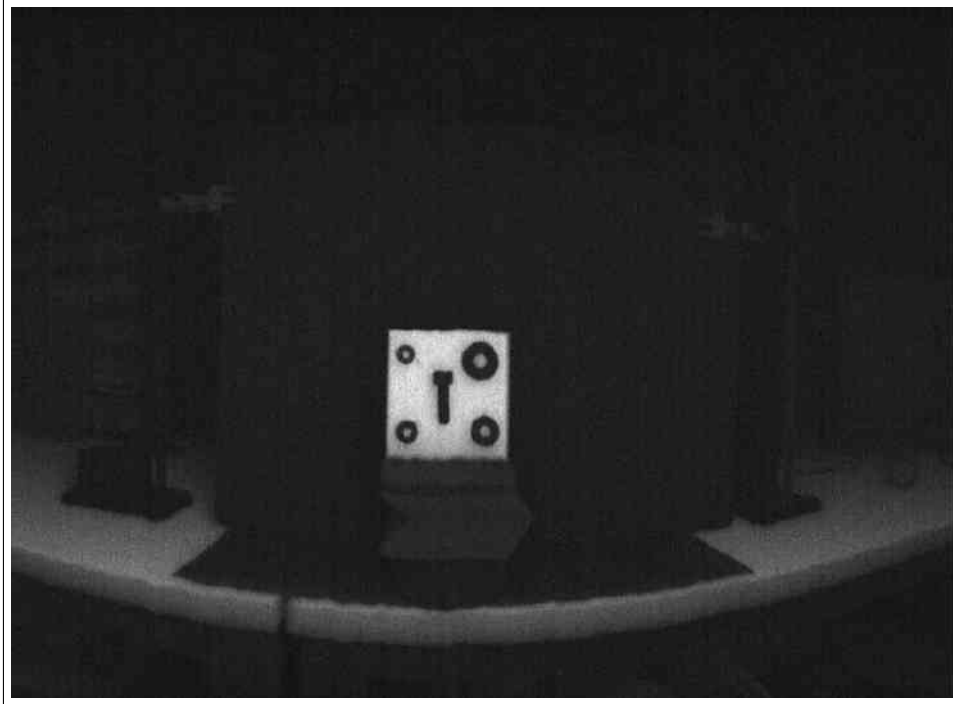
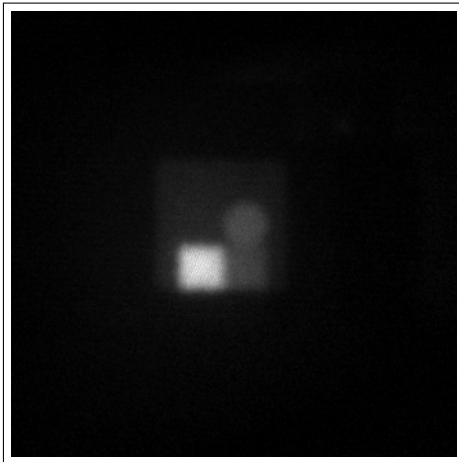(a) Flying Spot System
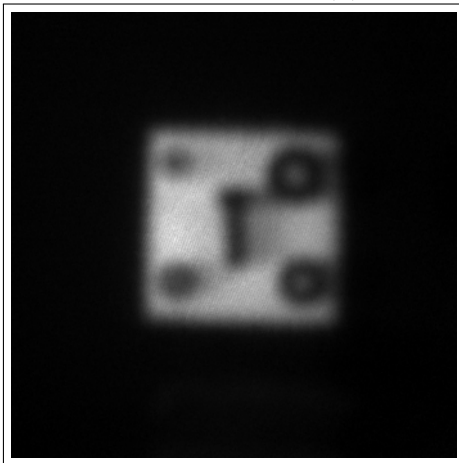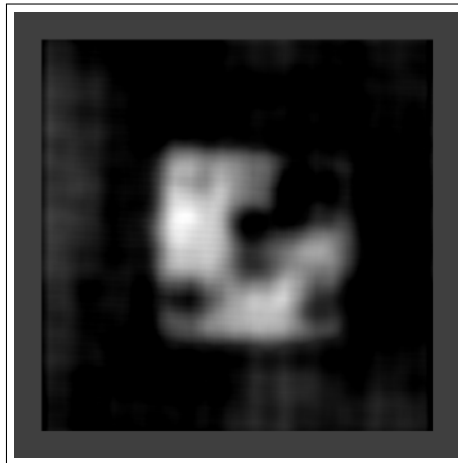
(b) 3 mm Pinhole

(c) 13 MURA NTHT

Figure 9.8: TMI & SMI of WWB without Barrier

Table 9.7: TMI & SMI of WWB without Barrier Results.

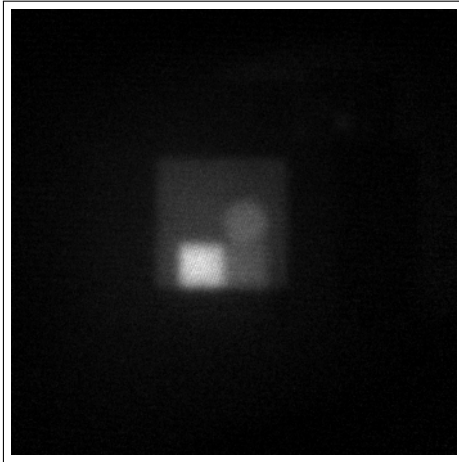| Imaging System / Mask	SNR	CNR	Edge Response
Flying Spot System	39.2	17.1	0.10 ± 0.01
3 mm Pinhole	32.9	31.7	0.12 ± 0.01
13 MURA NTHT	7.7	6.9	0.13 ± 0.01
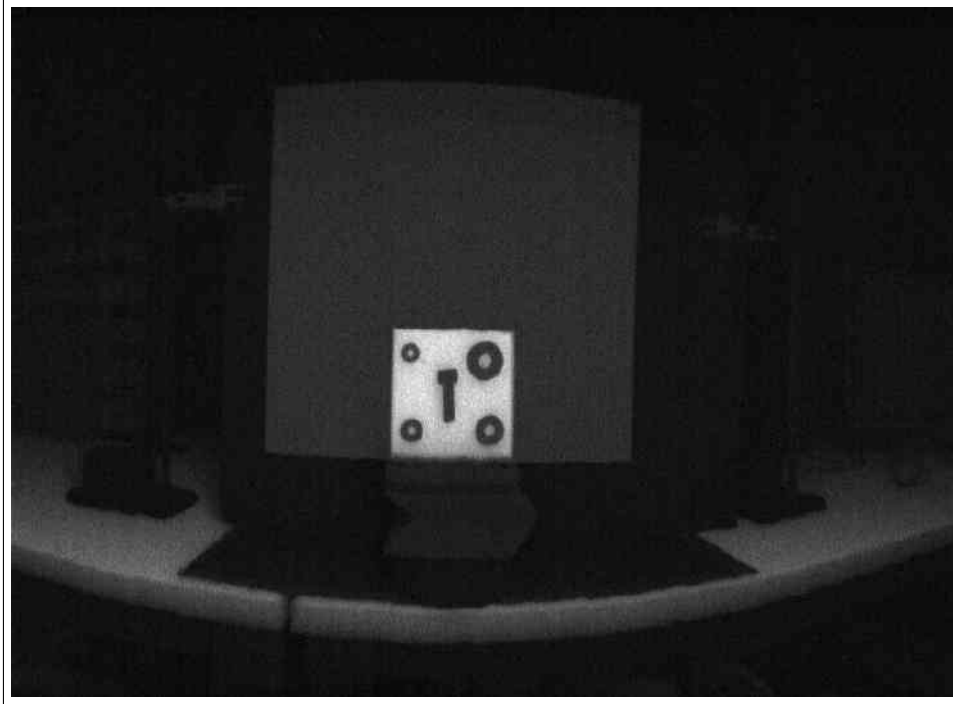
(a) Flying Spot System
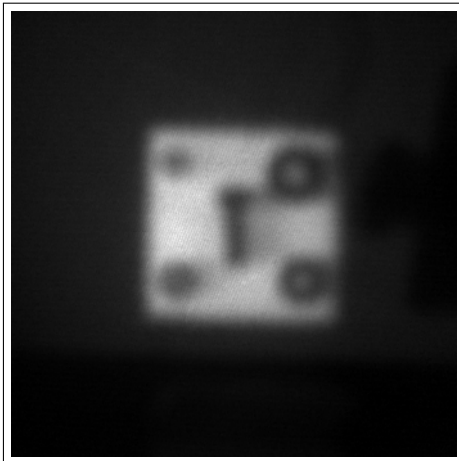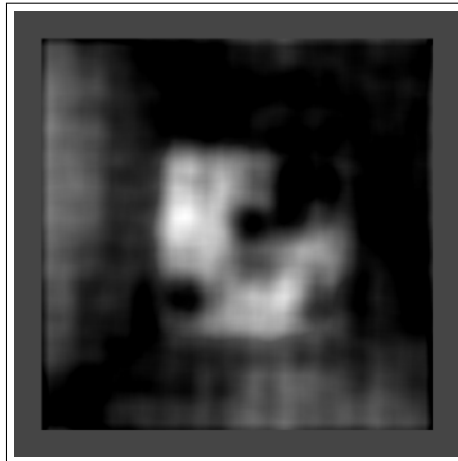
(b) 3 mm Pinhole

(c) 13 MURA NTHT

Figure 9.9: TMI & SMI of WWB with 3 mm Polypropylene Barrier

Table 9.8: TMI & SMI of WWB with 3 mm Polypropylene Barrier Results.

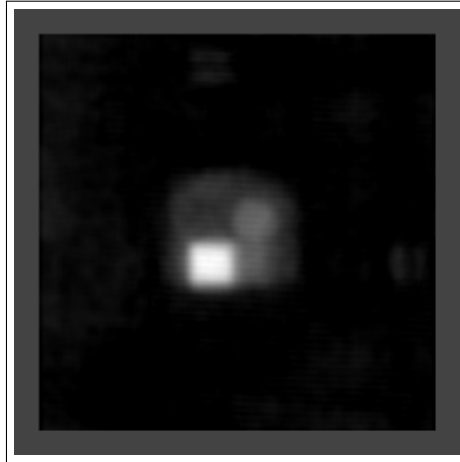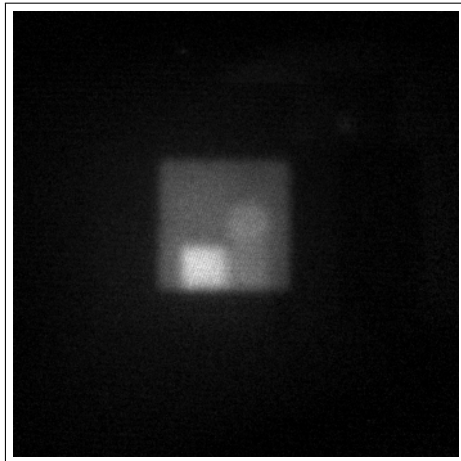| Imaging System / Mask	SNR	CNR	Edge Response
Flying Spot System	16.0	11.9	0.11 ± 0.01
3 mm Pinhole	13.2	11.7	0.18 ± 0.01
13 MURA NTHT	3.4	2.4	0.19 ± 0.01
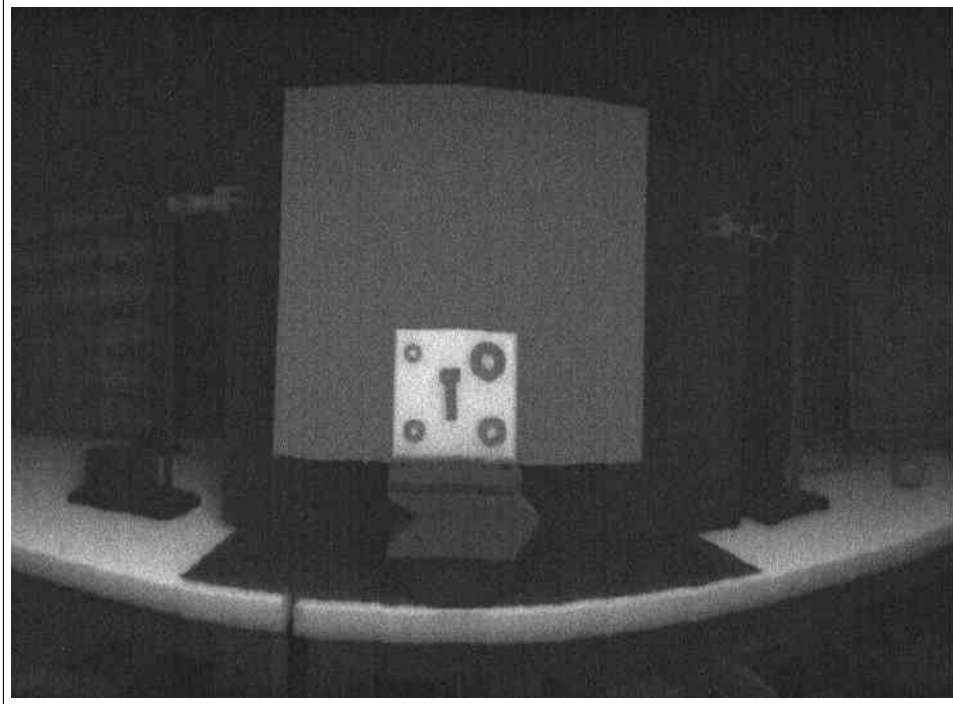
(a) Flying Spot System
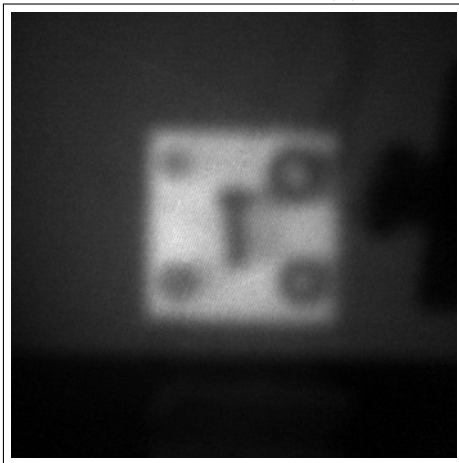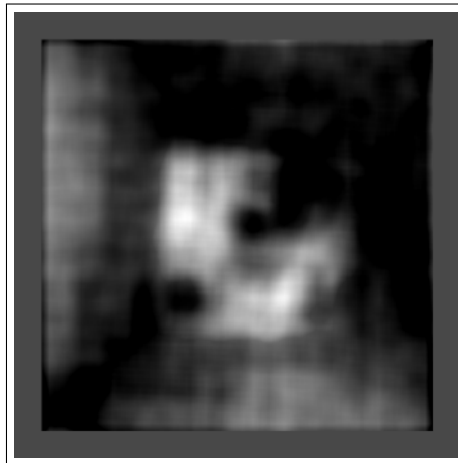
(b) 3 mm Pinhole

(c) 13 MURA NTHT

Figure 9.10: TMI & SMI of WWB with 2 mm Aluminium Barrier

Table 9.9: TMI & SMI of WWB with 2 mm Aluminium Barrier Results.

Imaging System / Mask	SNR	CNR	Edge Response
Flying Spot System	9.4	5.2	0.12 ± 0.01
3 mm Pinhole	8.5	6.9	0.16 ± 0.01
13 MURA NTHT	2.8	1.8	0.18 ± 0.01
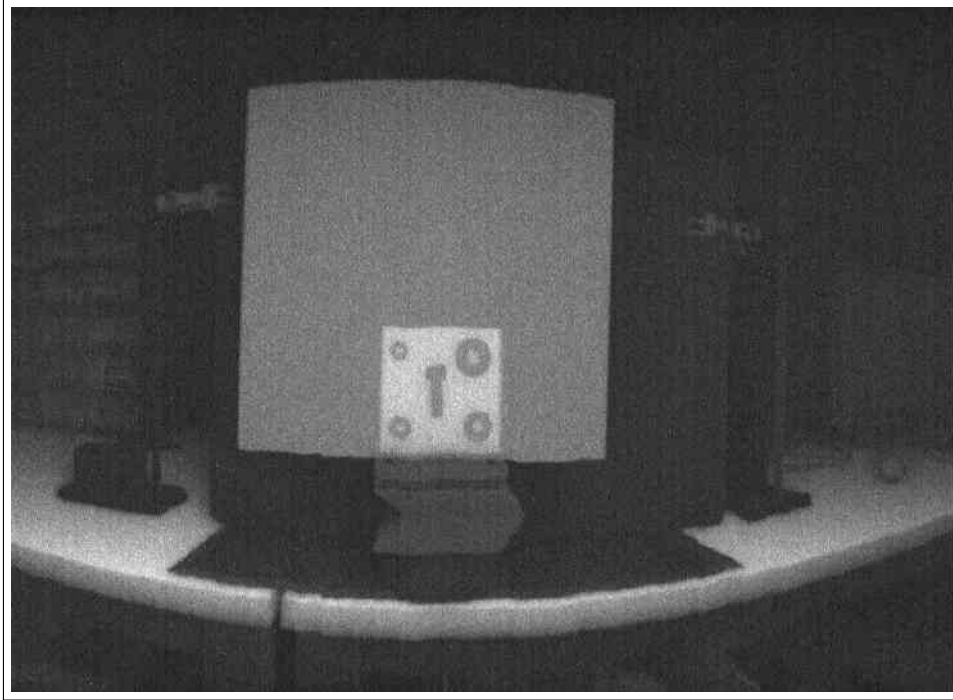
(a) Flying Spot System
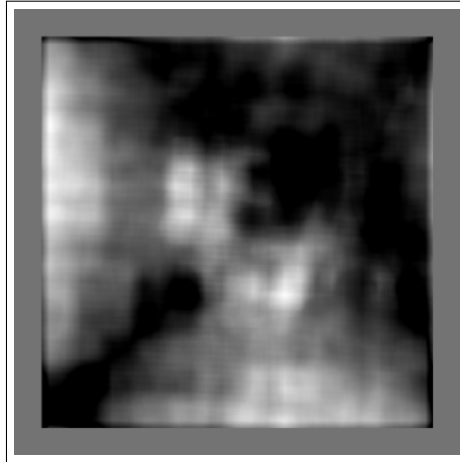
(b) 3 mm Pinhole

(c) 13 MURA NTHT

Figure 9.11: TMI & SMI of WWB with 4 mm Aluminium Barrier

Table 9.10: TMI & SMI of WWB with 4 mm Aluminium Barrier Results.

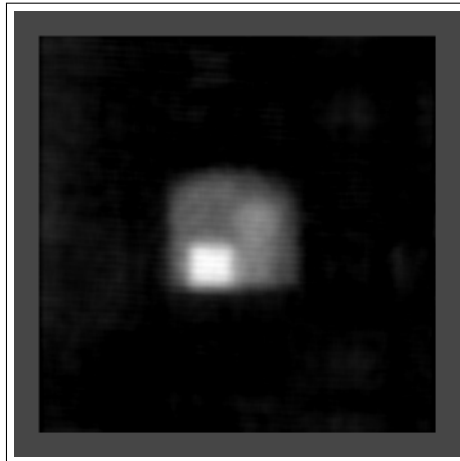| Imaging System / Mask	SNR	CNR	Edge Response
Flying Spot System	5.6	2.2	0.13 ± 0.01
3 mm Pinhole	5.2	3.6	0.16 ± 0.01
13 MURA NTHT	1.7	0.5	N/A

9.3 Discussion

The expected features from the quadrant in both SMI and TMI system exposures were resolved as expected. Exposures were quantified concerning SNR and CNR, with the flying spot system outperforming the SMI system when no barriers or shielding was used. However, images from the flying spot were subject to barrel distortion. The 19 MURA NTHT and 2 mm pinhole mask images ranked 2nd and 3rd for both SNR and CNR. The introduction of barriers in front of the quadrant changed the dynamics of both SNR and CNR, which saw the 19 MURA NTHT ranking first, followed by the 2 mm pinhole and then the flying spot system. Note, the X-ray source was collimated to illuminate only the object in interest (which was the quadrant). This was to reduce scatter, which had greater effects on coded mask imaging. Due to source collimation, parts of the square barrier were not illuminated in Fig. 9.4c, 9.5c and 9.6c and can be seen with the top rounded edges of the barrier.

Imaging the WWB object in the second experiment proved challenging due to the experimental setup. Consequently, the WWB object was only partially resolved for the 13 MURA NTHT and may be a result of PCFOV occurring from exposing the scene at such close distances (see Fig. 9.8, 9.9, 9.10 and 9.11). Additionally, resolution decreased with an increase in the barrier density for the 13 MURA NTHT. Although the signal from the WWB object was generally resolved, a shadow from parts of the camera was present in the pinhole images and would undoubtedly have an impact on SNR and CNR values. Also, the X-ray source could not be collimated due to the experimental setup and extreme angle of the X-ray generator. Nonetheless, the TMI system outperformed the SMI system with the 3 mm pinhole and 13 MURA NTHT ranking behind for both SNR and CNR. For resolution of both experiments the normalised edge response was taken by dividing the edge of the object by its entire width. Consequently, this is why the edge response values were dimensionless. This was performed because the images had different pixel resolutions which would result in an unfair comparison. The overall trend saw the flying spot system ranking the highest followed by the pinhole then CM. The associated error with the edge response was calculated from the error propagation. Note, the edge response for the 13 MURA in Fig. 9.11 was not calculated due to poor resolution of the object.

Eight sets of X-ray backscatter images were presented in Fig. 9.3 to 9.6 and Fig. 9.8 to 9.11. The corresponding SNR and CNR values for each image were ranked in Table. 9.2 to 9.5 and Table. 9.7 to 9.10. Each position in the table would score points for the flying spot system, CM and pinhole exposures; with a first-place position scoring 3 points and last receiving only one point. The overall score was out of a total of $3 \times 8 = 24$ points. Their final scores are presented in Table. 9.11 - 9.13. Note, the results in Table. 9.13 are out

of 21 as the last CM image could not be resolved in Fig. 9.11. Although the flying spot system produced good overall SNR and spatial resolution, images often were subject to barrel distortion and displayed a relatively inaccurate representation of the scene. For CNR, the pinhole mask outperformed all others followed by the CM.

Table 9.11: SNR Scores from the TMI & SMI Experiments.

Imaging System / Mask	Score out of 24
Flying Spot System	18/24
Pinhole	15/24
CM	15/24

Table 9.12: CNR Scores from the TMI & SMI Experiments.

Imaging System / Mask	Score out of 24
Pinhole	18/24
CM	16/24
Flying Spot System	14/24

Table 9.13: Resolution Scores from the TMI & SMI Experiments.

Imaging System / Mask	Score out of 21
Flying Spot System	21/21
Pinhole	14/21
CM	7/21

Chapter 10

Decoding with Blind Deconvolution

Previous chapters have introduced image decoding techniques via correlation and convolution with a kernel, template or decoding array. Image quality is partially determined by the PSF of the encoding array. Image degradation can occur from many factors such as atmospheric turbulence, camera or object motion and by other means. The degree by which the image is degraded may be to an extent where the object is unrecognisable. Blind deconvolution (BD) is an alternative decoding algorithm used to de-blur degraded images with initial information of the encoding array. Using an iterative approach the algorithm converges towards the maximum likelihood of the images accurate representation of the original scene (Biggs and Andrews, 1997; Fish et al., 1995; Lucy, 1974; Richardson, 1972) Sambo (2011, p. 64). The MATLAB 'deconvblind' function was used to reconstruct encoded CM exposures presented in this thesis. The decoding arrays $\dot{G}$ was imported into the function as the kernel[1], along with the encoded image to yield the final reconstructed image via BD (R^τ) with τ iterations. The optimum iteration for decoded exposures of the quadrant presented earlier was determined by taking the SNR at each τ as a positive integer. It was found that the highest SNR values were at $\tau = 30$ for each CM. All BD images presented in this thesis were summed (S_n^τ), as in Eq. 10.1, where n indicates the number of decoded exposures or terms.

$$S_n^\tau = R^\tau + \sum_{i=2}^{n} R_i^\tau \qquad (10.1)$$

$$= R^\tau + R_2^\tau + R_3^\tau + R_4^\tau + ... R_n^\tau$$

10.1 CMs of Difference Open Fractions

The encoded exposures used to reconstruct images via cross-correlation in Chapter. 8.2 were decoded in this chapter using BD and are presented in Fig. 10.1 and 10.2. Concerning the PLA/TEC 'URA' like CMs, SNR and CNR results from the 19 MURA were superior to all other low open fraction CMs; followed by the 26 BR, 17×21 Singer and 13 DURA (see Table. 10.1). Images from the low open fraction CMs were subject to a mere increase in noise with the signal appearing fainter than those from their correlated counterparts. Nonetheless, the expected signal from the quadrant were visible in all images.

Similarly, when comparing both BD images with low open fraction random arrays, the trend remained the same as their correlated counterpart. Namely,

---

[1]Referred to as the initial PSF in MATLAB

156

the 19 RANDA$^\alpha$ outperformed the 19 RANDA$^\beta$ with regards to SNR and CNR. Again, the results were lower for BD for this experiment.

19 MURA, $\chi = 0.50$	13 DURA, $\chi = 0.40$
17×21 Singer, $\chi = 0.34$	26 BR, $\chi = 0.25$
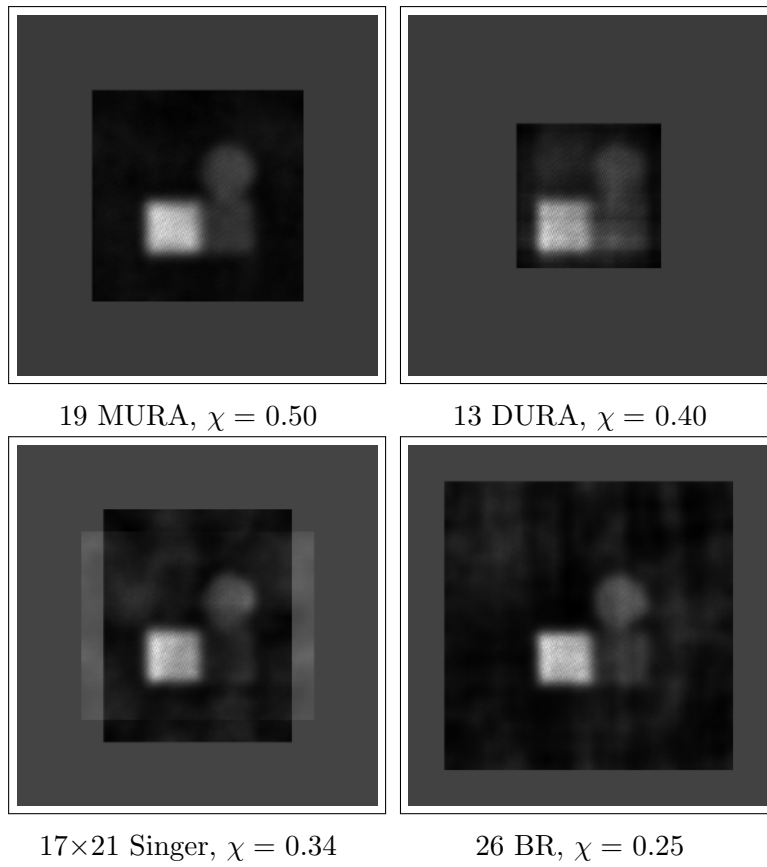
Figure 10.1: LOF 'URA' CM Images decoded via BD.

19 RANDA$^\alpha$, $\chi = 0.32$	19 RANDA$^\beta$, $\chi = 0.50$
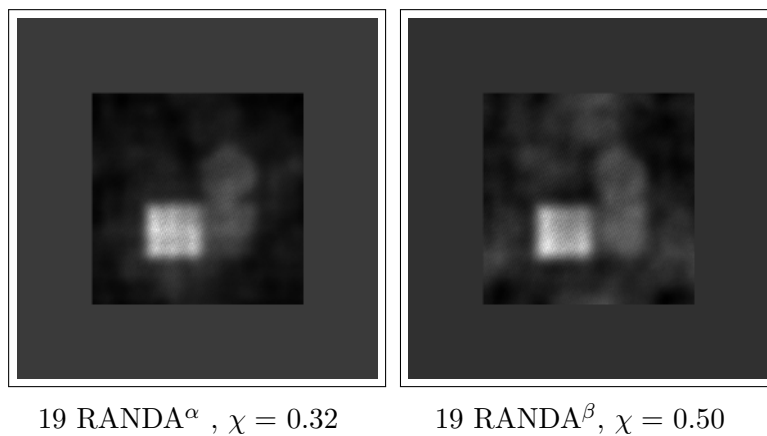
Figure 10.2: LOF RANDA CM Images decoded via BD.

Table 10.1: LOF 'URA' CM Images decoded via BD Results.

Coded Mask	χ	SNR	CNR
19 MURA	0.50	54.1	45.1
26 BR	0.25	22.7	19.9
17×21 Singer	0.34	19.2	16.4
13 DURA	0.40	13.5	11.8

Table 10.2: LOF RANDA CM Images decoded via BD.

Coded Mask	χ	SNR	CNR
19 RANDA$^{\alpha}$	0.32	18.6	16.0
19 RANDA$^{\beta}$	0.50	13.2	9.6

10.2 Comparison of PLA/TEC and MTA CMs

Encoded exposures used to reconstructed images in Chapter. 8.3, were decoded via blind deconvolution and presented in this chapter. The overall objectives were set out to determine the performance of PLA/TEC CMs with their MTA NTHT versions. From studying reconstructed BD images found in Fig. 10.3, it was clear that a small increase in noise and a decrease in signal strength was present; compared to images that were cross-correlated. Nevertheless, signals from the aluminium part of the quadrant was resolved in the final images. SNR and CNR results confirmed the PLA/TEC 19 MURA as the superior mask for imaging the quadrant when decoded via BD (see Table. 10.3). Otherwise, MTA NTHTs outperformed their PLA/TEC counterpart CMs.

10.3 Discussion

The overall results when comparing the SNR and CNR for all correlated and BD images from CMs used in this thesis are presented in Table. 10.4. It is clear that the 3D printed PLA/TEC 19 MURA was superior to other CMs in performance when its exposures were decoded via cross-correlation. Subsequent performers within the top five were the (1) MTA 13 DURA NTHT via $\otimes$, (2) PLA/TEC 19 MURA via BD, (3) PLA/TEC 26 BR via $\otimes$ and (4) MTA 19 MURA NTHT via BD. (5) the PLA/TEC 19 RANDA$^{\beta}$ decoded using both cross-correlation and blind deconvolution ranked last in the table.

As all CMs resolved the signal from expected parts of the quadrant in the experiment via BD. A similar experiment quantifying resolution of images of

PLA/TEC   **MTA**

19 MURA   19 MURA NTHT

13 DURA   13 DURA NTHT

19 RANDA$^\alpha$ 19 RANDA$^\alpha$ NTHT

17×21 Singer   17×21 Singer NTHT
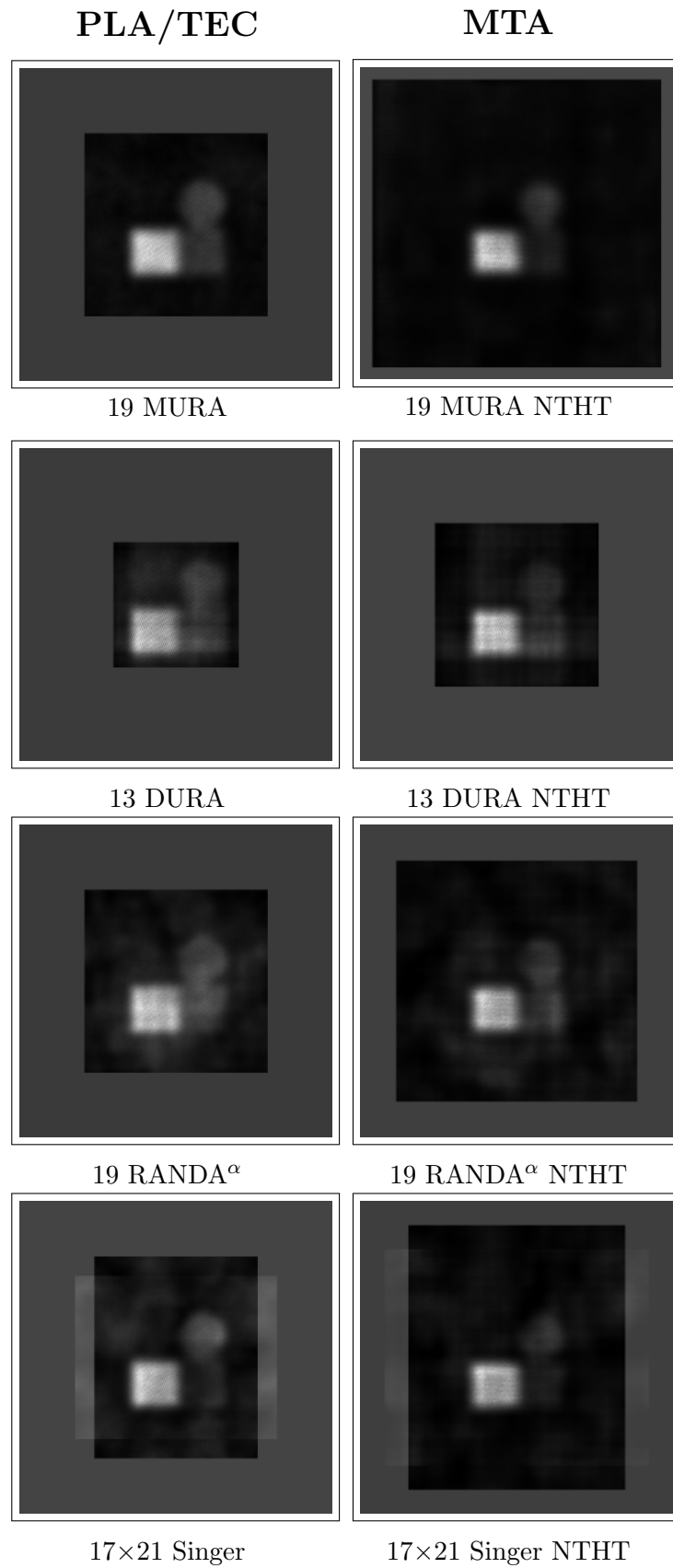
Figure 10.3: Comparing 3D Printed and MTA CMs decoded via BD.

Table 10.3: Comparing 3D Printed and MTA CMs decoded via BD Results.

Coded Mask	Material	SNR	CNR
19 MURA	PLA/TEC	45.1	45.2
19 MURA NTHT	MTA	44.0	44.6
17×21 Singer NTHT	MTA	25.3	23.2
13 DURA NTHT	MTA	22.5	21.1
19 RANDA$^\alpha$ NTHT	MTA	22.0	20.2
17×21 Singer	PLA/TEC	19.2	16.4
19 RANDA$^\alpha$	PLA/TEC	18.6	16.0
13 DURA	PLA/TEC	13.5	11.8

the Al line pair object was conducted, as in Fig. 8.6.

Table 10.4: Summary of SNR and CNR using Cross-Correlation and BD.

Coded Mask	Decoding	Material	SNR	CNR
19 MURA	$\otimes$	PLA/TEC	64.2	63.6
13 DURA NTHT	$\otimes$	MTA	54.0	53.6
19 MURA	BD	PLA/TEC	45.1	45.2
26 BR	$\otimes$	PLA/TEC	44.5	44.0
19 MURA NTHT	BD	MTA	44.0	44.6
13 DURA	$\otimes$	PLA/TEC	39.7	39.4
19 MURA NTHT	$\otimes$	MTA	34.6	33.7
17×21 Singer NTHT	BD	MTA	25.3	23.2
26 BR	BD	PLA/TEC	22.7	19.9
13 DURA NTHT	BD	MTA	22.5	21.1
19 RANDA$^\alpha$ NTHT	BD	MTA	22.0	20.2
17×21 Singer	BD	PLA/TEC	19.2	16.4
19 RANDA$^\alpha$	BD	PLA/TEC	18.6	16.0
17×21 Singer NTHT	$\otimes$	MTA	18.0	16.9
19 RANDA$^\alpha$	$\otimes$	PLA/TEC	17.1	16.7
19 RANDA$^\alpha$ NTHT	$\otimes$	MTA	16.9	16.4
17×21 Singer	$\otimes$	PLA/TEC	14.4	13.5
13 DURA	BD	PLA/TEC	13.5	11.8
19 RANDA$^\beta$	BD	PLA/TEC	13.2	9.6
19 RANDA$^\beta$	$\otimes$	PLA/TEC	9.6	8.8

However, when decoding images via BD for the line pair object it failed to resolve the imaging scene, even when using the optimum iteration of 30 along with other values. Consequently, it was concluded that image reconstruction via blind deconvolution is not a viable option for all scenes.

Chapter 11

Discussion

The X-ray backscatter imaging system constructed at Cranfield University had its limitations due to a number of reasons. This began with the limited FOV of the projected X-ray cone at 40°, illuminating only a small region at the maximum distance between the generator and the concrete wall. This prohibited the experimental conditions required to test the theoretical groundwork on aperture collimation as presented in Chapter. 3.2.1. Additionally, placing the X-ray generator further back on the optical bench resulted in the radiation cone clipping the edge of the bench. The photon sensitive camera also had limited factors which included a low-resolution detector. Subsequently, this placed restrictions on the final image quality. Also, the detector had a defect in the form of hot pixels in the top right-hand corner of the sensor resulting in all images being cropped to remove any artefacts. It is difficult to conclude from images taken with the XBI at Cranfield University because the factors above are only limited to this system. The question then would arise; what would be the outcome if the detector was replaced with one having higher spatial resolution and free of defects. Also, if the imaging system was not enclosed in a radiation cell and placed in a more open environment with less scatter from the immediate surroundings, how would the CMI and pinhole images be affected.

Fabricating hot cast CMs proved challenging throughout the 3D printing and casting process. This was because higher temperatures were required for printing and casting. It was sometimes found to be problematic when printing with ABS that demanded more attention than PLA. For example, adhering the print filament to the build plate was often tricky with the Ultimaker 2 Extended© 3D printer. Casting was also problematic and time-consuming because considerable time was necessary to melt the alloy, even when the correct temperature and settings were applied. Pouring the molten alloy mixture in the mould was an issue, due to the rapid cooling of the alloy during the pouring process. Overall, finish quality of the ABS print was inferior to that of PLA. Additionally, metallic elements became loose within the CM mould from the lack of adhesion (see Fig. 4.3). Subsequently, the problems faced above rendered cold casting to be the way forward. The cold casting process with PLA/TEC proved to be an easier alternative to manufacturing CMs via 3D printing and in general. Fewer risks were involved with higher quality yields. Fabricating 3D printed PLA/TEC CMs presented an economical option with the material cost of creating one MTA CM producing two to three 3D printed CMs. Besides, manufacturing can take place with off the shelf equipment, whereas MTA CMs require specialist equipment and the need for computer numeric control (CNC) operators for the production process.

The disadvantages of 3D printed PLA/TEC CMs included air pockets introduced into the mask. It was found that there was a rise in air pockets with increasing densities of the mixture (see Chapter. 4.4). Higher densities required more viscous TEC mixtures. When mixing the TEC, air pockets were

introduced which was less likely to escape with greater viscosity. Spin casting or casting in a vacuum would alleviate air pockets; however, this was not available. As a result, lower casting densities of 9.6 g cm^{-3} were chosen for the 3D printed PLA/TEC which was still more significant than that of hot cast CMs of 8.6 g cm^{-3}. Print quality was compromised when 3D printing CMs with smaller elements, resulting in the introduction of errors during the image decoding process. Solutions to this problem include choosing arrays with decreasing elements, avoid scaling the array down or using 3D printers with superior resolution (Munoz et al., 2017b; Muñoz et al., 2018b). Lastly, one must consider the contribution of internal X-ray scatter from the low Z 3D print PLA material and TEC. However, the overall, SNR results from Chapter. 8.3 did not show a clear trend of MTA NTHT CMs dominating over PLA/TECs which would render scatter in this case to be negligible.

2D arrays were calculated, addressing limitations in the number of LOF arrays in CMI (Muñoz et al., 2018a). Beginning with the DURA, 15 LOF arrays were presented along with details on their construction methods. Claims have been previously reported on arrays with 'URA' like imaging properties (Busboom et al., 1998) (see Chapter. 6). However, in reality, their PSFs were visually similar to that of a random array with examples including the Singer and biquadratic residue array (see Chapter. 2.2.3). PSFs of MURAs revealed a plateau and side-lobes that were completely flat and equal to zero. Although the PSFs of BRs and Singers were rather good, their side-lobes and plateau were not equal to zero. Any pattern with side-lobes not equalling to zero will result in a compromise in image quality. To the contrary, even though the PSFs of a DURA contained raised side-lobes the plateau was flat and equal to zero (see Chapter. 2.2.3 for examples). Consequently, other than the NRA and PNP, the DURA was the closest array to a URA than other patterns. Besides, the spacing of open elements within DURAs are uniformly redundant which supports their relationship to the URA. Conversely, other array spacings such as the BR and Singer are not uniformly redundant. Nonetheless, a common trait between the BR, Singer and MURA is that they are from the cyclic difference set family. The exact mathematical method of calculating the 1D sequence that form 2D DURAs from Barker codes has not been published. However, it is assumed that they too are part of the family of cyclic different sets. Possible clues may lay within the 23 MURA when its pattern is divided into four quarters, demonstrating a significant similarity to the 13 DURA (see Fig. 11.1).

(M)URA sizes and open fractions are easily identified by their vectors which are based on a prime number, with $\chi = 0.5$ for all patterns. The exact open fraction and vector size of every possible Singer and BR arrays are not known without prior calculation, as presented in Chapter. 2.2.3.7. Only a few arrays have been previously published elsewhere (Busboom et al., 1998; Shutler et al., 2013; In 't Zand et al., 1994), but an exhaustive catalogue of arrays is yet

(a) 13 DURA.   (b) 23 MURA.
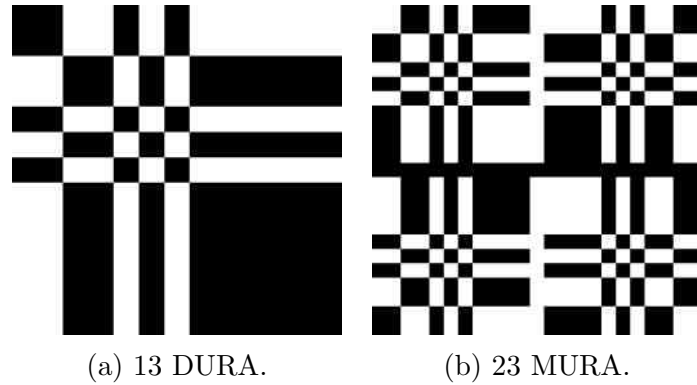
Figure 11.1: 13 DURA Features in the 23 MURA: There is a resemblance of the DURA in (a) with the four prominent features in the (b) invariant MURA pattern.

to be presented and published. The author partially achieved this goal by calculating and publishing 79 previously unreported Singers of $\chi < 0.5$ in (Muñoz et al., 2018a). Most would not be considered practical for imaging due to their extreme dimension deviating from perfectly square aspect ratios, although it is considered that they could find applications where specialised fan beam optics are used. That is to say, the dimensions for most imaging detectors adhere to the aspect ratios of 1:1, 3:2, 4:3, 16:9 and so on, so an array of 12×91 is impractical. Singer array vectors have been known to be based on co-prime numbers. Recent research found that strict co-prime rules were not fundamentally necessary. As a result, 6 unreported square Singers along with those with vectors suitable for imaging (9 arrays) are presented in Appx. A. In addition, 11 unreported BRs suitable for imaging with $\chi = 0.25$ are presented in Appx. A.

Comparisons of X-ray backscatter images using CMs of various open fractions revealed superior imaging qualities from the 19 MURA over other $\chi < 0.5$ arrays. This was presented in Chapter. 8.2. Although attempts were made to standardise the CM size to enable cross comparison, it was impossible because of the limited number of vector sizes for some variations of CM patterns. The difference in array size and PSFs may have played a role in SNR and CNR values. Namely, decoded images containing the quadrant saw the signal being constant in size for all images, but the overall size of the background changed due to the varying FOVs (see Fig. 8.3 for example). However, different sizes in the background may have caused a change in values; affect the overall results. Additionally, Chapter. 8.4 confirms such effect. Thus, a second experiment with RANDAs containing similar vectors sizes and PSFs (see Fig. 8.4). Superior results were found with the RANDA at $\chi < 0.5$. Ideally, an experiment with more RANDA CMs of the same size and PSFs would increase the validity of the trend, but this was not possible due to time constraints and limited materials for manufacturing new CMs. Nonetheless, results from the RANDA at

$\chi < 0.5$ were still inferior when compared to the 19 MURA (see Table. 10.4).

11.1   Coded Mask Imaging & Post Processing

Test imaging objects such as the quadrant were well resolved when imaging with some CMs as shown in Fig. 8.5. Although other objects such as the Al lp were resolved, image quality and resolution were diminished, with an example given for the 19 MURA in Fig. 8.6. This was also the case for 'real world' objects which exhibited greater noise. An example would extend to the car door that formed a very complex scene with scattering probably coming from all parts of the scene. As a result, collimating the X-ray source was a fundamental necessity otherwise an image would not be resolved. Namely, only the region of interest within a scene should be illuminated for an image to be successfully decoded and reconstructed. This would be balanced of course for radiological safety. When decoding CM exposures, other factors must be taken into account to extract good images of a scene. This included using the correct scaling parameters and ensuring the cropped region of the CM encoded exposures was done correctly. Additionally, aligning the encoded exposure with the decoding array reduces the introduction of errors and examples of this can be found in Fig. 11.2. Fig. 11.2 (a) shows a perfect superimposition of the encoded and decoding array and (b-c) demonstrate poor alignment. Similarly, the projected shadow of a CM pattern that is poorly resolved will introduce errors when the images are reconstructed with its decoding array.

Decoding CM exposures via BD proved successful for the quadrant as found in Chapter. 10.1, which resolved signals there were found to be challenging when using cross-correlation. The issues faced with decoding via BD were difficulties in reconstructing many other scenes at the optimum iteration and even with other values. Besides when SNR from CMs in Table. 10.4 were compared, 6/10 times cross-correlation yielded superior results. Hence CM imaging via cross-correlation would be the recommended method of decoding encoded exposures.SNR and CNR from the PLA/TEC 19 MURA outperformed all other CMs on numerous occasions. Performances from MTA and PLA/TEC were overall comparable as demonstrated in Table. 8.3. This was agreeable to results from Muñoz et al. (2018b). The order of results in Muñoz et al. (2018b) appears different due to experimental uncertainty and the different grey values of the reconstructed images.

Conducting experiments using the WWB object with the XBI system at Cranfield University to compare to that of the flying spot system at dstl's laboratory proved challenging. There was a compromise in CMI to accommodate settings that were similar to that of the flying spot system. Although both are X-ray backscatter imaging systems, they are completely different in the way they operate. For example, the resolution is partially determined by the aperture size
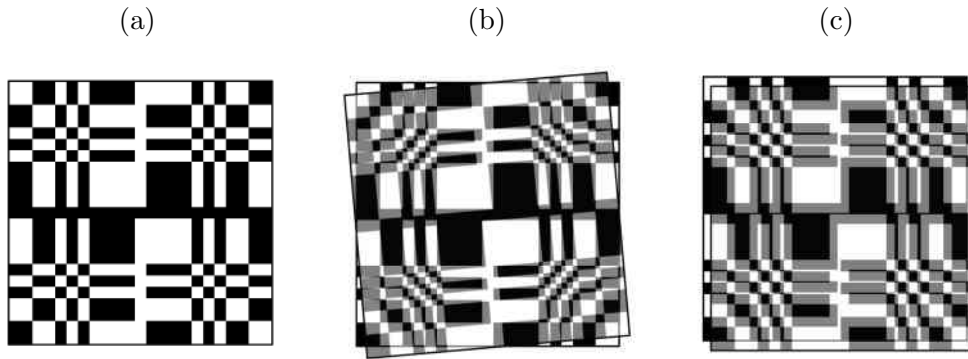
Figure 11.2: Decoding Alignment: (a) perfect superimposition of the encoded and decoding arrays. (b) and (c) demonstrates misalignment, which leads to errors in the decoding process.

for SMI, where it's the projected spot size for a flying spot system. Imaging at relatively close ranges was practical for TMI but not for CMI, due to PCFOV. In addition, it was sometimes required that the X-ray source was placed at extreme angles to project the radiation cone onto the targeted WWB object. Consequently, the radiation cone was obstructed by parts of the camera as shown in Figure. 9.7. When comparing TMI and SMI systems the flying spot system's X-ray potential energy output was limited to 70 kV and applications at higher voltages was not possible. Thus, it was difficult to determine how the system would perform at other voltages. Besides, the flying spot system was very large in size and it carried more weight; rendering it far less impractical for mobile applications. The XBI system at Cranfield University possessed greater mobility and would be the best-suited system to mount on a robotic mobile vehicle. The pinhole mask ranked second followed by the CM regarding SNR, CNR and spatial resolution. However, even though the pinhole mask images had slight advantages over those from the CM they were generally marginal and comparable. Nonetheless, the exposure times for CMs was significantly lower followed by the flying spot system and then the pinhole mask. CM exposure required collimation of the X-ray source to reduce the flux of radiation. Consequently, the CM would have the upper hand concerning radiation safety because the source would be collimated which minimises the radiation flux and exposures to radiation are short.

11.2 Image Quantification

The SNR and CNR values of images presented in this thesis were quantified using MATLAB to ensure consistency was upheld in the calculation process.

Nevertheless, the signal had to be cropped by eye for each image, introducing an uncertainty in the cropping process. There were occasions where determining the boundaries of the signal was challenging and would subsequently result in a small part of the background being included as signal. This was also true for the background of the image which would sometimes contain traces of the main signal. Image resolution had a role in this process which would see greater difficulties in distinguishing the signal from its background with exposures of lower quality.

Quantifying the spatial resolution of the images was sometimes challenging for both edge response and line pair method. Images within this thesis were of different sizes due to near-field magnification, variation in the CM's non-cyclic pattern size and exposures taken from different systems such as the flying spot. That is to say, images of the same scene would have different pixel densities and the edge response values, and the results would be meaningless. Therefore, the edge response was normalised by dividing the pixels that define the edge by the width of the object. X-ray backscatter Images in Fig. 8.6 where quantified using the line pair to determine their spatial resolution. It was difficult finding literature presenting techniques on quantifying the lines other than by eye. Thus, normalising edge response results were performed. However, this method may vary depending on the observer. A more effective way would be to classify a line pair in an image as resolved, where the space in between each pair has an intensity that is at least the half the maximum of the pair. So, only the first four pairs from left to right in Fig. 2.35 would be classed as resolved and then last two line pairs would be rendered unresolved. Nevertheless, a cross section of the line pair in Fig. 11.3 reveals the pixel intensity as plot, and none of the line pairs is resolved using the above due to poor contrast. However, line pairs can be resolved by eye. This was the case for the line pair exposures within this thesis, and subsequently, the only method of determining if a line pair was resolved was by eye.

11.3 Implications of Work

The research presented in this thesis may be used for multiple applications and can form the groundwork for continued research. All exposures presented earlier were not subject to any post-processing, enhancements or editing. Further image processing could see the improvement of image quality by removing the effects of barrel distortion, contrast enhancement and image de-blurring. Coded masks greatly increase the potential for imaging with short exposure times and this would be advantageous for scenes with moving objects, low X-rays and those where short exposures are imperative. Additionally, the prospects of XBI are vital for interrogating objects with limited access, short exposure times and overall would be useful for applications in defence and secu-

rity. The investigation into coded mask imaging in this project may have been limited by the factors mentioned above such as the low-resolution detector and the enclosed environment. Research into the experimental aspect of near-field X-ray backscatter CMI is limited, and there is an abundance of work found on the theoretical aspect of the topic. CMI has been applied to the medical sector and still yields potential for imaging X-rays and gamma rays. Examples of this are presented in Chapter. 7 with the possibilities of rapidly manufacturing CMs at lower costs in-house with off the shelve equipment. Also, the 3D printed MURA has demonstrated that better SNR is achieved by ideally retaining square elements of the mask, oppose to the traditional, complicated and more expensive NTHT version; which compromises imaging properties of the original CM pattern. Furthermore, CMI may have potential in industry for inspecting the internal structure of objects and other areas such as neutron detection and even panoramic imaging (Paradiso et al., 2017).
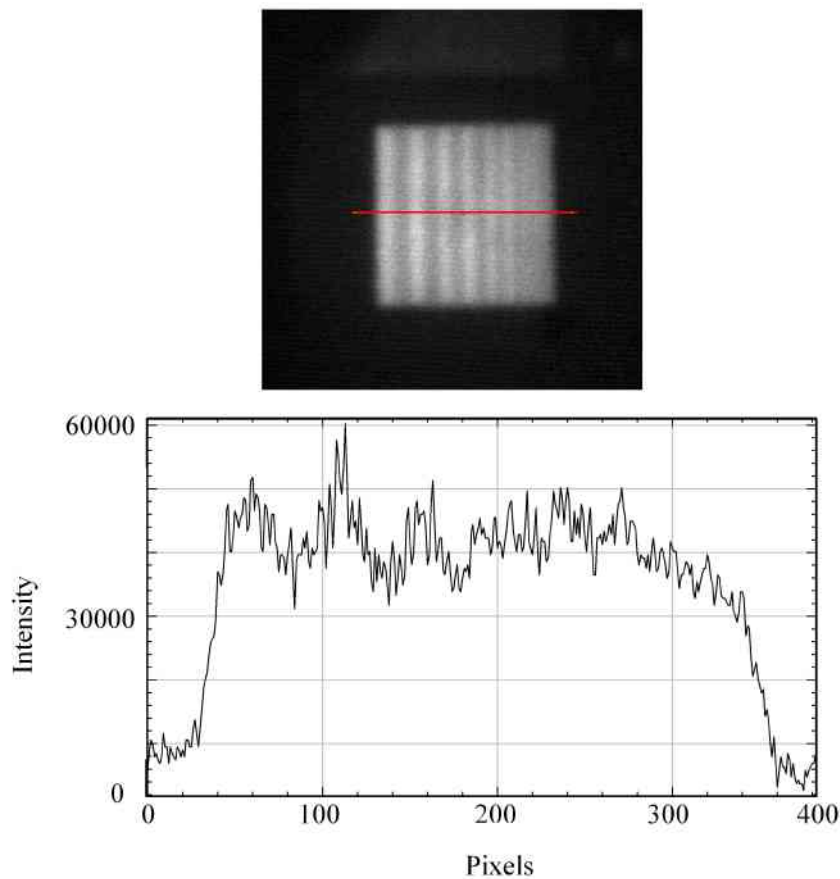

Figure 11.3: Line Pair Problem: Note how the line pair object in a real exposure is not clearly resolved as the theoretical version presented earlier in Fig. 2.35. Consequently, it renders difficulty in applying the Rayleigh criterion to determine if a line pair is resolved.

Chapter 12

Conclusion

The project began with the design and construction of an X-ray backscatter imaging system at Cranfield University to conduct various experiments. Novel methods of fabricating coded masks using 3D printing were introduced, along with manufacturing masks from MTA to use with the XBI system. Before the masks were made, investigations into the optimum mask thickness and aperture size of 2 mm for both were theoretically determined. Experimentally verifying the aperture at different positions within the mask revealed that the detectors view of a near-field imaging scene was relative and not exactly how previously reported in other literature.

12.1   Conclusion

A total of 111 low open fraction low open fraction arrays were calculated (including those published by the authour in Muñoz et al. (2018a)) and presented during the project. The overall number of arrays included 15 DURAs, 11 biquadratic residues, 6 square and 79 rectangular Singers. 32 of which would be classed suitable for imaging. The main objectives of the project were to investigate X-ray backscatter imaging using coded masks. A total of 11 CMs were made for the project and along the way, comparisons were made to pinhole masks and the flying spot system to determine its performance. It has been known for some time that the ability of coded masks to yield good quality images and short exposure times may be applied to medical radioactive isotope gamma-ray imaging. Chapter. 7 demonstrated such potential in medical applications, introducing a low-cost alternative solution and convenient manufacturing methods. The 3D printed PLA/TEC 19 MURA outperformed all other CMs when comparing multiple masks for radioactive isotope imaging.

The prospects of using coded masks for X-ray backscatter were found to be more complicated when applied to extended scenes. Although some imaging scenes such as the quadrant were well resolved when encoded exposures were decoded via cross-correlation others diminished in quality in terms of SNR and resolution . The Al lp object was an example of this. The same was true for decoding encoded exposures using blind deconvolution which had no overall benefits over cross-correlation. Investigations into the optimum CM for use with X-ray backscatter imaging at Cranfield University, revealed good quality images, regarding SNR and CNR deriving from the 3D printed PLA/TEC 19 MURA. The MTA 19 MURA NTHT ranked behind but was at the forefront for spatial resolution. Coded masks may have potential when imaging X-ray backscatter in other experimental set-ups, however, did not demonstrate consistency from scene to scene. Nevertheless, CMs are unmatched when it comes to shorter exposure times. Conversely, the 2 mm pinhole produced slightly better results than CMs for its SNR, CNR and spatial resolution. Overall, the best X-ray backscatter imaging results concerning SNR and spatial

resolution were from the flying spot system (see Fig. 12.1). Nonetheless, images were subject to barrel distortion. Comparing different imaging systems proved challenging as the parameters for CMI had to be compromised, and there are some aspects of the experiment that may have affected the overall results. Namely, such experiment resulted in a compromise in the settings for CM that were unfavourable. Firstly, the environment for both TMI and SMI were completely different with experiments conducted at Cranfield University in Shrivenham and Dstl at Fort Halstead. Consequently, different surroundings would have affected the way in which X-ray scattering occurred. Images from both TMI and SMI systems were different in grey scale and would have consequences in the final analysis. The difference in image quality changes with grey scaling and can be seen in a previous chapter. Secondly, although great care was taken to compare images from CMs of the same size, this was not entirely possible due to limitations in vector sizes. Subsequently, this may have had implications on the SNR and CNR with increasing object size as the background decreased. Nonetheless, the effects are probably negligible for smaller scenes and objects such as the quadrant. Lastly, it was found that coded mask images captured at Cranfield University required that the X-ray source to be collimated for most complex scenes to be resolved. All of the above factors must be born in mind when a conclusion is drawn in Fig. 12.1 and the fact that results may be specific to the experimental setup in this thesis.

Overall, even though the flying spot system produced good superior SNR and spatial resolution over those from the pinhole and CM, the pinhole mask displayed better results for CNR. Additionally, the flying spot system would probably be impractical for mobile applications, due to its size and weight. Additionally, the effects of barrel distortion were prominent. Results from CM images were overall comparable to the pinhole; however, the CM had a vast potential including significantly shorter exposure times than the other systems. In addition, it can be used for mobile applications as a result of being relatively smaller and lighter than the flying spot system. Research on experimental aspect of XBI with CMs is scarce. With the potential for short exposure time and good images, continued research could see an improvement in image quality that could be applied to numerous imaging technologies in the future.

12.2   Future Work

The ability to reconstruct coded mask X-ray backscatter images of a scene at Cranfield University was feasible with short exposure times. This thesis has begun bridging that gap between theoretical simulations and experiment by presenting a number of X-ray backscatter coded mask images. Although
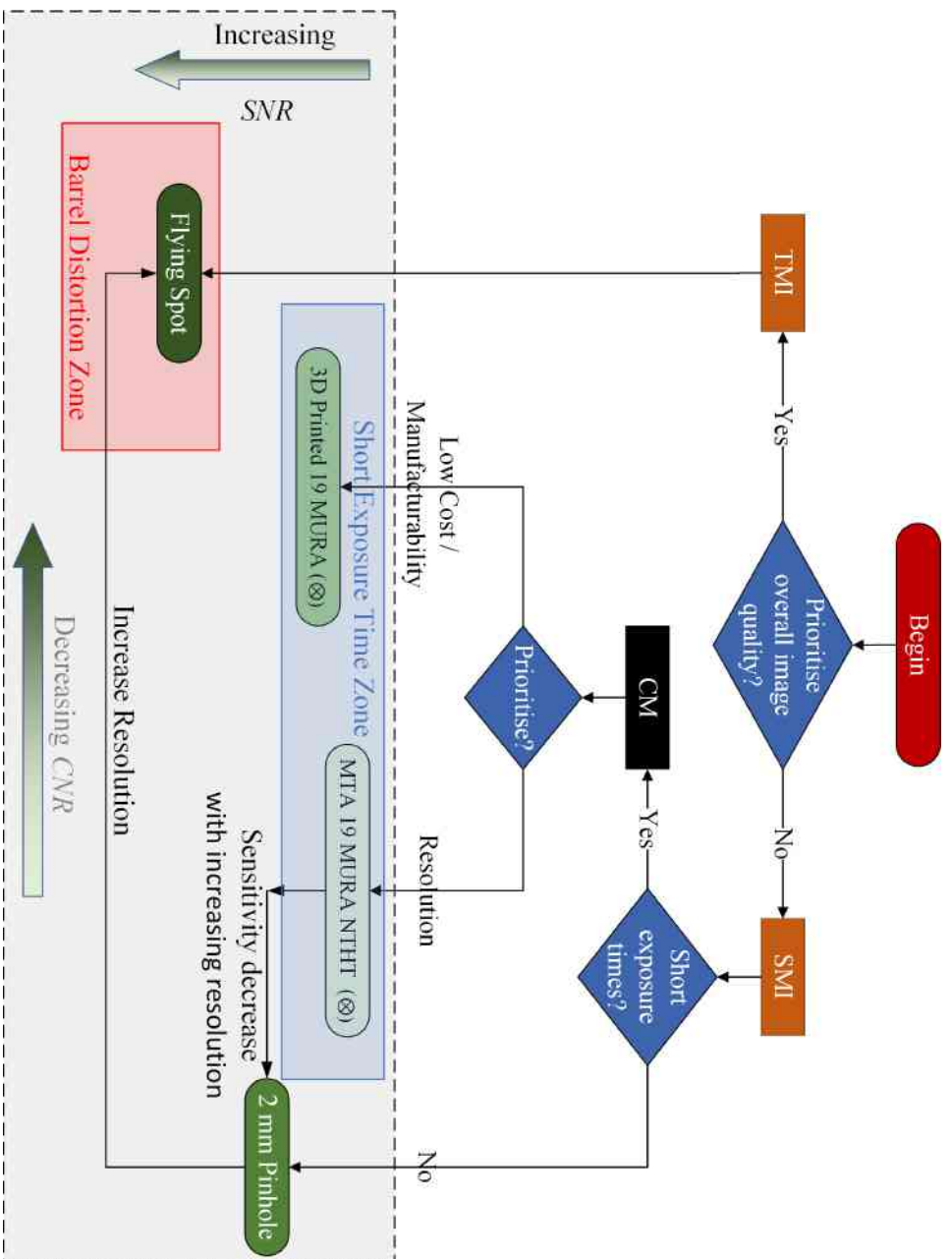
Figure 12.1: Summary of Optimal X-Ray Backscatter Systems: The diagram summarises the optimal XBI system for SNR, CNR, resolution and sensitivity.

172

the signal-to-noise and resolution of images were not as high as those from the flying spot system, the potential for further improvement may be possible. Future experiments are encouraged to conduct X-ray backscatter CMI in a less enclosed environment to determine the effects of scattering from alternative surroundings. Also, the use of a higher resolution X-ray sensitive detector may be beneficial, as the one used in this thesis was relatively low in resolution. Other future works may include further investigation into imaging low open fraction coded masks to confirm results presented in this thesis. The experiment could use multiple random arrays with the same vector size and PSFs. Lastly, investigations into the effects of 'relative perspective of a scene' to see how SNR, CNR and spatial resolution is impacted may prove beneficial to CMI. Additionally, further experiments are encouraged to confirm the effects of 'collimation' from a pinhole mask.

Glossary

Aperture Density The fraction of open elements of 1s in the array. (Also referred to as aperture density). p. 20

Autocorrelation A signal that is cross-correlated with itself. p. 17

Balanced Values for closed elements of the decoding array are $-\chi/1 - \chi$. p. 21

Bit-Depth The intensity range of colour or grey scale that comprise a pixel within an image. p. 14

Characteristic X-Rays X-rays with characteristics of a particular element, from the interaction of incident photons and electron in the atom. p. 12

Circular Shift Moving the elements of a sequence to the right so that the last element becomes the first, and subsequent elements are moved along to fill the vacant position. p. 25

Coded Mask A pattern of opaque and transparent regions on a mask that is used for encoding images. p. 20

Complex Scene An imaging scene that comprised of multiple points of light that are on and off axis to the central imaging axis. p. 43

Contrast A difference between two or more things, such a the colour, shade or intensity. p. 41

Convolution A mathematical operation used to find similarities between signals. p. 17

Cross-Correlation A mathematical operation used to find similarities between signals. p. 17

Cyclic Different Set A set of positive integers in an initial sequence modulo L, that is less than L. p. 22

Decoding Array An array with the same pattern as the encoding array which is used for decoding information. p. 20

Deconvolution The reverse operation of convolution. p. 19

Edge Response A measure of resolution from a sharpe edge within an image. p. 43

Encoding Array Array patterns that can be used to encode information. p. 20

Far-Field Referring to vast distances equivalent to that of a star in outer space. p. 4

Focal Length The distance between the convergence of radiation rays and focal point. p. 14

Focal Point A point where rays of radiation are converged to a singularity, resulting in a focused image. p. 14

Fourier Transform A conversion of signal from one domain to another. p. 19

Invariant A property that remains the same when a particular transformation takes place. p. 25

Kernel A small 2D array that is used in cross-correlation or convolution to alter the output array or image. Example kernels may be used for edge detection and blurring. p. 17

Lag The increment by which one signal slides over another during cross-correlation or convolution. p. 17

Light Radiation range that is visible to the human eye. p. 14

Line Pair A measure of resolution by distinguishing a pair of lines of the same width and separation distance. Units are typically in lp/mm. p. 44

Mapping A method of generating 2D arrays by entering the 1D binary sequence in the first row and column. Based on the value of the first column, each row is filled with the 1D binary sequence or its inverse. p. 23

Mask A radio-opaque medium placed in between an object and the detector that may contain a single or multiple apertures. p. 15

Matched The exact values for the encoding array is used for the decoding array. p. 22

Mismatched If the closed elements of the encoding array is 0 then this will become −1 for the decoding array. p. 22

Modulation Transfer Function The ability of a system to convert details of an object which is measured by the levels of greys within an image. p. 44

Near-Field Relatively short distances, typically a few meters. p. 4

No Two Holes Touching No two open elements of an array touching, due to the introduction of 0 elements between each row and column. p. 33

Noise Any signal that is unwanted. p. 37

Non-Redundant The spacing of open elements in an array that are non-repeating. p. 28

Open Fraction The fraction of open elements of 1s in the array. (Also referred to as open fraction). p. 20

Partially Redundant The distance between some open elements in an array are constant while others are not. p. 31

Pinhole Reference to a single aperture used to resolve an image. p. 15

Plateau The background or base of a PSF or δ-function. p. 21

Point Source An infinitesimal point of emitting radiation from an object. The object is comprised of a collection of these points to form an image. p. 14

Point Spread Function The imaging system response of a single point source. p. 20

Primary X-Rays Photons generated from the flow of high velocity electrons within an evacuated X-ray tube. p. 10

Resolving Medium A medium that is used to aid the process of resolving an image from radiation coming from all directions. An example includes a camera lens or a coded mask. p. 3

Rose Criterion A standard of measurement set by physicist Albert Rose that states, a signal is reliably distinguished from its background of noise for images when $SNR > 5$. p. 40

Side-Lobes Four thin regions in the background or base of a PSF that extend outwards to the edge of the array. Each lobe is perpendicular to the array's boundary. p. 21

Signal The conveyance of information with regards to the behaviour of some phenomenon. p. 14

Spatial Frequency The number of resolvable lines within a given unit distance. I.e, line pairs are an example. p. 44

Uniformly Redundant All separation distances of open regions in an array are constant. p. 24

Appendix A

Encoded Array Patterns

10×10	14×14	26×26	54×54
66×66	66×83	74×74	75×108
81×100	90×90	94×94	
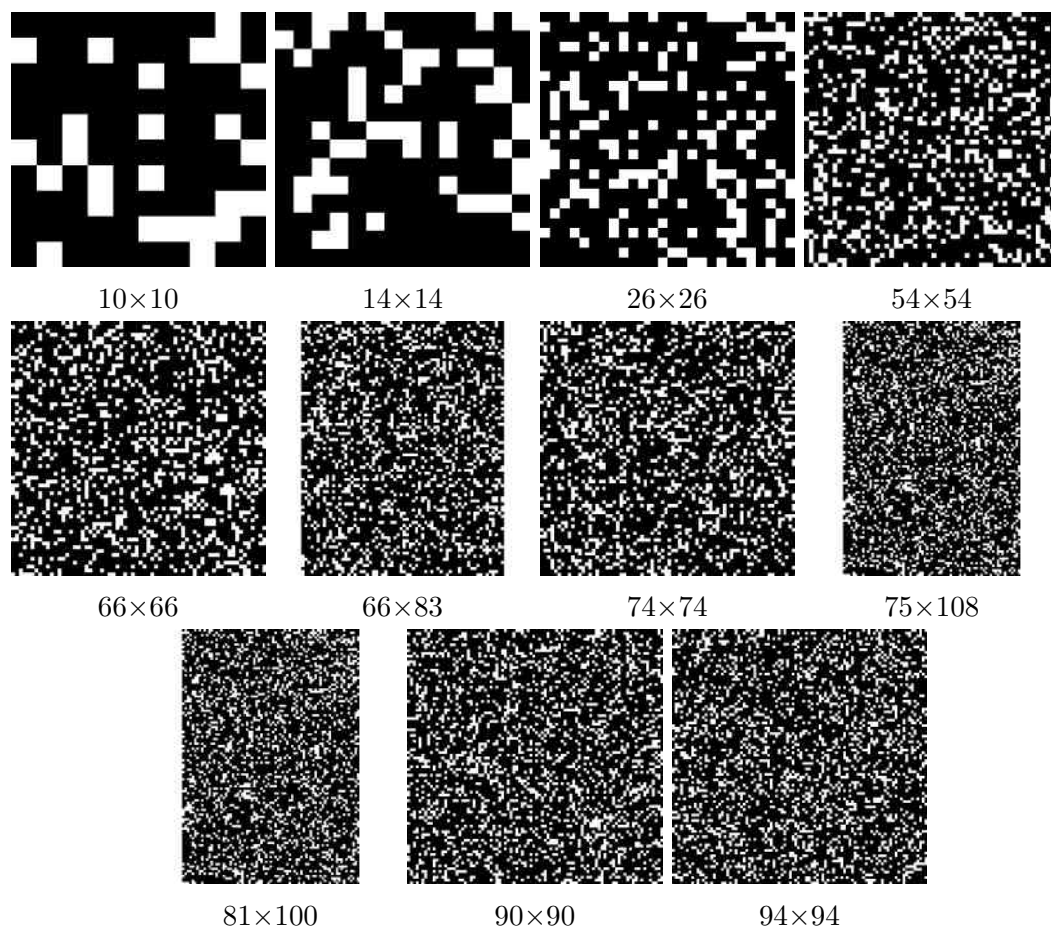
Figure A.1: Biquadratic Residues with $\chi = 0.25$.

13×13, χ = 0.43   13×21, χ = 0.40   13×31, χ = 0.38   13×57, χ = 0.36

13×73, χ = 0.36   21×21, χ = 0.36   21×31, χ = 0.34   21×57, χ = 0.31

21×73, χ = 0.30   31×31, χ = 0.31   31×57, χ = 0.28   31×73, χ = 0.27

57×57, χ = 0.24   57×73, χ = 0.23   73×73, χ = 0.22

Figure A.2: DURA Patterns.

11×14, $\chi = 0.20$ 15×23, $\chi = 0.25$ 16×21, $\chi = 0.25$ 16×23, $\chi = 0.33$

17×20, $\chi = 0.25$ 17×21, $\chi = 0.33$ 18×19, $\chi = 0.25$ 53×62, $\chi = 0.33$

71×77, $\chi = 0.25$ 11×11, $\chi = 0.33$ 19×19, $\chi = 0.34$ 20×20, $\chi = 0.14$

28×28, $\chi = 0.20$ 33×33, $\chi = 0.33$ 37×37, $\chi = 0.25$
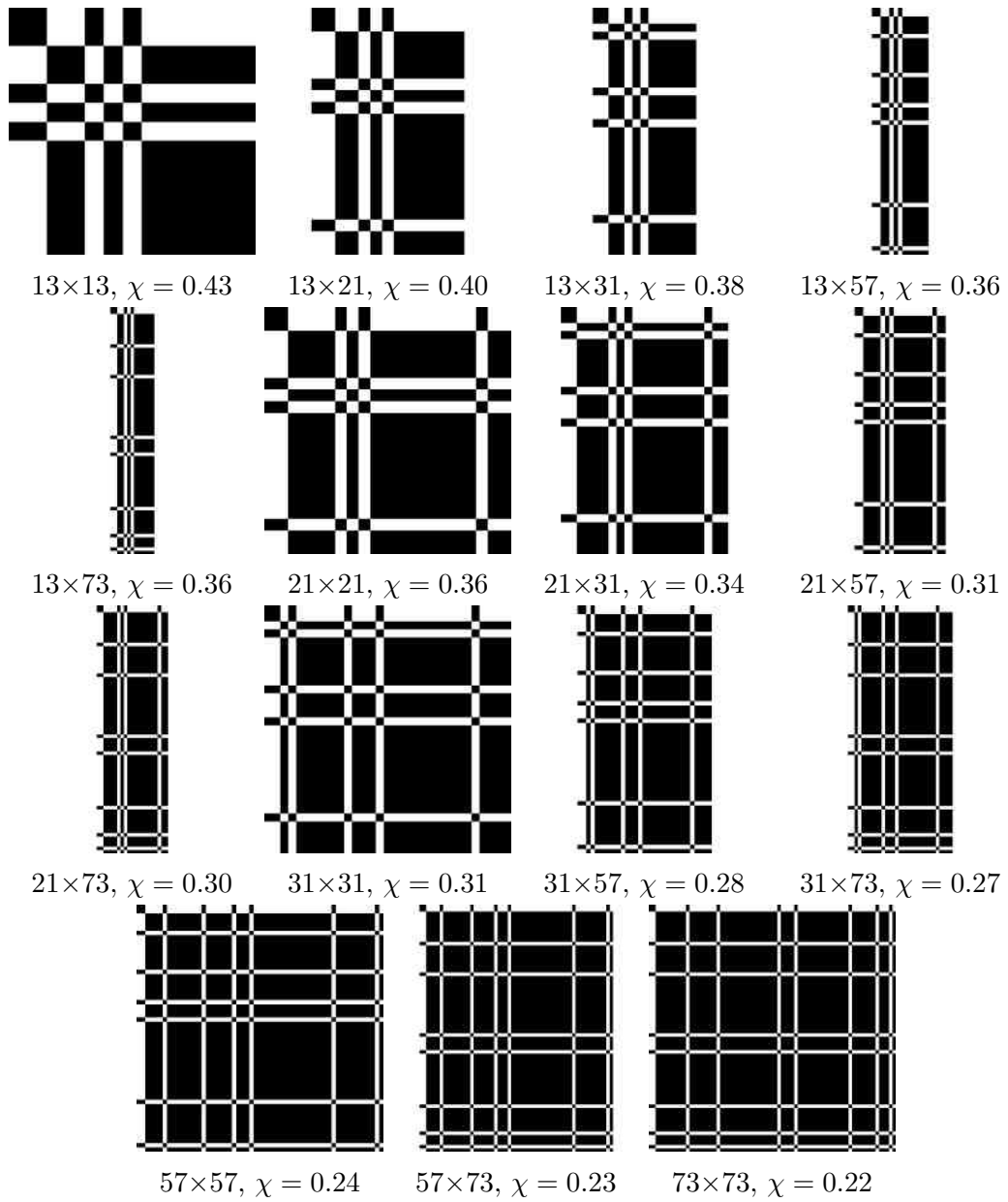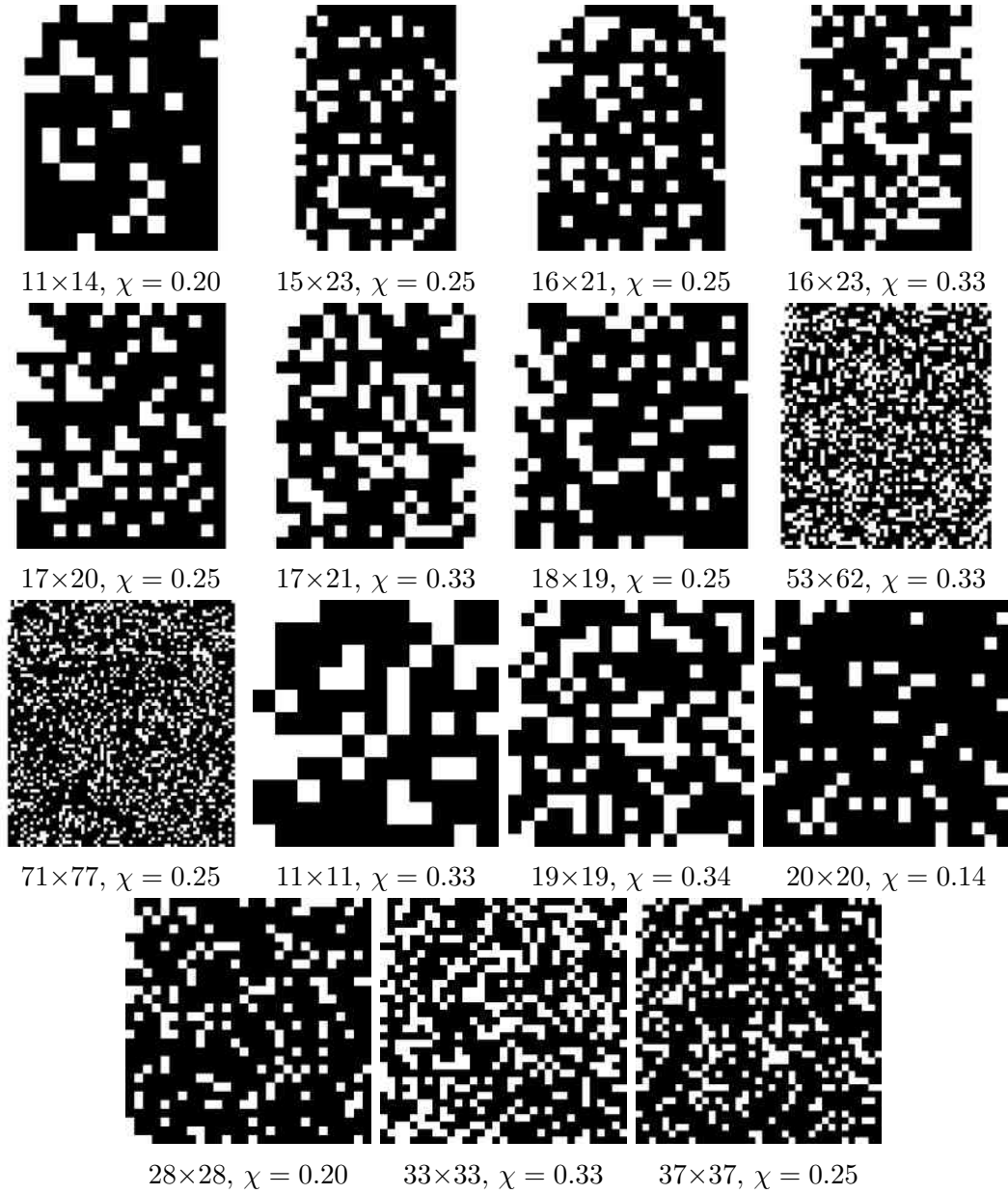
Figure A.3: Square and Rectangular Singer Arrays $\chi < 0.5$.

Appendix B

DURA PSFs

13×21, $\chi = 0.40$

13×31, $\chi = 0.38$

13×57, $\chi = 0.36$

13×73, $\chi = 0.36$
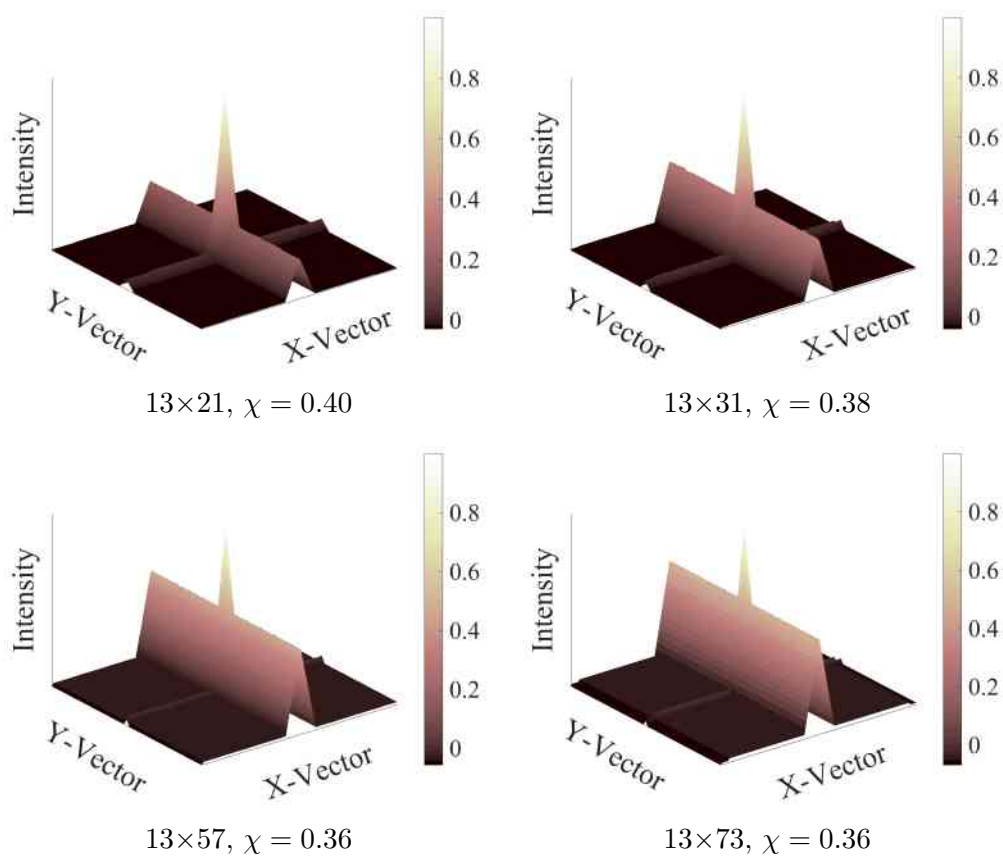
Figure B.1: Theoretical PSFs of Rectangular DURAs.

$21 \times 31, \chi = 0.34$

$21 \times 57, \chi = 0.31$

$21 \times 73, \chi = 0.30$

$31 \times 57, \chi = 0.28$

$31 \times 73, \chi = 0.27$

$57 \times 73, \chi = 0.23$
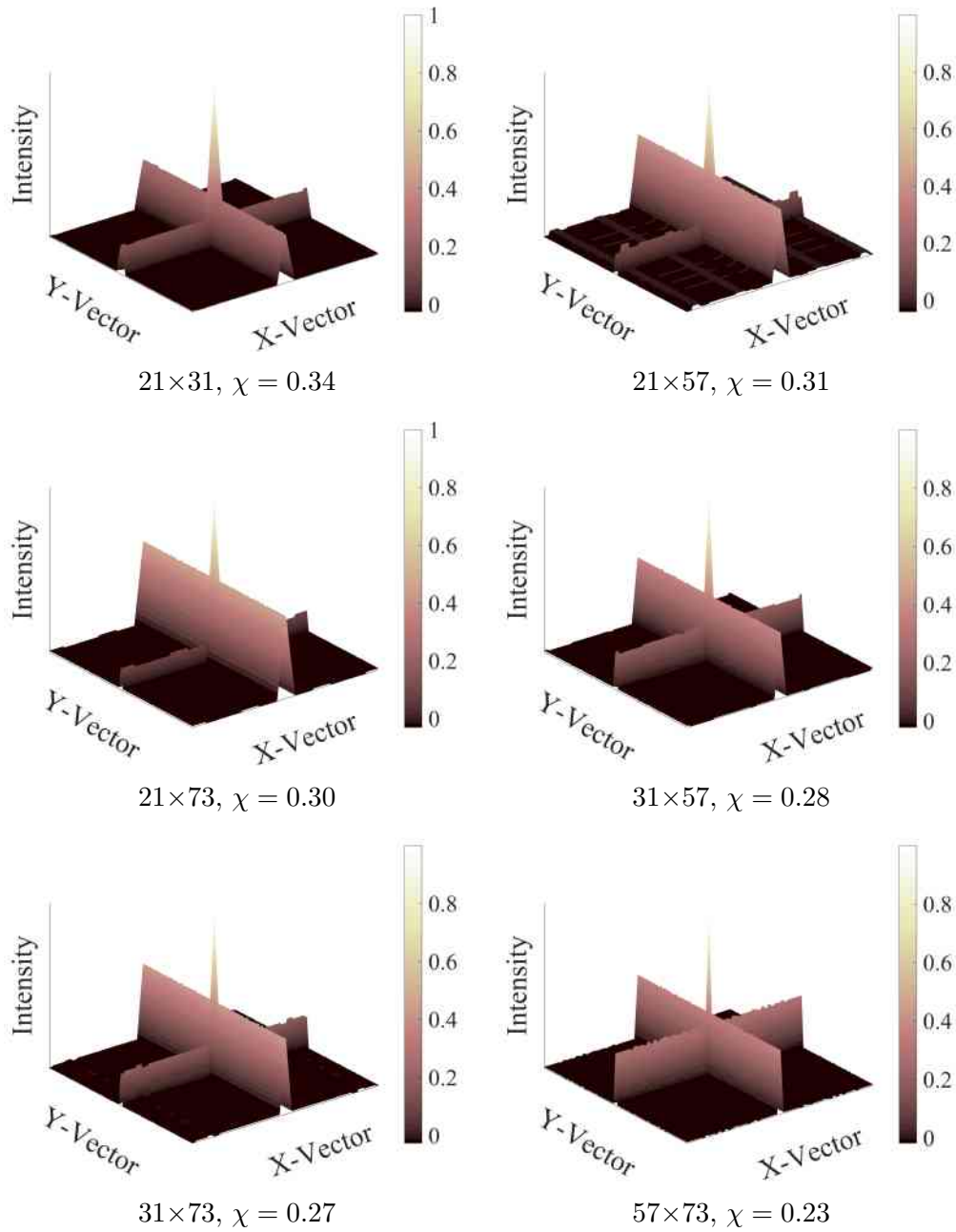
Figure B.2: Theoretical PSFs of Rectangular DURAs Continued.

13×13, $\chi = 0.43$

21×21, $\chi = 0.36$

31×31, $\chi = 0.31$

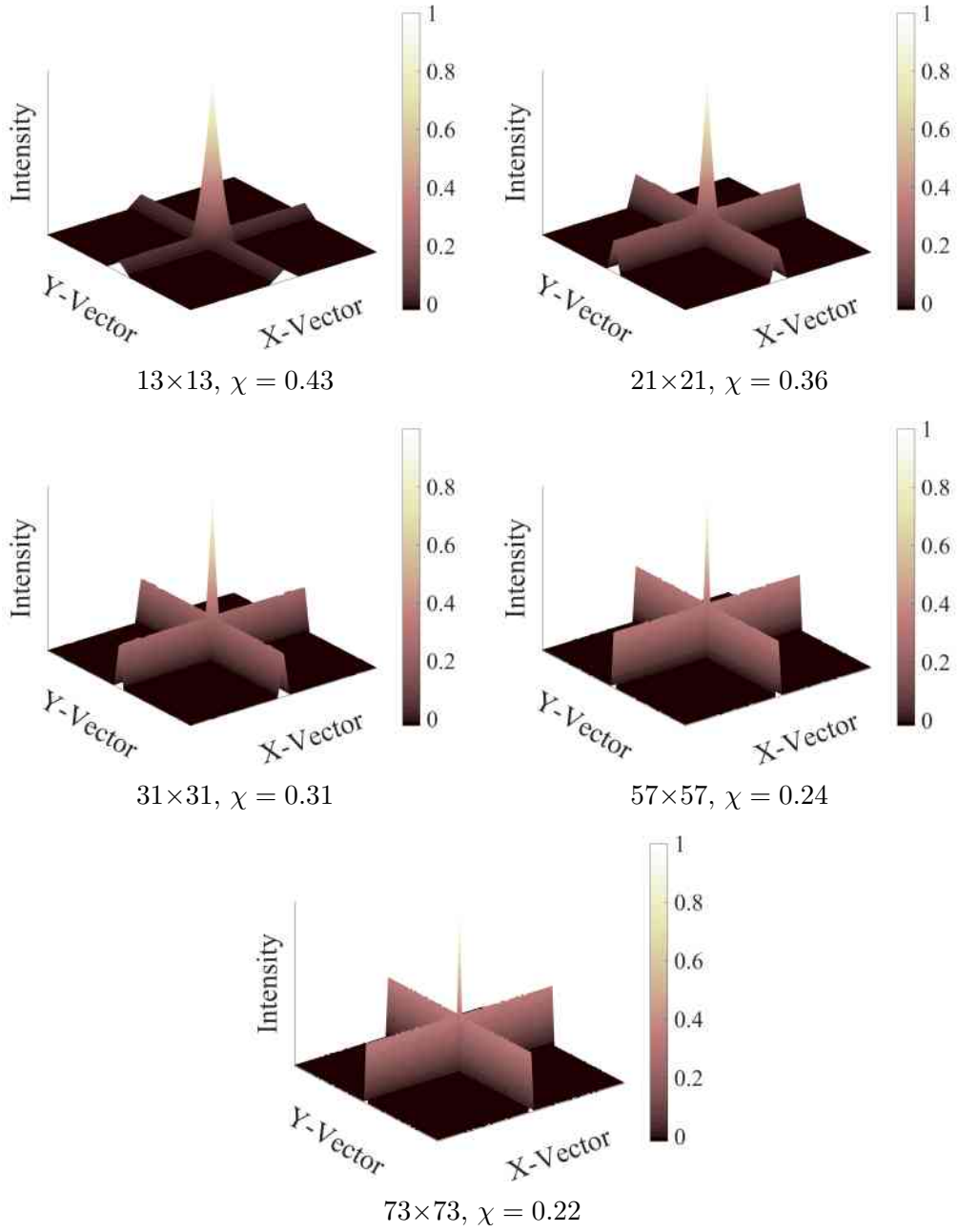57×57, $\chi = 0.24$

73×73, $\chi = 0.22$

Figure B.3: Theoretical PSFs of Square DURAs Continued.

Appendix C

Journal Publications

Title	*Low open fraction coded masks for X-ray backscatter imaging*
Authors	A. Muñoz, A. Vella, M. Healy, D. Lane, I. Jupp, D. Lockley
Journal	Optical Engineering
Publisher	SPIE
Accepted	30 August 2018
Reference	Muñoz et al. (2018a)

Title	*Rapid prototyping coded masks for x-ray backscatter imaging*
Authors	A. Muñoz, A. Vella, M. Healy, D. Lane, I. Jupp, D. Lockley
Journal	Optical Engineering
Publisher	SPIE
Accepted	7 August 2018
Reference	Muñoz et al. (2018b)

Appendix D

Conference Publications

Title	*X-ray backscatter radiography with lower open fraction coded masks*
Authors	A. Muñoz, A. Vella, M. Healy, D. Lane, I. Jupp, D. Lockley
Conference	SPIE 10393A (INVITED)
Accepted	7 September 2017
Reference	Munoz et al. (2017a)

Title	*3D-printed coded apertures for x-ray backscatter radiography*
Authors	A. Muñoz, A. Vella, M. Healy, D. Lane, I. Jupp, D. Lockley
Conference	SPIE 10393F (INVITED)
Accepted	7 September 2017
Reference	Munoz et al. (2017b)

Title	*Use of simulation to optimize the pinhole diameter and mask thickness for an x-ray backscatter imaging system*
Authors	A. Vella, A. Muñoz, M. Healy, D. Lane, D. Lockley
Conference	SPIE 103880Y
Received	23 August 2017
Reference	Vella et al. (2017a)

Title	*A fast and reliable approach to simulating the output from an x-ray tube used for developing security backscatter imaging*
Authors	A. Vella, A. Muñoz, M. Healy, D. Lane, D. Lockley, J. Zhou
Conference	SPIE 103880X
Received	23 August 2017
Reference	Vella et al. (2017b)

Bibliography

Accorsi, R. (2001). *Design of Near-Field Coded Aperture Cameras for High-Resolution Medical and Industrial Gamma-Ray Imaging*. PhD thesis, Massachusetts Institute of Technology.

Accorsi, R., Gasparini, F., and Lanza, R. C. (2001). Optimal coded aperture patterns for improved SNR in nuclear medicine imaging. *Nuclear Instruments and Methods in Physics Research Section A: Accelerators, Spectrometers, Detectors and Associated Equipment*, 474(3):273–284.

Accorsi, R. and Lanza, R. C. (2001). *Near-Field Artifact Reduction in Planar Coded Aperture Imaging*. PhD thesis, Massachusetts Institute of Technology.

Barker, R. H. (1953). Group Synchronizing of Binary Digital Sequences, in "Communication Theory". *Butterworth*, pages 273–287.

Barrett, H. H. and Swindel, W. (1981). *Radiological Imaging: The Theory of Image Formation, Detection, and Processing*. Academic Press.

Baumert, L. D. (1971). *Cyclic Difference Sets*, volume 182 of *Lecture Notes in Mathematics*. Springer Berlin Heidelberg, Berlin, Heidelberg.

Bell, J. T. (2009). *Detection of Improvised Explosive Devices at Long-Range Using Coded Aperture Imaging of Backscattered X-Rays with Dynamic Reconstruction*. PhD thesis, Massachusetts Institute Technology.

Biggs, D. S. C. and Andrews, M. (1997). Acceleration of Iterative Image Restoration Algorithms. *Applied Optics*, 36(8):1766–1775.

Bird, A. J., Bazzano, A., Malizia, A., Fiocchi, M., Sguera, V., Bassani, L., Hill, A. B., Ubertini, P., and Winkler, C. (2016). THE IBIS SOFT GAMMA-RAY SKY AFTER 1000 INTEGRAL ORBITS. *The Astrophysical Journal Supplement Series*, 223(1):15.

BJB Enterprises, I. (2014). TC-1600 A/B Data Sheet. Available from: http://bjbenterprises.com/media/wysiwyg/pdfs/Epoxies/TC-1600.pdf (Accessed 23 October 2018).

Bousselham, A., Barrett, H. H., Bora, V., and Shah, K. (2010). Photoelectron Anticorrelations and Sub-Poisson Statistics in Scintillation Detectors. *Nuclear Instruments and Methods in Physics Research Section A: Accelerators, Spectrometers, Detectors and Associated Equipment*, 620(2-3):359–362.

Bracewell, R. N. (2000). The Fourier Transform and its Applications. *McGraw-Hill*, pages 24–47.

Brigham, E. (1988). *The Fast Fourier Transform and its Applications.* Prentice- Hall Inc, 3rd edition.

Brown, C. (1974). Multiplex Imaging with MultiplePinhole Cameras. *Journal of Applied Physics*, 45(4):1806–1811.

Burgess, A. E. (1999). The Rose Model, Revisited. *Journal of the Optical Society of America A*, 16(3):633.

Busboom, A., Elders-Boll, H., and Dieter Schotten, H. (1997). Combinatorial Design of Near-Optimum Masks for Coded Aperture Imaging. *1997 IEEE International Conference on Acoustics, Speech, and Signal Processing*, 4:2817–2820.

Busboom, A., Elders-Boll, H., and Schotten, H. (1998). Uniformly Redundant Arrays. *Kluwer Academic Publishers*, 8:97–123.

Bushberg, J. T., Seibert, J. A., Leidholdt Jr, E. M., and Boone, J. M. (2012). The Essential Physics of Medical Imaging. *Lippincott Williams and Wilkins*, pages 38–94.

Bushong, S. (2017). *Radiologic Science for Technologists.* Elsevier, 11 edition.

Byard, K. (2014). Fast decoding Algorithms for Coded Aperture Systems. *Nuclear Instruments and Methods in Physics Research Section A: Accelerators, Spectrometers, Detectors and Associated Equipment*, 754:36–41.

Byard, K. and Shutler, P. M. (2017). Singer Product AperturesA coded Aperture System with a Fast Decoding Algorithm. *Nuclear Instruments and Methods in Physics Research Section A: Accelerators, Spectrometers, Detectors and Associated Equipment*, 856:147–153.

Cannon, T. M. and Fenimore, E. E. (1980). Coded Aperture Imaging: Many Holes Make Light Work. *Optical Engineering*, 19(3):282–289.

Cao, G., Zhang, J., Zhou, O., and Lu, J. (2009). Temporal Multiplexing Radiography for Dynamic X-ray Imaging. *Review of Scientific Instruments*, 80(9):093902.

Caroli, E., J., S., Di Cocco, G., Natalucci, L., and Spzzichino, A. (1987). Coded Aperture Imaging in X - and Gamma Ray Astronomy. *Kluwer Academic Publishers*, 45:349–403.

Cherry, S. R., Sorenson, J. A., and Phelps, M. E. (2012). Physics in Nuclear Medicine. *Saunders Elsevier*, pages 74–76.

Cieślak, M. J., Gamage, K. A., and Glover, R. (2016). Coded-Aperture Imaging Systems: Past, Present and Future Development A Review. *Radiation Measurements*, 92:59–71.

Dassault Systemes (2015). Solidworks. Available from: http://www.solidworks.co.uk/, (Accessed 23 October 2018).

Datema, C. P., Bom, V. R., and van Eijk, C. W. (2003). Monte Carlo Simulations of Landmine Detection using Neutron Backscattering Imaging. *Nuclear Instruments and Methods in Physics Research Section A: Accelerators, Spectrometers, Detectors and Associated Equipment*, 513(1-2):398–402.

DeWeert, M. J. and Farm, B. P. (2015). Lensless Coded-Aperture Imaging with Separable Doubly-Toeplitz Masks. *Optical Engineering*, 54(2):023102.

Dhillon, V. (2010). The CCD Equation. Available from: http://www.vikdhillon.staff.shef.ac.uk (Accessed 8 October 2018).

Dicke, R. H. (1968). Scatter-Hole Cameras for X-Rays and Gamma Rays. *Astrophysical Journal*, 153:L101.

Dinca, D.-C., Schubert, J. R., and Callerame, J. (2008). X-ray Backscatter Imaging. In Halvorson, C. S., Lehrfeld, D., and Saito, T. T., editors, *American Science and Engineering*, volume 6945, page 694516.

Faust, A. A. (2002). Detection of Explosive Devices using X-ray Backscatter Radiation. In Barber, H. B., Roehrig, H., Doty, F. P., Porter, L. J., and Morton, E. J., editors, *Penetrating Radiation Systems and Applications IV*, volume 4786, page 17.

Fenimore, E. E. and Cannon, T. M. (1978). Coded Aperture Imaging with Uniformly Redundant Arrays. *Applied optics*, 17(3):337–347.

Fenimore, E. E. and Cannon, T. M. (1981). Uniformly Redundant Arrays: Digital Reconstruction Methods. *Applied optics*, 20(10):1858–1864.

Fenimore, E. E. and Gottesman, S. (1989). New Family of Binary Arrays for Coded Aperture Imaging. *Applied optics*, 28(20):4344–4352.

Fish, D. a., Brinicombe, a. M., Pike, E. R., and Walker, J. G. (1995). Blind Deconvolution by Means of the RichardsonLucy Algorithm. *Journal of the Optical Society of America A*, 12(1):58.

Ghaye, J. M. (2015). *Image Processing on Reconfigurable Hardware for Continuous Monitoring of Fluorescent Biomarkers in Cell Cultures*. PhD thesis, Institute of Electrical Engineering.

Golay, M. J. E. (1971). Point Arrays Having Compact, Nonredundant Autocorrelations. *Journal of the Optical Society of America*, 61(2):272.

Gottesman, S. and Schneid, E. (1986). PNP - A New Class of Coded Aperture Arrays. *IEEE Transactions on Nuclear Science*, 33(1):745–749.

Gunson, J. and Polychronopulos, B. (1976). Optimum Design of A Coded Mask X-Ray Telescope for Rocket Applications. *Royal Astronomical Society*, 177:485–497.

Gupta, B. C. and Guttman, I. (2013). *Statistics and Probability with Applications for Engineers and Scientists*. Wiley.

Hainaut, O. (2005). Signal, Noise and Detection. Available from: https://www.eso.org/~ohainaut/ccd/sn.html (Accessed 10 August 2018).

Hammersley, A., Ponman, T., and Skinner, G. (1992). Reconstruction of images from a coded-aperture box camera. *Nuclear Instruments and Methods in Physics Research Section A: Accelerators, Spectrometers, Detectors and Associated Equipment*, 311(3):585–594.

Hausladen, P., Newby, J., Liang, F., and Blackston, M. (2013). A Deployable Fast-Neutron Coded-Aperture Imager for Quantifying Nuclear Material. *Oak Rige National Laboratory*, 248(July):1–5.

Hecht, E. (2017). *Optics*. Pearsons.

Hendee, W. R. and R, R. E. (2002). Medical Imaging Physics. *Wiley-Liss Inc*, pages 57–59.

Herr, M. D., Mclnerney, J. J., Copenhaver, G. L., and Lamser, D. L. (1994). A Flying Spot X-Ray System for Compton Backscatter Imaging. *IEEE Transactions on Medical Imaging*, 13(3):461–469.

HITACHI (2001). SU5000 SEM. Available from: http://www.hitachi-hightech.com/(Accessed 25 January 2018).

Howell, S. B. (1989). Two-Dimensional Aperture Photometry - Signal-to-Noise Ratio of Point-Source Observations and Pptimal Data-Extraction Techniques. *Publications of the Astronomical Society of the Pacific*, 101(June):616.

Howell, S. B. (2006). Handbook of CCD Astronomy. *Cambridge University Press*, pages 53–56.

194

Hubbell, J. H., Seltzer, S. M., Hubblell, H. J., and Seltzer, M. S. (1996). Tables of X-Ray Mass Attenuation Coefficients. Available from: http://www.nist.gov/pml/data/xraycoef/index.cfm, (Accessed 19 August 2018).

Hughes, I. G. and Hase, T. P. (2010). Measurements and their Uncertainties. *Oxford University Press*, page 14.

In 't Zand, J., Heise, J., and Jager, R. (1994). The Optimum Open Fraction of Coded Apertures. With an Application of the Wide Field X-ray Cameras of SAX. *European Southern Observatory*, 288:665–674.

Inc, A. (2015). X-Ray Fluorescence. Available from: http://www.amptek.com/xrf/, (Accessed 19 August 2018).

Inc, T. H. P. (2001). Technon / Poly Kit. Available from: http://www.thpap.com/(Accessed 8 February 2018).

Ivanov, O., Sudarkin, A., Stepanov, V., and Urutskoev, L. (1999). Portable X-ray and Gamma-Ray Imager with Coded Mask: Performance Characteristics and Methods of Image Reconstruction. *Nuclear Instruments and Methods in Physics Research Section A: Accelerators, Spectrometers, Detectors and Associated Equipment*, 422(1-3):729–734.

Jayanthi, U. and Braga, J. (1991). Physical Implementation of an Antimask in URA Based Coded Mask Systems. *Nuclear Instruments and Methods in Physics Research Section A: Accelerators, Spectrometers, Detectors and Associated Equipment*, 310(3):685–689.

Jennings, D. and Byard, K. (1997). An Extension for Residue Difference Sets. *Discrete Mathematics*, 167–168:405–410.

Jordan, D. W. and Smith, P. (2008). *Mathematical Techniques.* Oxford University Press, 4 edition.

Jupp, I. (1996). *The Optimisation of Discrete Pixel Coded Aperture Telescopes.* PhD thesis, University of Southampton.

Klein, O. and Nishina, Y. (1929). Uber die Streuung von Strahlung durch freie Elektronen nach der neuen relativistischen Quantendynamik von Dirac. *Zeitschrift fur Physik*, 52(11-12):853–868.

Kopilovich, L. (1988). Cpnstruction of Nonredundant Masks over Square Grids using Different Sets. *Optics Communication*, 68(1):7–10.

Lakshmanan, M. N., Greenberg, J. A., Samei, E., and Kapadia, A. J. (2017). Accuracy assessment and characterization of x-ray coded aperture coherent scatter spectral imaging for breast cancer classification. *Journal of Medical Imaging*, 4(1):013505.

Laserlines (2017). Desktop Metal Studio System. Available from: https://3dprinting.co.uk/metal-3d-printers/desktop-metal-studio-system/ (Accessed 19 July 2018).

Lucy, L. B. (1974). An Iterative Technique for the Rectification of Observed Distributions. *The Astronomical Journal*, 79(6):745–754.

MathWorks (2018). MATLAB. Available from: http://uk.mathworks.com/products/matlab/, (Accessed 24 January 2018).

Mertz, L. and Young, N. O. (1961). Fresnel Transformation of Images. In *Optical Instruments and Techniques (Chapman and Hall Ltd)*, pages 305–310.

MI, M. (2015). Wolfmet Tungsten Alloys. Available from: https://www.mimaterials.com/news/wolfmet-tungsten-alloys-announces-new-3d-additive-manufacturing-capability (Accessed 19 July 2018).

Micromeritics (1996). Accupyc 1330 Pycnometer. Available from: http://www.micromeritics.com/(Accessed 25 January 2018).

Mielenz, K. D. (1999). On the diffraction limit for lensless imaging. *Journal of Research of the National Institute of Standards and Technology*, 104(5):479.

Miller, B. W., Moore, J. W., Barrett, H. H., Fry, T., Adler, S., Sery, J., and Furenlid, L. R. (2011). 3D printing in X-Ray and Gamma-Ray Imaging: A Novel Method for Fabricating High-Density Imaging Apertures. *Nuclear Instruments and Methods in Physics Research, Section A: Accelerators, Spectrometers, Detectors and Associated Equipment*, 659(1):262–268.

Morrison, J. C. (2010). Modern Physics for Scientists and Engineers. *Academic Press*, pages 13–14.

Mortara, L. and Fowler, A. (1981). Evaluations Of Charge-Coupled Device (CCD) Performance For Astronomical Use. *SPIE*, 290:28–32.

Mu, Z. and Liu, Y. H. (2006). Aperture Collimation Correction and Maximum-Likelihood Image Reconstruction for Near-Field Coded Aperture Imaging of Single Photon Emission Computerized Tomography. *IEEE Transactions on Medical Imaging*, 25(6):701–711.

Munoz, A. A. M., Lane, D. W., Healy, M. J. F., Vella, A., Lockley, D., and Jupp, I. D. (2017a). X-ray Backscatter Radiography with Lower Open Fraction Coded Masks. In Grim, G. P., Barber, H. B., and Furenlid, L. R., editors, *Radiation Detectors in Medicine, Industry, and National Security XVIII*, page 9. SPIE.

Munoz, A. A. M., Vella, A., Healy, M. J. F., Lane, D. W., Jupp, I., and Lockley, D. (2017b). 3D-Printed Coded Apertures for X-Ray Backscatter Radiography. In *Radiation Detectors in Medicine, Industry, and National Security XVIII*, page 14. SPIE.

Muñoz, A. A. M., Vella, A., Healy, M. J. F., Lane, D. W., Jupp, I., and Lockley, D. (2018a). Low Open Fraction Coded Masks for X-Ray Backscatter Imaging. *Optical Engineering*, 57(09):1.

Muñoz, A. A. M., Vella, A., Healy, M. J. F., Lane, D. W., Jupp, I., and Lockley, D. (2018b). Rapid Prototyping-Coded Masks for X-Ray Backscatter Imaging. *Optical Engineering*, 57(08):1.

Nagell, T. (1951). *Introduction to Number Theory*. Wiley.

Newberry, M. V. (1991). Signal-to-Noise Considerations for Sky-Subtracted CCD Data. *Publications of the Astronomical Society of the Pacific*, 103(January):122.

Norton, J. A. (2004). Observing the Universe. *The Open University*, page 23.

Paradiso, V., Amgarou, K., Lanaute, N. B. D., Schoepff, V., Amoyal, G., Mahe, C., Beltramello, O., and Liénard, E. (2017). A Panoramic Coded Aperture Gamma Camera for Radioactive Hotspots Localization. *Journal of Instrumentation*, 12(11):P11010–P11010.

Park, C. (1972). Lecture Notes in Mathematics Conference. *Lecture Notes in Mathematics*, page 1.

Photonic Science (2017). Gemstar X-Ray Camera. Available from: http://www.photonic-science.co.uk/(Accessed 25 June 2018).

Prince, J. L. and M, L. J. (2015). Medical Imaging Signals and Systems. *Pearson Education Inc*, pages 116–117.

Rayleigh, L. (1891a). Some Applications of Photography. *Nature*, 44(1133):249–254.

Rayleigh, L. (1891b). X. On Pin-Hole Photography. *The London, Edinburgh, and Dublin Philosophical Magazine and Journal of Science*, 31(189):87–99.

Redus, R. H., Huber, A. C., and Sperry, D. J. (2008). Dead Time Correction in the DP5 Digital Pulse Processor. In *2008 IEEE Nuclear Science Symposium Conference Record*, pages 3416–3420. IEEE.

Richardson, W. H. (1972). Bayesian-Based Iterative Method of Image Restoration. *Journal of the Optical Society of America*, 62(1):55.

Richmond, M. (2018). Signal Versus Noise. Available from: http://spiff.rit.edu/classes/phys373/lectures/signal/signal_illus.html (Accessed 10 August 2018).

Rubio, M. and Mainardi, R. T. (1984). Determination of X-Ray Spectra Including Characteristic Line Intensities From Attenuation Data. *Physics in Medicine and Biology*, 29(11):1371–1376.

Sambo, L. (2011). *An Iterative Method to Deconvolve Coded-Mask Images.* PhD thesis, Universita degli Studi di Ferrara.

Schmeelk, J. (1994). Two-Dimensional Dirac Delta Reconsidered. *Kluwer Academic Publishers-Plenum Publishers*, 7(4):315–332.

Schroeder, D. J. (2000). Astronomical Optics. *Academic Press*, page 433.

Serway, R. A. and Jewett Jr, J. W. (2011). Physics for Scientists and Engineer with Modern Physics. *Brookes/Cole*, page 1011.

Shutler, P. M., Springham, S. V., and Talebitaher, A. (2014). Periodic Wrappings in Coded Aperture Imaging. *Nuclear Instruments and Methods in Physics Research Section A: Accelerators, Spectrometers, Detectors and Associated Equipment*, 738:132–148.

Shutler, P. M. E., Springham, S. V., and Talebitaher, A. (2013). Mask design and fabrication in coded aperture imaging. *Nuclear Instruments and Methods in Physics Research, Section A: Accelerators, Spectrometers, Detectors and Associated Equipment*, 709:129–142.

Simpson, R. G. (1978). *Annular Coded-Aperture Imaging System for Nuclear Medicine.* PhD thesis, The University of Arizona.

Simpson, R. G. and Barrett, H. H. (1980). Imaging for Medicine. In *Imaging for Medicine*, chapter 8, pages 217–311. Plenum Press.

Skinner, G. K. (1984). Imaging With Coded-Aperture Masks. *Nuclear Instruments and Methods in Physics Research*, 221:33–40.

Smith, S. W. (1999). *The Scientist and Engineer's Guide to Digital Signal Processing.* California Technical Puplishing, 2 edition.

Starfield, D. M. (2009). *Towards Clinically Useful Coded Apertures for Planar Nuclear Medicine Imaging.* PhD thesis, University of the Witwatersrand.

Sun, S., Zhang, Z., Shuai, L., Li, D., Wang, Y., Liu, Y., Huang, X., Tang, H., Li, T., Chai, P., Jiang, X., Ma, B., Zhu, M., Wang, X., Zhang, Y., Zhou, W., Zeng, F., Guo, J., Sun, L., Yang, M., Zhang, Y., Wei, C., Ma, C., and Wei, L. (2015). Development of a Panorama Coded-Aperture Gamma Camera for Radiation Detection. *Radiation Measurements*, 77:34–40.

Talebitaher, A., Springham, S. V., Shutler, P. M. E., Lee, P., and Rawat, R. S. (2012). Imaging of Plasma Focus Fusion by Proton Coded Aperture Technique. *Journal of Fusion Energy*, 31(3):234–241.

Thompson, A., Attwood, D., Gullikson, E., Howells, M., Kim, K.-J., Kirz, J., Kortright, J., Lindau, I., Pianetta, P., Robinson, A., Scofield, J., Underwood, J., and Williams, G. (2009). X-Ray Data Booklet: Scattering of X-Rays from Electrons and Atoms. *Lawrence Berkeley National Laboratory*, pages 3.1–3.12.

Towe, B. C. and Jacobs, A. M. (1981). X-Ray compton scatter imaging using a high speed flying spot X-ray tube. *IEEE Transactions on Biomedical Engineering*, BME-28(10):717–721.

Ultimaker (2015). Ultimaker 2 Extended. Available from: https://ultimaker.com (Accessed 29 January 2018).

van den Heuvel, J. and Fiore, F. (2012). Simulation Study of X-Ray Backscatter Imaging of Pressure-Plate Improvised Explosive Devices. In Broach, J. T. and Holloway, J. H., editors, *Detection and Sensing of Mines, Explosive Objects, and Obscured Targets XVII*, volume 8357, page 835716.

Vella, A., Munoz, A., Healy, M., Lane, D., and Lockley, D. (2018). An artificial X-Ray Wire Test Emitter and Calculations on the Resolution and Field of View of X-Ray Pinhole Optics by Simulation. *Nuclear Instruments and Methods in Physics Research Section A: Accelerators, Spectrometers, Detectors and Associated Equipment*, 905(July):119–128.

Vella, A., Munoz, A. A. M., Healy, M. J. F., Lane, D. W., and Lockley, D. (2017a). The use of Simulation to Optimize the Pinhole Diameter and Mask Thickness for an X-Ray Backscatter Imaging System. In Sawhney, K. and Chubar, O., editors, *Advances in Computational Methods for X-Ray Optics IV*, page 34. SPIE.

Vella, A., Munoz, A. M. A., Healy, M. J. F., Lane, D. W., Lockley, D., and Zhou, J. G. (2017b). A Fast and Reliable Approach to Simulating the Output from an X-Ray Tube used for Developing Security Backscatter Imaging. In Sawhney, K. and Chubar, O., editors, *Advances in Computational Methods for X-Ray Optics IV*, page 33. SPIE.

VJT (2017). VJ Technology. Available from: http://www.vjt.com/(Accessed 25 June 2018).

Welvaert, M. and Rosseel, Y. (2013). On the Definition of Signal-To-Noise Ratio and Contrast-To-Noise Ratio for fMRI Data. *PLoS ONE*, 8(11):1–10.

Wild, W. J. (1983). Dilute Uniformly Redundant Sequences for use in Coded-Aperture Imaging. *Optics Letters*, 8(5):247–249.

Wolfmet (2016). Tungsten Alloys Technical Information. Available from: https://www.wolfmet.com/wp-content/uploads/2017/01/Wolfmet_Tungsten_Alloys_Technical_Information.pdf (Accessed 13 January 2018).

Woolf, R. S., Phlips, B. F., Hutcheson, A. L., and Wulf, E. A. (2015). Fast-Neutron, Coded-Aperture Imager. *Nuclear Instruments and Methods in Physics Research Section A: Accelerators, Spectrometers, Detectors and Associated Equipment*, 784:398–404.

Young, M. (1971). Pinhole Optics. *Applied optics*, 10(12):2763–2767.

Zhang, L., Lanza, R., Horn, B., and Zimmerman, R. (1982). High Energy 3-D Nuclear Medicine Imaging using Coded Apertures with a Conventional Gamma Camera. In *1998 IEEE Nuclear Science Symposium Conference Record. 1998 IEEE Nuclear Science Symposium and Medical Imaging Conference*, volume 3, pages 1532–1534. IEEE.

Index